5-2013

Measurement of The Temperature Dependence of Radiation Induced Conductivity in Polymeric Dielectrics

Jodie Corbridge Gillespie
Utah State University

UtahStateUniversity
MERRILL-CAZIER LIBRARY

MEASUREMENTS OF THE TEMPERATURE DEPENDENCE OF RADIATION INDUCED

CONDUCTIVITY IN POLYMERIC DIELECTRICS

by

Jodie Gillespie

A thesis submitted in partial fulfillment
of the requirements for the degree

of

MASTER OF SCIENCE

in

Physics

Approved:

_____   _____
Dr. JR Dennison   Dr. D. Mark Riffe
Major Professor   Committee Member

_____   _____
Dr. David Peak   Dr. Mark R. McLellan
Committee Member   Vice President for Research and
                                         Dean of the School of Graduate Studies

UTAH STATE UNIVERSITY
Logan, Utah

2013

ABSTRACT

Measurements of the Temperature Dependence of Radiation

Induced Conductivity in Polymeric Dielectrics

by

Jodie Gillespie, Master of Science

Utah State University, 2013

Major Professor: Dr. JR Dennison
Department: Physics

This study measures Radiation Induced Conductivity (RIC) in five insulating polymeric materials over temperatures ranging from ~110 K to ~350 K: polyimide (PI or Kapton HN[TM] and Kapton E[TM]), polytetraflouroethylene (PTFE or Teflon[TM]), ethylene-tetraflouroethylene (ETFE or Tefzel[TM]), and Low Density Polyethylene (LDPE). RIC occurs when incident ionizing radiation deposits energy and excites electrons into the conduction band of insulators. Conductivity was measured when a voltage was applied across vacuum-baked, thin film polymer samples in a parallel plate geometry. RIC was calculated as the difference in sample conductivity under no incident radiation and under an incident ~4 MeV electron beam at low incident dose rates of 0.01 rad/sec to 10 rad/sec. The steady-state RIC was found to agree well with the standard power law relation, $\sigma_{RIC}(\dot{D}) = k_{RIC}(T)\, \dot{D}^{\Delta(T)}$ between conductivity, σ_{RIC} and adsorbed dose rate, $\dot{D}$.   Both the proportionality constant, k_{RIC}, and the power, Δ, were found to be temperature-dependent above ~250 K, with behavior consistent with photoconductivity models developed for localized trap states in disordered semiconductors. Below ~250 K, k_{RIC} and Δ exhibited little change in any of the materials.

(178 pages)

PUBLIC ABSTRACT

Measurements of the Temperature Dependence of Radiation

Induced Conductivity in Polymeric Dielectrics

by

Jodie Gillespie, Master of Science

Utah State University, 2013

Radiation Induced Conductivity (RIC) is the change in conductivity of a material due to bombardment from incident high energy radiation. This study is to determine the effect of RIC and RIC's temperature dependence in polymeric dielectrics, specifically Kapton HN, Kapton E, PTFE Teflon, Tefzel, and Low Density Polyethylene (LDPE). Interest in these materials arises from applications for use in future spacecraft, specifically the James Webb Space Telescope (JWST).

One major issue in the design of JWST, as in all spacecraft, is the charging and arcing of exposed materials, resulting in fatal damage to the electronics and/or the craft itself. Particles prevalent in space environments bombard spacecraft, resulting in charge deposition. The electric field within the bombarded sample increases over time, finally resulting in a high enough potential difference to cause arcing from high potential surfaces to low potential surfaces. One possibility of avoiding such serious occurrences is charge dissipation due to the effect of RIC, σ_{RIC}.

A broad experimental program to study the RIC of polymeric dielectric materials has been performed by the Materials Physics Group at Utah State University. The project studied a set of approximately twelve materials to be used in the construction of the James Webb Space Telescope. Extensive instrumentation was designed, built, and tested. Characterization measurements were carried out at USU and three experimental runs were performed at the Idaho Accelerator Center (IAC) to measure the RIC of these materials.

RIC measurements were taken at the Idaho Accelerator Center in Pocatello, Idaho using a monoenergetic 4 MeV electron beam. Dose rates ranging from 0.01 rad/sec to 10.0 rad/sec were used. A

voltage of approximately 50% of breakdown was applied across the samples, and resulting currents were measured to determine the conductivity. The change in conductivity at each dose rate was calculated and plotted on a log-log scale. Values for the k_{RIC} and Δ material parameters were obtained from fits to the data. Data were also taken at ~113K, 219K, 234.5K, 296.5K, and 333K for temperature-dependent resistivity comparisons.

ACKNOWLEDGMENTS

CONTENTS

LIST OF TABLES

LIST OF FIGURES

LIST OF SYMBOLS

A	= area of electrode
a	= average nearest neighbor trap separation
a_d	= average nearest neighbor defect separation
b	= thermal energy of the effective Fermi level below the conduction band
C	= arbitrary constant
C_o	= free air capacitance
D	= sample thickness
$\dot{D}$	= absorbed radiation dose rate
E_c	= energy at the bottom of the conduction band
$E_{centroid}$	= mean energy of all (occupied and unoccupied) trap for DOS
E_d	= energy required to create a static defect
E_{eh}	= mean energy for electron-hole pair creation by radiation
E_F	= Fermi energy
E_f	= Fermi level
E_0^t	= single trap energy of delta function DOS
E_0^A	= mean energy of occupied traps for general DOS
E_0^G	= mean energy of occupied traps for Gaussian DOS
E_0^L	= mean energy of occupied traps for linear DOS
E_0^P	= mean energy of occupied traps for power law DOS
E_0^U	= mean energy of occupied traps for uniform DOS
E_1^U	= upper bound of uniform DOS
E_2^U	= lower bound of uniform DOS
E_0^X	= mean energy of occupied traps for exponential DOS
E_F^{eff}	= effective Fermi level
E_{F0}^{eff}	= effective Fermi level at $T = 0$

E_{GAP} = energy width of the bandgap

E_v = energy at the top of the valence band

$erf(x)$ = error function evaluated at x

F = electric field

F_{ESD} = electric field at breakdown

f = number of optical excitations per volume per second

f_{A0} = fraction of occupied states for general DOS distribution

$f_{FD}(E,T)$ = Fermi-Dirac distribution function

g_{eh} = electron-hole pair generation rate

h = Planck's constant

$\hbar$ = Planck's constant divided by 2π

I = current

I_{CV} = current measured using the constant voltage method

I_{LEAK} = long-term current measured through material using constant voltage method

I_T = transient current

I_{lim} = lower limit of measureable current

J = current density

K_0 = an arbitrary constant in RIC derivation (also K_1, K_2, K_3)

k_B = Boltzmann constant

k_{RIC} = temperature-dependent RIC proportionality constant

m_e = mass of an electron

m_e* = effective mass of an electron

m_h = mass of a hole

m_h* = effective mass of a hole

N_c = density of available electron states in the conduction band

N_t = total trap state density (occupied and unoccupied)

N_v = density of available electron states in the valence band

n	= density of charge carriers
$n_A(E)$	= general energy-dependent DOS for trap states
n_b	= density of traps at energy b below the conduction band
n_c	= density of free carriers (in the conduction band)
n_C^o	= density of free carriers in the conduction band at T=0 K
$n_D(E, E_o^t)$	= energy-dependent DOS for defect states
$n_{US}(E, E_o^U)$	= energy-dependent uniform step DOS for trap states
$n_{UT}(E, E_1^U, E_2^U)$	= energy-dependent uniform top hat DOS for trap states
n_d	= density of defects
n_e	= density of free carriers (in the conduction band)
n_p	= density of primary centers (fixed holes)
$n_t(E)$	= density of occupied traps at energy, E
$n_x(E, E_o^X)$	= energy-dependent exponential DOS for trap states
J	= current density
q	= carrier charge
q_e	= charge on electron ($q_e < 0$)
p	= material density
P	= collision probability
R	= electron range or penetration depth
R_o	= ESTAR continuous slow down approximation (CSDA) range
s_c	= capture cross section of primary centers for free electrons
T	= absolute temperature
T_1	= physical parameter in RIC derivation
T_{cr}	= critical temperature
T_M	= melting temperature
T_o^A	= temperature at which carriers are "frozen" into traps for a general DOS
T_o^L	= temperature at which carriers are "frozen" into traps for a linear DOS

T_o^P	= temperature at which carriers are "frozen" into traps for a power law DOS
T_o^t	= absolute temperature corresponding to a single trap energy
T_o^U	= temperature at which carriers are "frozen" into traps for a uniform DOS
T_o^X	= temperature at which carriers are "frozen" into traps for an exponential DOS
t	= time
V	= applied voltage
V_{CV}	= constant voltage applied to a material
v_T	= thermal velocity of free electron
$W(z)$	= Lambert W function
$W_0^+(z)$	= real-valued upper principle branch of the Lambert W function
z	= depth into sample
β_{PF}	= Poole-Frenkel coefficient
Δ	= temperature-dependent power in RIC power-law equation
ΔH	= trap depth
λ	= material parameter used in RIC rise behavior
ε_o	= permittivity of free space
ε_r	= relative dielectric constant
μ	= carrier mobility
μ_e	= electron mobility in the conduction band
μ_e^{NF}	= mobility of nearly free electrons
μ_{tot}	= total mobility, sum of mobility from each type of charge carrier
ρ	= resistivity
ρ_{lim}	= limit of measureable resistivity
ρ_{DC}	= dark current resistivity
ρ_{RIC}	= portion of resistivity due to incident radiation
ρ_{total}	= total measured resistivity under incident radiation

σ	= electrical conductivity
σ_{DC}	= dark current conductivity
σ_d	= defect limited conductivity
σ_{PF}	= enhanced conductivity due to high applied electric fields
σ_{RIC}	= radiation induced conductivity (RIC)
σ_{TAH}	= thermally activated hopping (TAH) conductivity
σ_{VRH}	= variable range hopping (VRH) conductivity
τ_d	= mean free lifetime of an electron due to defect scattering
τ_e	= mean free lifetime of an electron
τ_{pol}	= material transient current decay time due to polarization
τ_{eh}	= mean time for recombination of an electron-hole pair
v	= frequency of carrier hopping
ξ	= coefficient for temperature-dependent effective Fermi level
$\Phi(E, E_o^t, E_o^G)$	= cumulative probability distribution function for a Gaussian with mean E_0^t and standard deviation E_0^G

LIST OF ABBREVIATIONS

BG	Bandgap
CB	Conduction Band
CSDA	Continuous Slow Down Approximation
DC	Dark Current
DOS	Density of States
EMI	Electromagnetic Interference
ESD	Electrostatic Discharge
ESTAR	Electron Stopping Power and Range
ETFE	Ethylene-Tetrafluoroethylene or Tefzel^{TM}
HDIM	Highly disordered insulating materials
IAC	Idaho Accelerator Center
JWST	James Webb Space Telescope
MPG	Materials Physics Group
LINAC	High-Repetition Rate Linear Accelerator
LDPE	Low Density Polyethylene
LN_2	Liquid Nitrogen
NIST	National Institute of Standards and Technology
PI	Polyimide or Kapton^{TM}
PTFE	Polytetrafluoroethylene or Teflon^{TM}
RIC	Radiation Induced Conductivity
SDL	Space Dynamics Laboratory
TAH	Thermally Activated Hopping
USU	Utah State University
VB	Valence Band
VRH	Variable Range Hopping

CHAPTER 1

INTRODUCTION

The conductivity of the material (and its inverse, the resistivity, $\rho = 1/\sigma$) are the relevant properties for determining mobility of charge carriers and dissipation rate of accumulated charge within the material. Conductivity is a measure of the transport of charged particles under the influence of an applied electric field, F, within a material and can be determined simply by measuring the current density, J, and using the intrinsic form of Ohm's law,

$$\sigma \equiv J \, / \, F \, .$$
(1.1)

By a simple extension of Ohm's law, using the applied voltage, $V=F{\cdot}D$, and current, $I=J{\cdot}A$, the conductivity across a sample of thickness, D, and area, A can be easily calculated from measured quantities as

$$\sigma \equiv \frac{I \cdot D}{V \cdot A} \, .$$
(1.2)

While the conductivity of a given material can be obtained with straightforward measurements and calculations, it may also have a complex dependence on time, temperature, electronic field, and magnetic field, as well as the magnitude and rate of energy deposition. The response of any given material is largely determined by the microscopic structure of its electronic states.

One way of increasing the conductivity of a material is by exciting electrons into a conduction band, and hence, increasing the number of free charged particles. This can be achieved in a number of ways including temperature, electric or magnetic fields, photoexcitation, or (in the present case) under incident high energy radiation. When the incident energy is high enough, the penetration depth of the radiation can exceed the thickness of the sample material, thereby avoiding charge deposition (Rose, 1951; Dennison *et al.*, 2009a). Under this condition, the enhanced conductivity, or Radiation Induced Conductivity (RIC), of the material can be compared to a photoconductivity and is the starting point for understanding the mechanisms involved (Rose, 1951, 1963; Fowler, 1956a, 1956b, 1959; Dennison *et al.*, 2009a).

RIC has been found to follow a simple power law with respect to deposited power or dose rate (Fowler, 1956; Wintle, 1983; Dennison *et al.*, 2009a)

$$\sigma_{RIC}(\dot{D}) = k_{RIC}(T)\,\dot{D}^{\Delta(T)} \quad , \tag{1.3}$$

where σ_{RIC} is the enhanced conductivity due to incident radiation and $\dot{D}$ is the incident radiation's absorbed power per unit mass or dose rate, while T is the sample's absolute temperature. The RIC coefficient and power exponent, k_{RIC} and Δ respectively, are temperature-dependent material parameters, which ultimately depend on the atomic and electronic structure of the material. Highly disordered insulating materials (HDIM) can be classified or grouped according to each material's spatial and energy distribution of localized charge carrier trap states. These distributions control the mobility of charge carriers, and by extension, the insulators' electrical behavior under incident radiation and applied field. For example, at low temperature, a uniform distribution of traps typically yields $\Delta \sim 0.5$ and a highly exponential distribution of traps (with energy depth below the conduction band) yields $\Delta \sim 1.0$ (Rose, 1951; Fowler, 1956a, 1956b). At low E-fields, materials with a uniform distribution of traps are expected to have conductivities that show little temperature dependence, while those with a more exponential distribution will have higher temperature dependence. Even RIC transient current behavior is influenced by a material's trap distribution. After incident radiation is turned on (off), those with uniform distributions are expected to exhibit a large initial rise (drop) in induced current and rise (decay) to equilibrium quickly. Those with exponential distributions should have smaller initial current jumps and longer rise (decay) times.

This thesis describes a study undertaken to extend the understanding of RIC for HDIM with a particular emphasis on temperature-dependent behavior (Dennison *et al.*, 2009a). RIC data were obtained and analyzed for five different insulating polymeric materials: polyimide (PI or Kapton HN^{TM} and Kapton E^{TM}), polytetraflouroethylene (PTFE or Teflon^{TM}), ethylene-tetraflouroethylene (ETFE or Tefzel^{TM}), and Low Density Polyethylene (LDPE). Interest in this study arises from charging issues found in orbiting spacecraft, and efforts were made to reproduce environments found in space. Experiments were conducted under high vacuum conditions. Material outgassing was performed prior to RIC tests to drive off absorbed

water and volatile contaminants and to release trapped charge carriers by baking samples under vacuum according to ASTM D5229 (2012) and ASTM E595 (2006). Incident high energy radiation was obtained using a 4 MeV electron linear accelerator beam with pulse widths between 0.2 µs and 3 µs and a repetition rate of 10 to 150 Hz. RIC data were taken at six different temperatures ranging from 100 K to 330 K and for various applied electric fields and incident radiation beam conditions.

Chapter 2 reviews existing theories for RIC and develops an extension to expressions for the temperature dependence of k_{RIC} and Δ. Since these data were acquired using a new test chamber, Chapter 3 provides a detailed description of the instrumentation and analysis methods, along with an assessment of the associated errors and reproducibility of the data. The resulting analysis of these materials' conductivities, presented in Chapter 4, contains calculations of RIC for each sample material at each temperature, as well as their corresponding k_{RIC} and Δ values. Plots included consist of raw current data, resistivity data, and full data sets of each material for temperature comparisons. A discussion of the results and a comparison with those found in the literature is found in Chapter 5. Finally, also found in Chapter 5, the observed temperature dependences of k_{RIC} and Δ for the polymeric HDIM are discussed in terms of the theoretical models presented in Chapter 2.

CHAPTER 2

BACKGROUND AND THEORY

In thermal equilibrium, the dark conductivity (the conductivity in the absence of deposited light or radiation energy) of a material is determined by the number of holes and electrons in free energy states. When energy is absorbed—by heat, light, incident high energy particles, etc.—more electrons are excited into free states and the conductivity is increased. Since the total number of free electrons is proportional to their lifetime in these free energy states, a steady-state condition is reached when recombination processes balance the excitations of these electrons. Unfortunately, models based on a simple recombination process of electrons with their holes rarely fit (Rose, 1951).

The electrical conductivity of a given material can be calculated in terms of an applied voltage and the resultant current, as described in Eq. (1.2). However, the conductivity can be calculated in a number of ways and may depend on time, temperature, absorbed energy, etc. In general, the conductivity is given as a sum of contributions from each type of free charge carrier; each contribution is a product of the carrier charge, q_i, density of charge carriers, n_i, and carrier mobility, μ_i,

$$\sigma = \sum_i^{carrier\ types} q_i n_i \mu_i \ . \tag{2.0.1}$$

Both n_i and μ_i can reflect the electronic structure of the material, and may depend on time, temperature, and electric field. Since, in most cases, charge migration is dominated by electron transport, I will assume $q_i \rightarrow q_e$ unless otherwise specified.

2.1 Review of conduction mechanisms in conductors

In conductors, the mobility, μ_e, rather than the electron density, n_e, limits the total conductivity. This is because there are numerous empty energy states within the same conduction band (and with slightly higher energies) as filled electron states, which can easily be excited even at very low temperatures. The conductivity is, instead, limited by the mobility, μ_e, through electron scattering mechanisms – mainly defect scattering (at low T) and phonon scattering (at high T) (Ashcroft and Mermin, 1976).

In the free electron model for conductors (Kittel, 1956),

$$\mu_e = \frac{q_e \tau_e}{m_e} \quad , \tag{2.1.1}$$

where m_e is the mass of an electron and τ_e is its mean free carrier lifetime—the time between when the electron is excited and when it undergoes an inelastic scattering event that returns it to a lower energy state. Because electrons are easily excited into free energy states in conductors, n_e does not significantly depend on T, F, D or $\dot{D}$; all such dependence must be contained in μ_e through τ_e.

Phonon scattering is dependent on the number of phonons, which is given by the Fermi distribution. At high temperatures (typically above ~20 K), a phonon energy quanta is $h\nu \ll k_B T$, and the Fermi distribution is proportional to T while τ, μ, and σ are all proportional to T^{-1}. On the other hand, at very low temperatures, one would expect the conductivity to be relatively high if not for scattering events caused by static crystal defects. These defects include impurities, grain boundaries, vacancies, or other irregularities in the ordered pattern of a perfect crystal.

Note, $\delta t/\tau_e$ is the probability a collision will occur in time, δt. In general, the collision probability, P, is proportional to the density of charge carriers, which can undergo collisions and the density of scattering sites where a collision can occur.

$$P \propto n_{carrier} \cdot n_{scatterer} \quad . \tag{2.1.2}$$

Since scattering probabilities for different mechanisms are additive and $\delta t/\tau_e$ is the probability that a collision will occur in time, δt, the total probability is

$$P_{Total} = \sum_{i}^{mechanisms} P_i \quad or \quad \tau_{Total}^{-1} = \sum_{i}^{mechanisms} \tau_i^{-1} \quad . \tag{2.1.3}$$

It follows from these relationships [Eqs. (2.1.2) and (2.1.3)] that $\sigma_{defect} \propto n_{defect}$. Because the defect density, n_{defect} or n_d, is (to a good approximation) fixed by the material, the mean free lifetime of charge carriers due to defect scattering, τ_d, does not depend on temperature (at least not strongly) and the defect limited conductivity, σ_{defect} or σ_d, provides a constant contribution at all temperatures. It is interesting to recognize

that phonons can be viewed as dynamic crystal defects; that is, as deviations in the position of ions as they oscillate in time about their equilibrium crystal lattice sites.

2.2   Review of conductivity in semiconductors

A semiconductor is a material with a resistivity somewhere between that of a conductor and that of an insulator and may depend on the material's temperature. Semiconducting materials have conductivities whose magnitudes are highly dependent on atomic structure and can be found to fall within one of two major categories, intrinsic or extrinsic. Intrinsic semiconductors are those without static defect states. Extrinsic semiconductors not only have static defect states, but the magnitudes of their conductivities are dominated by them. This section will briefly look at the conduction mechanisms of both types of semiconductors.

Electronic charge in intrinsic semiconductors is transported primarily by electrons that have been thermally excited from states in the valence band to states in the conduction band (Ashcroft and Mermin, 1976). In contrast to conductors, the conductivity of intrinsic semiconductors is limited by the density of free electron charge carriers in the conduction band, n_e,

$$n_e(T) = N_v e^{-E_F/2 k_B T} \; .$$
(2.2.1)

Here N_v is the density of available electron states in the valence band within $k_B T$ of the Fermi energy, E_F. For a more detailed derivation, see Ch. 28 of Ashcroft and Mermin (1976), which considers the density of available states in both the valence band and conduction bands in terms of quadratic densities of state and effective masses for electrons and holes (m_e^* and m_h^*, respectively) and replaces the Fermi energy, E_F, with a temperature-dependent chemical potential (Fermi level).

Excitation of an electron from the valence band to the conduction band leaves an empty state (a hole). This is referred to as electron-hole pair creation. In intrinsic semiconductors, with no accumulated charge, the number of free electrons must equal the number of holes. Ultimately, these excited electrons will return to their ground state, through a process known as electron-hole pair recombination. In equilibrium, the rate of excitation equals the rate of recombination. Therefore, the mean time for a recombination to occur, τ_{eh}, is directly related to the density of free electrons in the conduction band.

$$n_e = n_h = g_{eh} \cdot \tau_{eh} \quad . \tag{2.2.2}$$

Here, g_{eh} is the generation rate of electron-hole pairs per unit volume and $g_{eh} = g_{he}$.

While many electrons are thermally excited, it should be noted that electrons can be excited in a number of ways (photoconductivity, radiation induced conductivity, etc.). Any process that deposits sufficient energy to excite trapped electrons into the conduction band can result in an electron-hole pair generation rate proportional to the adsorbed energy flux, or dose rate, $\dot{D}$.

$$g_{eh} \propto \dot{D} \quad . \tag{2.2.3}$$

It should be noted that it is possible to introduce excess charge carriers into a material, such as through charged particle beams or by contact with a biased electrode. If these injected carriers are in an excited state, they may be in the conduction band and also act as charge carriers. Such injection is the basis for common semiconductor devices such as diodes and transistors.

The mobility of excited electrons in semiconductors is similar in form to that for conductors [see Eq. (2.1.1)]. The impurity mobility is infinite for intrinsic semiconductors, since by definition the static defect density is zero. The phonon-limited mobility is proportional to T^{-1} as for conductors. However, the temperature dependence of the mobility is overwhelmed by the exponential temperature dependence of the carrier density in Eq. (2.2.1). Using these results, the conductivity of intrinsic semiconductors due to thermally activated electron-hole pair production can be approximated by

$$\sigma_{eh}(T) = \sigma_{eh}^0 \, e^{-E_F/2k_BT} \qquad \text{with} \qquad \sigma_{eh}^0 \equiv q_e \, N_e \, \mu_e(T) \tag{2.2.4}$$

with σ_{eh}^0 only weakly dependent on temperature through $\mu_e(T)$.

While intrinsic semiconductors do not have static defect densities, extrinsic semiconductors have conductivities dominated by static defects. A semiconductor is defined as extrinsic if its conductivity is dominated by free electrons contributed to the conduction band via static defects. Conversely, a

semiconductor is defined as intrinsic if its conductivity is dominated by carrier electrons that have been excited (thermally or otherwise) from the valence band to the conduction band.

Static crystal defects can result from atomic scale point defects, such as vacancies and substitutional impurities, or from larger scale linear or planar defects, such as dislocations, stacking faults, grain boundaries, surfaces and other irregularities in the ordered pattern of a perfect crystal. Doping is perhaps the most important source of extrinsic semiconductors, resulting from substitution of a native atom in the crystal lattice by an impurity atom with a different valence atom than the original atom in the semiconductor.

For this discussion of extrinsic semiconductors, and for the upcoming extension of these theories to the applications of crystalline and disordered insulators, we restrict ourselves to a more general treatment that relies on the more universal properties of defects.

Continuing with our assumption of electrons as the only mobile charge carrier, we restrict our discussion to n-type semiconductors. Defects can contribute electrons to the conduction band and produce localized traps, even within the bandgap. Assuming a high concentration of defect sites and using a straightforward calculation of the minimum free energy condition for defects as a function of temperature to balance the energy increase required to create a defect, E_d, against the increased entropy from formation of the defect, Boltzmann showed that in equilibrium, the concentration of any generic defect is

$$n_d(T) = C n_d^0 \, e^{-E_d/k_B T} \quad , \tag{2.2.5}$$

where n_d^0 is the concentration of possible defect sites and C is a constant, often taken as unity (Kittel, 1956; Ashcroft and Mermin, 1976). This assumes that there is no interaction between defects, or equivalently, that the mean separation of defects is larger than their interaction range. Note: This is equivalent to the approximation above, assuming a high concentration of defect sites compared to the concentration of free electrons in the conduction band or $n_c << n_d^0$ or $E_d << k_B T$. In this approximation, the free electron density varies as the square root of the donor density. This means

$$n_c(T) = C \, n_d^{0 \, 1/2} \, e^{-E_d/2k_BT} \quad . \tag{2.2.6}$$

The scattering by ionized donors or acceptors in extrinsic semiconductors has been solved by Conwell and Weisskopf (1950), who found the mobility to be (Kittel, 1956)

$$\mu_e(T) = \frac{2^{7/2} \, (\varepsilon_r \varepsilon_o)^2 \left(k_B T\right)^{3/2} \log\!\left(1 + x^2\right)}{n_e \pi^{3/2} \, q_e^3 \, m_e^{*1/2}} \quad \text{with} \quad x = 3a_d \varepsilon_r \varepsilon_o k_B T / q_e^2 \quad , \tag{2.2.7}$$

where a_d is the average distance between ionized donor defect neighbors. The temperature dependence of the conductivity in extrinsic conductors is similar to that of intrinsic semiconductors. The exponential in the electron density will dominate the temperature dependence of the conductivity. The conductivity can be written in similar form to Eq. (2.2.4) using the electron density in Eq. (2.2.7) as

$$\sigma_d(T) = \sigma_d^0 \, e^{-E_d/2k_b T} \qquad \text{with} \qquad \sigma_d^0 \equiv C \mu_e(T) q_e n_d^{0 \, 1/2} \, . \tag{2.2.8}$$

This thermal excitation conduction mechanism for semiconductors is negligible in insulators at reasonable working temperatures (again, $n_e \rightarrow 0$ for insulators); indeed, one distinction between semiconductors and insulators is that thermally activated transitions between extended states are highly improbable in insulators, because the band gap energy separating the states is much larger than the average thermal energy of the electrons (e.g., $E_{gap} \gg k_B T$). In well-ordered semiconductors, these states are extended states, but can be localized for topologically (structurally) disordered states or chemically disordered (e.g., dopant or intrinsic defect) states. While this reduces the activation energy to as little as the separation between the conduction and valence band mobility edges, the gap is still much larger than the thermal energy. Operationally, another definition of a semiconductor (opposed to an insulator) is that $E_{gap} \gg (^1/_{100})k_B T_M$, where T_M is the material's melting temperature; in other words, an insulator melts before there are significant numbers of thermally excited carriers.

2.3   Hopping conductivity and dark current conductivity in polymeric insulators

While it is relatively easy to determine carrier density and mobility in semiconductors, the same quantification is complicated in insulating polymers. Concentrations of impurity atoms or chains are difficult to quantify; the polymer chains do not lend themselves to the simplifications of a lattice construct, and polar groups attached to the chains have significant influence on carrier mobility. These polar groups can also contribute to an overall material polarization that influences the internal electric field felt by the carriers (Mott and Davis, 1979; Wintle, 1983). The most promising theoretical possibilities for explaining electrical behavior in insulating polymers are hopping conductivity models and concepts that have proven successful in application to semiconductors and amorphous solids (Wintle, 1983; Zallen, 1983). These theories are well tested for semiconductors, but remain largely unverified for insulators (Wintle, 1983), mainly because of the difficulty in adequately defining the nature of localized states with such complex molecular structure and disorder. Limited experimental data do suggest that hopping conductivity models effectively describe some aspects of conductivity in polymers.

Using hopping conductivity models, we can consider different conduction mechanisms that contribute to the total conductivity in insulators: transient conductivities due to polarization diffusion, and dispersion; and steady-state conductivities due to thermally activated hopping (TAH), σ_{TAH}, variable range hopping (VRH), σ_{VRH}, and photoexcitation or radiation induced conductivity (RIC), σ_{RIC} (Dennison and Sim, 2012; Hodges, 2012). As shown below, in the experiments conducted for this thesis, σ_{RIC} can be isolated from other transient and steady-state signals due to the relaxation times involved for the different processes. A brief discussion of these other conductivity mechanisms follows to help justify this separation.

Dark current conductivity and transient conductivities

Initial polarization, diffusive, and dispersive transient currents can be allowed to decay in order to study a material's steady-state conductivity. The strength and behavior of these transient currents are determined by the electronic structure of the material, as well as the applied electric field. An example of transient polarization currents in low-density polyethylene (LDPE) is shown in Fig. 2.1 (Dennison and Brunson, 2008; Dekany *et al.,* 2012, 2013). In addition to the rapidly decaying polarization current with an
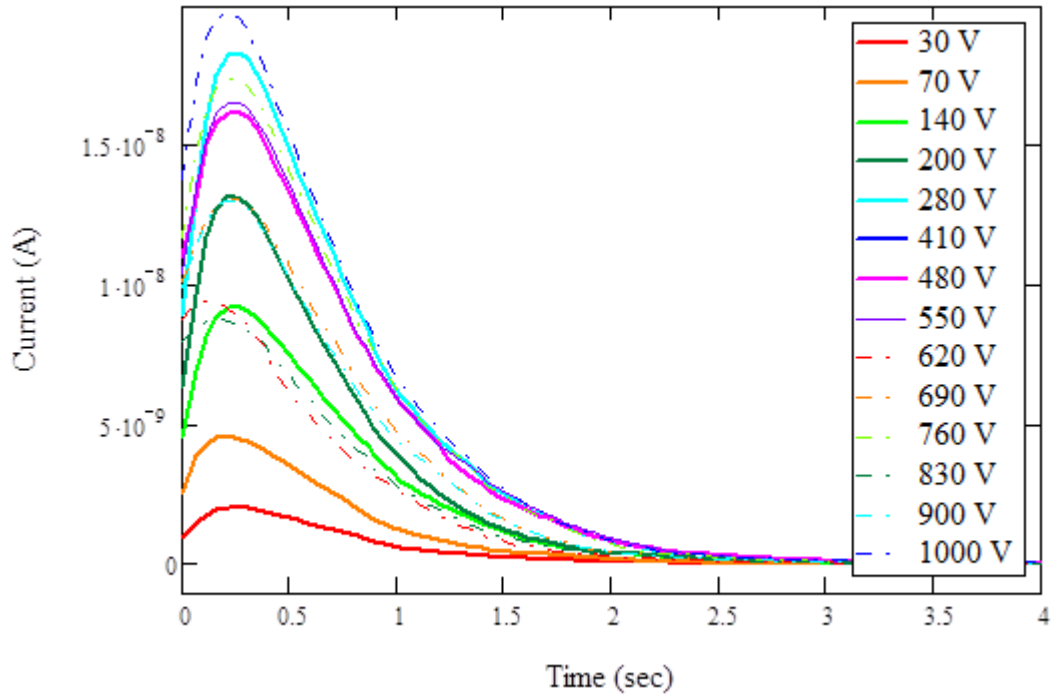
FIG. 2.1. Initial current decay due to internal polarization and response to an applied electric field on a 25 μm LDPE sample. Applied voltages are 30 V, 70 V, 140 V, 200 V, 280 V, 340 V, 410 V, 480 V, 550 V, 620 V, 690 V, 760 V, 830 V, 900 V, and 1000 V (Brunson, 2010). The initial time dependence is attributed to the exponential rise of the voltage supply with a time constant of 0.20 ± 0.05 sec. The subsequent decay of the polarization current has a time constant, $\tau_{pol} \approx 0.80 \pm 0.05$ sec, independent of applied voltage.

exponential time dependence, there are very slowly decaying diffusive, dispersive, and transient currents with power law dependence. For experiments described here, the RIC analysis is conducted after a constant applied voltage has been applied for >1 hr. After such time, the polarization current has decayed to negligible values. Further, after such a conditioning period, the power law, time-dependent currents are small and slowly varying over the time to perform a RIC cycle so that the small residual diffusive, dispersive, and transient currents can be included with the dark current conductivity as a quasi-equilibrium current. Once these transient currents have decayed, the quasi-steady-state current can be measured and the resultant conductivity, called the dark current conductivity (DC conductivity, σ_{DC}), can be calculated. It should be noted that while σ_{DC} is characteristic of the material under consideration, it is also dependent on the sample's electric field and temperature.

For this constant voltage method of measuring DC resistivity, a macroscopic first-principles model exists that contains both the initial current due to diffusion and dispersion and the long-time leakage current

though the material (Dennison *et al.*, 2005a).

$$I_{CV}(t) = I_T(t) + I_{Leak} = V_{CV} \, C_o \left[\left(\frac{\varepsilon_r^\infty - \varepsilon_r^o}{\tau_{pol}} \right) e^{-t/\tau_{pol}} + \frac{\sigma_{DC}}{\varepsilon_o \varepsilon_r^\infty} \right] . \tag{2.3.1}$$

Other relevant terms in Eq. (2.3.1) are the relative dielectric constant of the material, ε_r; the permittivity of free space, ε_o; the free air capacitance, C_o; the dark current conductivity, σ_{DC}; and the material polarization decay time, τ_{pol}. This model can also be used to approximate the length of time needed for the transient currents to decay.

Hopping conductivity models

Fundamental assumptions of hopping conductivity models applied to semiconductors include the identification of electrons or holes as the primary charge carriers. Their motion through the material is governed by availability of localized states treated as potential wells in the lattice, as illustrated in Fig. 2.2. The electron, or hole, moves through the material by hopping between localized states or traps. Energy is required to release the carrier from the trap and the conductivity is proportional to the probability that hopping will occur. In reality, the finite thickness of the sample introduces multiple layers of trapping sites and can significantly change the density of charge carriers, $n_i(T)$. It is typically assumed, for simplicity, that shallow traps provide the bulk conductivity while deep traps do not contribute to charge mobility (Rose, 1951).

Application of an electric field across the sample lowers the activation energy needed for the electron to hop the potential barrier, as shown in Fig. 2.3 (Mott and Davis, 1979; Wintle, 1983). The conductivity is dependent on carrier mobility, which in turn is influenced by both the applied electric field, F, and the temperature, T. In general, the probability of hopping is directly related to conductivity such that,

$$\sigma_{hop}(F,T) = \left[\frac{2 \cdot n_i(T) \cdot v_{hop} \cdot a_d \cdot q}{F} \right] \exp\left[\frac{-\Delta H}{k_B \cdot T} \right] \sinh\left[\frac{\varepsilon_o \varepsilon_r \cdot F \cdot a_d}{2 \cdot k_B \cdot T} \right] , \tag{2.3.2}$$
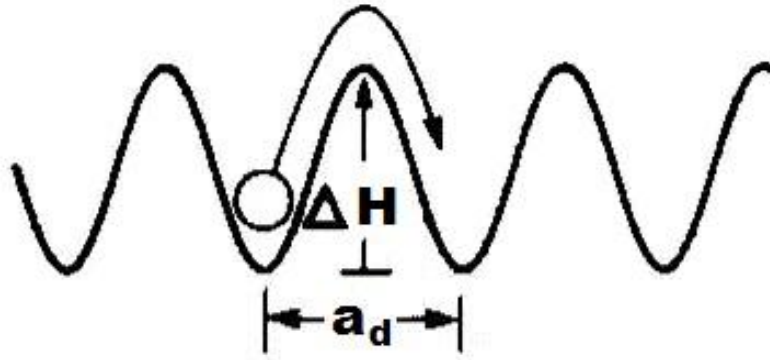
Fig. 2.2. Representation of carrier motion by way of hopping between potential wells. ΔH and a_d correspond to mean well depth or trapped site binding energy and mean well separation, respectively (after Wintle, 1983).

which contains terms accounting for both electric field enhanced conductivity and for thermally activated conductivity (Miller and Abrahams, 1960; Mott and Davis, 1979; Wintle, 1983). Separation of these terms allows each behavior to be tested independently. Other parameters that appear in Eq. (2.3.2) are the frequency of hops, v_{hop}, the density of charge carriers, $n_i(T)$, the well depth, ΔH, and well separation, a_d.

This theory of thermal assisted hoping conductivity, developed by Mott and Davis (1979), provides a model for the temperature hopping conductivity of materials. Hopping between localized states is driven by thermal excitation. At higher temperatures and low electric fields, where it is energetically favorable for an electron to overcome potential well barriers and hop to nearest neighbor states, the hopping conductivity is proportional to a Boltzmann factor with the trap depth, ΔH, setting the energy scale. Thus, from Eq. (2.3.2)

$$\sigma_{TAH}(T,F) \propto exp\left[-\frac{\Delta H}{k_B T}\right] \quad . \tag{2.3.3}$$

At lower temperatures, the conductivity transitions to a more gradual decrease in temperature dependence with a $T^{1/4}$ dependence in the exponent.

$$\sigma_{VRH}(T,F) \propto exp\left[-\frac{A}{T^{1/4}}\right] \quad . \tag{2.3.4}$$
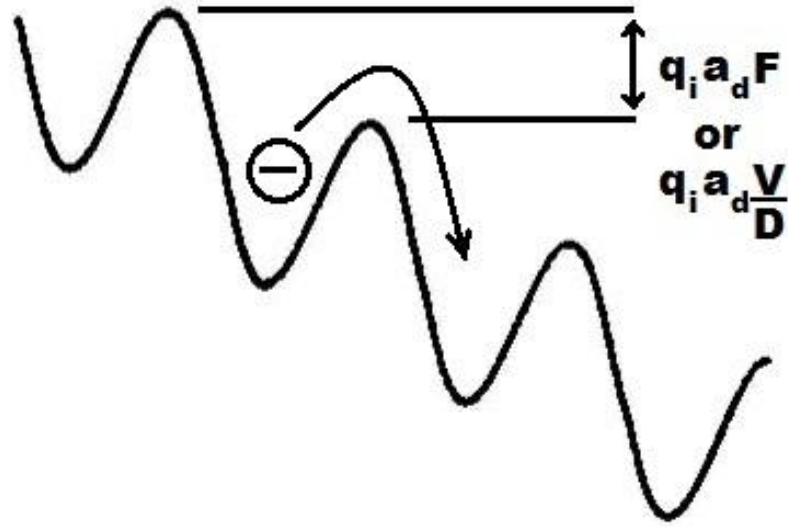
FIG. 2.3. Change to carrier motion due to application of an electric field, F. Application of an electric field enhances the hopping conductivity by lowering the amount of energy needed to move between trap sites (after Wintle, 1983).

This corresponds theoretically to the onset of variable-range hopping, where it is energetically favorable for the electron to hop to lower energy states beyond the nearest neighbor states through quantum tunneling rather than by thermal excitation. Therefore, hopping conductivity models predict that the conductivity should be proportional to an exponential with powers of T^{-1} and $T^{-1/4}$ according to the temperature range.

For constant temperature conditions, the enhanced conductivity due to high applied electric fields (on the order of $\geq 30\%$ of the electrostatic breakdown voltage) is expected to approximately follow Poole-Frenkel behavior (Poole, 1917; Ieda *et al.*, 1971) such that

$$\sigma(F,T) = \sigma^o_{PF}(T) \, exp\left[\beta_{PF} \, F^{1/2}\middle/ k_B T\right] \quad , \tag{2.3.5}$$

where β_{PF} is the Poole-Frenkel coefficient and is dependent on the charge of the carrier and the dielectric constant of the material,

$$\beta_{PF} = \sqrt{e^3\middle/ \pi \varepsilon_o \varepsilon_r} \quad . \tag{2.3.6}$$

This equation, while successful in the field of amorphous semiconductors, has not been verified well for insulators. An effort to include testing for Poole-Frenkel behavior was made in this experiment by varying the applied voltage from ~10% of electrostatic breakdown voltage up to ~50%. However, analysis of the results shows no appreciable change in sample conductivity (see material tables in Appendices A-E).

2.4   Radiation induced conductivity

Radiation Induced Conductivity (RIC) is the change in conductivity of a material due to the effects of energy deposition from incident high energy radiation. This incident energy is deposited in the material, increasing the number of free electrons, and hence, the mobile carrier density $n_e(T)$ [see Eq. (2.2.1)]. This conductivity increase occurs in a manner similar to that from effects of thermal energy on dark current conductivity discussed above. This section utilizes the induced conductivity model first developed by Rose in relation to insulating crystals to acquire the temperature dependence of RIC (Rose, 1951; Molinié *et al.*, 2012). Rose's work for disordered semiconductors was extended to disordered polymers by Fowler (1956b) and later by Vissenberg (1998). Please note that the following discussion assumes electrons as mobile charge carriers and references electron energy in relation to the lower edge of the conduction band. Hence, from this point forward, the density of free electrons in the conduction band will be denoted by n_c rather than by n_e.

The increase in conductivity from the material's dark current conductivity due to RIC is additive.

$$\sigma_{total} = \sigma_{DC} + \sigma_{RIC} \quad . \tag{2.4.1}$$

As materials are bombarded with a flux of high energy radiation, the large energy of the incident particles is shared through a series of low energy inelastic collisions with many bound (valence) electrons within the material. These are excited into higher energy extended states, thereby facilitating their mobility. The conductivity of the material is, therefore, enhanced primarily by energy deposition, rather than by direct charge deposition. This is illustrated by various studies of RIC versus radiation dose rate for polyethylene terephthalate (Mylar^{TM}, PET) shown in Fig. 2.4 and Table 2.1. Using Eq. (1.3), the excellent agreement of a power law fit over 10 orders of magnitude of dose rate for five different studies using a variety of
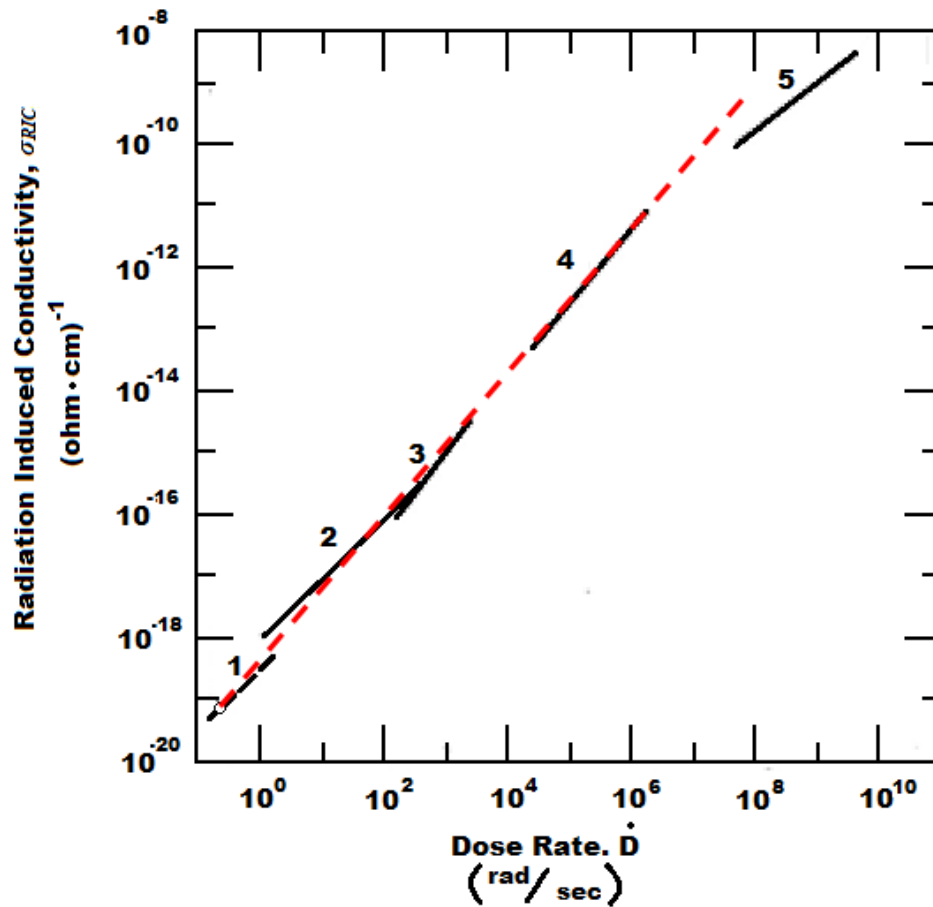
FIG. 2.4. Five studies of RIC versus the absorbed radiation dose rate for polyethylene terephthalate (PET, Mylar[TM]) at room temperature (~295 K). The excellent agreement of a power law fit over 10 orders of magnitude of dose using a variety of different species of radiation implies that RIC is largely independent of the beam energy and type of radiation used. An approximate power law fit to the composite data, using Eq. (1.3), is shown as a dashed line with $k_{RIC} = 1.0 \cdot 10^{-18}$ and $\Delta = 1.0$. Note that results from Compton *et al.* (1965) suggest that saturation effects may begin to be noticeable above ~10^8 rad/s. (after Campbell, 1983).

TABLE 2.1. Data types and references for power law fits in Fig. 2.4.

Curve Segment	Type of Radiation	Energy	Dose Rate	Mode	Reference
1	x-rays	250 keV	0.13 rad/s	Steady-state	Fowler (1956a)
2	x-rays	15-30 keV	1 to 400 rad/s	Steady-state	Adamec (1968)
3	γ-rays	1.17 and 1.33 MeV	200 to 3500 rad/s	Steady-state	Conrad and Marcus (1962)
4	Pulse reactor neutrons and γ-rays	Mixed	6.5×10^4 to 3.8×10^6 rad/s	13 ms pulses	Conrad and Marcus (1962)
5	electrons	30 MeV	5×10^7 to 7×10^9 rad/s	4.5 μs pulses	Compton *et al.* (1965)

different species of radiation (x ray, gamma, electron, neutron, pulsed and continuous beams) implies that RIC is largely independent of the beam energy and type of radiation used. Calculation of the mean free path of 4 MeV electrons (the beam energy used in this experiment) confirms negligible charge deposition in the sample materials. (See Chapter 3, Table 3.2 for results.)

Since the amount of energy deposited is the principle factor in determining the magnitude of RIC, the radiation induced steady-state condition has strong parallels to that achieved with optical illumination or thermal excitation. We now derive the temperature-dependent behavior of RIC. For a more detailed derivation in terms of the density of states, please see Appendices G and H. Using the usual Boltzmann factor, the density of free electrons in the conduction band is given by

$$n_c = N_c \cdot e^{-E_F^o / k_B T} \quad , \tag{2.4.2}$$

where N_c is the density of available energy states in the conduction band (within a few $k_B T$ of the bottom of the conduction band, E_c), T is the absolute temperature, and b is the thermal distance of the Fermi limit below the conduction band. If the energy (as measured below E_c) of the steady-state Fermi limit due to illumination is

$$E_b = b \cdot k_B \quad , \tag{2.4.3}$$

then Eq. (2.4.2) can be solved for b to obtain

$$b = T \cdot ln(N_c/n_c) = E_b / k_B \quad . \tag{2.4.4}$$

Now consider an exponential distribution of traps below E_c such that the trap density, n_b, below the conduction band scales as

$$n_b = K_o \, e^{-b/T_1} \quad . \tag{2.4.5}$$

K_o and T_1 are physical parameters. T_1 is a temperature higher than room temperature, and physically, could indicate the temperature at which traps are "frozen in" as the material cools (Rose, 1951). With this exponential distribution, the density of traps below the steady-state Fermi limit (at $E_c - bk_B$) is

$$n_t = \int_b^\infty n_b(E)\,db = \int_b^\infty K_o e^{-b'/T_1}\,db' = K_o T_1 e^{-b/T_1} \quad . \tag{2.4.6}$$

In order for trapping to be effective, the number of trapped electrons must exceed the number of free electrons such that the density of primary centers, n_p, will be approximately equal to the density of traps.

$$n_p = n_t + n_c \approx n_t \quad . \tag{2.4.7}$$

In the steady-state condition, the rate of excitation of electrons equals the rate of recombination with primary centers.

$$f = v_T s_c n_c n_p \qquad \text{or} \qquad n_c = \frac{f}{v_T s n_p} \quad . \tag{2.4.8}$$

Here v_T is the thermal velocity of electrons, s_c is the capture cross section of primary centers for free electrons (in cm^2), and f is the number of optical excitations per volume per second. If we make an assumption that all of the traps below bk_B are filled and all above bk_B are empty, then $n_t = n_p$, the density of primary centers (fixed holes). Using Eq. (2.4.6),

$$n_c = \frac{f}{v_T s_c}\left[\int_b^\infty n_b(E)\,db\right]^{-1} = \frac{f}{v_T s_c}\left[K_o T_1 e^{-b/T_1}\right]^{-1} \quad . \tag{2.4.9}$$

If we insert b from Eq. (2.4.4), then e^{b/T_1} becomes

$$e^{b/T_1} = \exp\left[\frac{T}{T_1}\ln(N_c/n_c)\right] = \exp\left[\ln(N_c/n_c)^{T/T_1}\right] = \left(\frac{N_c}{n_c}\right)^{T/T_1} \quad , \tag{2.4.10}$$

and Eq. (2.4.9) becomes

$$n_c = \frac{f}{v_T \, s_c \, K_o T_1} \left(\frac{N_c}{n_c}\right)^{T/T_1} .$$

(2.4.11)

Solving for n_c yields

$$n_c = \left[\frac{f}{v_T \, s_c \, K_o T_1}\right]^{\frac{T_1}{T+T_1}} (N_c)^{\frac{T}{T+T_1}} .$$

(2.4.12)

We can find expressions for v_T, f, and N_c. By setting the thermal energy of a free electron equal to its kinetic energy, we can obtain an equality for v_T.

$$\frac{3}{2} k_B T = \frac{1}{2} m_e v_T^2 .$$

(2.4.13)

Solving for v_T, yields (in cm/s)

$$v_T = \sqrt{\frac{3 k_B T}{m_e}} \approx 10^7 \sqrt{\frac{T}{300}} .$$

(2.4.14)

The frequency, f, has units of number optical excitations per second per volume (in cm^3). The incident dose rate, $\dot{D}$, has units of Joules absorbed per kilogram per second. By multiplying the dose rate by the material density, p (kg/m^3), and dividing by the relative permittivity of the material, ε_r (Joules absorbed/optically excited electron), we can find an expression for f.

$$f = 10^6 \, \dot{D} \cdot p / \varepsilon_r = \frac{\# \, optical \, excitation}{sec \, ond \, cm^3} .$$

(2.4.15)

Finally, assuming $m_e = m_h$ (the mass of a hole), the density of available states has been derived by Ashcroft and Mermin (1976) to be

$$N_c = 2\left(\frac{m_e k_B T}{2\pi\hbar^2}\right)^{3/2}\left(\frac{m_e^* m_h^*}{m_e m_h}\right)^{3/4} \quad . \tag{2.4.16}$$

Inserting these values into Eq. (2.4.12) yields

$$n_c = \left[\frac{10^6 p}{s_c \varepsilon_r K_o T_1}\sqrt{\frac{m_e^*}{3k_B T}}\right]^{\frac{T_1}{T+T_1}}\left[2\left(\frac{m_e k_B T}{2\pi\hbar^2}\right)^{3/2}\left(\frac{m_e^* m_h^*}{m_e m_h}\right)^{3/4}\right]^{\frac{T}{T+T_1}}\dot{D}^{\frac{T_1}{T+T_1}} \quad . \tag{2.4.17}$$

In order to calculate a material's RIC through Eq. (2.0.1), we also need to know the mobility, μ_e, and by extension, the mean free lifetime of an electron, τ_e. The charge carrier mobility in the free electron model for conductors is given by Eq. (2.1.1). In general, the mobility of free electrons can be found by replacing the electron mass with its effective mass

$$\mu_e = \frac{q_e \tau_e}{m_e^*} \quad . \tag{2.4.18}$$

The frequency of optical excitations per unit volume, f, is equal to the density of free electrons divided by τ_e.

$$f = \frac{n_c}{\tau_e} \quad . \tag{2.4.19}$$

An expression for τ_e can be obtained by equating Eq. (2.4.19) to Eq. (2.4.8) and solving for τ_e.

$$\tau_e = \frac{1}{v_T s_c n_p} \quad . \tag{2.4.20}$$

Since n_p is approximately equal to n_t [Eq. (2.4.7)], Eq. (2.4.20) then becomes [using Eq. (2.4.6)]

$$\tau_e = \frac{e^{b/T_1}}{v_T\, s_c\, K_o\, T_1} \quad .$$

(2.4.21)

With this expression for τ_e and inserting -1 for q_e, the mobility in Eq. (2.4.18) can now be calculated using Eq. (2.4.14).

$$\mu_e = \frac{-e^{b/T_1}}{s_c\, m_e^*\, K_o\, T_1}\sqrt{\frac{m_e}{3k_B T}} \quad .$$

(2.4.22)

Finally, the conductivity due to incident radiation, using Eq. (2.0.1), is predicted to be

$$\sigma_{RIC} = \frac{e^{b/T_1}}{s_c\, m_e^*\, K_o\, T_1}\sqrt{\frac{m_e}{3k_B T}}\left[\frac{10^6\, p}{s\varepsilon_r T_1}\sqrt{\frac{m_e^*}{3k_B T}}\right]^{\frac{T_1}{T+T_1}}\left[2\left(\frac{m_e k_B T}{2\pi\hbar^2}\right)^{3/2}\left(\frac{m_e^* m_h^*}{m_e m_h}\right)^{3/4}\right]^{\frac{T}{T+T_1}}\dot{D}^{\frac{T_1}{T+T_1}} \quad .$$

(2.4.23)

Standard RIC theory (Fowler, 1956a; Frederickson, 1977; Hastings and Garrett, 1996) predicts that σ_{RIC} is primarily dependent on the radiation dose rate, $\dot{D}$, (a measure of the energy deposited per unit time and unit mass) raised to the power Δ through a power law

$$\sigma_{RIC}(\dot{D}) = k_{RIC}(T)\, \dot{D}^{\Delta(T)}$$

(2.4.24)

with proportionality constant, k_{RIC}. Both k_{RIC} and Δ are temperature-dependent material parameters. k_{RIC} is comparatively small for most organic dielectrics relative to inorganic dielectrics, which can be two or more orders of magnitude higher. Δ usually lies between 0.5 and 1.0, with higher values being more common. By comparing Eq. (2.4.24) with Eq. (2.4.23), Δ and k_{RIC} are seen to be

$$\Delta(T) = \frac{T_1}{T+T_1} \quad \text{, and}$$

(2.4.25)

$$k_{RIC}(T) = \left[\frac{e^{b/T_1}}{s_c m_e^* K_o T_1} \sqrt{\frac{m_e}{3k_B T}} \right] \left[\frac{10^6 p}{s \varepsilon_r T_1} \sqrt{\frac{m_e^*}{3k_B T}} \right]^{\frac{T_1}{T+T_1}} \left[2 \left(\frac{m_e k_B T}{2\pi \hbar^2} \right)^{3/2} \left(\frac{m_e^* m_h^*}{m_e m_h} \right)^{3/4} \right]^{\frac{T}{T+T_1}} .$$

(2.4.26)

Values of Δ existing between 0.5 and 1.0 are obtained with T_1. When $T_1 \gg T$, $\Delta \approx 1.0$, and to a good approximation, is temperature-independent. When $T_1 \approx T$, $\Delta \approx 0.5$, and small changes to T have a large effect on Δ. As can be seen in Eq. (2.4.5), these limits are an indication of the extent to which a material has a uniform trap distribution ($T_1 \gg T$) or an exponential trap distribution ($T_1 \approx T$).

For the sake of clarity in discussing the theoretical behavior of k_{RIC}, consider three functions K_1, K_2, and K_3 such that

$$K_1(T) = \frac{e^{b/T_1}}{s_c m_e^* K_o T_1} \sqrt{\frac{m_e}{3k_B T}} ,$$

(2.4.27)

$$K_2(T) = \frac{10^6 p}{s_c \varepsilon_r T_1} \sqrt{\frac{m_e^*}{3k_B T}} , \text{ and}$$

(2.4.28)

$$K_3(T) = 2 \left(\frac{m_e k_B T}{2\pi \hbar^2} \right)^{3/2} \left(\frac{m_e^* m_h^*}{m_e m_h} \right)^{3/4} .$$

(2.4.29)

This leaves k_{RIC} as

$$k_{RIC}(T) = K_1(T) \left[K_2(T) \right]^{\frac{T_1}{T+T_1}} \left[K_3(T) \right]^{\frac{T}{T+T_1}} .$$

(2.4.30)

In the limit of a uniform trap distribution, $T_1 \gg T$; then the exponents for K_2 and K_3 reduce to 1 and 0, respectively. The T^{-1} temperature dependence for this limiting case results from the product of the K_1 and $K_2 T^{-1/2}$ denominators. It is, however, overwhelmed by $(T_1)^2$ so that k_{RIC} is expected to be approximately temperature-independent. In the limiting case of an exponential trap distribution, $T_1 \approx T$, and the exponents in Eq. (2.4.30) [and hence $k_{RIC}(T)$] become highly temperature-dependent.

To summarize overall RIC behavior, materials having a uniform distribution of traps below the conduction band are expected to have Δ values of approximately 1.0 and to have temperature-independent conductivities. Materials having an exponential distribution, on the other hand, are expected to have Δ values of approximately 0.5 and have highly temperature-dependent conductivities.

In an idealized model, when incident radiation is turned on at t_{on}, the conductivity, $\sigma_{time}(t)$, instantaneously increases from σ_{dc} to $\sigma_{dc} + \sigma_{RIC}$, and instantaneously decreases at t_{off} (Fig. 2.5).

In reality, when the radiation is turned on, a finite period is required for the measured conductivity to approach the equilibrium RIC (Fig. 2.6). A simple, semi-empirical model exists for the rise in conductivity after the beam is turned on (Harrison *et al.*, 1963; Weaver *et al.*, 1977),

$$\sigma_{rise}(\dot{D}, k_{RIC}(T), \Delta(T), \lambda(\dot{D}, T)) = k_{RIC}(T)\, \dot{D}^{\Delta(T)} \cdot \left[1 - e^{-(t - t_{on}) \cdot \lambda(\dot{D}, T)} \right]; \quad t_{on} \leq t \leq t_{off} \quad .$$
$$(2.4.31)$$

The λ parameter is not well understood. However, observations have shown a dependence on incident dose rate and temperature. An extension to this model adds for the additional possibility of a second component to $\sigma_{rise}(t)$ that is much more rapid, approaching the instantaneous behavior shown in Fig. 2.5. This term is approximated using a Heaviside step function as $[k_{step} \cdot H(x)(t_{on} - t_{off})]$. Then Eq. (2.4.31) becomes,

$$\sigma_{rise}(\dot{D}, k_{step}, k_{RIC}(T), \Delta(T), \lambda(\dot{D}, T)) = \left[k_{step} + H(t - t_{on}) \cdot k_{RIC}(T) \cdot \left[1 - e^{-(t - t_{on}) \cdot \lambda(\dot{D}, T)} \right] \right] \dot{D}^{\Delta(T)};$$
$$t_{on} \leq t \leq t_{off} \quad . \quad (2.4.32)$$

The parameter $\lambda(\dot{D}, T)$ is treated here as a semi-empirical parameter, which has been shown experimentally to depend on both temperature and dose rate.
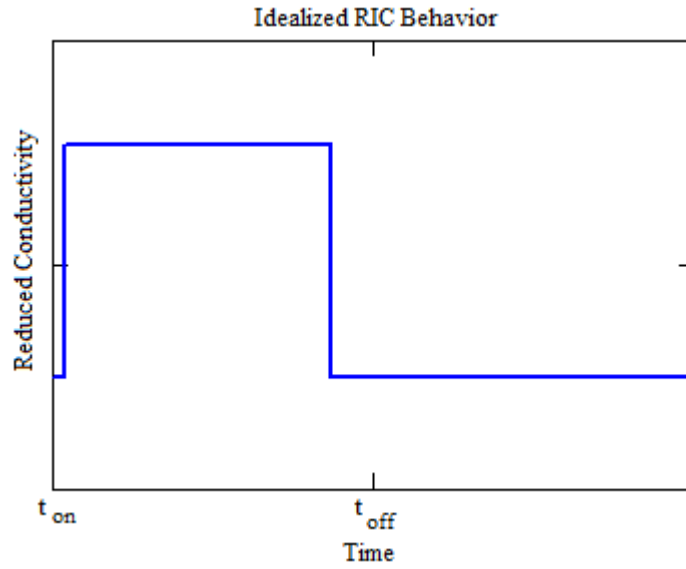
FIG. 2.5. Ideal RIC Behavior showing an instantaneous increase
and decrease with incident radiation.

Similarly, when the radiation is turned off, the measured conductivity also takes a finite amount of time to decay to the material's initial (zero dose rate) conductivity. The decay in RIC after the beam is turned off is generally accepted to decay hyperbolically with time. This decay has been observed to depend on incident dose rate, as well as the magnitude of the total radiation dose. A semi-empirical model based on the hyperbolic nature of the decay, but excluding the total radiation dose dependence, is given by Fowler (1956a):

$$\sigma_{decay}(\dot{D}, T, k_{RIC}(T), \Delta(T)) = \frac{k_{RIC}(T) \cdot \dot{D}^{\Delta(T)}}{1 + \frac{k_{RIC}(T) \cdot (t - t_{off})}{T}}; \quad t_{off} \leq t \quad . \tag{2.4.33}$$

A similar extension of Eq. (2.4.33) to include a rapid (or instantaneous) contribution to the decay (as shown in Fig. 2.6) yields an expression

$$\sigma_{decay}(\dot{D}, T, k_{RIC}(T), \Delta(T)) = \left[k_{RIC}(T) - k_{drop}(T) - \frac{k_{RIC}(T) \cdot H(t - t_{off})}{1 + \frac{k_{RIC}(T) \cdot (t - t_{off})}{T}} \right] \dot{D}^{\Delta(T)}; \quad t_{off} \leq t \quad .$$

$$\tag{2.4.34}$$
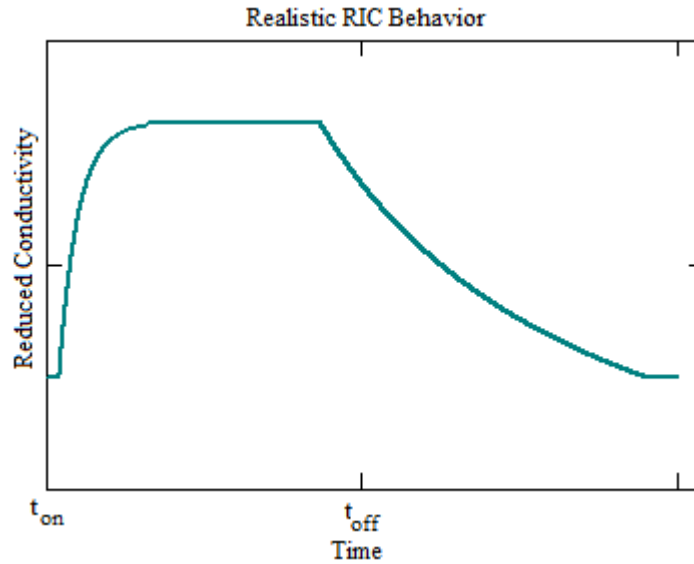
FIG. 2.6. Realistic RIC behavior showing a finite amount of time for the measured current to come to equilibrium after the radiation and turned on and off.

More complete dynamic models on rate equations (Vissenberg, 1998; Tyutnev *et al.*, 2000, 2004) have extended the semi-empirical time-dependent models of Eqs. (2.4.31) – (2.4.34). In general, they find relations between the parameters k_{step}, $\lambda(\dot{D},T)$, $k_{RIC}(T)$, and $\Delta(T)$ and other more fundamental parameters, including the shape of the distribution for the energy-dependent density of trap sites and the rates of electron capture and release in trap states.

The scope of this thesis is limited to the equilibrium behavior of RIC. Comments in Section 5.4 briefly address extending the analysis of the extensive time-dependent data presented in this thesis with the dynamic RIC models outlined in this section. Alec Sim and JR Dennison are currently working to develop this dynamical theory of RIC and extend the analysis of this data to time-dependent results.

Also worth noting, is that at lower trap population, the number of newly-filled traps can be expected to scale as the energy deposited by the radiation; that is, σ_{RIC} is proportional to dose rate. However, at higher fluxes and incident energies, the radiation can produce significant numbers of new traps via radiation damage, leading to enhanced conductivity (Fowler, 1956a). For this experiment, repeated dose rate measurements yielded no change in resultant current indicating consistent results and negligible damage to the materials during our RIC tests.

CHAPTER 3

EXPERIMENTAL METHODS AND ANALYTIC PROCEDURES

Outlined in this chapter are details of the RIC chamber design, IAC's accelerator characteristics, and the setup and conditions used in this experiment. Portions of this thesis, especially the detailed instrumentation descriptions and images below, have been written and included in an effort to provide documentation for future presentations and publications. The design and construction of the chamber, and its various extensions, as well as the circuitry and software necessary to perform RIC test were a collaborative effort of the Materials Physics Group at Utah State University. I would like to acknowledge everyone on the team who helped me pull together images and understand the details necessary in order to organize the information in this chapter.

3.1   Sample characterization

A number of different measurements were done on each sample in preparation for RIC experiments and calculations. Many members of the Materials Physics Group contributed in adequately characterizing the materials tested. These characterizing measurements include sample thicknesses, densities, dielectric constants, electrostatic breakdown voltages, DC resistivities, and the mean free paths of incident electrons (see Tables 3.1, 3.2, and 4.1).

Material thicknesses were measured at five different locations on each sample and then averaged. The resultant measured variations in the sample thicknesses were ~11% standard deviation or ~6% standard deviation of the mean. Values are listed in Table 3.3.

Densities and dielectric constant measurements were taken and checked with available literature. Differences between measured values and those listed in literature were within the limits of equipment uncertainty. Therefore the values listed in the literature were used for RIC calculations (refer to Table 4.1).

For the purposes of this experiment, the electrostatic breakdown is defined as an irreversible drop in resistivity at high fields. The point at which the material breaks down is called the electrostatic discharge breakdown voltage, or ESD voltage, measured in volts (V). ESD voltage measurements were taken on all materials using modified ASTM methods (ASTM, 1997) (refer to Table 4.1). The resultant

TABLE 3.1. Dark current resistivities at various voltages and temperatures as measured at Utah State University.

Sample Name/ Thickness	Applied Voltage (V)	Temperature (K)	DC Resistivity* (ohm·cm)
Kapton HN 50.3 μm	1884 ± 4 (0.2%)	333 ± 5	$1.3 \cdot 10^{19}$
	1256 ± 3 (0.2%)	333 ± 5	$1.4 \cdot 10^{19}$
	2450 ± 17 (0.7%)	295 ± 1	$1.4 \cdot 10^{19}$
	2100 ± 4 (0.2%)	295 ± 1	$1.5 \cdot 10^{19}$
	1400 ± 3 (0.2%)	295 ± 1	$1.6 \cdot 10^{19}$
	6875 ± 31 (0.4%)	232 ± 5	$5.3 \cdot 10^{18}$
	6875 ± 31 (0.4%)	214 ± 5	$5.1 \cdot 10^{18}$
	5000 ± 31 (0.6%)	123 ± 5	$1.3 \cdot 10^{19}$
	2450 ± 17 (0.7%)	103 ± 2	$1.2 \cdot 10^{20}$
Kapton E 23.0 μm	5500 ± 25 (0.4%)	295 ± 1	$4.1 \cdot 10^{17}$
	2450 ± 17 (0.7%)	295 ± 1	$3.1 \cdot 10^{18}$
	5500 ± 25 (0.4%)	232 ± 5	$5.3 \cdot 10^{17}$
	5500 ± 25 (0.4%)	214 ± 5	$5.9 \cdot 10^{17}$
	2450 ± 17 (0.7%)	103 ± 2	$3.7 \cdot 10^{21}$
PTFE 72.9 μm	2200 ± 10 (0.4%)	295 ± 1	$1.6 \cdot 10^{19}$
	2200 ± 10 (0.4%)	232 ± 5	$3.9 \cdot 10^{20}$
	2200 ± 10 (0.4%)	214 ± 5	$1.4 \cdot 10^{21}$
	1800 ± 10 (0.6%)	123 ± 5	$2.0 \cdot 10^{23}$
	1675 ± 12 (0.7%)	103 ± 3	$2.0 \cdot 10^{23}$
Tefzel 53.1 μm	2669 ± 5 (0.2%)	333 ± 5	$3.6 \cdot 10^{18}$
	550 ± 1 (0.2%)	333 ± 5	$9.0 \cdot 10^{18}$
	3025 ± 13 (0.4%)	295 ± 1	$1.1 \cdot 10^{19}$
	2975 ± 6 (0.2%)	295 ± 1	$1.1 \cdot 10^{19}$
	2394 ± 4 (0.1%)	295 ± 1	$1.3 \cdot 10^{19}$
	1925 ± 13 (0.7%)	295 ± 1	$1.6 \cdot 10^{19}$
	612 ± 1 (0.2%)	295 ± 1	$3.3 \cdot 10^{19}$
	3025 ± 13 (0.4%)	232 ± 5	$2.3 \cdot 10^{20}$
	2200 ± 13 (0.6%)	123 ± 5	$2.0 \cdot 10^{23}$
LDPE 27.4 μm	314 ± 0.6 (0.2%)	333 ± 5	$1.3 \cdot 10^{17}$
	79 ± 0.2 (0.2%)	333 ± 5	$1.4 \cdot 10^{17}$
	1650 ± 7 (0.4%)	295 ± 1	$8.4 \cdot 10^{17}$
	314 ± 1 (0.2%)	295 ± 1	$1.2 \cdot 10^{18}$
	88 ± 0.1 (0.2%)	295 ± 1	$1.3 \cdot 10^{18}$
	1650 ± 7 (0.4%)	232 ± 5	$5.0 \cdot 10^{19}$
	1650 ± 7 (0.4%)	214 ± 5	$9.7 \cdot 10^{19}$
	2800 ± 17 (0.6%)	123 ± 5	$2.8 \cdot 10^{21}$

ESD electric fields determined the target applied voltage (~10% and ~50% of ESD) used in the RIC experiments. Some measurements had not been completed at the time of the RIC experiments. In these cases, the ESD electric fields listed in the literature were used as a guide. Table 3.1 lists the applied voltages for all runs for all five materials studied. The first table in Appendices A – E for each material lists the applied voltage and breakdown strength, as well as the resultant fraction of F_{ESD} applied in each data set.

The ESD repeated measurements were between two and seven for each sample type at different ramp rates. Ramp rates of 20 V/s to 500 V/s were studied; the voltage was incremented in a single step once per second. It should be noted that clear dependence was observed with the ESD electric field increasing with increasing ramp rate. For these RIC calculations, the most conservative values were chosen.

The measured ESD electric fields were consistently higher (~20% to 180% higher) than those reported by the manufacturer with typical errors of ~8% estimated as the standard deviation of the mean of the valid measurements. Since manufacturer measurements were most likely taken in air at room temperature under relative humidity on unbaked samples, one would expect the ESD electric fields for these samples to be higher. The conditions for ESD measurements done at USU were more representative of space conditions and were also more reproducible than many of the literature values.

DC resistivity measurements at the voltages and temperatures under consideration were made by Jerilyn Brunson and Steve Hart at Utah State University (USU) using the Constant Voltage Method (see Table 3.2). Details of the methods and instrumentation can be found in Brunson (2010) and Dennison and Brunson (2008). Please also refer to these papers for a detailed discussion of the methods and their inherent limits to measured resistivity. As established in Chapter 2 and discussed below in Section 3.3, DC resistivity values vary according to the applied electric field and the sample temperature (Dennison *et al.*, 2009b).

Calculation of the range of 4 MeV electrons (the energy of the beam used in this study) was done to verify that no charge was deposited in the samples during irradiation. The calculation was done using an online program by the National Institute of Standards and Technology (NIST) called ESTAR, Electron Stopping Power and Range, which makes its calculations according to the methods described in ICRU Reports 37 and 49. In the program, a selection from a list of over 250 materials may be made or a user-defined material may be input. User-defined materials require a name, density, and the fractional weights of the material's molecules or elements. Kapton polyimide film (Kapton HN), polyethylene, and polytetrafluoroethylene (PTFE) were available in ESTAR to be selected. Tefzel (ethylene-tetrafluoroethylene or ETFE), a 1:1 copolymer of ethylene (C_2H_4) and tetrafluoroethylene (C_2F_4), was unavailable and had to be input as a user-defined material. The exact composition of Kapton E was

TABLE 3.2. Electron range and percent penetration as calculated by NIST's ESTAR program.

Sample Name	CSDA Range, R_o (g/cm^2)	Sample Density, p (g/cm^3)	Electron Range, R (µm)	Sample Thickness, D (µm)	% Sample Penetration
Electron Range of 4 MeV Electrons					
Kapton HN	2.2	1.4	$1.6 \cdot 10^4$	50.8	$3.1 \cdot 10^4$
Kapton E	2.2*	1.7	$1.3 \cdot 10^4$	23.0	$5.7 \cdot 10^4$
PTFE	2.4	2.2	$1.1 \cdot 10^4$	76.2	$1.4 \cdot 10^4$
Tefzel	2.1	1.7	$1.2 \cdot 10^4$	50.8	$2.4 \cdot 10^4$
Polyethylene	2.0	0.94	$2.1 \cdot 10^4$	125	$1.7 \cdot 10^4$

*Due to lack of detailed compositional information of Kapton E, a similar composition to Kapton HN was assumed.

unavailable at the time of this study, but was known to be closely related to Kapton HN with a slightly higher density of nitrogen atoms. Therefore, Kapton HN was assumed to have a close enough composition to Kapton E to be used in its ESTAR program calculations.

Continuous slow down approximation (CSDA) range data output from ESTAR was converted to depth penetration range by dividing each CDSA range, R_o, by the corresponding material's density, p.

$$R = Ro/p \quad .$$ (3.1.1)

Percent penetration of the electron through each sample material was then calculated by simply dividing the electron penetration range, R, by the sample thickness, D.

$$\%Penetration = R/D \quad .$$ (3.1.2)

A summary of the range output from ESTAR and the calculated results are given in Table 3.3. Note that the calculated values, $>10^4$, are much larger than 10^2 or 100%, where the electron travels completely through the sample, showing that negligible charge was deposited in the samples from the high energy electron beam.

3.2 Sample preparation procedures

Interest in this study is primarily in relation to spacecraft charging and dissipation, specifically in relation to the conditions NASA's James Webb Space Telescope (JWST) will experience at the second

Lagrangian point – L2. Sample materials were prepared so as to reflect these conditions. Because of the requirements to maintain surface cleanliness and dissipate water and other volatile materials absorbed within materials used on spacecraft, standard outgassing tests as a function of conditioning time were performed at the USU Space Dynamics Laboratory (SDL) according to ASTM D5229 (2012) and ASTM E595 (2006). See Fig. 3.1. A manual for use of this instrument was prepared as part of this thesis work.

Three ~1 cm^2 pieces of each sample were cut and baked at 383 K. Mass measurements were initially taken after baking eight hours at temperature. Subsequent measurements were made after every 20 hour interval thereafter until a mass loss of <0.05% per interval was obtained. Heating and cooling times were not included in baking intervals. An exception to the 383 K bakeout temperature was LDPE, which has a working temperature around 363 K. Conditioning tests on LDPE were performed at a lower temperature of 338 K, so as to be more than 20 K below the working temperature.

Values of 0.05% of the sample masses of both Kapton HN and Kapton E were comparable to the measureable limit of our mass balance, ~3 μg. In these cases, the absolute mass changes were examined. Samples were considered dry, when the absolute change had dropped below this limit. Results of sample conditioning tests are listed in Table 3.3.

Polymer samples used for RIC tests were preconditioned using appropriate parts of ASTM D618, (2008). Specifically, samples were cleaned using standard organic solvents, spectral grade methanol and/or isopropyl alcohol. Once cleaned the samples were handled only with gloves in a clean environment. Samples were cut to a size and shape to overlay the pie electrodes. A 25 μm thick Kapton H^{TM} sheet was attached to the 101 μm thick stainless steel window using Kapton tape with double-sided adhesive (see Fig. 3.2). A 13 μm thick Al grounded electrode was then attached using Kapton tape with double-sided adhesive. The area of the electrode (excluding the tab visible in Fig. 3.2 used to make electrical connection) determined the effective sample size of 80.0 cm^2 (±1%). The thin film samples were next attached to the Kapton sheet over the grounded electrodes using Kapton tape with double-sided adhesive.

TABLE 3.3. Summary table of conditioning tests done at USU's Space Dynamics Laboratory.

Sample	Bakeout Temperature (K)	Time Required for < 0.05% mass change (hrs.)	Total Time Baked (hrs.)
Kapton HN	383	48	92
Kapton E	383	28	92
PTFE	383	28	28
Tefzel	383	28	48
LDPE	338	48	48
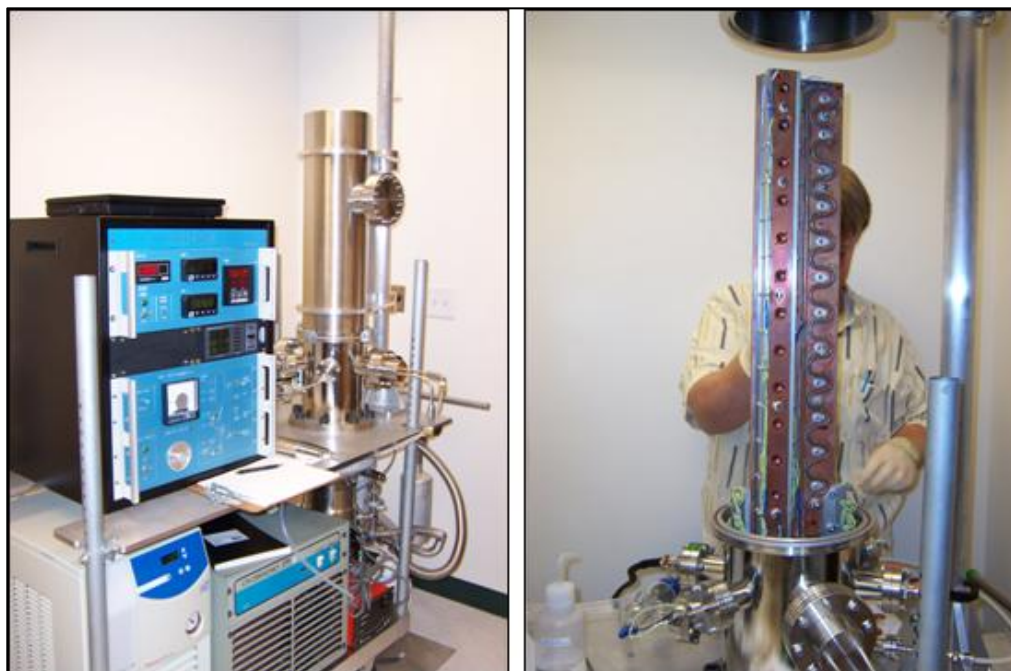
FIG. 3.1. Bakeout chamber and control box used for conditioning tests at SDL. Bakeout chamber and control box (left). Chamber open for sample tests (right). The round holes seen on the left side are slots for individual samples. The curving bar on the right is the heater bar.

The entire sample window assembly and samples then underwent a vacuum bakeout (excluding the LDPE samples, as noted below). They were placed in a mechanically pumped vacuum ($<10^{-2}$ Torr) furnace at ~383 K for a minimum of 68 hrs, excluding time for heating and cooling of the samples. This low-humidity, vacuum environment reduced adsorbed and absorbed water. In addition, the windows were in a grounded environment during conditioning, so that any residual charge in the thin film materials was dissipated at the greatly reduced resistivity at these higher conditioning temperatures. The LDPE samples were baked out separately at USU at a lower temperature of 345 K (below the LDPE working temperature
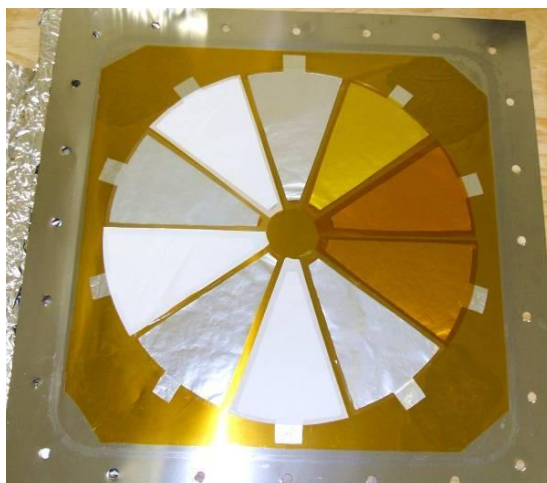
FIG. 3.2. Sample window for RIC experiments.

at ~363 K) with a diffusion pump vacuum system ($<10^{-4}$ Torr). Once the LDPE samples were baked out, they were mounted on the baked sample window assembly. After conditioning, the samples and sample window assembly were stored in an inert dry nitrogen environment in a large zip-lock bag before being mounted on the RIC chamber for testing. The samples were inserted in the large bag and then alternately flushed with dry nitrogen and pumped out in several repeated cycles to purge contaminating gas.

3.3   Chamber overview

Radiation induced conductivity was studied with a modified constant voltage method used while the sample was subject to intense radiation. Methods described by Frederickson (1977), Beckley *et al.* (1976), and Meyer *et al.* (1956) use a thin film polymer sample sandwiched between two electrodes with a constant voltage, *V*, across them (see Fig. 3.3). The current is simultaneously measured with a picoammeter. The lower limit of current measured with the picoammeter, I_{lim} (typically 2 pA for experiments reported here), coupled with the relatively large sample area, *A* (~80 cm^2), limits the measurable resistivity, ρ_{lim}, to ~10^{18} or 10^{19} ohm-cm (Fredrickson, 1977; Levy *et al.*, 1985) as determined by the expression

$$\rho_{lim} = \frac{V \cdot A}{I_{lim} \cdot D} \quad .$$

(3.3.1)

Note, low-field or low-temperature measurements for some of the samples were beyond the limit of the instrument.

A cross-sectional diagram for the RIC chamber test configuration is shown in Fig. 3.4. The diagram shows, from top to bottom: (i) the 100 μm thick grounded stainless steel sheet that acts as a vacuum window and a substrate on which the samples are mounted, (ii) a thin 25 μm Kapton insulation sheet to electrically isolate the subsequent electrode, (iii) a thin 12 μm Al foil conductive grounded electrode attached to the picoammeter circuit and made as thin as practical to minimize the charge deposited in the electrode foil by the high energy beam, (iv) the test sample ranging from 12 μm to 125 μm thick, (v) a 6.35 mm thick high voltage "pie wedge" electrode designed to stop the incident high energy radiation and to support the pressure load on the vacuum window, (vi) four sapphire rod standoffs per pie wedge to support the pie wedges and provide a very high leakage path to ground for the high voltage electrodes, (vii) a 19 mm thick grounded baseplate, and (viii) a grounded chamber vacuum wall. Figure 3.5 shows the inside of the RIC chamber, including the high voltage pie wedge electrodes and sapphire rod supports.

An electrical schematic for data acquisition in this study is shown in Fig. 3.6. In order to test samples with a wide range of electrical properties, including electrostatic breakdown voltage, a voltage divider was developed by Joshua Hodges at USU which allowed for a unique applied voltage to be applied to each sample. Sample voltages were tapped from a string of precision (1%) metal film high resistance (four 10 MΩ plus ten 2 MΩ plus eight 1 MΩ) resistors with low thermal resistance coefficients. The resistor string was attached to a high power supply (Accopian, Model P020HA1.5; 0 − 20 kV, 1.5 A) to provide between 100 V and 7 kV sample biases. Voltages on the samples were monitored through a voltage divider circuit.

Currents were measured with a picoammeter (Keithley, Model 6485) with an inherent resolution of ±0.4% (±100 fA). The ten sample currents were multiplexed to the picoammeter using a low current switching card (Keithley, Model 17158) and a multiplexer unit (Keithley, Model 7001), which had a higher leakage current that set the detectable current limit to ~2 pA with a ≤1% relative error. The picoammeter and multiplexer were controlled by a Labview[TM] program through a standard GPIB interface.
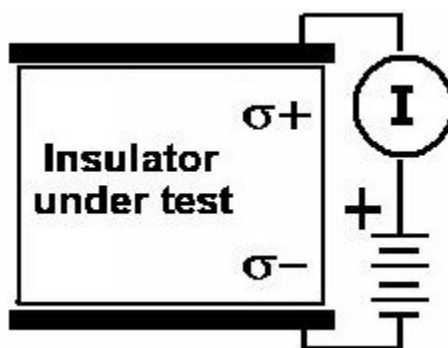
FIG. 3.3. Basic electrical schematic of the
Constant Voltage Conductivity (CVC) method.

The chamber vacuum was monitored using a nude ion gauge and several Convectron^{TM} gauges controlled by a standard vacuum controller (Stanford Research Systems, Model SRS IGC-1000), interfaced through an RS-232 connection. The chamber was pumped with a standard 30 l/s turbomolecular pump (Pfeiffer) backed with a two-stage mechanical pump with a base pressure of $< 10^{-4}$ Pa.

The current monitoring electronics and multiplexer, high voltage supply and voltage divider circuits, and vacuum controller were housed, along with a local control computer (Dell Optiplex Pentium IV) in a blue metal enclosure directly below the RIC chamber (see Fig. 3.7). To minimize the effects of the large amplitude frequency noise associated with the accelerator hall, all of the gaps were tightly sealed with metal tape and the latched door was sealed with an EMI gasket (Tech-Etch, Model 250T). All cables between the chamber and the electronics enclosure were highly shielded and were enclosed in metal conduit (see Fig. 3.8). To further minimize noise, the electronics inside the electronics controller were all run by a single AC line attached to a low noise AC circuit in the reactor hall, which was fed to an EMI shield power filter mounted inside the electronics enclosure. The local computer was interfaced to a main control computer located in the accelerator control room via a single shielded Ethernet cable. Due to the elaborate noise mitigation measures taken, we experienced no computer glitches and saw no evidence of noise in the sensitive current signals when the accelerator was in operation.
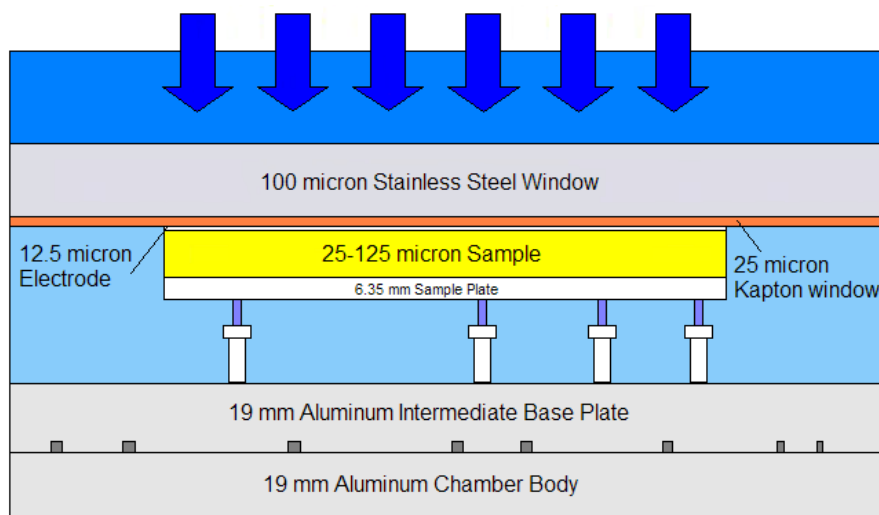
FIG. 3.4. Cross-sectional diagram on the RIC chamber. Blue arrows from above indicate the direction of incident radiation. Note that the drawing is not to scale.
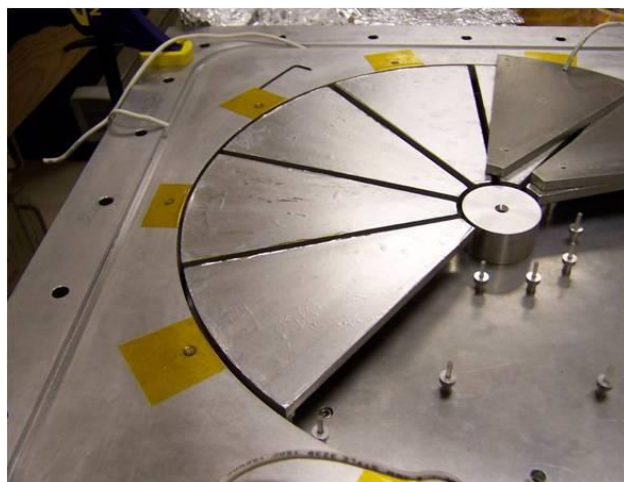
FIG. 3.5. Picture of the interior of the RIC chamber. Details shown include the pie wedge mounts (lower right), the pie wedge electrodes (upper right), and the mounted pie wedge electrodes (left).
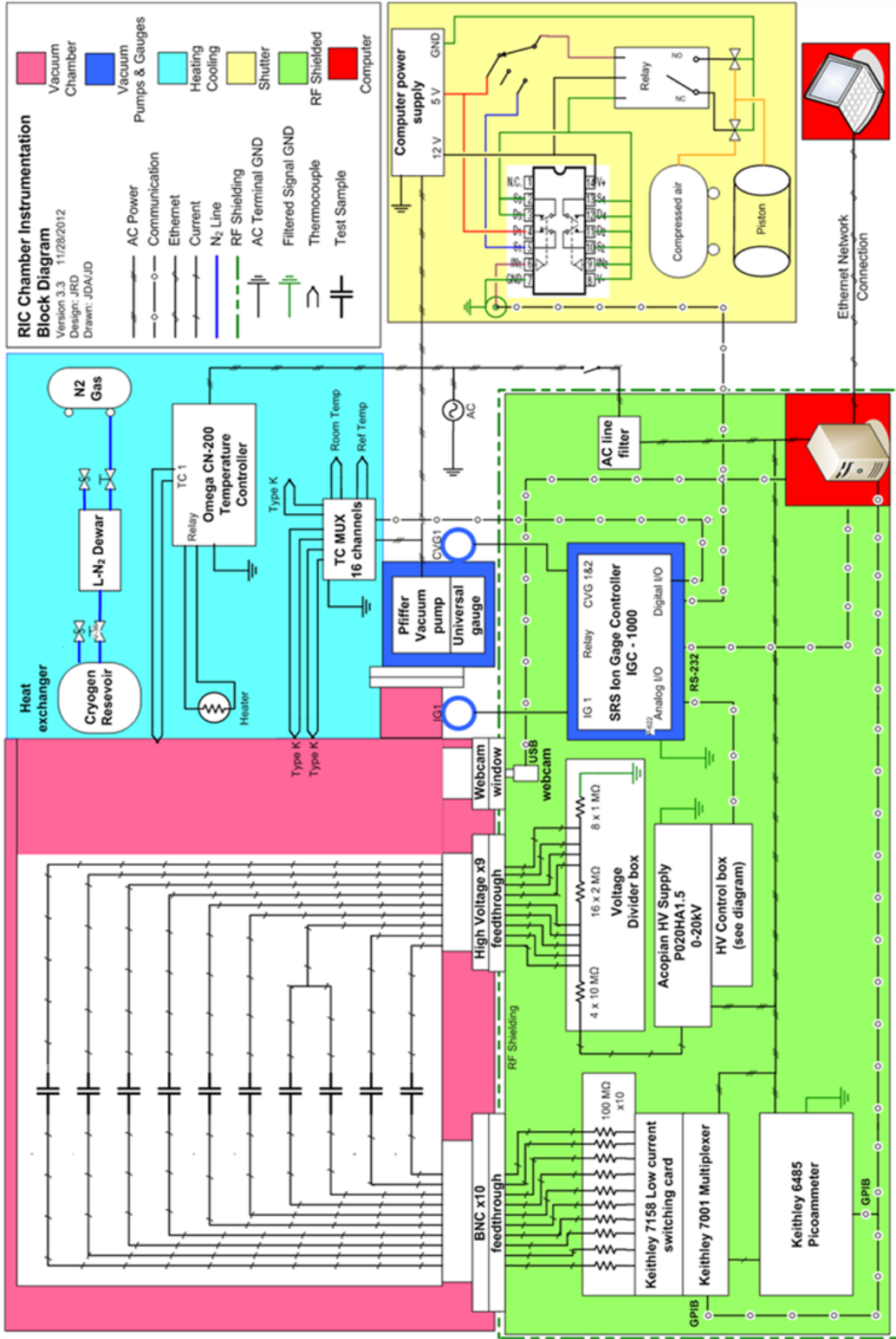
FIG. 3.6. Electronic schematic of RIC data acquisition.

FIG. 3.7. Metal electronics enclosure located below the RIC chamber. Additional polyblocks were placed so as to provide additional radiation shielding (left).

3.4   Experimental setup

RIC measurements were made at the Idaho Accelerator Center (IAC) in Pocatello, ID using the IAC 2 MeV to 25 MeV High-Repetition Rate Linear Accelerator (LINAC) pulsed electron accelerator (see Fig. 3.9). This accelerator is a side coupled, standing wave electron LINAC operating a fundamental frequency of ~2.8 GHz. An accurate beam current value is obtained by measuring an induced current in an aluminum toroidal coil (pickup loop) placed around the accelerator aperture. See Table 3.4 for the key parameters of the LINAC accelerator. For the RIC experiments, a 4 MeV beam was used with pulse widths between 200 ns and 3 μs and a repetition rate of 10 to 150 Hz.

Precise beam-on and beam-off times were controlled with a shutter assembly (see Fig. 3.10) designed and built at Utah State University by Joshua Hodges. The beam size was adjusted with the use of
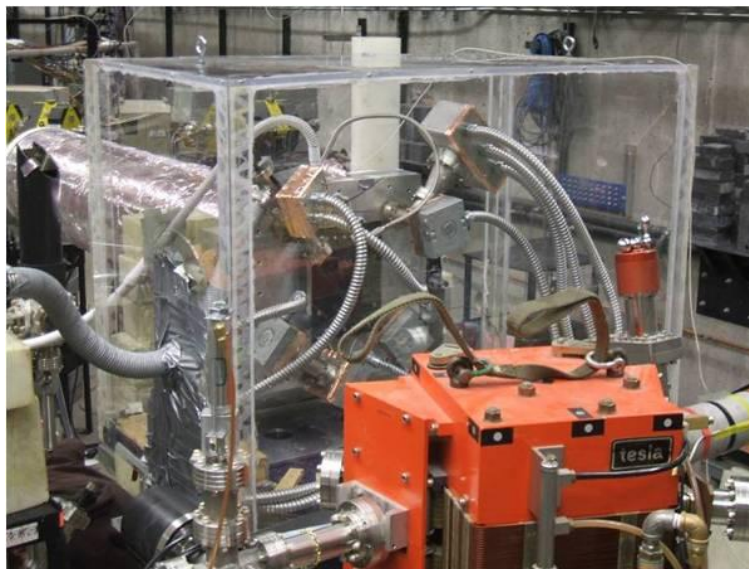
FIG. 3.8. Rear view of RIC chamber showing EMI interference shielding cable conduits, the vacuum line, and the cryogenic enclosure.
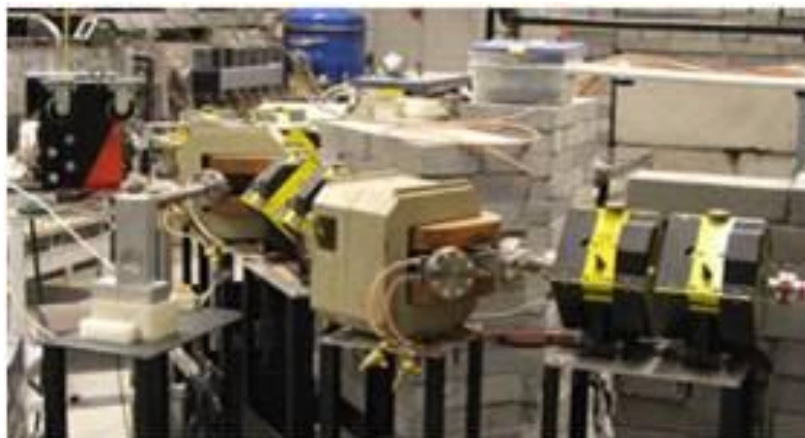
FIG. 3.9. Idaho Accelerator Center's LINAC.

a collimator and Al scattering foils to match the ~ 33 cm diameter of the total sample area shown in Fig.

3.2. The modular pneumatic electron beam shutter assembly was designed to:

- allow the beam operator to tune the electron beam while the RIC chamber was in place and operational;
- allow recorded computer time stamps of when the beam was on and off;
- align the chamber with the beam; and
- distribute the beam energy more evenly over the samples.

TABLE 3.4. Key parameters of the IAC's Linear Accelerator (LINAC).

Parameter	Value
Electron Energy	4-24 MeV
Fundamental RF Frequency	~2.8 GHz
Pulse Width	20 ns to 5μs
Repetition Rate	1 shot to 1,000 Hz
Maximum Charge per Pulse	500 nC
Maximum Time Averaged Current	100 μA
Maximum Beam Power	2 kW
Peak Electron Dose Rate	~10^8 Gray/sec
Maximum Time Averaged Electron Dose Rate	~10^5 Gray/sec
Peak γ-Ray Dose Rate	~10^3 Gray/sec
Maximum Time Averaged γ-Ray Dose Rate	~2 Gray/sec

The shutter components and their functions are described in order progressing from the accelerator side to the RIC chamber. They are a 2 ¾" collar that fits over the accelerator beam pipe 2 ¾" Conflat[TM] flange, the water-cooled first collimator, the pickup loop, the shutter, and the second collimator. All components of the shutter assembly are mounted to a base plate as shown in Fig. 3.10.

The shutter assembly was aligned with the RIC chamber and samples by placing two double-axis bubble levels on the shutter base plate and adjusting the height of threaded feet until the bubbles were both level. A self-leveling laser level was then placed on the base plate; the centerline of the laser level and the center line of the base plate were adjusted to be collinear. The laser was then adjusted left and right. By tightening the set screw on one side of the beam pipe while loosening the other, the entire assembly was moved while keeping the assembly tight and minimizing the torque on the accelerator beam pipe. Major adjustments were done by hand with both set screws loose.

The first collimator was used strictly for beam alignment and calibration. It was water cooled, since it dissipated most of the beam's energy. The current from the electrically isolated first collimator was connected to an ammeter through a BNC cable; this current was minimized during alignment, while maximizing the current through the pickup-loop located directly behind the first collimator. This was done while the shutter was closed and/or the RIC chamber was not in place, to minimize irradiating the samples. Measurements showed that leakage through the shutter was ~1% of the dose rate seen when the shutter was open.

Fig. 3.10. RIC shutter assembly. (Above) Beam
restricting shutter assembly and aluminum pickup coil
(shown in blue) used to measure beam current. (Below)
Shutter assembly located between LINAC aperture and the
drift tube.

The pneumatic shutter could be operated remotely by the main Labview™ program, RICmain.vi,
or manually by the shutter switch on the control box. The shutter opening rate was controlled pneumatically
by the amount of pressure applied from the nitrogen tank (typically 20-25 psi); the shutter closing rate was
controlled by the aperture of the solenoid release valve.

The second collimator and the scattering foils are modular and can be interchanged according to
the experiment requirements. The scattering foils are attached to the shutter and can be electrically isolated
to measure current, if needed. There are aluminum scattering foils of various thicknesses (0.001 in, 0.002
in, 0.003 in, 0005 in , 0.010 in, 0.100 in, and 0.125 in), as well as frames to hold the smaller scattering foils.

The foils can be stacked to provide other thicknesses and beam attenuations. The second collimator (with an outside diameter of 2 in) can also be removed or replaced.

The shutter assembly was positioned between the LINAC aperture and a drift tube, used to minimize beam scattering by ambient air. The drift tube was placed between the accelerator and the RIC chamber (Fig. 3.11) and backfilled with helium. The beam scatter was reduced by about 85%, roughly the ratio of the density of He to air. The ~15 m drift tube was made of common PVC sewer pipe of up to 50 cm in diameter. It was covered with 12.5 μm Al foil, and grounded to prevent charge buildup.

In addition, precautions were taken to shield all electronics from high energy radiation. Electronics were placed in a steel electronics enclosure underneath the RIC chamber, as described above. Polycarbonate blocks were also placed in front of the box during all RIC experiment runs as seen in Fig. 3.11 for additional shielding, particularly from neutron radiation. All cables coming out of the RIC chamber were covered with electromagnetic interference (EMI) shielding cable conduits (see Fig. 3.8).

3.5 Sample temperature characterization

High sample temperature (338 K) was obtained with a ~200 W oven heater plate sandwiched between two aluminum plates and connected to the back of the RIC chamber (Fig. 3.12). Power to the heater was supplied by a DC supply (Lauda, 60 V DC, 10 A) through a relay regulated by the standard PID temperature controller (Omega^R Model 9000 CN controller). Sample and electronics temperatures were monitored with up to 12 type K thermal couples.

Cold sample temperatures (232 K, 214 K, 123 K, and 103 K) were obtained with a liquid nitrogen (LN$_2$) temperature reservoir located on the back of the RIC chamber (Fig. 3.13). The temperature was controlled by adjusting the rate of LN$_2$ flow through the reservoir. To further facilitate acquiring low temperatures, a cryogenic enclosure was placed over the RIC chamber and backfilled with cold vented N$_2$ for thermal insulation during cold temperature runs (Fig. 3.8). For low temperature runs close to LN$_2$ temperatures (123 K and 103 K), two light bulbs (100 W and 240 W) and a fan (for air circulation) were used inside the electronics enclosure to prevent electronic failure due to low ambient temperatures.

Uniformity of temperature across all of the samples was tested by placing four thermocouples on the front of the chamber as shown in Fig. 3.14. Sample temperature was then cooled to ~-35°C and the

FIG. 3.11. The IAC beam line configuration showing (left to right) accelerator, beam shutter assembly, He-filled drift tube, cryogenic enclosure, sample window, and RIC chamber.

readings from the thermocouples were compared (Fig. 3.15). In addition, uniformity of temperature was tested between the front of the stainless steel RIC window (i.e., sample temperature) and the back side of the sample's high voltage plate (labeled '6.35 mm Sample Plate' in Fig. 3.4).

Analysis of the data from the front thermocouples (Fig. 3.15 – top) shows good temperature uniformity from sample to sample and a ~5 K difference between the front sample temperatures and the center of the RIC window. Analysis of the data from the thermocouples on front of the RIC window and behind the high voltage plate (Fig. 3.15 – bottom) showed a ~5 K temperature difference between the front and the back of the sample plates. It also showed that the center front thermocouple temperatures matched up with the back high voltage plate temperatures to within 2 K.

After temperature characterization, additional insulation was added to the RIC chamber in the form of a styrofoam covering on the front of the RIC chamber window, with a hole cut to match the size of the circle of samples (Fig. 3.16). The hole was then covered with plastic wrap (232 K and 214 K) or a 54 µm sheet of Kapton HN (123 K or 103 K). The temperature reservoir exit hose was fed into the styrofoam enclosure (Fig. 3.16), so the evaporated LN_2 would facilitate the cooling process.
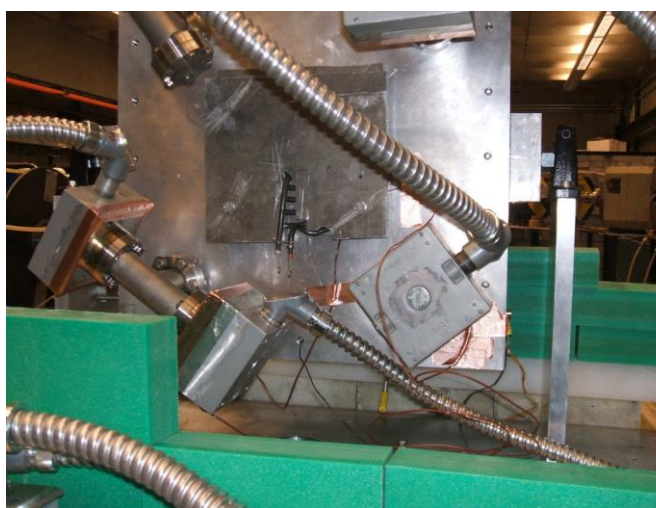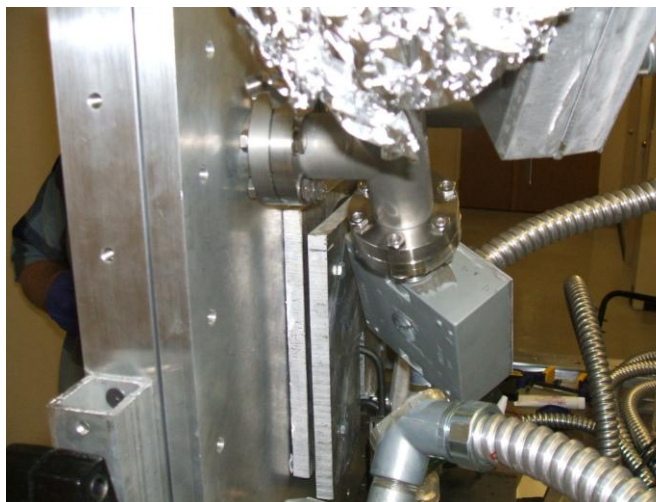
FIG. 3.12. Heater plate connected to back of RIC chamber (two images).

To begin each set of measurements, the chamber was heated or cooled to the desired equilibrium temperature, then held at constant temperature for >30 min under constant applied electric field to reach dark current equilibrium at the initial T before RIC measurements began. Sample temperature was monitored to ±2 K and showed variations of about ±5 K during a several hour run.

3.6   Dose rate measurement and calibration

Tests were typically conducted over three orders of magnitude of dose rate from 10^{-2} rad/sec to 10^{+1} rad/sec. The general range of incident radiation at the accelerator was set through a combination of increased source-to-sample separation (~16 m) and attenuation from the scattering foils and the vacuum

FIG. 3.13. Cryogenic temperature reservoir (left). Two reservoirs connected in series on the back of the RIC chamber (right).

wall, insulating film and front electrode. The specific sample dose rates were set primarily by adjusting the beam current and—at the higher dose rates—by increasing the repetition rate. Relative dose rate at the center of the beam (where there were no samples) was monitored in real time during each RIC test with a miniature ionization chamber monitor positioned outside the RIC chamber window, hanging between the large end of the He drift tube and the vacuum window (see Fig. 3.17).
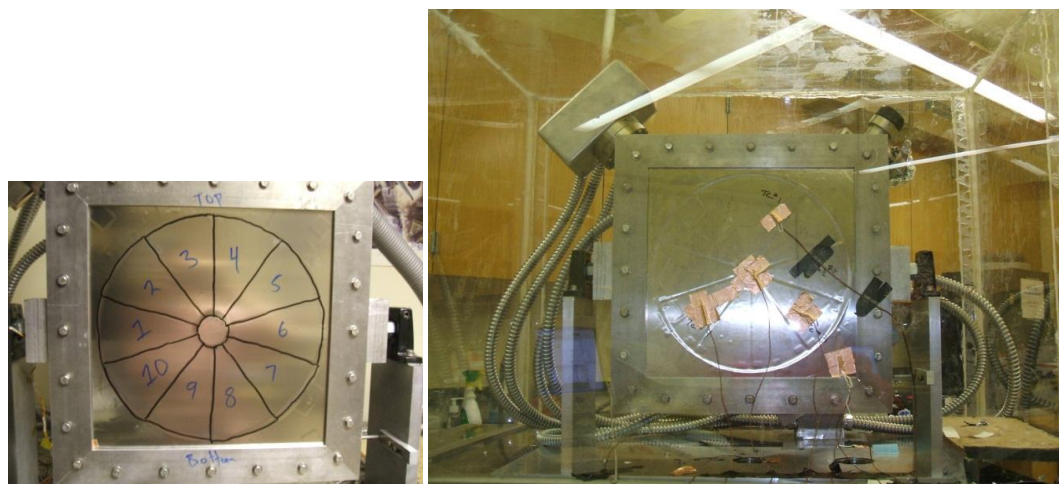
FIG. 3.14. Front of RIC chamber with sample and high voltage plate location numbers (left). Setup for temperature characterization testing (right). Thermocouples are located over samples 4, 7, and 10 and in the center of the window.
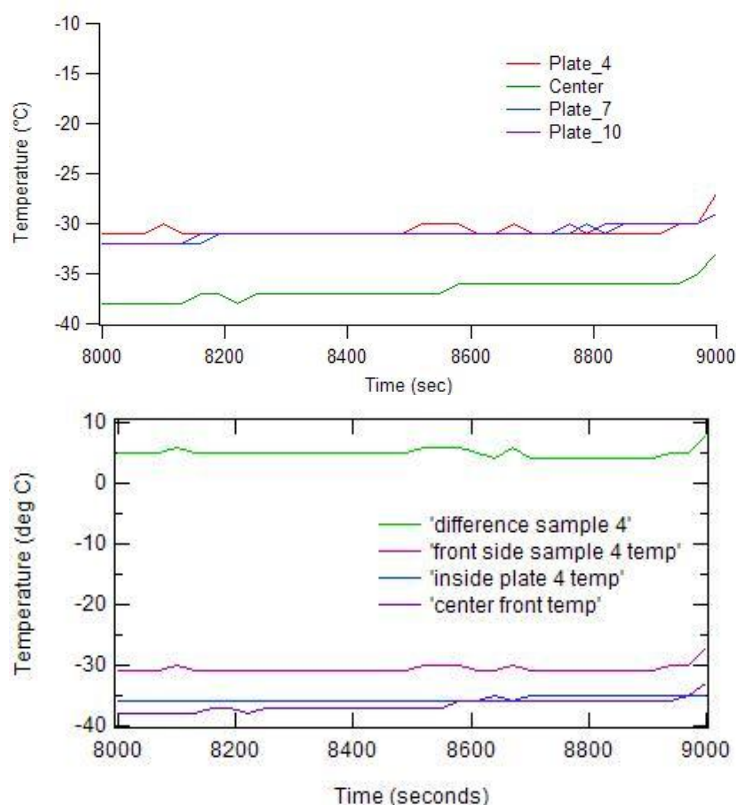
FIG. 3.15. Temperature comparison of thermocouples on the front of the RIC chamber (top). Temperature comparison of thermocouples on front of the RIC chamber, behind the high voltage plate, and the center front thermocouple (bottom). Average temperature difference between the front window and the back plate of sample 4 is 5 K. The center front thermocouple shows temperatures comparable to those on the back of the high voltage plates.

The ionization chamber had an inherent error of ~5%. Measurements using the miniature ionization chamber moved radially across the full beam (in both horizontal and vertical directions) showed that the relative intensity of the incident beam was quite uniform over the full sample area, with a Gaussian profile with a relative deviation from mean of ±5% (see Fig. 3.18). Because the samples were radial wedge shaped, the average dose rate of the samples had very small variations from sample to sample. The beam profile was confirmed and absolute dose rate calibration measurements were performed for calibration runs using optically stimulated luminescence dosimeters (Landauer, InLight MicroStarReader) placed at up to 15 locations on the RIC chamber window. The sensors and reader were calibrated at the Radiological and Environmental Science Laboratory using a NIST traceable ^{137}Cs source. These calibrations, including

FIG. 3.16. Cryogenic setup at IAC showing the liquid nitrogen hose fed into the styrofoam insulation.

various systematic errors, gave an estimated accuracy of ~20% and a precision of ~8% for the dose, at any given time.

3.7   Summary of error analysis

Given the discussions of the measurement methods, instrumentation, and uncertainties given above, we can estimate the precision and accuracies of the derived quantities for the RIC tests. The total resistivity for a single dose and voltage, calculated with Eq. (1.2), is found as the errors added in quadrature for the thickness (~6% accuracy), cross-sectional area (≤1% accuracy), applied voltage (≤1% accuracy and precision), and current (≤1% relative error and ±2 pA absolute error). Since the sample thickness and area remained constant, they do not contribute to precision estimates.

At lower resistivities, with measured currents above ~50 pA and dose rates of ~0.2 rad/s, the precision of a single total resistivity value is ~2% dominated by uncertainties in voltage and current measurements and the accuracy is ~8% dominated by variations in the thickness. At higher resistivities, near ρ_{lim} as given by Eq. (3.3.1), the uncertainties were dominated by the absolute uncertainty in current. Values of ρ_{lim} for each data set are shown as horizontal lines on Fig. 4.2 (and similar curves for other data sets shown in the Appendices A-E) and listed in Table 4.1 (and similar tables for other data sets shown in the Appendices A-E). Calculations of ρ_{RIC} from the subtraction of ρ_{DC} from the total resistivity [see Eq. (2.4.1)], introduce an additional error in ρ_{RIC} equal to the uncertainty in ρ_{DC} as shown in Fig. 4.2 and listed

FIG. 3.17. Miniature ionization chamber positioned between the RIC chamber window and the drift tube.

in Table 4.1 (and similar figures and tables in the Appendices A-E). However, the error in ρ_{RIC} is not significant above dose rates of ~0.03 rad/s and so is dominated by errors from ρ_{lim}.

Errors in the dose rate result from errors in the measured instantaneous dose rate and from approximations made in calculating the dose rate. As noted above, the measured instantaneous dose rate had an estimated accuracy of ~20% and a precision of ~8%. The dose rate was estimated from the range [see Eq. (3.1.1)] listed in the NIST database (assuming the continuous slow down approximation with an estimated accuracy of ≤20%) and the density (with precision and accuracy <1%). The cumulative uncertainties in dose rate are ~30% accuracy and ~8% precision.

The uncertainties in the materials parameters k_{RIC} and Δ are derived from Eq. (2.4.24). At higher dose rates, above <0.03 rad/s, the uncertainties are

$$\frac{\delta \Delta}{\Delta} \approx \frac{\delta k_{RIC}}{k_{RIC}} \approx \sqrt{\frac{1}{N_{pts}} \left[\left| \frac{\delta \rho_{RIC}}{\rho_{RIC}} \right|^2 + \left| \Delta \frac{\delta \dot{D}}{\dot{D}} \right|^2 \right]} \quad . \tag{3.7.1}$$

The uncertainties in k_{RIC} and Δ are ~20% accuracy and ~6% precision, dominated by uncertainties in the dose rate, but reduced by ~$\sqrt{2}$ since three to six data points are used to calculate the slope and intercept. At lower dose rates, where $\rho_{RIC} \le \rho_{lim}$, the data are not reliable for use in calculating the slope and intercept.
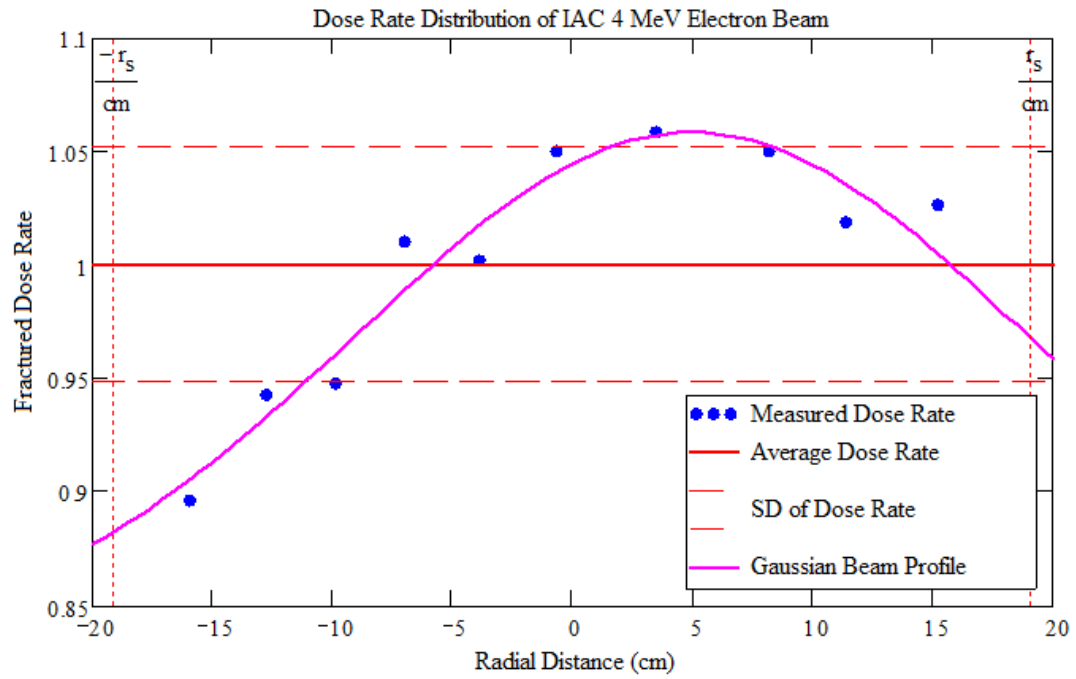
FIG. 3.18. Relative intensity of the incident radiation beam used for RIC experiments at IAC.

CHAPTER 4

DATA ANALYSIS

Analysis of RIC data requires a number of different stages to take raw current data to the point of temperature comparison of RIC parameters. This chapter provides a step-by-step understanding of the analytical procedures used in the analysis, along with example graphs. After a summary list of the key parameters studied, details of these analytical procedures will be given using Kapton E as an example to illustrate the graphs and tables generated. Complete graphs and tables summarizing results for Kapton E, Kapton HN, LDPE, PTFE, and Tefzel are provided in Appendices A – E.

4.1   Summary of key parameters studied

The key parameters obtained and analyzed in this experiment are:

i)   Determination of the equilibrium current and the equivalent resistivity due to radiation induced conductivity on the sample as a result of each incident dose rate.

ii)   Exploration of the k and Δ values for each material by fitting the RIC resistivity values on a log-log plot according to Eq. (4.1) below.

iii)   Discovery of the temperature dependence of RIC resistivities, k values, and Δ values using data taken at various temperatures, ranging from 103 K to 356 K.

iv)   Determination of experimental validity by taking room temperature runs on each test date and comparing their resultant k and Δ values.

v)   Definition of the long-term effect from total incident dose, as well as any effect from beam pulse characteristics on RIC. This was done by:

   a.   Taking repeated measurements on the samples at the same dose rate while varying the beam characteristics.

   b.   While keeping the total current on the sample constant, the pulse width and beam current were varied (done during June 19 data run).

   c.   Finally, the total charge per pulse and the pulse rep rate were varied, keeping a constant total current (done separately).

A number of different analysis programs exist to facilitate the organization and analysis of RIC data. A Labview^{TM} program initially formats RIC current value data in preparation for importation into Microsoft Excel^{TM}. In Excel^{TM}, RIC data is plotted and labeled according to beam on/off times. Final RIC analysis is performed in two Mathcad^{TM} sheets, one of which plots RIC data and allows k and Δ value fits. The other Mathcad^{TM} sheet performs temperature dependence analysis of both the k and Δ values, as well as of the complete RIC temperature data.

4.2   Step-by-step analysis procedures

1) RIC analysis begins with a semilogarithmic plot of raw rear-electrode current data versus time. Data initially was taken in ~23 sec. time intervals in November 2006. However, by February 2007 the resolution was improved to ~10 sec intervals. Currents ranged from 0.001 nA to a saturation limit of ~5 nA. These plots were generated in Microsoft Excel^{TM} and include labels indicating beam-on and beam-off times and the incident dose rates. See Fig. 4.1, as an example. Seven beam-on intervals at 0.02, 0.19, 0.52, 0.66, 0.83, 2.55, and 4.32 rad/s are shown. The resistivity resolution was measured with applied voltage across the samples, but with no incident current, at the beginning of each trip to IAC. Peak values at each incident dose rate were found by averaging current values during equilibrium. Note: Before averaging data, point values corresponding to random current spikes were removed. Also, in taking RIC data, polarization currents (such as those discussed in relation to Fig. 2.1) had been allowed to decay for ~30 minutes before turning on incident radiation in order to achieve an approximately constant value, $< 1\%$ of initial polarization values.

2) Once current plots are generated, the point at which equilibrium current is achieved is estimated (see Fig. 4.2.). Current values from the time equilibrium is established until the beam is turned off are then averaged. The standard deviation in this interval provides an estimate of the uncertainty in the measured currents.

3) The resultant average equilibrium current from step 2 is then used to calculate the resistivity change due to incident high energy radiation. By using the incident dose rate, the current average can be
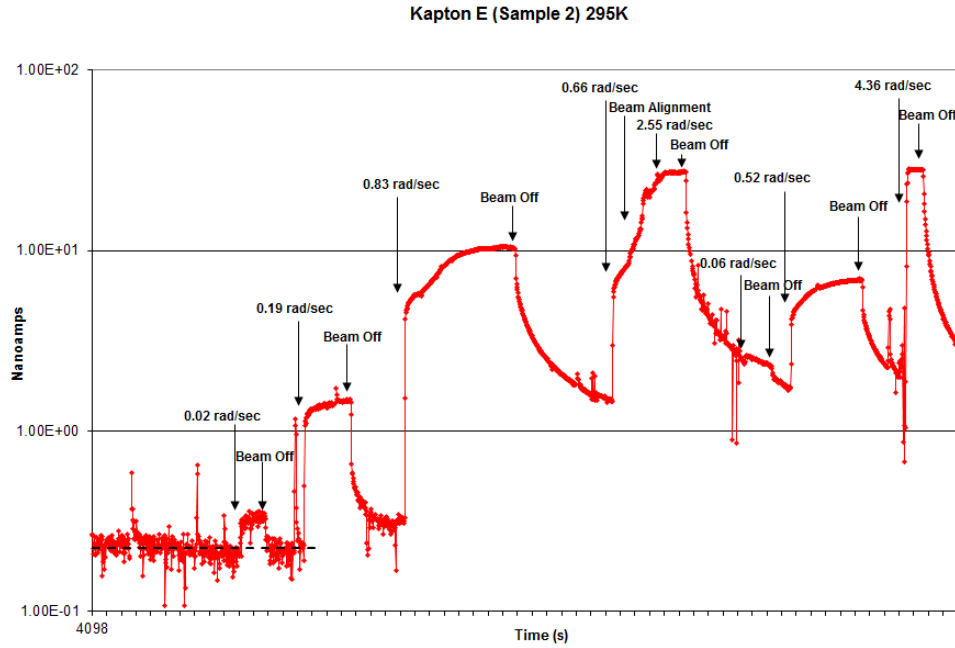
FIG. 4.1. Sample RIC current graph. Current data for Kapton E taken at 295 K on February 28, 2007. Spikes in data were found in every data run. Generally, they were only over one data point, but occasionally they lasted longer. Spikes were ignored in the analysis. The approximate baseline current value of $2.3 \cdot 10^{-1}$ nA is also shown. These currents had been allowed to decay for ~30 min before turning on radiation, to values of $<$ 1% of initial polarization values.

converted to a resistivity value with the intrinsic form of Ohm's law [Eq. (1.1)]. Using the applied voltage, $V=F \cdot D$, and current, $I=J \cdot A$, Ohm's law becomes [see also Eq. (1.2)].

$$\rho_{total} = \frac{V \cdot A}{I \cdot D} \ ,$$
(4.1)

where V is the applied voltage, A is the effective sample area, I is the averaged equilibrium current, and D is the sample thickness. The uncertainty in ρ_{tot} is dominated by the uncertainty in current as discussed in Section 3.7.

4) The conductivity of a material is enhanced with incident radiation as discussed in Chapter 2 [see Eq. (2.4.24)], the resistivity changes according to an inverse law:

Kapton E (Sample 10) 295K
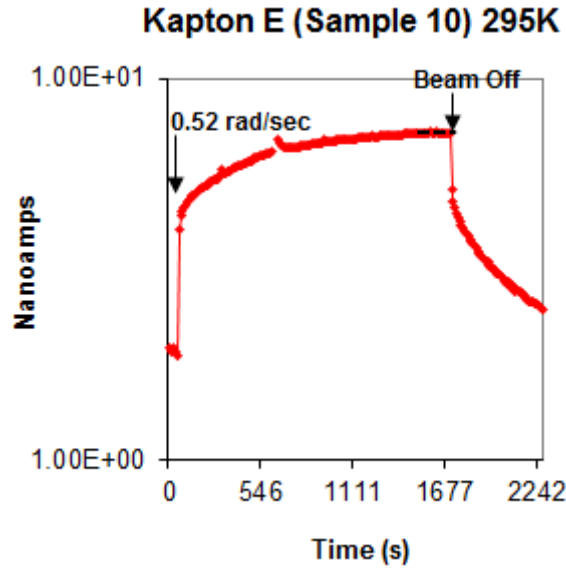
FIG. 4.2. Current versus time of a single measured dose rate. Typical measurement features include an initial rapid rise in current followed by a gradual rise to equilibrium current (dashed line). Similarly, when the radiation beam is turned off, a large initial drop in current is seen followed by a gradual decrease to dark current conductivity current.

$$\frac{1}{\rho_{total}} = \frac{1}{\rho_{DC}} + \frac{1}{\rho_{RIC}} \quad , \tag{4.2}$$

where ρ_{total} is the total resistivity in the sample under incident radiation, ρ_{DC} is the sample's dark current resistivity, and ρ_{RIC} is the resistivity due to the incident radiation. Dark current resistivities were obtained from independent measurements as discussed in Section 3.1. Equation (4.2) is solved for the RIC resistivities, which are then graphed versus dose rate on a log-log scale. (See Fig. 4.3)

5) Each resistivity graph is fit according to the theory discussed in Chapter 2 surrounding Eq. (2.4.24). The equivalent equation in terms of resistivity is given by

$$\rho_{RIC} = \frac{1}{\sigma_{RIC}} = \frac{1}{k_{RIC} \cdot \dot{D}^{\Delta}} \qquad or \qquad log\left[\rho_{RIC}\right] = log\left[k^{-1}\right] - \Delta\, log\left[\dot{D}\right] \quad , \tag{4.3}$$

where $\dot{D}$ is the dose rate and k_{RIC} and Δ are material parameters. The RIC resistivity data fit is optimized by adjusting the values of k_{RIC} and Δ by trial and error (see Fig. 4.3). The DC resistivity is

the equivalent to a measurement under no incident dose or $\dot{D}=0$. Since the graphs are log-log, the DC resistivities were included in the fits by adding 1 μrad/sec to the dose rates. On a log-log plot, the slope of Eq. (4.3) is given by $-\Delta$. At $\dot{D}=1$ rad/sec, log $[\dot{D}]=0$ and $\log[\rho_{RIC}]=\log[k_{RIC}^{-1}]$ or $k_{RIC} = \left[\rho_{RIC}\right]^{-1}$ rad/sec. Also shown in each graph are horizontal lines representing values of the DC resistivity as measured at USU (ρ_{DC}) and the limit of measureable current during each data run (ρ_{limit}). Resistivities at lower dose rates can be found by extrapolating the fit down (shown by a dashed line extension of the fit).

6) Temperature comparisons were done by color-coding and plotting typical results and fits for each temperature on the same log-log graph. See Fig. 4.4.

7) Temperature comparisons of k_{RIC} and Δ were done by plotting k_{RIC} and Δ values versus temperature. The k_{RIC} fits include a simple exponential [see Eq. (4.4)] and a two-part exponential fit. The two-part exponential fit assumes a constant value, k_0, up to a critical temperature, T_{cr}, with an exponential increase above T_{cr} [see Eq. (4.5)]. Also included is the mean k_{RIC} value, $\overline{k}_{RIC}$. See Fig. 4.5. Error bars show estimated error values of 20% uncertainty, as discussed in Section 3.7. Values of the fitting parameters k_0, k_1, k_2, and T_1 are listed in Table 4.1. Also listed in Table 4.1 are the sample thickness, D, density, p, dielectric constant, ε_r, and the breakdown electric field, F_{ESD}.

$$k_{RIC} = k_0 \cdot \left[1 + exp\left[-k_1 \cdot \left(\frac{T_{cr}-T}{T} \right) \right] \right] \quad , \text{ and} \qquad (4.4)$$

$$k_{RIC} = k_0 \cdot e^{k_2 \cdot (T-T_{cr})} \quad . \qquad (4.5)$$

Δ fits include a similar two-part linear fit, which assumes a constant value up to T_{cr} and uses a linear fit above T_{cr} [see Eq. (4.6)]. The other fit included is the fit proposed by Fowler [see Eq. (2.4.25)]. The last fit used is simply the mean Δ value, $\overline{\Delta}$. See Fig. 4.5. Error bars show estimated

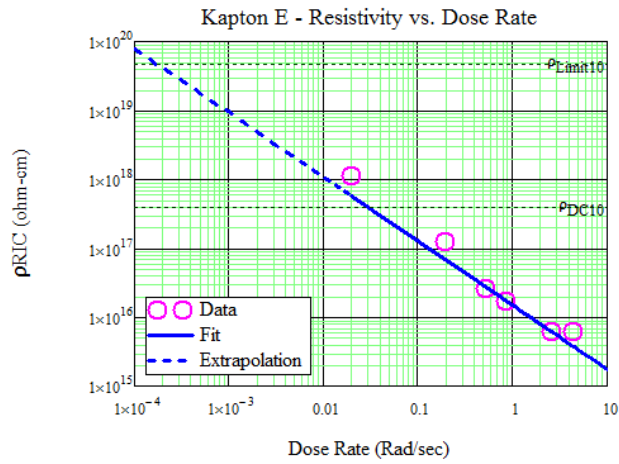FIG. 4.3. Sample resistivity data and fit for Kapton E taken at 295 K on February 28, 2007.
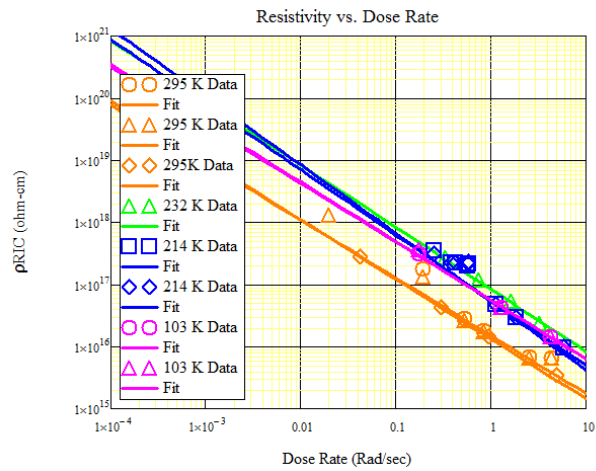

FIG. 4.4. Data and temperature-independent fits for Kapton E taken at temperatures ranging from 103 K to 295 K.

error values of 20% uncertainty, as discussed in Section 3.7. The values of the Δ fitting parameters, Δ_1 and T_1, is also listed in Table 4.1.

$$\Delta = 1 + \Delta_1 \cdot (T - T_{cr}) \quad . \tag{4.6}$$

TABLE 4.1. Sample table of complete results for Kapton E.

Date Acquired / Carousel Position	Temp (K)	Thickness (μm)	Applied (% of Breakdown)		Approximate Resistivity Resolution (Ω-cm)	Dark Current Resistivity (Ω-cm)	RIC Power Law Fit Parameters	
			Voltage (V)	E-Field (MV/m)			k (sec-Rad^{-1}/ Ω-cm)	Δ
6/19/07 Position 9	295 ± 0.5	24.5 ± 6%	(22%)		$2 \cdot 10^{19}$	$3.3 \cdot 10^{18} \pm$ 20%	$7.2 \cdot 10^{-17} \pm$ 20%	0.92 ± 20%
			2450 ± 1%	96 ± 10%				
2/28/07 Position 2	295 ± 0.5	24.5 ± 6%	(50%)		$5 \cdot 10^{19}$	$6.5 \cdot 10^{17} \pm$ 20%	$8.0 \cdot 10^{-17} \pm$ 20%	1.39 ± 20%
			5500 ± 1%	217 ± 10%				
2/28/07 Position 10	295 ± 0.5	24.5 ± 6%	(50%)		$5 \cdot 10^{19}$	$6.5 \cdot 10^{17} \pm$ 20%	$8.0 \cdot 10^{-17} \pm$ 20%	1.39 ± 20%
			5500 ± 1%	217 ± 10%				
3/1/07 Position 2	232 ± 1	24.5 ± 6%	(50%)		$5 \cdot 10^{19}$	$1.0 \cdot 10^{18} \pm$ 20%	$1.4 \cdot 10^{-17} \pm$ 20%	1.0 ± 20%
			5500 ± 1%	217 ± 10%				
3/2/07 Position 2	214 ± 2	24.5 ± 6%	(50%)		$5 \cdot 10^{19}$	$1.2 \cdot 10^{18} \pm$ 20%	$1.8 \cdot 10^{-17} \pm$ 20%	1.1 ± 20%
			5500 ± 1%	217 ± 10%				
3/2/07 Position 10	214 ± 2	24.5 ± 6%	(50%)		$5 \cdot 10^{19}$	$1.2 \cdot 10^{18} \pm$ 20%	$1.8 \cdot 10^{-17} \pm$ 20%	1.05 ± 20%
			5500 ± 1%	217 ± 10%				
6/19/07 Position 3	103 ± 3	24.5 ± 6%	(22%)		$2 \cdot 10^{19}$	$7.0 \cdot 10^{21} \pm$ 20%	$1.8 \cdot 10^{-17} \pm$ 20%	0.94 ± 20%
			2450 ± 1%	96 ± 10%				
6/19/07 Position 4	103 ± 3	24.5 ± 6%	(22%)		$2 \cdot 10^{19}$	$7.0 \cdot 10^{21} \pm$ 20%	$1.7 \cdot 10^{-17} \pm$ 20%	1.0 ± 20%
			2450 ± 1%	96 ± 10%				
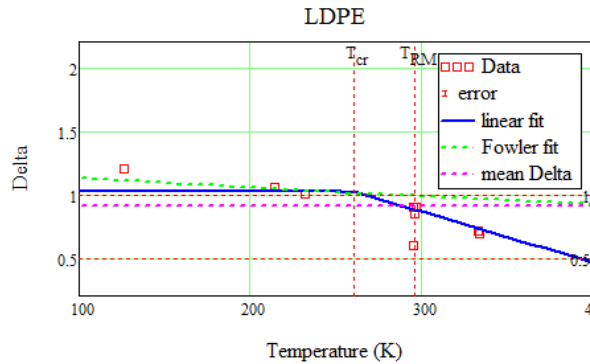
FIG. 4.5. Sample plot of Δ values found for Kapton E with a two-part linear fit and the fit proposed by Fowler [see Eq.(2.4.25)]. Also plotted is the mean Δ value, $\overline{\Delta}$.

8) Temperature comparisons similar to RIC resistivity vs. temperature plots shown in Fig. 4.3 were also done by color-coding and plotting results and fits using k_{RIC} and Δ values extrapolated from the fits from Step 7 (see Fig. 4.6), rather than the k_{RIC} and Δ values determined by directly fitting the individual data runs. See Fig. 4.4.

9) A table (Table 4.2) was created listing each data run and the resultant k_{RIC} and Δ values obtained by directly fitting data from each individual run in Mathcad^{TM}. Reproducibility was analyzed by comparing k_{RIC} and Δ values for all 295 K runs.   Results were also checked visually with a graph
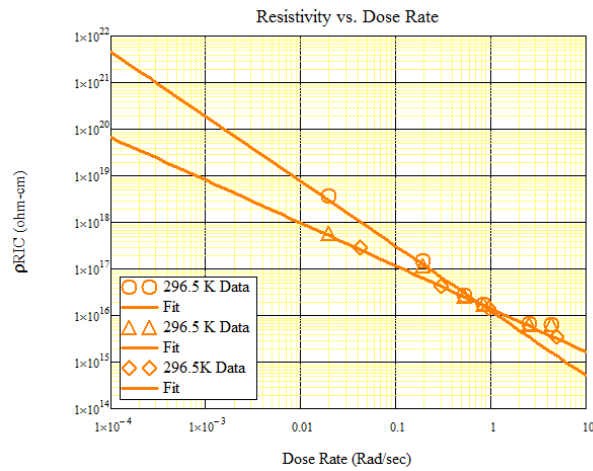
FIG. 4.6. Sample graph of all room temperature data for Kapton E. Notice two of the three fits overlay each other (triangles and diamonds). The circle current data saturated on the two highest data points, making a valid fit more difficult.

showing the data and fits for all 295 K runs (Fig. 4.7).

10) The long-term effect from total incident dose was determined, as well as any effect from beam pulse characteristics on RIC. This was done by taking repeated measurements on the samples at the same dose rate while varying the beam characteristics. While keeping the total current on the sample constant, the pulse width and beam current were varied (done during June 19 data run). Refer to Fig.4.8. Similarly, the total charge per pulse and the pulse rep rate were varied, keeping a constant total current (done separately). Refer to Fig. 4.9.
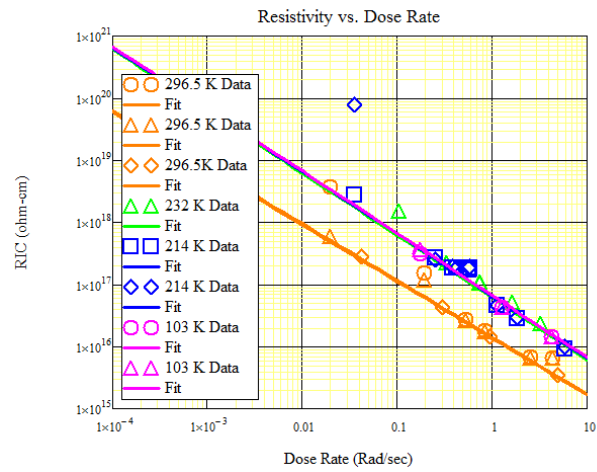
FIG. 4.7. Data and temperature-dependent fits for Kapton E taken at temperatures ranging from 103 K to 295 K.
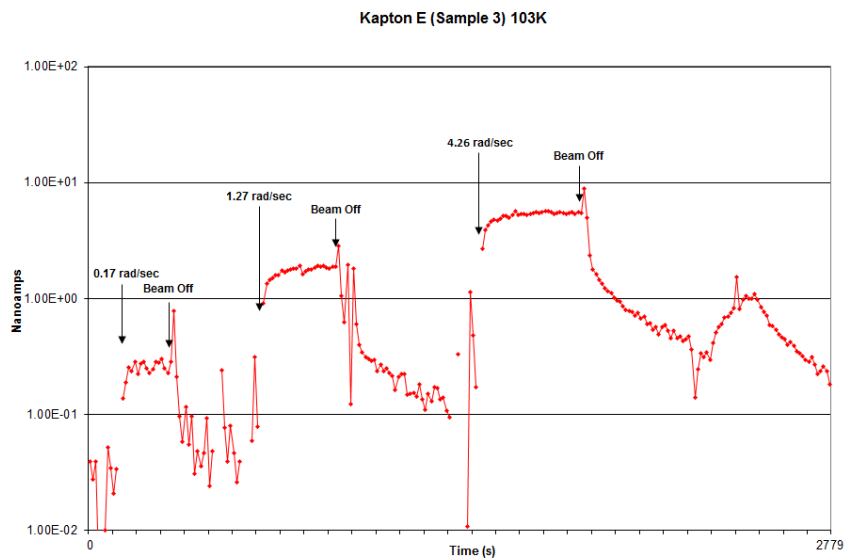
FIG. 4.8. Sample current graph with beam characteristic testing. Data run taken at 103 K on June 19, 2007. During the data run, the pulse width and beam current were together varied to maintain a constant total current. No significant change was observed.
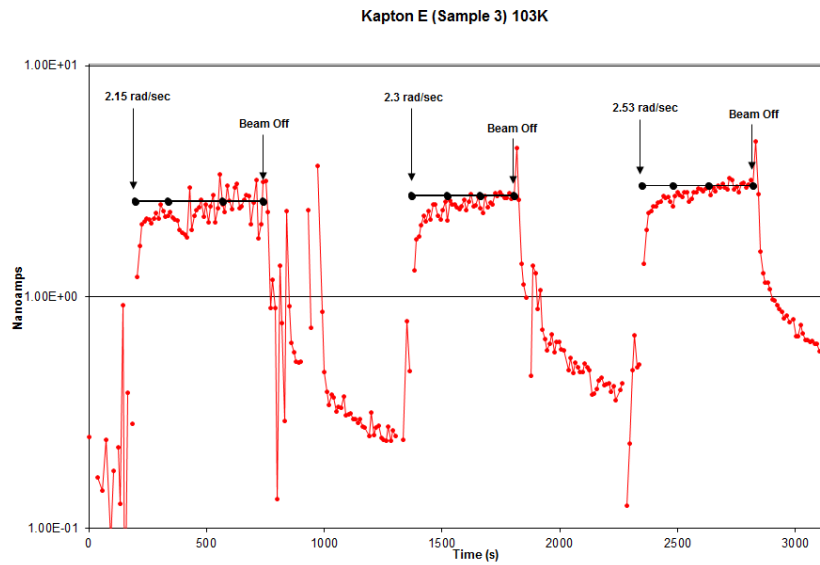
FIG. 4.9. Sample graph of repeat dose and beam characteristic testing. While maintaining a constant dose rate and current, the pulse repetition rate and the charge per pulse were varied on the incident beam. No significant change was observed.

CHAPTER 5

RESULTS AND CONCLUSIONS

Insulators can be classified or grouped according to each material's distribution of holes or traps. These distributions have been observed to control the mobility of charge carriers, and by extension, the insulators' electrical behavior under incident radiation. In general, a uniform distribution of shallow traps (monotonically decreasing in trap density with depth in energy below the conduction band edge) will yield $\Delta \sim 1.0$ and a highly exponential distribution of traps will yield $\Delta \rightarrow 0.5$ (Rose, 1951; Fowler, 1956a). At low E-fields, materials with a uniform distribution of shallow traps ($\Delta \sim 1.0$) are expected to have conductivities that show little temperature dependence, while those with a more exponential distribution ($\Delta \rightarrow 0.5$) will have higher temperature dependence. The overview of this topic provided in Sec. 2.4 is extended in Appendices G and H. While it is difficult to determine trap distributions in highly disordered insulating materials, such as those polymers used in this study; general observations can be made in regards to each material's temperature dependence in relation to its Δ values.

This chapter begins with a summary of the limited results available in literature in Section 5.1. Section 5.2 contains a discussion of the data acquired in this study in relation to the literature and the theory. In Section 5.3, the precision and accuracy of this experiment are discussed, as well as the effect of any extended radiation exposure and of varying the LINAC pulse characteristics. Section 5.4 addresses those conclusions that were beyond the scope of this thesis, but that could be the focus of future work. A final conclusion is given in Section 5.5.

5.1   Literature comparison

Unfortunately, only a limited amount of published studies exist with which to compare these results. The difficulty lies more in the nature of the conditions under which this study was undertaken than in a complete lack of enhanced conductivity experiments. Since the primary interest in this work revolves around the James Webb Space Telescope and its space environmental conditions, the materials in this investigation were prepared with a vacuum bakeout to release any trapped contaminants. Most other studies did not require such a rigorous sample preparation, and as a result, some variation in RIC values is to be expected due to the presence of water and volatile contaminants. Another distinctive aspect of this

work is the use of high energy radiation. Many papers have been published studying the effects of radiation on charge transport, or diffusion, using a low-energy incident radiation beam, which only partially penetrates the sample material with beam energies <50 keV (Dienes and Damask, 1958; Marton *et al.*, 1988; Sessler, 1992; Marka *et al.*, 2003; Sessler *et al.*, 2004) and 1-2 MeV (Newman *et al.*, 1983; Priolo *et al.*, 1988). Nonpenetrating beams deposit charge, which is then allowed to dissipate throughout the sample material (Wilson *et al.*, 2013). In contrast, the main focus of this work has been on the effect of high energy radiation on a material's overall conductivity without the added complexity of additional charge buildup (often referred to as space charge) and internal electric fields. In fact, specific care was taken to avoid charge buildup by deliberately selecting a beam energy high enough to allow the incident radiation to completely penetrate the samples without charge deposition (see Section 3.1). Rather, the beam excites electrons into conduction levels by depositing energy as it travels through, thereby enhancing the overall sample conductivity. For lack of more relevant literature, general observations and comparisons will be done with the few literature results available that use an incident high energy radiation beam with no bakeout. Table 5.1 provides a comparison of literature values of k_{RIC} and Δ with those from this study.

While LDPE is not specifically relevant to the JWST project, it was included in this study for the simple reason that it is more widely studied than any of our other available materials. Yahagi and Shinohara (1966) did an extensive study on trap distribution in polyethylene over a temperature range of ~190 K to ~300 K. While the results lack a necessary subtraction of dark current conductivity, Δ values ranging from ~0.6 to ~0.8 increase with decreasing T. Fowler (1956a) found a consistent value of 0.81 for Δ over a temperature range of 293 K to 355 K. He used a wide variety of LDPE type of materials, which produced k_{RIC} values of ~5 x 10^{-16} sec·rad^{-1}/ohm·cm. Harrison (1962) studied RIC at three temperatures: 311 K, 322 K, and 333 K. He found Δ=0.74 and k_{RIC} ranging from 1.5 x 10^{-15} sec·rad^{-1}/ohm·cm to 4.5 x 10^{-15} sec·rad^{-1}/ohm·cm. Hanks and Hamman (1969) also found a consistent value for Δ=0.74 over temperatures ranging from 311 K to 333 K, with k_{RIC} values ranging from 5 x 10^{-16} sec·rad^{-1}/ohm·cm to 1 x 10^{-15} sec·rad^{-1}/ohm·cm. Meyer *et al.* (1956) reported that between the temperatures of 78 K and 273 K the induced current, and by extension k_{RIC}, was nearly independent of temperature.

TABLE 5.1. Summary results for materials used in RIC study. Also included is a summary of the results from available literature. Note that Kapton E and Tefzel had no literature with which to compare.

Material	Temperature Range (K)	k-value Range (sec·Rad^{-1}/ohm·cm)	Δ-value Range	Mean Δ-value (295K)
Kapton E	103 – 295	$1.2 \cdot 10^{-17} – 7.6 \cdot 10^{-17}$	0.93 – 1.05	0.94
Kapton HN	103 – 333	$4.2 \cdot 10^{-18} – 6.1 \cdot 10^{-17}$	0.85 – 1.32	0.97
Kapton HN[a]	283 – 333	---	0.81 – 0.90	0.86
LDPE	123 – 333	$2.3 \cdot 10^{-18} – 1.2 \cdot 10^{-15}$	0.69 – 1.20	0.88
LDPE[b]	190 – 350	$5.0 \cdot 10^{-16} – 4.5 \cdot 10^{-15}$	0.60 – 0.80	0.81
PTFE	103 – 295	$3.9 \cdot 10^{-18} – 2.9 \cdot 10^{-17}$	0.91 – 1.23	1.23
PTFE[c]	294 – 383	---	0.54 – 0.73	0.70
Tefzel	232 – 333	$2.2 \cdot 10^{-18} – 8.5 \cdot 10^{-17}$	0.75 – 1.10	0.95

a. See Hedvig (1964), and Yang and Sessler (1992).
b. See Fowler (1956b), Harrison (1962), Yahagi and Danno (1963), and Hanks and Hamman (1969).
c. See Fowler (1956b).

Rather than a constant Δ value, the current results (see Table C.1 and Fig. C.10) show a temperature-dependent trend similar to that of Yahagi and Danno (1963). Figure 5.1 shows a comparison of the values of Δ for LDPE. It could be that Fowler (1956a) and Hanks and Hamman (1969) had too narrow a high temperature range to see a clear dependence, and that any trend was lost in their experimental uncertainties. However, the range of values is in agreement with those of other researchers. Remember that at low temperatures, Δ is nearly temperature-independent and approaches a value of 1 [Eq. (2.4.25)]. As the temperature rises, Δ becomes more temperature-dependent and has a value approaching 0.5. It should be noted that empirical fits are used in Section 4.2 to model the temperature dependence of k_{RIC} and Δ. The k_{RIC} fits include either a simple exponential [Eq. (4.5)] or a two-part exponential fit [Eq. (4.4)]. Δ fits [Eq. (4.6)] include a similar two-part linear fit. Both fits assume a constant k_{ric}/Δ value up to T_{cr} and use an exponential/linear fit above T_{cr}.

Kapton E is a relatively new material on the market and, unfortunately, there is a lack of temperature-dependent literature values with which to compare. However, it has a similar composition as that of Kapton HN with a slightly lower concentration of nitrogen atoms. The only published values available for polyimide seem to be Δ values. Both Hedvig (1964) and Yang and Sessler (1992) have Δ values slightly lower than those obtained in this study. Hedvig (1964) found $\Delta \approx 0.90$ between 283 K and 333 K, and Yang and Sessler (1992) found $\Delta \approx 0.81$ at room temperature (~295 K). Both the Kapton E and Kapton HN samples in this study had a nearly constant value of ~0.95 for Δ, and exhibited a temperature-
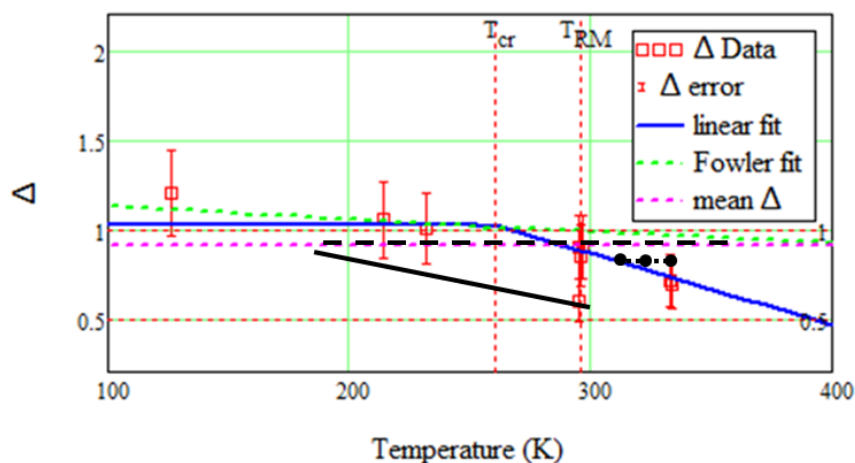
FIG. 5.1. Comparison of Δ values for LDPE. Red data points show results of the current study from Fig. C.10. Literature values are shown in black: solid line, (Yahagi and Danno, 1963); dashed line, (Fowler, 1956a); dots (Harrison, 1962); and dotted line (Hanks and Hamman, 1969).

independent conductivity. This was supported by data for k_{RIC}, which only showed a slight increase with temperature. Kapton HN and Kapton E were found to have similar values. Kapton HN had a slightly higher Δ value than Kapton E, although it exhibited the higher temperature dependence (Tables A.1 and B.1 and Figs. A.10 and B.10).

Fowler (1956a, 1956b) included PTFE in his study of RIC over a wide range of materials. He found Δ values between 0.54 and 0.73 with a temperature trend indicating higher values at lower temperatures, although he predicted a constant value and took an average. The current study found a Δ value of ~1.2, except for the lowest temperature at 103 K. These 103 K data runs produced Δ values of ~0.9, but also had a lot of noise. The data obtained for k_{RIC} showed only a slight increase with increasing temperature, as one would expect with these high Δ values (Table D.1 and Fig. D.10).

Tefzel is another relatively new material with a dearth of relevant temperature-dependent RIC literature to compare with data presented here. This study found a nearly constant Δ value of ~0.90. This value for Δ allowed for a slight amount of temperature dependence, which was found in k_{RIC}, with a constant value up to T_{cr}, chosen as 235.00 K, and an increasing value with temperature above T_{cr} (Tables 4.1 and E.1).

5.2   Material results

As mentioned before, theory predicts that materials with a uniform distribution of shallow traps with depth will be temperature independent and will have $\Delta \approx 1.0$ (refer to Section 2.4 and Appendix G). Materials with an exponential (or highly disordered) distribution of shallow traps with depth have a lower Δ value approaching $\Delta \approx 0.5$ and will exhibit a higher temperature dependence. A more complex temperature dependence of Δ can result for peaked distributions of deep traps, which depend on the value of the effective Fermi level relative to the peaks of the deep trap distribution (refer to Appendix G and Rose, 1951). Polymeric materials, such as those used in this study, are typically highly disordered materials by nature. Long and complex atomic chains make quantifying the nature of trap distributions difficult, but a high degree of disorder is certain. The results of this study for the most part support the theory developed in Chapter 2.

LDPE clearly exhibited the most temperature dependence (Fig. C.11), and had the lowest Δ values (Table 5.1). PTFE had the highest Δ value at a nearly constant 1.2 (Table D.1 and Fig. D.10). A satisfactory explanation for a Δ value greater than unity is still to be found. However, it is interesting to note that while PTFE exhibited temperature-independent RIC behavior, as expected (Fig. D.9), it showed a DC conductivity dependence on temperature (Table D.1). Perhaps the results for PTFE were skewed by the fact that PTFE can store a very large amount of charge and has an extremely low conductivity, which leads to extremely low charge dissipation. Kapton E had a Δ value ~1.0 and had the least temperature dependence. Because of their similar atomic composition, Kapton E and Kapton HN were expected to show similar behavior. This was true, for the most part, with Kapton HN having a slightly higher temperature dependence (see Figs. A.10 and B.12.)

5.3   Uncertainty, reproducibility, and validity

The details of uncertainty calculations can be found in Section 3.7 and a summary of the results are listed in Table 5.2. An interesting feature to note is the accuracy of the measured resistivity, which was found to depend on different parameters depending on the relative value of the absorbed dose rate. At all but the lowest dose rates (~0.2 rad/sec), the measured resistivity was dominated by the variations in the

TABLE 5.2. Summary of accuracy and precision of related RIC parameters.

Measurement/Calculation	Accuracy	Precision
Temperature (T)	$\pm$ 5 K	$\pm$ 2 K
Incident Dose Rate	~20%	~8%
Absorbed Dose Rate ($\dot{D}$)	~30%	~8%
Applied Voltage (V)	< 1%	< 1%
Thickness (D)	~6%	---
Cross-Sectional Area (A)	~1%	---
Measured Current (I)	< 1% (relative)	---
	$\pm$ 2 pA	
Measured Resistivity (ρ) (lower limit with $I \geq 50$ pA and $\dot{D} \geq$ ~0.2 rad/sec)	~8% (dominated by variations in D)	~2% (dominated by uncertainties in V and I)
Measured Resistivity (ρ) (upper limit near ρ_{lim})	~2% (dominated by absolute uncertainty in I)	~2%
Calculated RIC resistivity (ρ_{RIC})	Same as measured ρ	Same as measured ρ
RIC coefficient, (k_{RIC})	~20%	~6%
RIC coefficient, (Δ)	~20%	~6%

sample thickness. At the lowest dose rates, the accuracy was instead dominated by the absolute uncertainty in the measured current.

Reproducibility of these results was checked by taking a data run at room temperature (295 K) during each trip to the IAC. The graphs of these runs can be found in Appendix F. Multiple 295 K data runs could not be obtained for all of the samples. However, the three materials with valid data (Kapton E, Kapton HN, and Tefzel) showed a consistent value of k_{RIC} within the calculated percent error (Section 3.7). Therefore, the data of this study taken on three different trips to IAC and covering a total of seven different dates has been considered valid for comparison.

Fowler (1956a) suggested the possibility of a reduced equilibrium RIC with excessive absorbed dose. He introduced a total dose, ~10^6 rad, on polystyrene in order to validate his measurements, but found no change in conductivity. A more thorough study on conductivity versus total dose was done on the same materials as those in this study by Hanks and Hamman (1969). Hanks and Hamman (1969) found a damage threshold on TFE materials (PTFE and ETFE or Tefzel) at ~$1.7 \cdot 10^4$ rad, on polyimide material at ~$8.6 \cdot 10^5$ rad, and on LDPE to be > 10^7 rad (Table 5.3). Calculation of total absorbed dose experienced by each sample was estimated using methods described by Cheek and Linnenbom (1960) for an incident photon beam energy of 4 Mev. In effect, a coefficient is multiplied by the total incident dose. Total

TABLE 5.3. Total absorbed dose damage thresholds as reported by Hanks and Hamman (1969).

Material	Material Atomic Composition	Damage Threshold (as reported by Hanks, 1969)	Approximate Absorbed Dose Coefficient
Kapton HN	$C_{22}H_{10}O_5N_2$	8.6E+05 rad	0.89
Kapton E	Similar to Kapton HN with a higher composition of N	~8.6E+05 rad*	0.89*
PE (LDPE)	C_2H_4 (more C branches)	> 1.0E+07 rad	0.98**
TFE (PTFE and ETFE)	$C_4H_4F_4$	1.7E+04 rad	0.89

*Even if all of the C were replaced with N, the absorbed dose coefficient would only change by 0.4%.
** Increasing the concentration of C, lowers the absorbed dose coefficient.

incident dose was calculated by multiplying each incident dose by the time of beam exposure. See Table 5.4 for a list of the total incident dose seen by the samples on each experiment date.

As seen from Tables 5.3 and 5.4, only PTFE and ETFE ever approached the damage threshold. By examining repeat measurement data taken on PTFE (Figs F.5 and F.6) on June 19 at 103 K, the percent difference between the expected current values from k_{RIC} and Δ and the actual average current values only increased to a maximum difference of ~15% by the end of the experiment run. The first calculated percent different of the three was only 4%. All values were well within the uncertainty of k_{RIC} and Δ at ~20%. It is possible that this increase resulted from an increase in the total number of defect states, N_T, from radiation damage, although there is insufficient data to confirm this. An increase in N_T could lead to more stored charge and a concomitant rise in Δ, perhaps explaining the measured Δ in excess of 1.

Further repeated measurements at consistent dose rates were taken on March 2, 2007 at 214 K (Figs. A.5, A.6, B.7, C.7, and D.3). On both of these occasions, repeated measurements were taken after the regular data had been acquired; that is, after the sample materials had already experienced typical levels of absorbed dose. Beam characteristics of pulse width and repetition rate were also varied in these repeat dose measurements. However, no significant change in equilibrium current was seen when plotted with the rest of the data on the corresponding RIC graphs (with fits). In June, in addition to any long-term effects of absorbed dose, efforts were also made to quantitatively examine any effect varying beam characteristics might have on resultant data by varying the charge per pulse and the repetition rate, while keeping the total charge per pulse constant. The first measurement was taken with an incident dose rate of 2.15 rad/sec with an 86 nC charge/pulse, a repetition rate of 100 Hz, and a pulse width of 2 μsec. The second measurement

TABLE 5.4. Total incident dose seen by sample materials on each experiment date. Also, listed is the number of runs included in the calculations.

Date	Total Incident Dose (rad)	Number of Runs Taken
November 20, 2006	7.8E+03	1 (295 K)
November 21, 2006	1.2E+04	2 (295 K and 333 K)
February 28, 2007	7.4E+03	1 (295 K)
March 1, 2007	6.0E+03	1 (232 K)
March 2, 2007	7.0E+03	1 (214 K)
June 18, 2007	2.9E+03	1 (123 K)
June 19, 2007	1.3E+04	2 (295 K and 103 K)

was taken with an incident dose rate of 2.3 rad/sec with a 48 nC charge/pulse, a repetition rate of 200 Hz and a pulse width of 2 μsec. The last measurement was taken with an incident dose rate of 2.53 rad/sec with a 71 nC charge/pulse, a repetition rate of 100 Hz, and a pulse width of 2 μsec. Resultant equilibrium current was compared to the predicted value using the k_{RIC} and Δ values found at that temperature. No calculated values were outside ~20% of those found at equilibrium as mentioned above (see Figs F.2-6). This margin of error was acceptable considering, (i) there is a high degree of difficulty in maintaining a constant temperature at 103 K (temperatures varied by as much as 5 K over a single measurement), and (ii) varying beam characteristics introduces an additional margin of error in the calculations. We conclude that all tests indicate valid data, and that RIC is independent of varying beam characteristics to within 20%. This is not surprising since the data compilation in Fig. 2.2 strongly suggests that RIC is largely independent of how the energy is deposited, both by the type of particle used in the incident radiation beam (high or low energy electrons, neutrons, ions, etc.) as well as the repetition rate of beam used (DC, msec pulses, μsec pulses, etc.).

5.4   General observations for further study

A number of interesting features presented themselves in the course of this study, which are beyond the scope of this thesis, but indicate a need for further investigation. As shown in the raw current data curves in Appendices A – E, there are rich dynamic behaviors in the RIC current data. These include both a rapid initial rise in current occurring when the beam is turned on (Fig. 5.2, circle A), followed by an exponential time-dependent approach to an equilibrium value (Fig. 5.2, circle B). Similarly, a rapid decrease in current occurs when the beam is turned off (Fig. 5.2, circle C), followed by a longer, hyperbolic decay of current with time.

While this general behavior was found to occur in all of the sample materials, it was more pronounced at temperatures above T_{cr}. All of the materials used had a clear rapid rise in current once the beam had been turned on by opening the shutter (blue circle in Fig. 5.2). This rise lasted over the course of ~23 sec. An exception to this is Tefzel, which had a rapid rise time lasting ~34 – 46 sec. LDPE, Tefzel, and PTFE also had a slightly more gradual exponential rise to equilibrium compared to the polyimides above T_{cr}. A semi-empirical model for the time-dependent behavior was outlined in Section 2.4, followed by brief comments about more sophisticated dynamic theories. The time-dependent data presented here is extensive enough and of high enough quality to be able to derive values for important fundamental properties of the trap states in the materials by fitting the data to these theories. Work has already been begun by Alec Sim and JR Dennison of the USU Materials Physics Group to do just this.

The values of the k_{RIC} and Δ values as a function of temperature from this study can be merged with literature values to produce a more extensive data set extending over a wider temperature range. This extended data set may provide sufficient detail to warrant analysis of the temperature dependence of k_{RIC} and Δ in terms of the more detailed theoretically motivated expressions developed in Sec. 2.4 and Appendices G and H beyond the empirical fits [Eqs. (4.4), (4.5), and (4.6)] used in this study.

An interesting feature that presented itself on a number of occasions is an unexpected peak in the decay curve after the entire experimental run has ended and the hyperbolic current decay is being observed. This was observed both at a high temperature (at 333 K on November 21, 2006) and at low temperatures (at 123 K and at 103 K in June 2007). For an example of this feature refer to Figs. B.1-2, and B.8-11 of Kapton HN; note, however, this feature was observed in all material data sets on those dates.

One material feature observed in this study is the calculated Δ values of PTFE > 1.0. Current RIC theory only provides for a Δ range of 0.5 to 1.0 (Section 2.4). Future work could be done in theoretical development to allow for higher Δ values.

A final topic to address is to complete the analysis of other materials that were studied during RIC runs described in this thesis. In addition to the five materials analyzed in detail in the thesis (Kapton HN, Kapton E, LDPE, PTFE, and Tefzel), temperature-dependent data were also acquired for Kapton FN and expanded polytetraflouroethylene (ePTFE). Initial analysis has been completed for all these materials, and the results have been incorporated into a Mathcad^{TM} tool to calculate conductivity as a function of
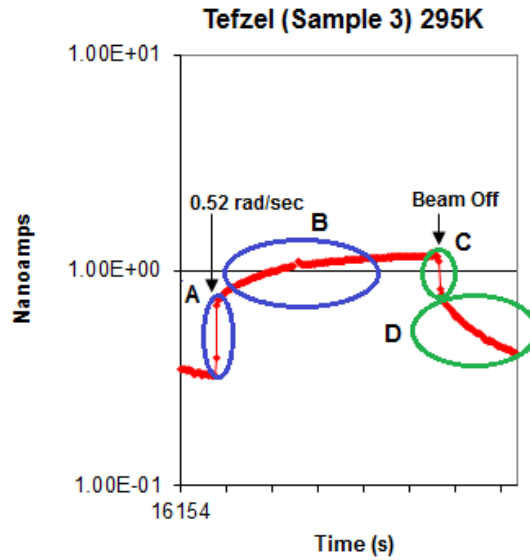
FIG. 5.2. Time-dependent current behavior before rising to equilibrium value. A) Initial rapid rise in current after beam is turned on. B) Gradual exponential approach to equilibrium current. C) Initial rapid decrease in current after beam is turned off. D) Long-term hyperbolical current decrease. Data were taken for Tefzel at 295 K on February 28, 2007.

temperature, dose rate, and applied electric field for about a dozen common spacecraft materials (Dennison *et al.*, 2009b). In addition, a new data set has been recently acquired for fused silica from 60 K to 330 K (Hoffmann *et al.*, 2013). Work is in progress to extend the results in a more extensive database (Dennison *et al.*, 2005b) similar to the NASCAP parameters materials database developed for the NASA Space Environments, Effects Charge Collector (Dennison *et al.*, 2003). These results are of critical importance to the spacecraft community.

5.5 Conclusion

The theory developed in Chapter 2 has provided a good understanding of the mechanisms involved in RIC. Observed temperature-dependent behaviors corresponded well with predictions based on $\Delta(T)$ values. Polymeric materials in general have a high degree of structural trap disorder, and the corresponding Δ values found between 0.9 and 1.0 at 295 K support this. While only a minimal amount of literature is available on the temperature dependence of $\Delta(T)$ and k_{RIC} for the materials studied with which to compare—and none available under the same conditions—a good correlation has been found with those

that do exist. The results of this study will be extremely useful for a wide variety of low temperature applications, most notably in the study and mitigation of spacecraft charging issues for spacecraft, such as the James Webb Space Telescope.

REFERENCES

Adamec, V., 1968, "Dielectric Relaxation Process Below the Glass Transition in Atactic Polystyrene," J. of Polym. Sci., Part A-2, **6**, 1241.

Ashcroft, N. W., and N. D. Mermin, 1976, *Solid State Physics* (W. B. Saunders Company, New York, NY).

ASTM D3755, 1997, "Standard Test Method for Dielectric Breakdown Voltage and Dielectric Strength of Solid Electrical Insulating Materials Under Direct Voltage Stress," ASTM International, West Conshohocken, PA, 1997, DOI: 10.1520/D3755-97 www.astm.org.

ASTM D5229, 2012, "Standard Test Method for Moisture Absorption Properties and Equilibrium Conditioning of Polymer Matrix Composite Materials," ASTM International, West Conshohocken, PA, 2012, DOI: 10.1520/D5229_D5229M-12 www.astm.org.

ASTM D618, 2008, "Standard Practice for Conditioning Plastics for Testing," ASTM International, West Conshohocken, PA, 2008, DOI: 10.1520/D0618-08 www.astm.org.

ASTM E595, 2006, "Standard Test Method for Total Mass Loss and Collected Volatile Condensable Materials from Outgassing in a Vacuum Environment," ASTM International, West Conshohocken, PA, 2006, DOI: 10.1520/E0595-06 www.astm.org.

Beckley, L. M., T. J. Lewis, and D. M. Taylor, 1976, "Electron-beam-induced Conduction in Polyethylene Terephthalate Films," J. Phys. D: Appl. Phys., **9**, 1355-1365.

Brunson, J., 2010, "Measurement of Charge Decay Time and Resistivity of Spacecraft Insulators Using Charge Storage Method and Application to Theoretical Modeling of Charging Behavior of Insulators," Ph. D. thesis, (Utah State University).

Campbell, F. J., 1983, "Radiation Effects on the Electrical Properties of Solid Insulation," *Engineering Dielectrics Volume IIA Electrical Properties of Solid Insulating Materials: Molecular Structure and Electrical Behavior, American Society for Testing and Materials*, edited by R. Bartnikas, (American Society for Testing and Materials, Philadelphia, PA).

Cheek, C. H., and V. J. Linnenbom, 1960, "Calculation of Absorbed Dose," Technical Report NRL-5548.

Compton, D. M. J., G. T. Cheney, and R. A. Poll, 1965, "Radiation Induced Conductivity in Plastic Films at High Dose Rates, J. Appl. Phys. **36:8**, 2434.

Conrad, F. E., and S. M. Marcus, 1962, "Gamma-Induced Photoconductivity in A Polyethylene Terephthalate Capacitor," Report TR-1037, Diamond Ordinance Fuze Laboratories, Washington, D. C.

Conwell, E., and V. F. Weisskopf, 1950, "Theory of Impurity Scattering in Semiconductors," Phys. Rev. **77**, 388.

Dekany, J., A. M. Sim, J. Brunson, and J. R. Dennison, 2012, "Electron Transport Models and Precision Measurements in a Constant Voltage Chamber," *Proceedings of the* 12*th Spacecraft Charging Technology Conference,* Kitakyushu, Japan.

Dekany, J., A. M. Sim, J. Brunson, and J. R. Dennison, 2013, "Electron Transport Models and Precision Measurements in a Constant Voltage Chamber," IEEE Trans. Plasma Sci. (unpublished).

Dennison, J. R., J. Kite, C. D. Thomson, J. Corbridge, R. Berry, and C. Ellsworth, 2003, "Final Report Part IV: Additional Materials Reports," NASA Space Environments and Effects Program Grant, *Electronic*

Properties of Materials with Application to Spacecraft Charging. Published by NASA electronically at http://see.msfc.nasa.gov/ee/db_chargecollector.htm.

Dennison, J. R., P. V. Swaminathan, R. Jost, J. Brunson, N. W. Green, and A. R. Frederickson, 2005a, "Proposed Modifications to Engineering Design Guidelines Related to Resistivity Measurements and Spacecraft Charging," *Proc. of the 9th Spacecr. Charging Technol. Conf.,* Epochal Tsukuba, Tsukuba, Japan.

Dennison, J. R., A. R. Frederickson, N. W. Green, C. E. Benson, J. Brunson, and P. Swaminanthan, 2005b, "Materials Database of Resistivities of Spacecraft Materials.," Final Report, NASA Space Environments and Effects Program, Contract No. NAS8-02031, "Measurement of Charge Storage Decay Time and Resistivity of Spacecraft Insulators," 739 pages, Published electronically by NASA Space Environments and Effects Program as part of the *Charge Collector Knowledgebase 3rd Ed*. at http://see.msfc.nasa.gov/ee/db_chargecollector.htm.

Dennison, J. R., and J. Brunson, 2008, "Temperature and Electric Field Dependence of Conduction in Low-Density Polyethylene," IEEE Trans. Plasma Sci. **36**(5), 2246-2252.

Dennison, J. R., J. Gillespie, J. Hodges, R. C. Hoffmann, J. Abbott, S. Hart, and A. Hunt, 2009a, "Temperature Dependence of Radiation Induced Conductivity in Insulators," *AIP Conf. Proc. Series* **1099**, 203-208.

Dennison, J. R., A. Sim, J. Brunson, J. Gillespie, S. Hart, J. Dekany, C. Sim, and D. Arnfield, 2009b, "Engineering Tool for Temperature, Electric Field and Dose Rate Dependence of Low Conductivity Spacecraft Materials," *2009 AIAA Aerospace Sciences Meeting*, AIAA 2009-562.

Dennison, J. R., and A. M. Sim, 2012, "Unified Density of States Based Model of Electron Transport and Emission of Spacecraft Materials," *Proc. of the 12th Spacecraft Charging Techn. Conf.,* Kitakyushu, Japan.

Dienes, G. J., and A. C. Damask, 1958, "Radiation Enhanced Diffusion in Solids," J. Appl. Phys. **29**:12, 1713.

Fowler, J. F., 1956a, "X-Ray Induced Conductivity in Insulating Materials," M. S. thesis (University of London).

Fowler, J. F., 1956b, "X-Ray Induced Conductivity in Insulating Materials," *Proc. of the Royal Soc. of London A*, **236**, 464-480.

Fowler, J. F., 1959, "Radiation-induced Conductivity in the Solid State, And Some Applications," Phys. Med. Biol. **3**, 395.

Frederickson, A. R., 1977, "Radiation Induced Currents and Conductivity in Dielectrics," IEEE Trans. on Nucl. Sci. **NS-24**, 2532-2539.

Friedel, J. , 1969, in *The Physics of Metals*, edited by J. M. Ziman, (Cambridge Univ. Press, New York, NY).

Hanks, C. L., and D. J. Hamman, 1969, "The Effect of Radiation on Electrical Insulating Materials," REIC Report No. 46.

Harrison, S. E., 1962, "A Study of Gamma-Ray Photoconductivity in Organic Dielectric Materials," M. S. thesis (University of New Mexico).

Harrison, S. E., F. N. Coppage, and A. W. Snyder, 1963, "Gamma-ray and Neutron-induced Conductivity in Insulating Materials," IEEE Trans. on Nucl. Sci., **NS-10**, 118.

Harrison, W. A., 1989, *Electronic Structure and the Other Properties of Solids: The Physics of the Chemical Bond* (Dover Publications, New York, NY).

Hastings, D., and H. Garrett, 1996, *Spacecraft-Environment Interactions* (Cambridge Press, Cambridge, MA).

Hedvig, P., 1964, "Radiation-Induced Electrical Conductivities in Polymide Copolymers," J. of Polymer Sci. A, **2**, 4097.

Hodges, J. L., 2012, "In Situ Measurements of Electron Beam Induced Surface Voltage of Highly Resistive Materials," M. S. thesis (Utah State University).

Hoffmann, R., J. R. Dennison, A. E. Jensen, and G. Wilson, 2013, "The Correlation Between Radiation Induced Conductivity (RIC) and Electron Beam Induced Luminescence in Disordered SiO_2, *2013 IEEE International Conference on Solid Dielectrics (ICSD)*, Bologna, Italy.

Ieda, M., G. Sawa, and S. Kato, 1971, "A Consideration of Poole-Frenkel Effect on Electric Conduction in Insulators," J. Appl. Phys. **42**, 3737-3740.

Jackson, J. D., 1975, *Classical Electrodynamics*, 2nd Ed. (Wiley, New York, NY).

Kittel, C., 1956, *Introduction to Solid State Physics* (John Wiley & Sons, Inc., New York, NY).

Levy, L., D. Sarrail, and J. M. Siguier, 1985, "Conductivity and Secondary Emission Properties of Dielectrics As Required by NASCAP", *Proc. of The Third Euro. Symp. on Spacecr. Materials in Space Environ.*, Noordwijk, The Netherlands, **ESA SP-292**, 113.

Marka, Z., R. Pasternak, R. G. Albridge, S. N. Rashkeev, S. T. Pantelides, and N. H. Tolk, 2003, "Two-color Optical Technique for Characterization of X-ray Radiation-enhanced Electron Transport in SiO_2," J. Appl. Phys. **93**:4, 1865.

Marton, D., J. Fine, and G. P. Chambers, 1988, "Temperature-dependent Radiation-enhanced Diffusion in Ion-Bombarded Solids," Phys. Rev. Lett. **61**:23, 2697.

Meyer, R. A., F. L. Bouquet, and R. S. Alger, 1956, "Radiation Induced Conductivity in Polyethylene and Teflon," J. Appl. Phys. **27**:9, 1012-1018.

Miller, A., and E. Abrahams, 1960, "Impurity Conduction at Low Concentrations," Phys. Rev. **120**, 745.

Molinié, P., R. Hanna, T. Paulmier, M. Belhaj, B. Dirassen, D. Payan, and N. Balcon, 2012, "Photoconduction and Radiation-induced Conductivity on Insulators: A Short Review and Some Experimental Results," in *Proc. of the 12th Spacecraft Charging Techn. Conf.,* Kitakyushu, Japan.

Mott, N. F., and E. A. Davis, 1979, *Electronic Processes in Non-Crystalline Materials,* 2nd Ed. (Oxford University Press, Oxford).

Newman, R. C., J. H. Tucker, and F. M. Livingston, 1983, "Radiation-enhanced Diffusion of Oxygen in Silicon at Room Temperature," J. Phys. C: Solid State Phys. L151.

Poole, H. N., 1917, "On the Dielectric Constant and Electrical Conductivity of Mica in Intense Fields," Philos. Mag.*, **34**, 195-204.

Priolo, F., J. M. Poate, D. C. Jacobson, J. Linnros, J. L. Batstone, and S. U. Campisano, 1988, "Radiation-enhanced diffusion of Au in amorphous Si," Appl. Phys. Lett. **52**:15, 1213.

Rose, A., 1951, "An Outline of Some Photoconductive Processes," RCA Review **12**, 362-414.

Rose, A., 1963, *Concepts in Photoconductivity and Allied Problem* (John Wiley and Sons, New York).

Sessler, G. M., 1992, "Charge Dynamics in Irradiated Polymers," IEEE Trans. on Electrical Insulation **27**:5, 961.

Sessler, G. M., M. T. Figueiredo, and G. F. Leal Ferreira, 2004, "Models of Charge Transport in Electron-beam Irradiated Insulators," IEEE Trans. on Dielectrics and Electrical Insulation **II**:2, 192.

Sim, A. M., 2013, "Unified Model of Charge Transport in Insulating Polymeric Materials," Ph. D. thesis, (Utah State University).

Tyutnev, A. P., D. N. Sadovnichii, V. S. Saenko, and E. D. Pozhidaev, 2000, Poly. Sci., Ser. A, **42**, 10.

Tyutnev, A. P., V. S. Saenko, and E. D. Pozhidaev, 2004, Poly. Sci., Ser. B, **46**, 362.

Vissenberg, M. C. J. M., 1998, "Theory of the Field-Effect Mobility in Amorphous Organic Transistors," Phys. Rev. **57**, 12964-12968.

Weaver, L., J. K. Shultis, and R. E. Faw, 1977, "Analytical Solutions of a Model for Radiation-Induced Conductivity in Insulators" J. Appl. Phys. **48**, 2762-2770.

Wilson G., A. Evans, J. Dekany, and J. R. Dennison, 2013, "Charging Effects of Multilayered Dielectric Spacecraft Materials: Surface Voltage, Discharge and Arcing," IEEE Trans. Plasma Sci. (unpublished).

Wintle, H. J., 1983, "Conduction Processes in Polymers," in *Engineering Dielectrics—Volume IIA: Electrical Properties of Solid Insulating Materials: Molecular Structure and Electrical Behavior*, edited by R. Bartnikas, (American Society for Testing and Materials, Philadelphia, PA).

Wintle, H. J, 1991, "Models for the Decay of Radiation-induced Conduction," IEEE Trans. on Electrical Insulation, **26:**1, 26-34.

Yahagi, K., and A. Danno, 1963, J. Appl. Phys. **34**, 804-809.

Yahagi, K., and K. Shinohara, 1966, "Effects of Carrier Traps in Polyethylene under Gamma-Ray Irradiation," J. Appl. Phys. **37**:1, 310-315.

Yang, G. M., and G. M. Sessler, 1992, "Radiation-induced Conductivity in Electron-beam Irradiated Insulating Polymer Films," IEEE Trans. on Electrical Insulation, **27**:4, 843.

Zallen, R., 1983, *The Physics of Amorphous Solids* (John Wiley and Sons, New York).

APPENDICES

75

APPENDIX A

KAPTON E TABLE AND GRAPHS

TABLE A.1. Table of results for Kapton E.

Date Acquired / Carousel Position	Temp (°C)	Thickness (μm)	Applied (% of Breakdown) Voltage (V)	E-Field (MV/m)	Approximate Resistivity Resolution (Ω-cm)	Dark Current Resistivity (Ω-cm)	RIC Power Law Fit Parameters k (sec-Rad⁻¹/Ω-cm)	Δ
2/28/07 Position 2	295 ± 0.5	24.5 ± 6%	(50%) 5500 ± 1%	217 ± 10%	$5 \cdot 10^{19}$	$4.1 \cdot 10^{17} \pm$ 20%	$6.7 \cdot 10^{-17} \pm$ 20%	0.93 ± 20%
2/28/07 Position 10	295 ± 0.5	24.5 ± 6%	(50%) 5500 ± 1%	217 ± 10%	$5 \cdot 10^{19}$	$4.1 \cdot 10^{17} \pm$ 20%	$6.7 \cdot 10^{-17} \pm$ 20%	0.93 ± 20%
6/19/07 Position 9	295 ± 0.5	24.5 ± 6%	(22%) 2450 ± 1%	96 ± 10%	$2 \cdot 10^{19}$	$3.1 \cdot 10^{18} \pm$ 20%	$7.6 \cdot 10^{-17} \pm$ 20%	0.96 ± 20%
3/1/07 Position 2	232 ± 1	24.5 ± 6%	(50%) 5500 ± 1%	217 ± 10%	$5 \cdot 10^{19}$	$5.3 \cdot 10^{17} \pm$ 20%	$1.2 \cdot 10^{-17} \pm$ 20%	1.0 ± 20%
3/2/07 Position 2	214 ± 2	24.5 ± 6%	(50%) 5500 ± 1%	217 ± 10%	$5 \cdot 10^{19}$	$5.9 \cdot 10^{17} \pm$ 20%	$1.8 \cdot 10^{-17} \pm$ 20%	1.05 ± 20%
3/2/07 Position 10	214 ± 2	24.5 ± 6%	(50%) 5500 ± 1%	217 ± 10%	$5 \cdot 10^{19}$	$5.9 \cdot 10^{17} \pm$ 20%	$1.8 \cdot 10^{-17} \pm$ 20%	1.05 ± 20%
6/19/07 Position 3	103 ± 3	24.5 ± 6%	(22%) 2450 ± 1%	96 ± 10%	$2 \cdot 10^{19}$	$3.7 \cdot 10^{21} \pm$ 20%	$1.8 \cdot 10^{-17} \pm$ 20%	0.94 ± 20%
6/19/07 Position 4	103 ± 3	24.5 ± 6%	(22%) 2450 ± 1%	96 ± 10%	$2 \cdot 10^{19}$	$3.7 \cdot 10^{21} \pm$ 20%	$1.8 \cdot 10^{-17} \pm$ 20%	0.95 ± 20%

FIG. A.1. Kapton E data taken at 295 K on February 28, 2007. Raw current data (above). Fit to current data (below).
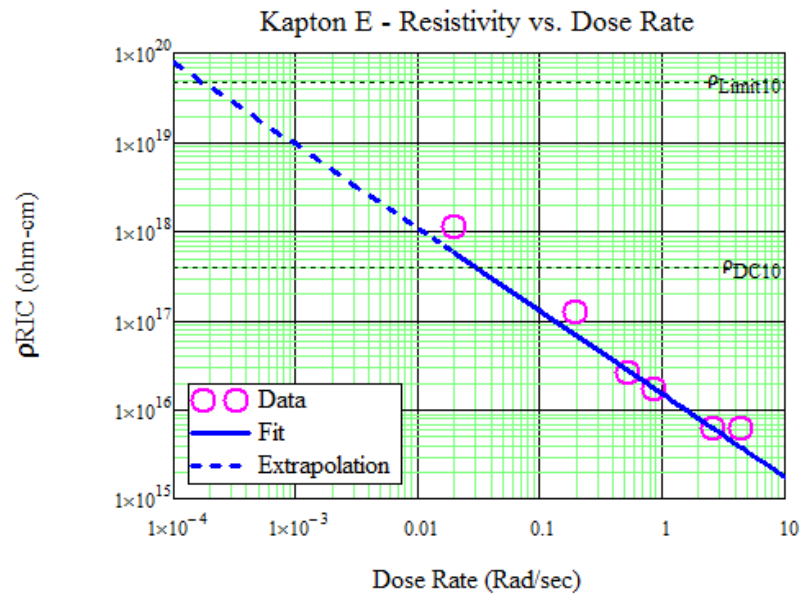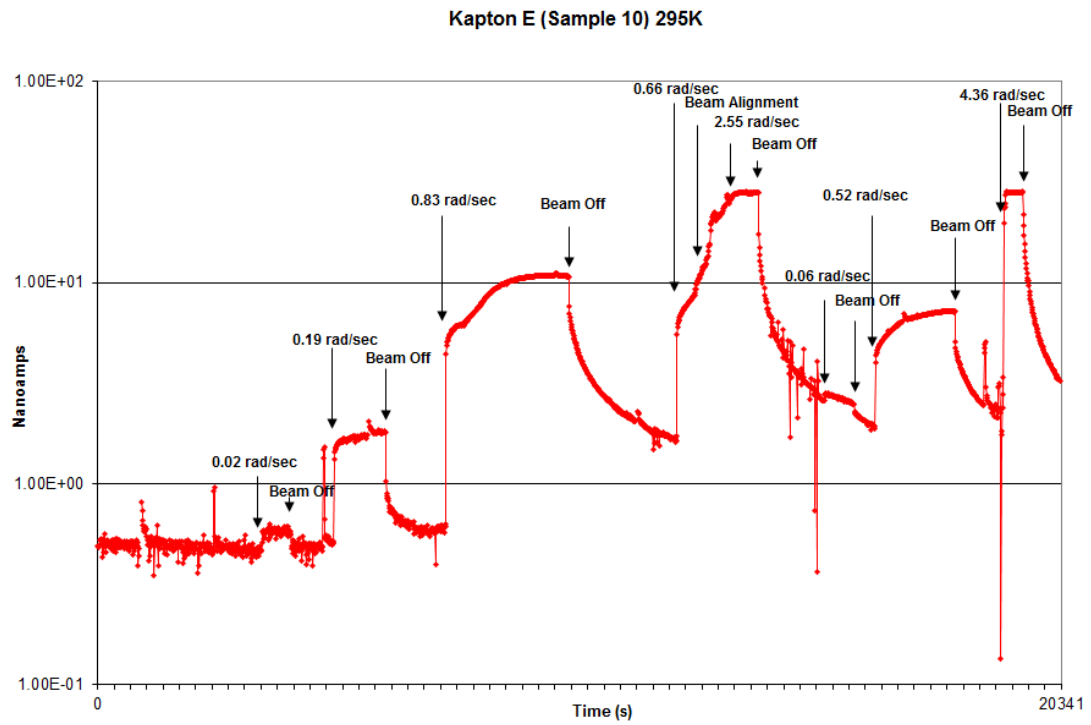
FIG. A.2. Kapton E data taken at 295 K on February 28, 2007. Raw current data (above). Fit to current data (below).
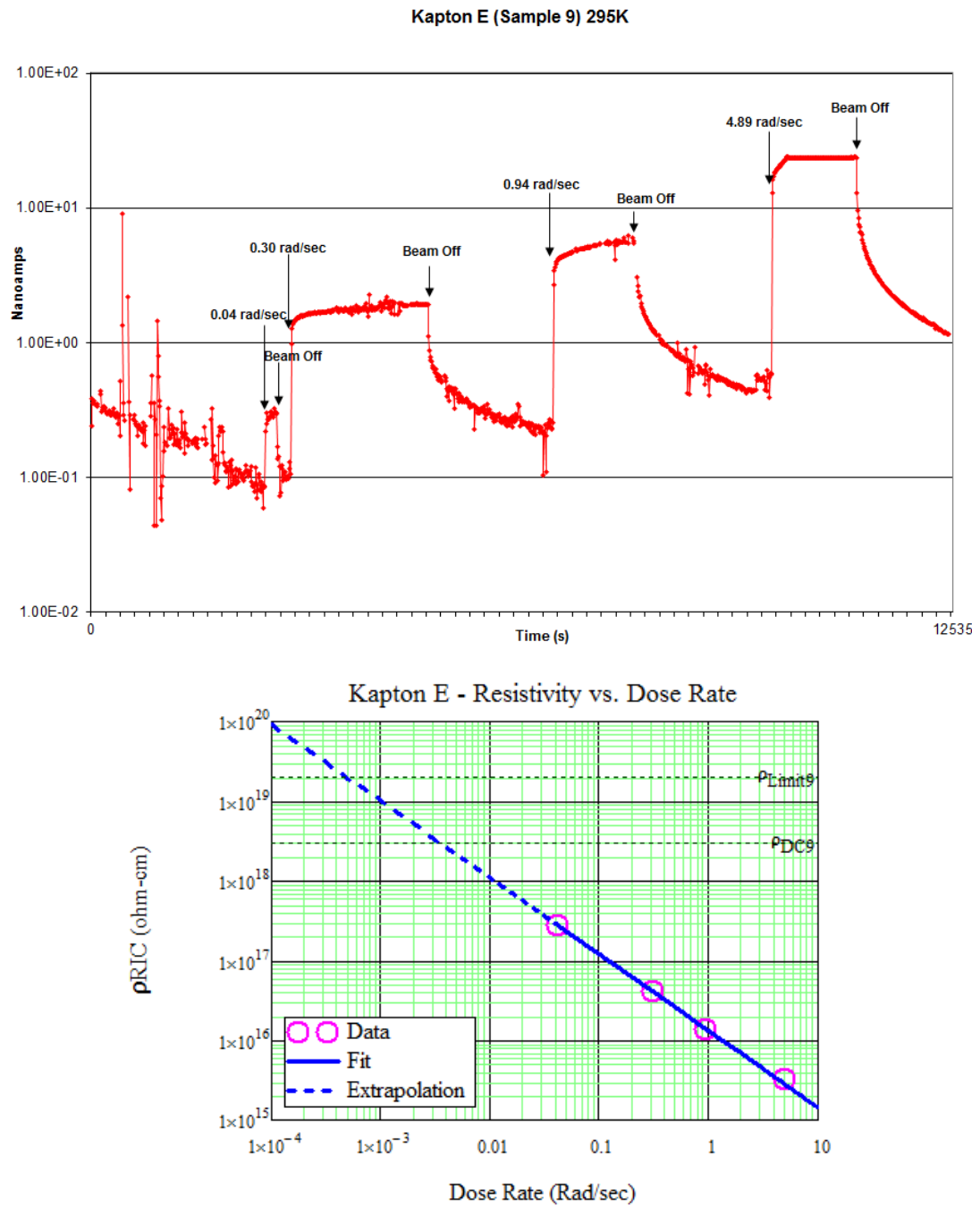
FIG. A.3. Kapton E data taken at 295 K on June 19, 2007. Raw current data (above). Fit to current data (below).
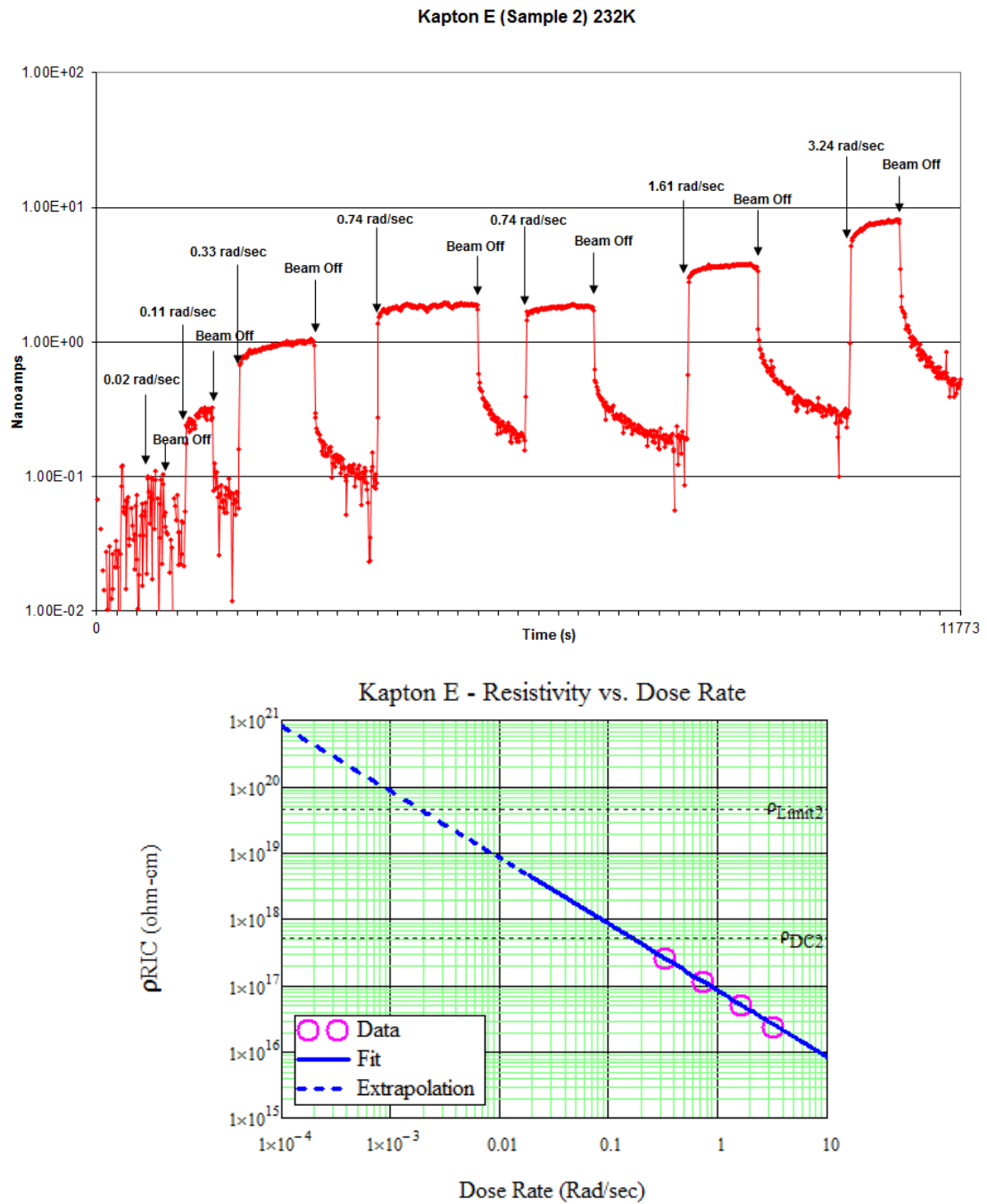
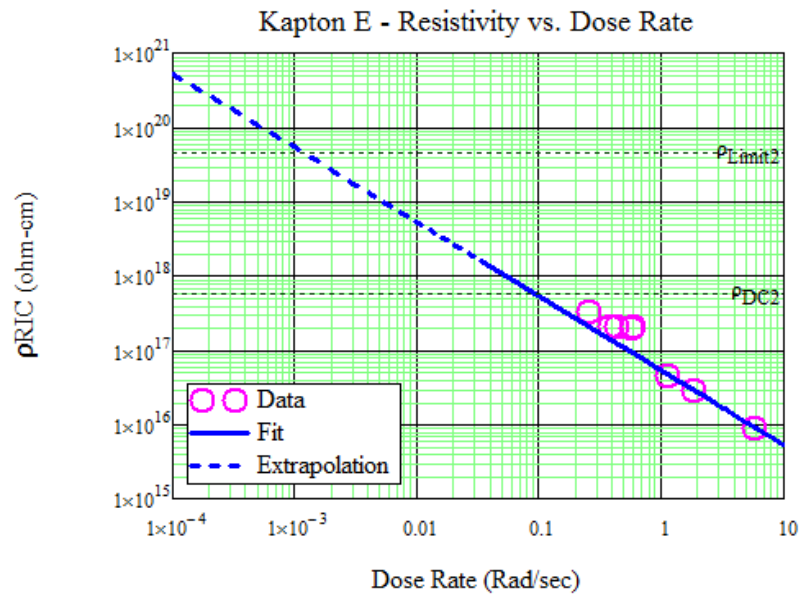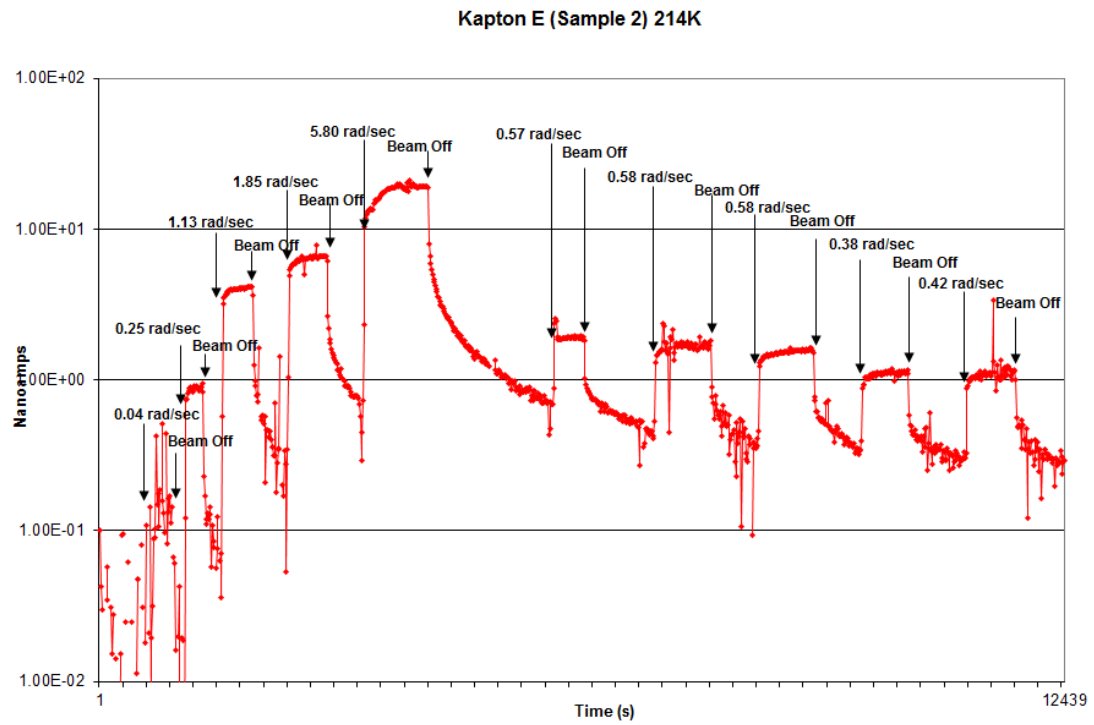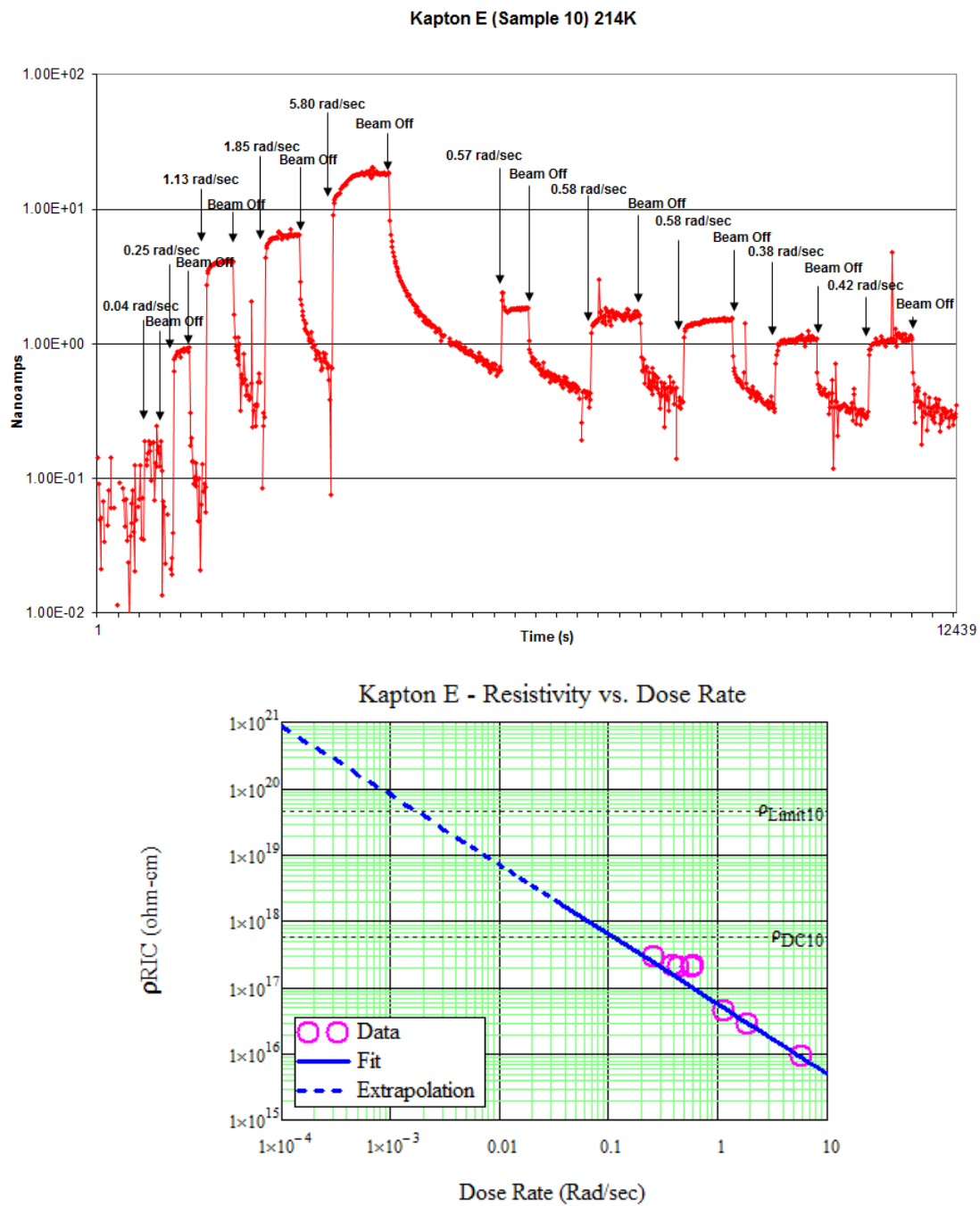FIG. A.4. Kapton E data taken at 232 K on March 1, 2007. Raw current data (above). Fit to current data (below).

FIG. A.5. Kapton E data taken at 214 K on March 2, 2007. Raw current data (above). Fit to current data (below).
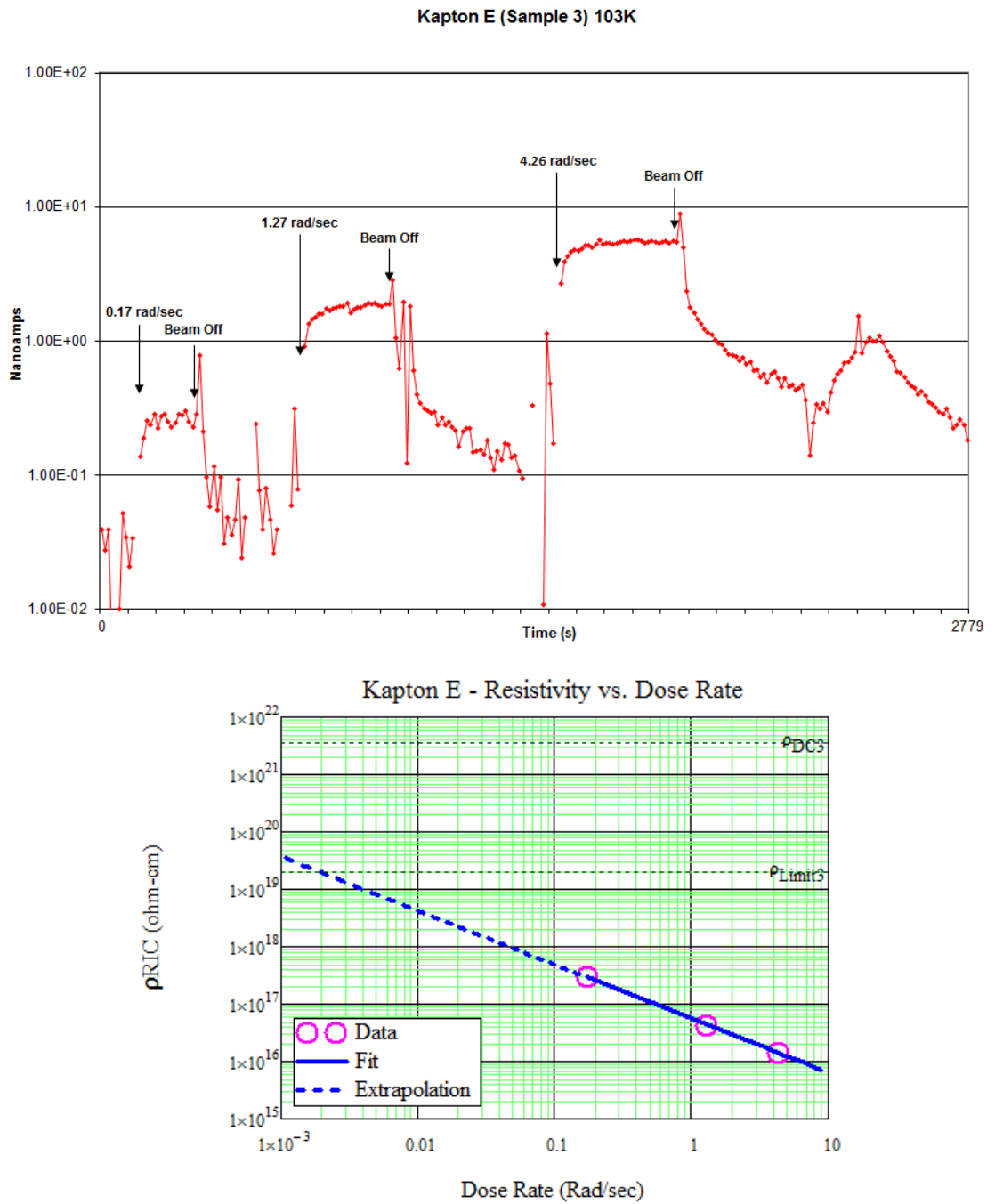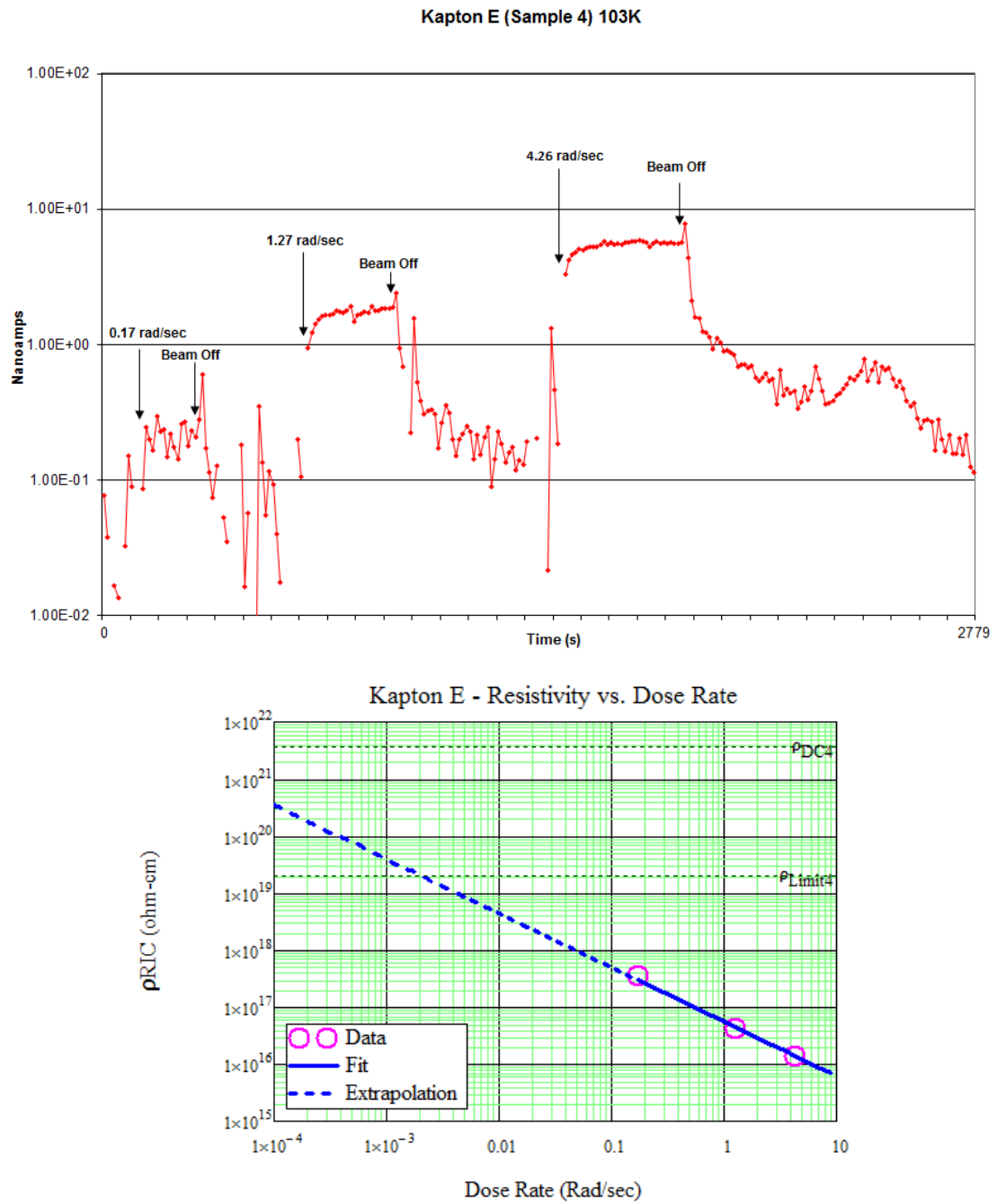
FIG. A.6. Kapton E data taken at 214 K on March 2, 2007. Raw current data (above). Fit to current data (below).

Kapton E (Sample 3) 103K

Kapton E - Resistivity vs. Dose Rate

FIG. A.7. Kapton E data taken at 103 K on June 19, 2007. Raw current data (above). Fit to current data (below).

Kapton E (Sample 4) 103K

Kapton E - Resistivity vs. Dose Rate

FIG. A.8. Kapton E data taken at 103 K on June 19, 2007. Raw current data (above). Fit to current data (below).
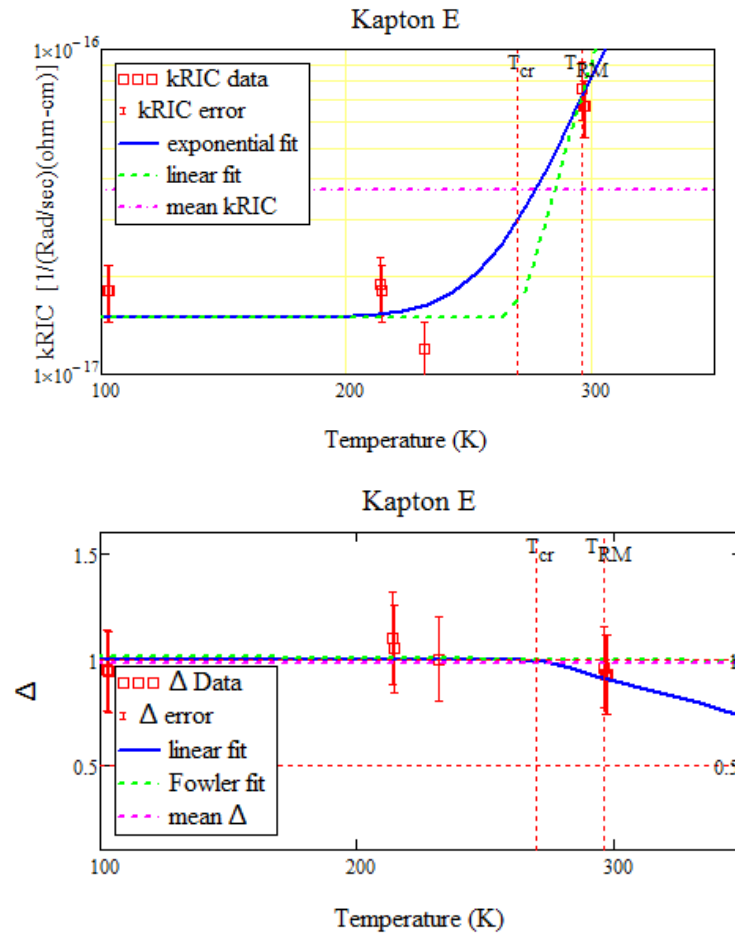
FIG. A.9. Kapton E k and Δ data and temperature-dependent fits. k–value data and temperature-dependent fits (above). Δ–value data and temperature-dependent fits (below).
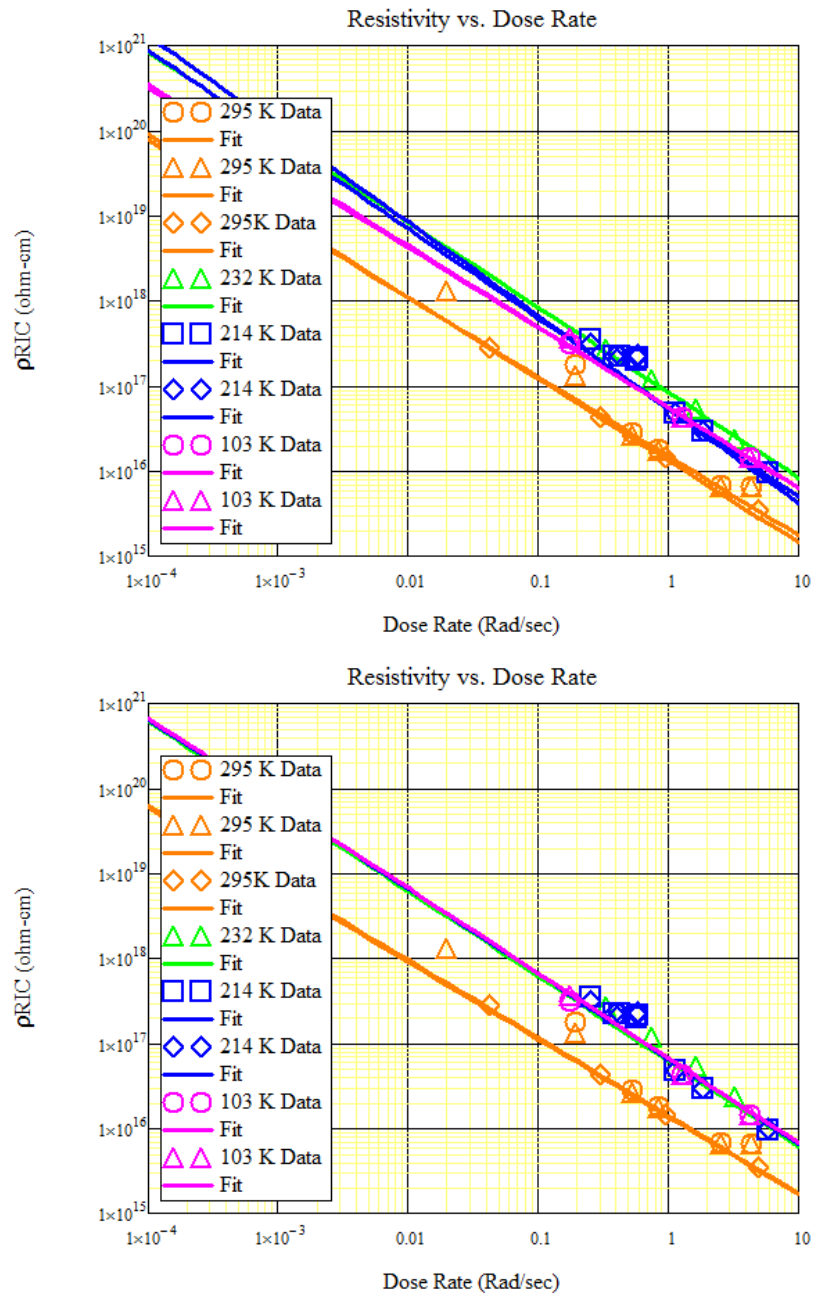
FIG. A.10. RIC Kapton E data and temperature fits. *T*-independent fits to Kapton E data (top). *T*-dependent fits to Kapton E data (bottom).

APPENDIX B

KAPTON HN TABLE AND GRAPHS

TABLE B.1. Table of results for Kapton HN.

| Date Acquired Carousel Position	Temp (°C)	Thickness (µm)	Applied (% of Breakdown)		Approximate Resistivity Resolution (Ω·cm)	Dark Current Resistivity (Ω·cm)	RIC Power Law Fit Parameters	
			Voltage (V)	E-Field (MV/m)			k (sec·Rad^{-1}/ Ω·cm)	Δ
11/21/06 Position 7	333 ± 1	50.8 ± 6%	(14%)		$3 \cdot 10^{17}$	$1.3 \cdot 10^{19}$ ± 20%	$2.0 \cdot 10^{-17}$ ± 20%	0.92 ± 20%
			1884 ± 1%	37 ± 10%				
11/21/06 Position 9	333 ± 1	50.8 ± 6%	(9%)		$2 \cdot 10^{17}$	$1.4 \cdot 10^{19}$ ± 20%	$1.5 \cdot 10^{-17}$ ± 20%	1.05 ± 20%
			1256 ± 1%	25 ± 10%				
11/21/06 Position 7	295 ± 0.5	50.8 ± 6%	(15%)		$2 \cdot 10^{19}$	$1.5 \cdot 10^{19}$ ± 20%	$2.3 \cdot 10^{-17}$ ± 20%	1.00 ± 20%
			2100 ± 1%	41 ± 10%				
11/21/06 Position 9	295 ± 0.5	50.8 ± 6%	(10%)		$1 \cdot 10^{19}$	$1.6 \cdot 10^{19}$ ± 20%	$1.7 \cdot 10^{-17}$ ± 20%	1.00 ± 20%
			1400 ± 1%	28 ± 10%				
6/19/07 Position 10	295 ± 0.5	50.8 ± 6%	(18%)		$1 \cdot 10^{19}$	$1.4 \cdot 10^{19}$ ± 20%	$6.1 \cdot 10^{-17}$ ± 20%	0.91 ± 20%
			2450 ± 1%	48 ± 10%				
3/1/07 Position 1	232 ± 1	50.8 ± 6%	(50%)		$3 \cdot 10^{19}$	$5.3 \cdot 10^{18}$ ± 20%	$2.2 \cdot 10^{-17}$ ± 20%	0.92 ± 20%
			6875 ± 1%	135 ± 10%				
3/2/07 Position 1	214 ± 2	50.8 ± 6%	(50%)		$3 \cdot 10^{19}$	$5.1 \cdot 10^{18}$ ± 20%	$7.7 \cdot 10^{-18}$ ± 20%	0.95 ± 20%
			6875 ± 1%	135 ± 10%				
6/18/07 Position 9	123 ± 3	50.8 ± 6%	(36%)		$2 \cdot 10^{19}$	$1.3 \cdot 10^{19}$ ± 20%	$5.9 \cdot 10^{-18}$ ± 20%	1.32 ± 20%
			5000 ± 1%	98 ± 10%				
6/18/07 Position 10	123 ± 3	50.8 ± 6%	(36%)		$2 \cdot 10^{19}$	$1.3 \cdot 10^{19}$ ± 20%	$6.9 \cdot 10^{-18}$ ± 20%	1.26 ± 20%
			5000 ± 1%	98 ± 10%				
6/19/07 Position 1	103 ± 3	50.8 ± 6%	(18%)		$1 \cdot 10^{19}$	$1.2 \cdot 10^{20}$ ± 20%	$4.2 \cdot 10^{-18}$ ± 20%	0.85 ± 20%
			2450 ± 1%	48 ± 10%				
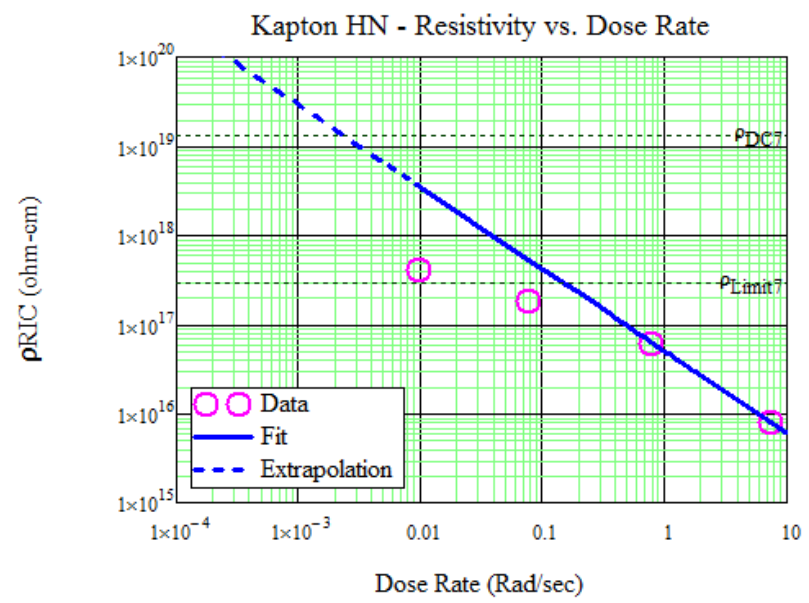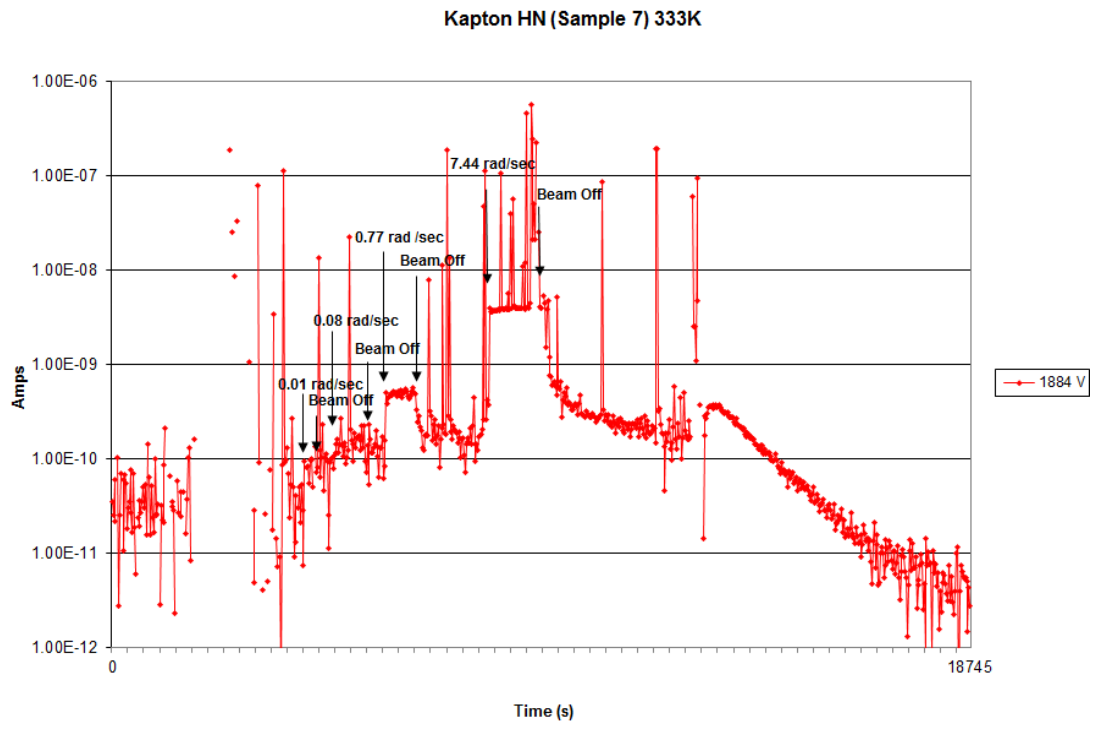
FIG. B.1. Kapton HN data taken at 333 K on November 21, 2006. Raw current data (above). Fit to current data (below).

FIG. B.2. Kapton HN data taken at 333 K on November 21, 2006. Raw current data (above). Fit to current data (below).
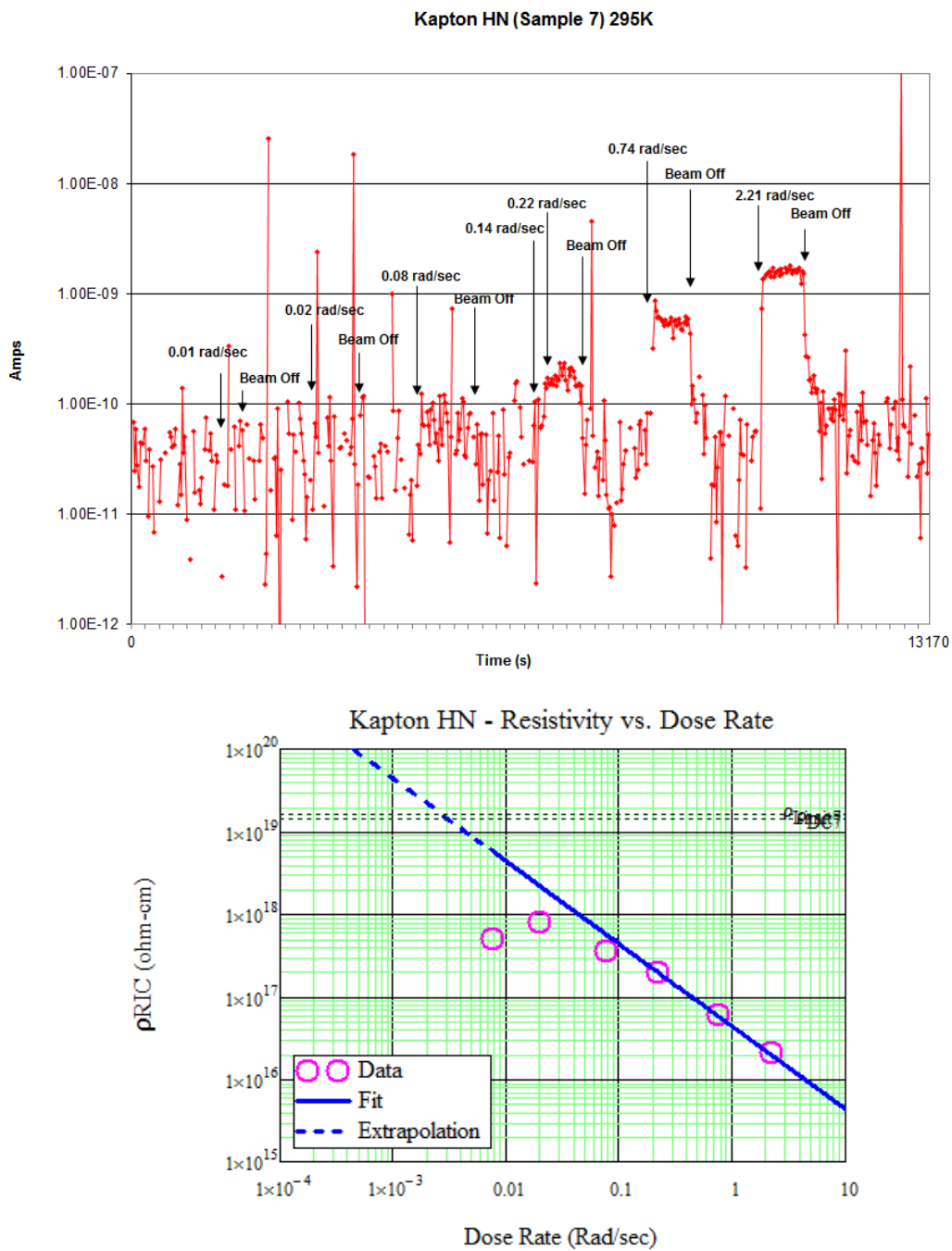
Kapton HN (Sample 7) 295K

Kapton HN - Resistivity vs. Dose Rate
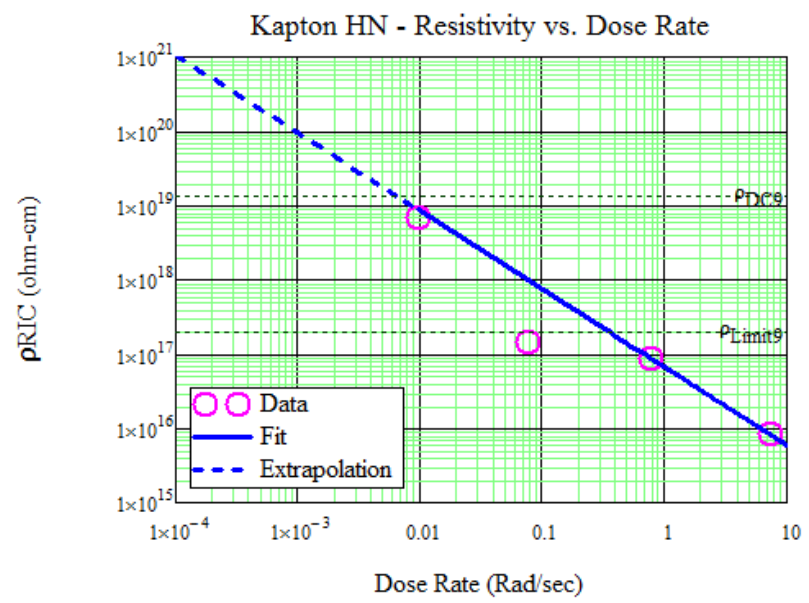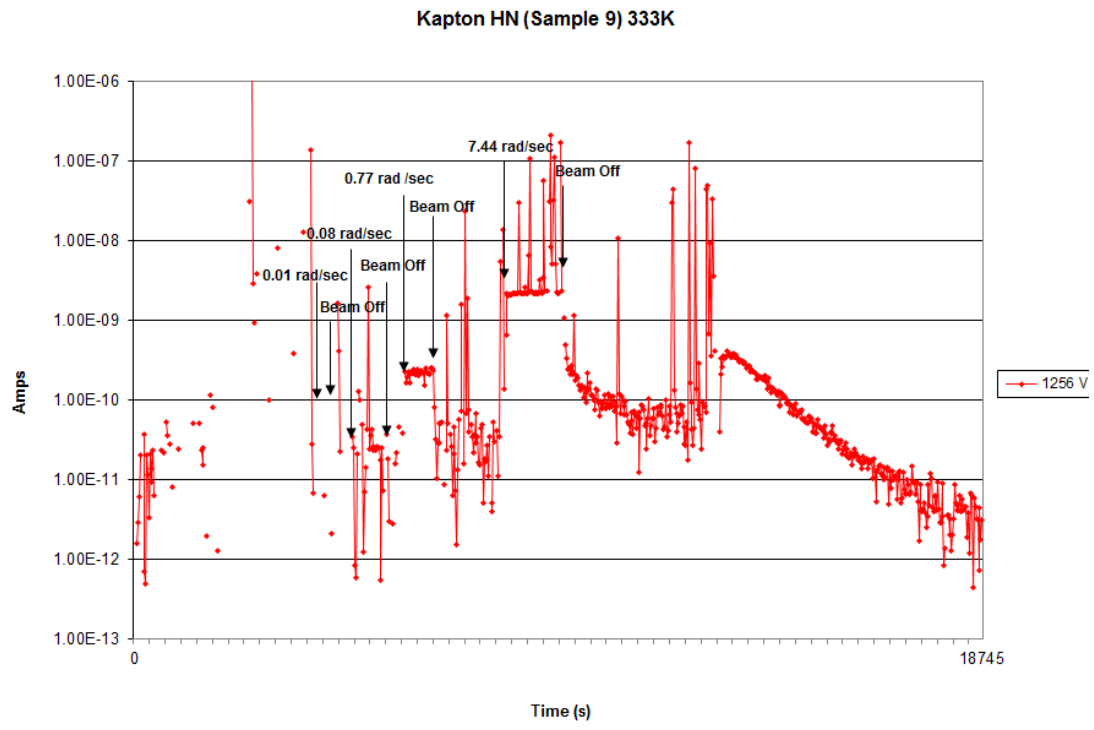
FIG. B.3. Kapton HN data taken at 295 K on November 21, 2006. Raw current data (above). Fit to current data (below).
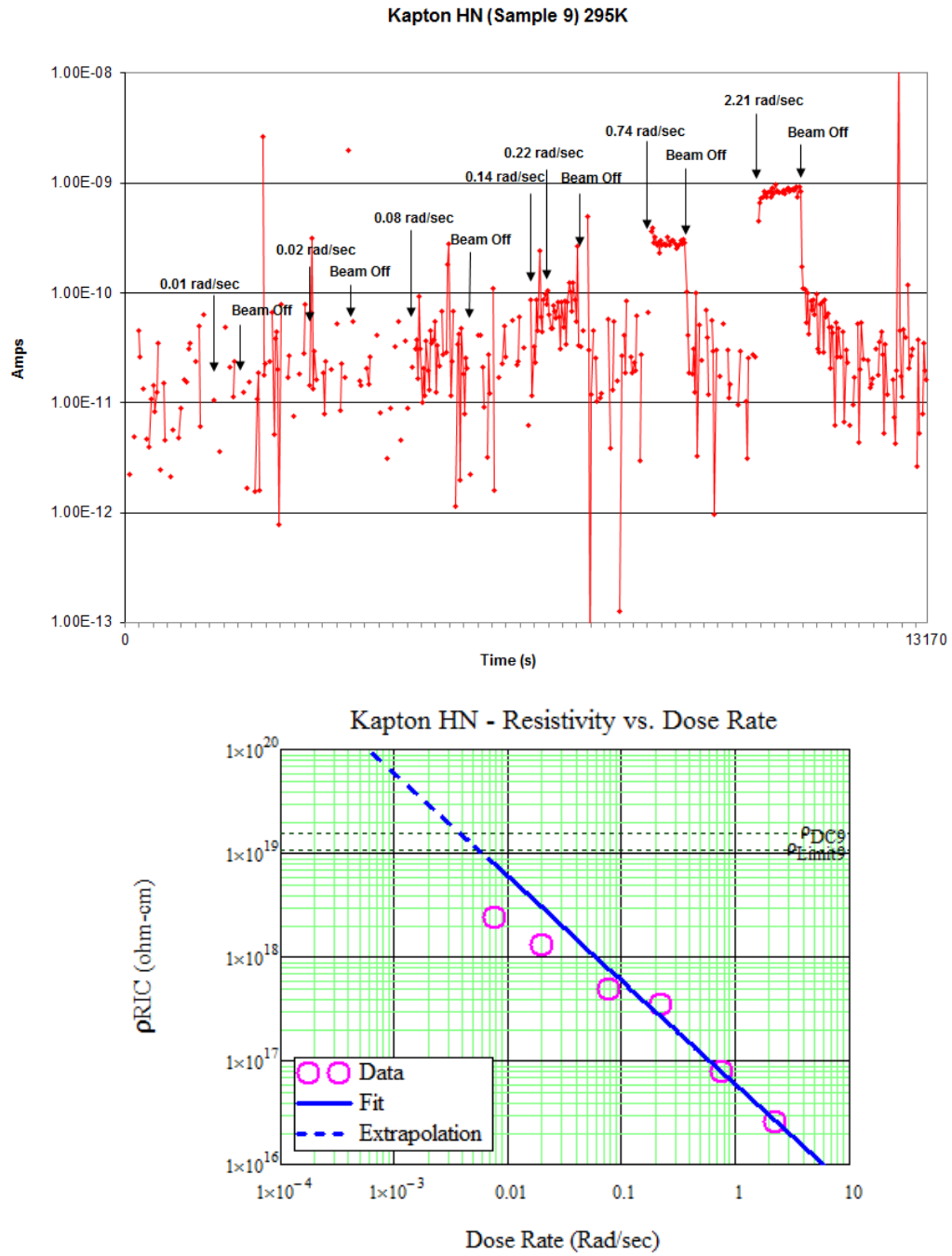
FIG. B.4. Kapton HN data taken at 295 K on November 21, 2006. Raw current data (above). Fit to current data (below).
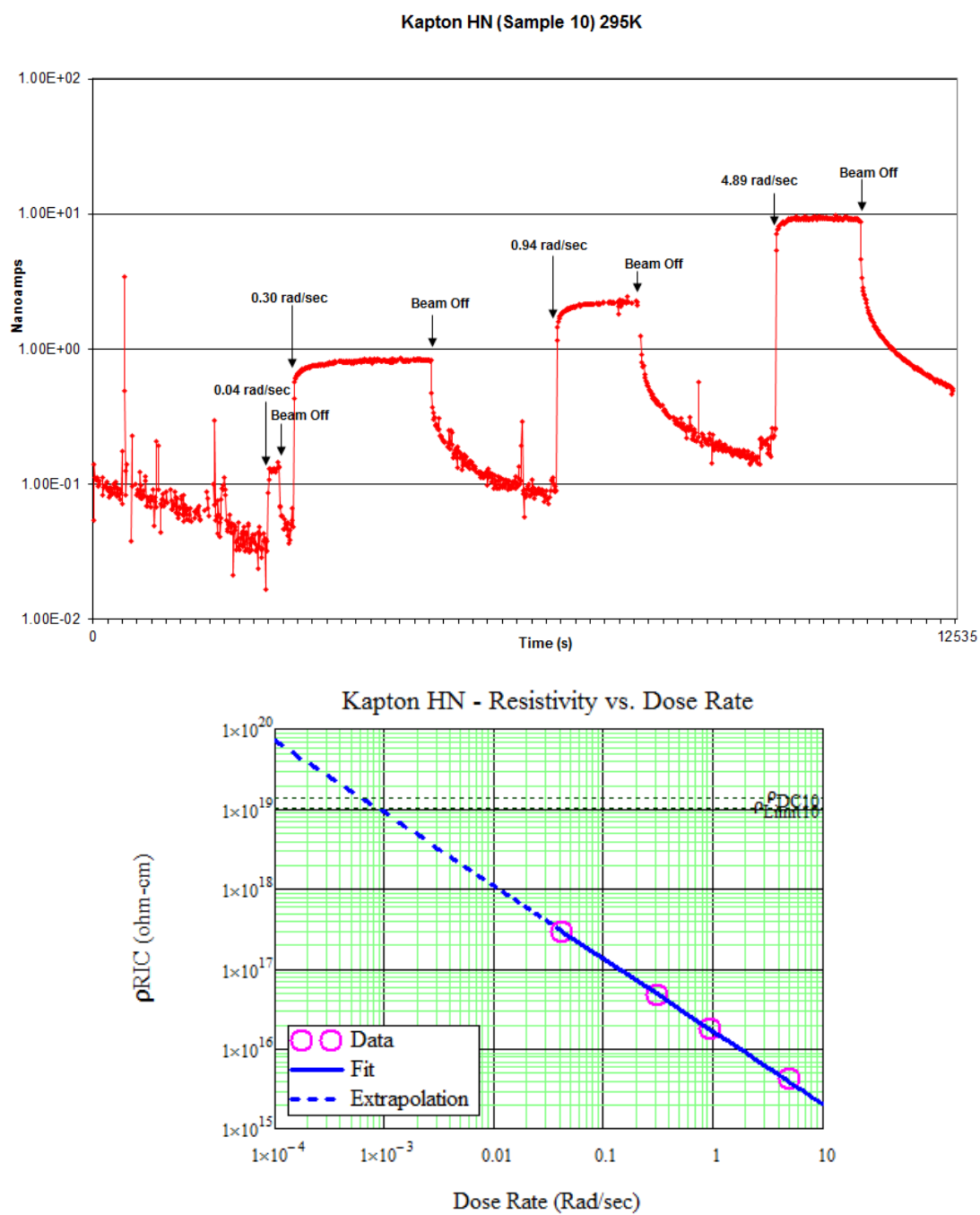
FIG. B.5. Kapton HN data taken at 295 K on June 19, 2007. Raw current data (above). Fit to current data (below).
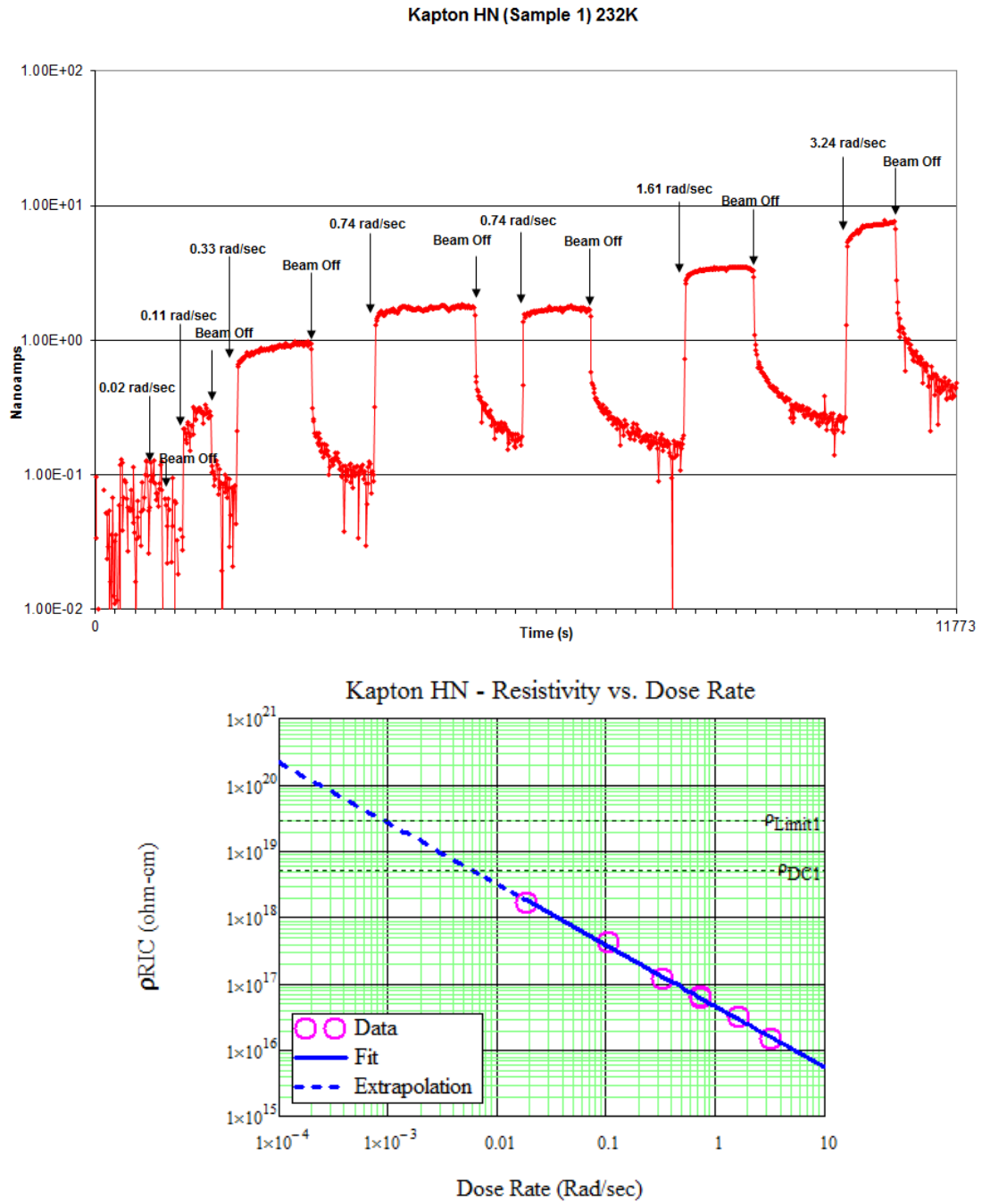
FIG. B.6. Kapton HN data taken at 232 K on March 1, 2007. Raw current data (above). Fit to current data (below).
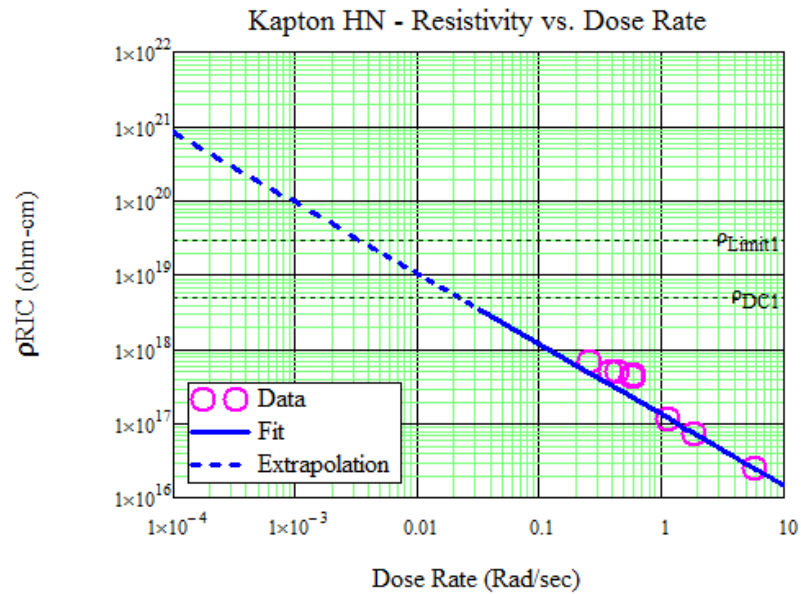
Kapton HN (Sample 1) 214K

FIG. B.7. Kapton HN data taken at 214 K on March 2, 2007. Raw current data (above). Fit to current data (below).

Kapton HN (Sample 9) 123K

Kapton HN - Resistivity vs. Dose Rate

FIG. B.8. Kapton HN data taken at 123 K on June 18, 2007. Raw current data (above). Fit to current data (below).

Kapton HN (Sample 10) 123K

FIG. B.9. Kapton HN data taken at 123 K on June 18, 2007. Raw current data (above). Fit to current data (below).
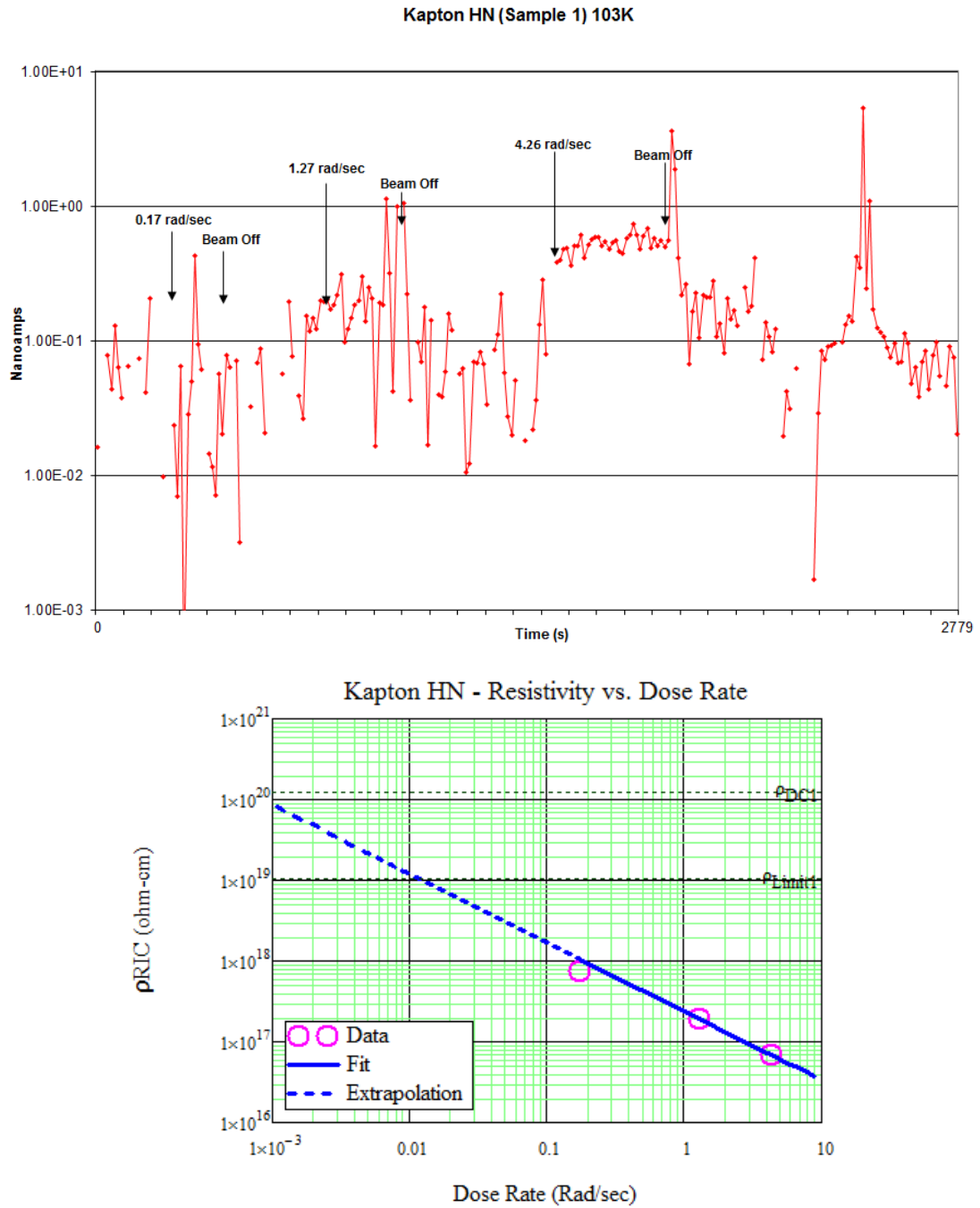
FIG. B.10. Kapton HN data taken at 103 K on June 19, 2007. Raw current data (above). Fit to current data (below).
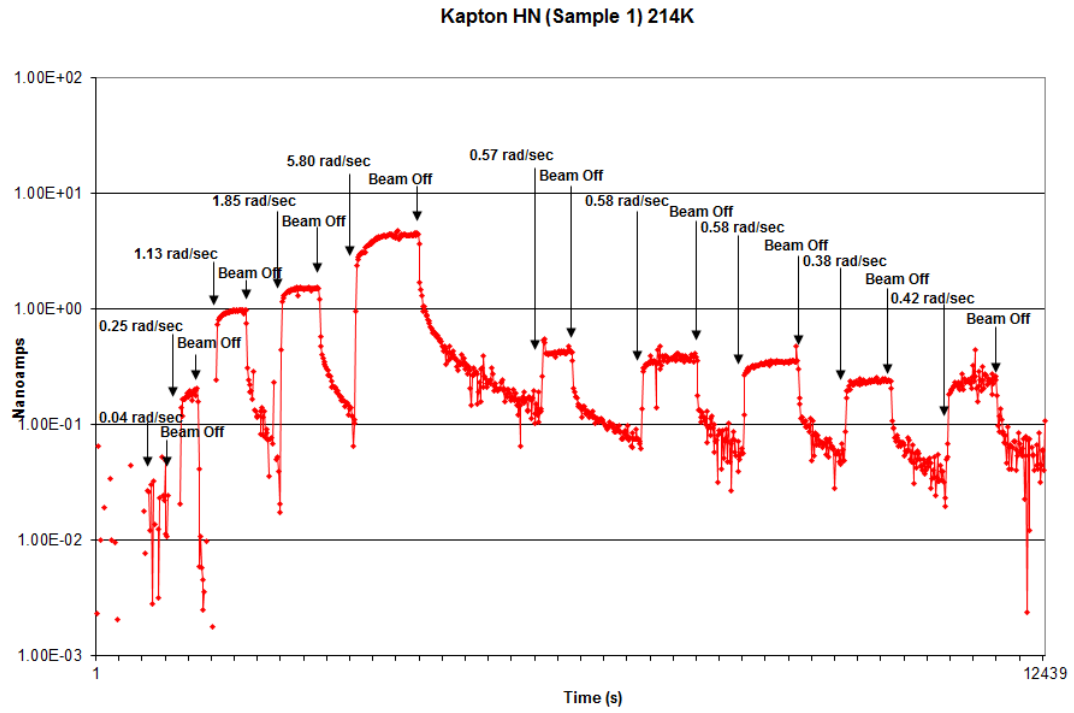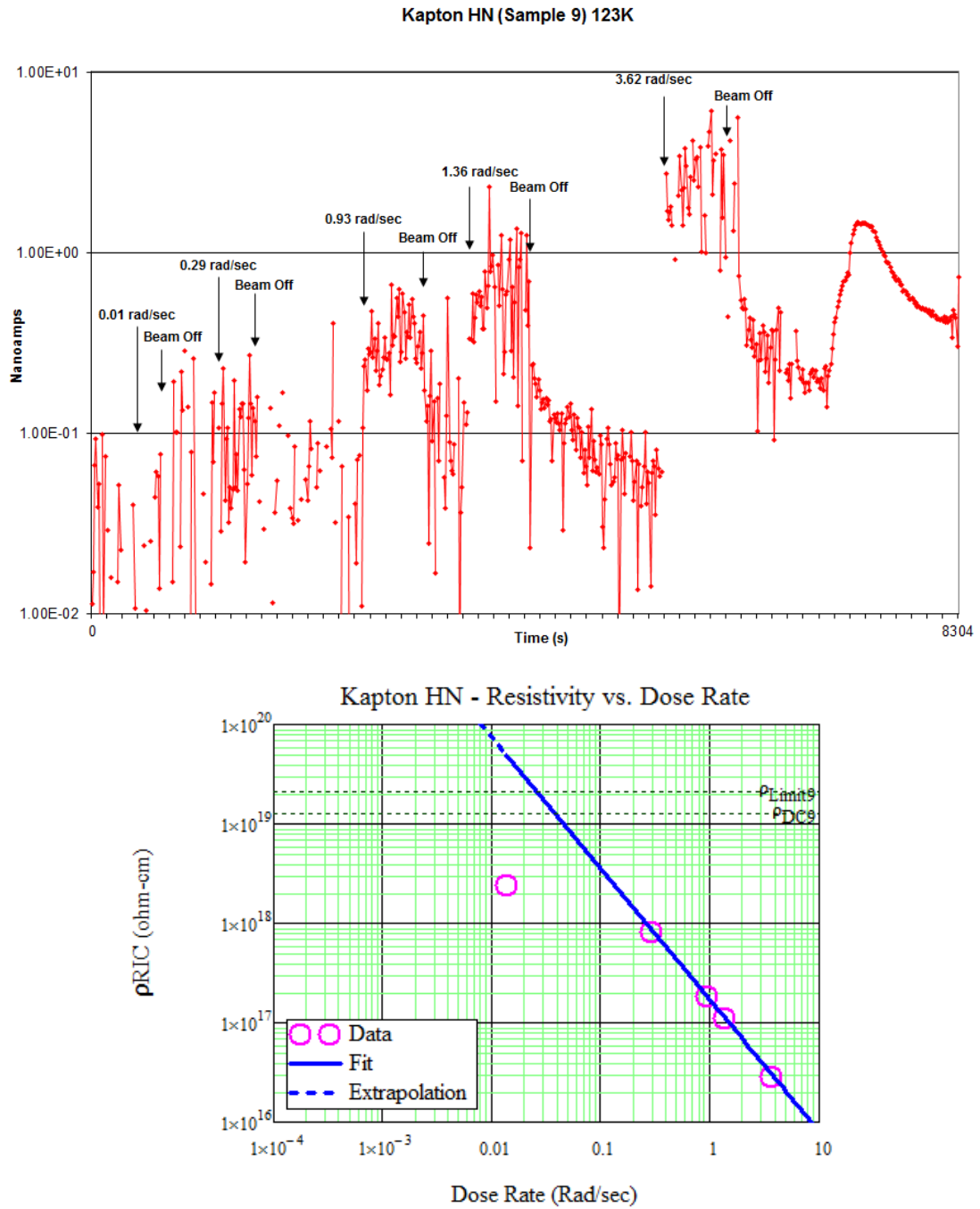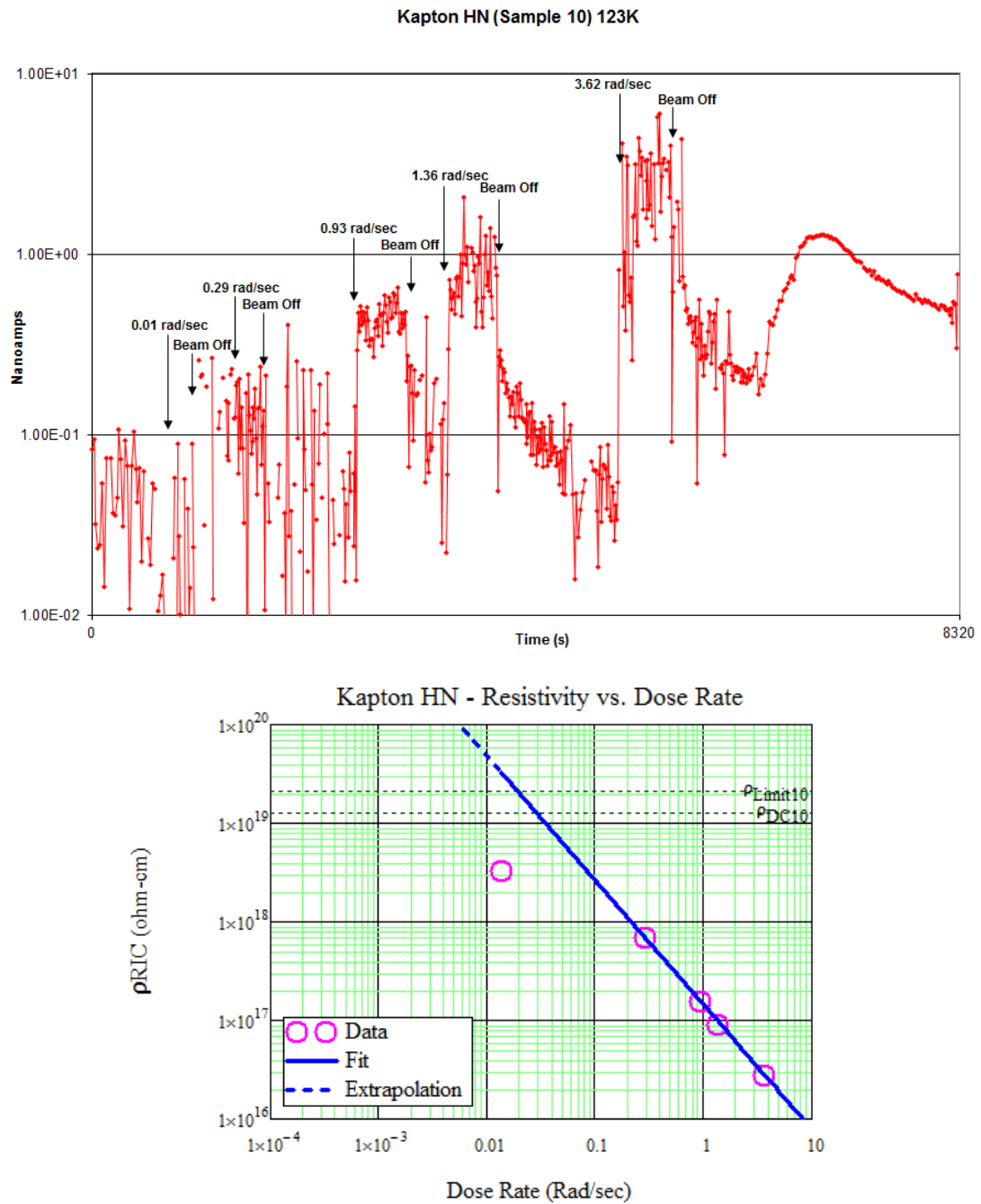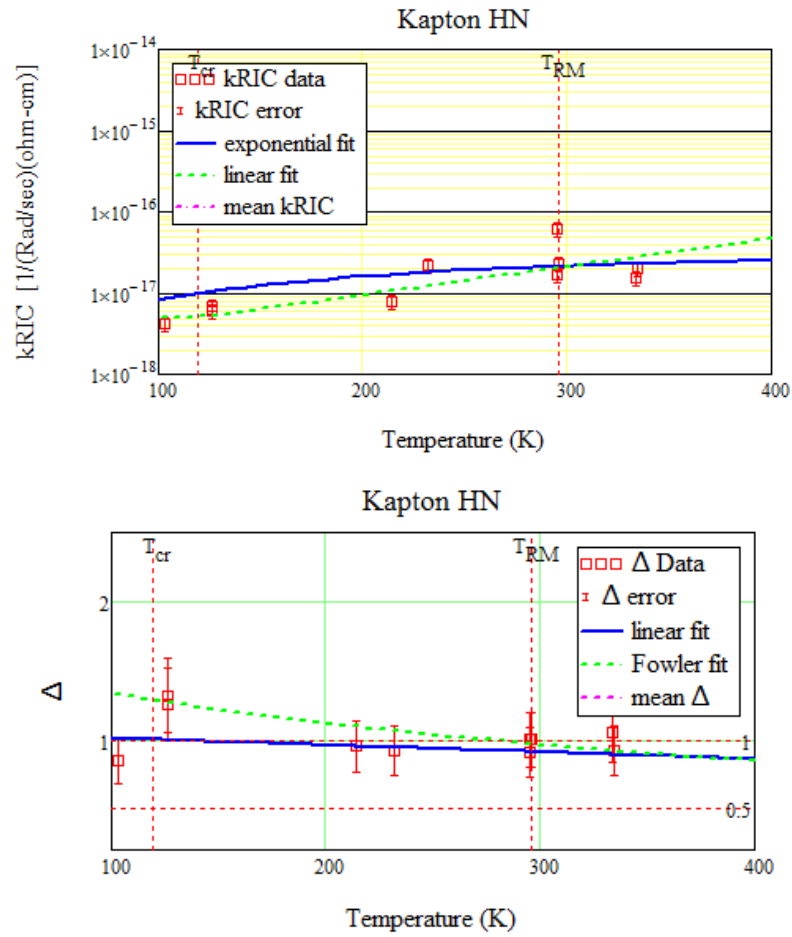
FIG. B.11. Kapton HN k and Δ data and temperature-dependent fits. *k*–value data and temperature-dependent fits (above). *Δ*–value data and temperature-dependent fits (below).
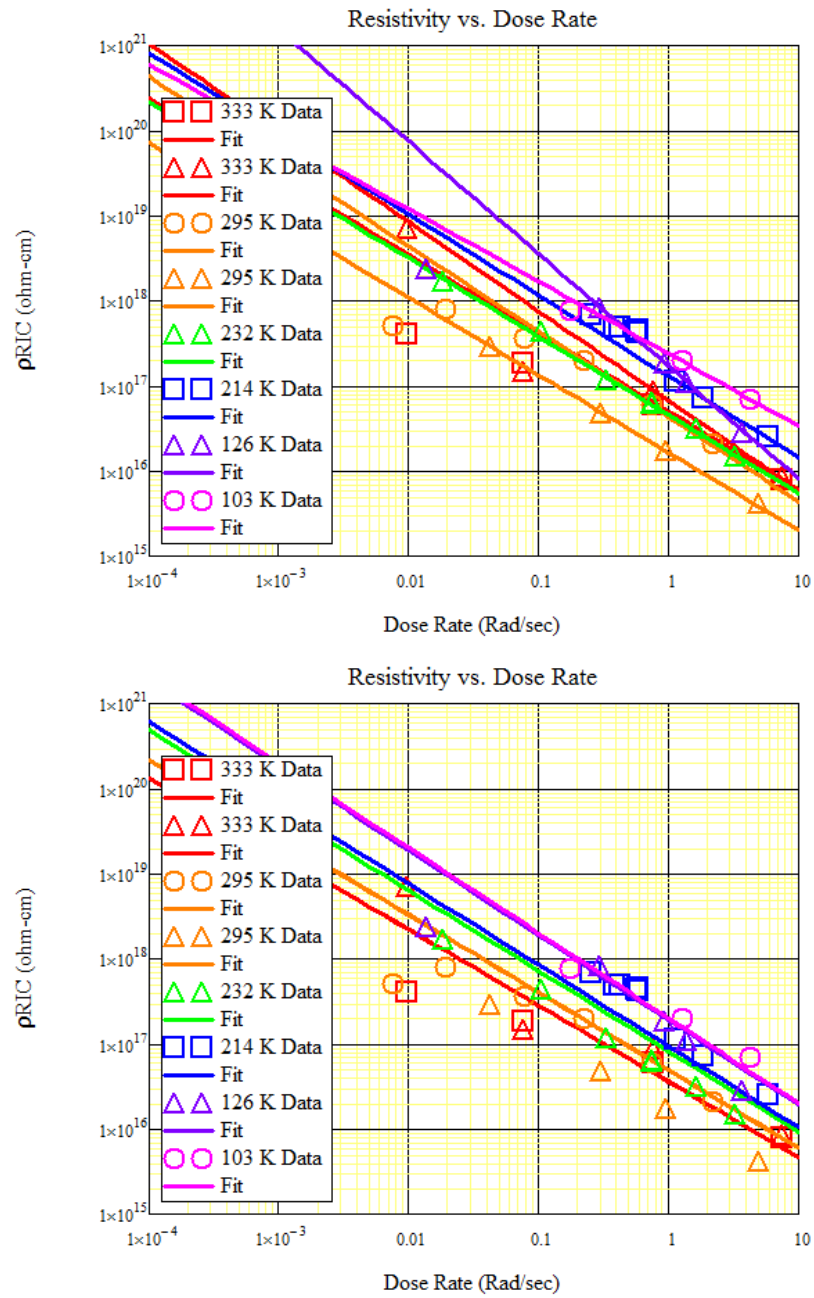
FIG. B.12. RIC Kapton HN data and temperature fits. *T*-independent fits to Kapton HN data (top). *T*-dependent fits to Kapton HN data (bottom).

APPENDIX C

LDPE TABLE AND GRAPHS

TABLE C.1. Table of results for LDPE.

Date Acquired Carousel Position	Temp (K)	Thickness (µm)	Applied (% of Breakdown) Voltage (V)	E-Field (MV/m)	Approximate Resistivity Resolution (Ω-cm)	Dark Current Resistivity (Ω-cm)	RIC Power Law Fit Parameters k (sec-Rad^{-1}/Ω-cm)	Δ
11/21/06 Position 1	333 ± 1	127.4 ± 6%	(0.8%)		$2 \cdot 10^{16}$	$1.3 \cdot 10^{17} \pm$ 20%	$1.2 \cdot 10^{-15} \pm$ 20%	0.69 ± 20%
			314 ± 1%	2.5 ± 10%				
11/21/06 Position 2	333 ± 1	127.4 ± 6%	(0.2%)		$5 \cdot 10^{15}$	$1.4 \cdot 10^{17} \pm$ 20%	$5.6 \cdot 10^{-16} \pm$ 20%	0.71 ± 20%
			78.5 ± 1%	0.6 ± 10%				
11/21/06 Position 1	295 ± 0.5	127.4 ± 6%	(0.9%)		$1 \cdot 10^{18}$	$1.2 \cdot 10^{18} \pm$ 20%	$2.3 \cdot 10^{-16} \pm$ 20%	0.90 ± 20%
			350 ± 1%	2.7 ± 10%				
11/21/06 Position 2	295 ± 0.5	127.4 ± 6%	(0.2%)		$3 \cdot 10^{17}$	$1.3 \cdot 10^{18} \pm$ 20%	$1.1 \cdot 10^{-16} \pm$ 20%	0.85 ± 20%
			87.5 ± 1%	0.7 ± 10%				
2/28/07 Position 7	295 ± 0.5	127.4 ± 6%	(4.5%)		$3 \cdot 10^{18}$	$8.4 \cdot 10^{17} \pm$ 20%	$1.1 \cdot 10^{-17} \pm$ 20%	0.90 ± 20%
			1650 ± 1%	13 ± 10%				
3/1/07 Position 7	232 ± 1	127.4 ± 6%	(4.5%)		$3 \cdot 10^{18}$	$5.0 \cdot 10^{19} \pm$ 20%	$3.4 \cdot 10^{-18} \pm$ 20%	1.00 ± 20%
			1650 ± 1%	13 ± 10%				
3/2/07 Position 7	214 ± 2	127.4 ± 6%	(4.5%)		$3 \cdot 10^{18}$	$9.7 \cdot 10^{20} \pm$ 20%	$2.3 \cdot 10^{-18} \pm$ 20%	1.05 ± 20%
			1650 ± 1%	13 ± 10%				
6/18/07 Position 3	123 ± 3	127.4 ± 6%	(7.6%)		$5 \cdot 10^{18}$	$2.8 \cdot 10^{21} \pm$ 20%	$4.7 \cdot 10^{-18} \pm$ 20%	1.20 ± 20%
			2800 ± 1%	22 ± 10%				
6/18/07 Position 4	123 ± 3	127.4 ± 6%	(7.6%)		$5 \cdot 10^{18}$	$2.8 \cdot 10^{21} \pm$ 20%	$4.3 \cdot 10^{-18} \pm$ 20%	1.20 ± 20%
			2800 ± 1%	22 ± 10%				

FIG. C.1. LDPE data taken at 333 K on November 21, 2006. Raw current data (above). Fit to current data (below).

FIG. C.2. LDPE data taken at 333 K on November 21, 2006. Raw current data (above). Fit to current data (below).
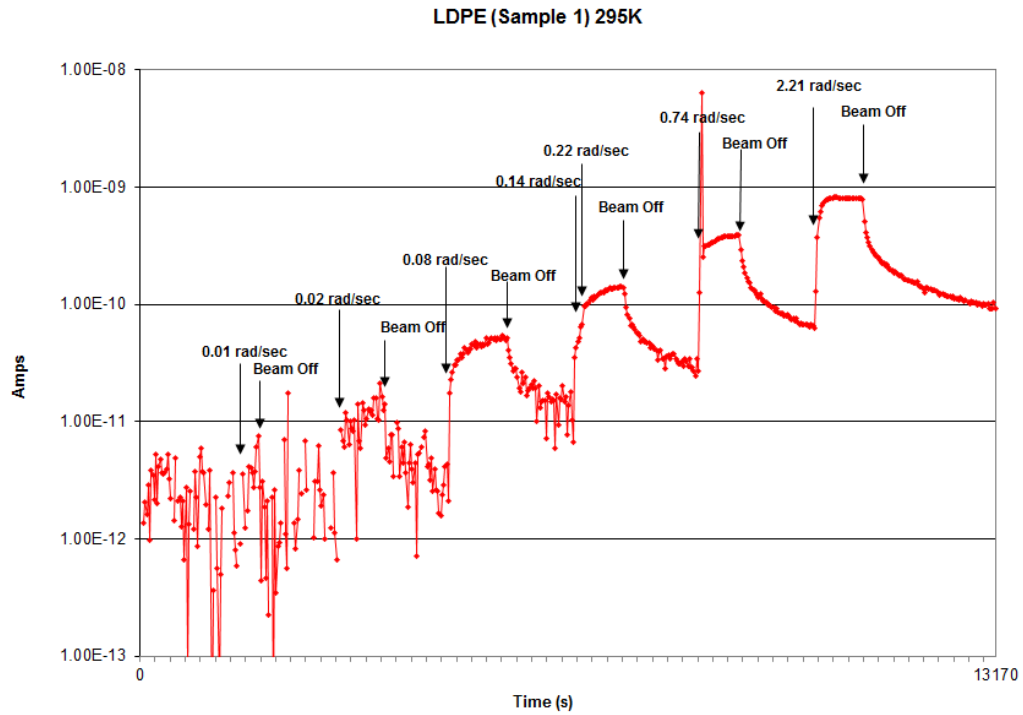
FIG. C.3. LDPE data taken at 295 K on November 21, 2006. Raw current data (above). Fit to current data (below).

FIG. C.4. LDPE data taken at 295 K on November 21, 2006. Raw current data (above). Fit to current data (below).

FIG. C.5. LDPE data taken at 295 K on February 28, 2007. Raw current data (above). Fit to current data (below).

LDPE (Sample 7) 232K

FIG. C.6. LDPE data taken at 232 K on March 1, 2007. Raw current data (above). Fit to current data (below).
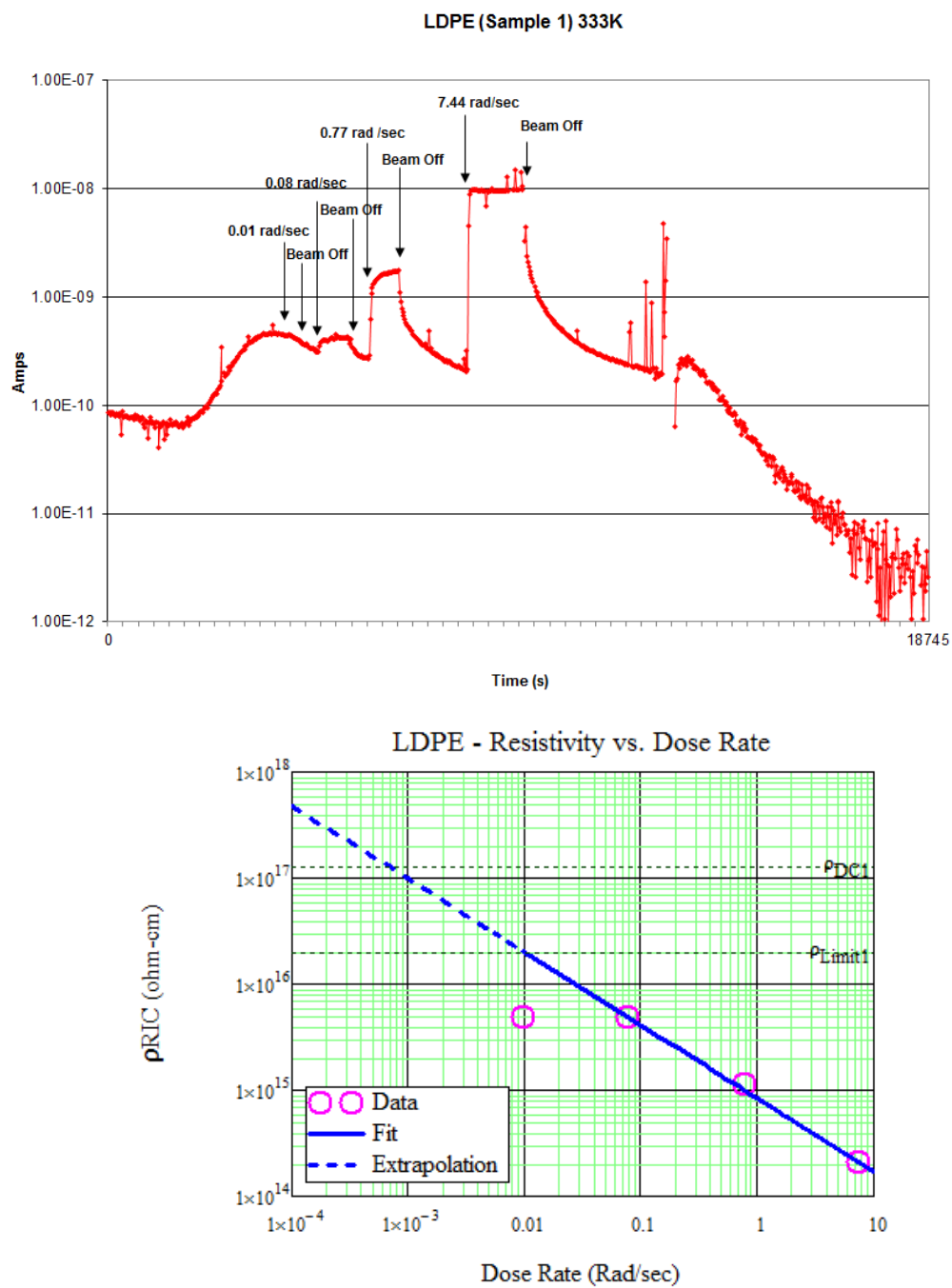
FIG. C.7. LDPE data taken at 214 K on March 2, 2007. Raw current data (above). Fit to current data (below).

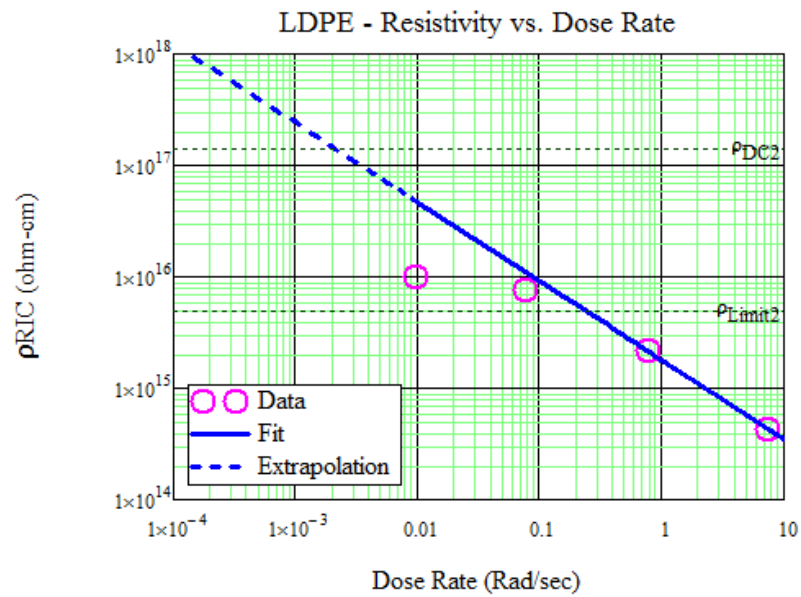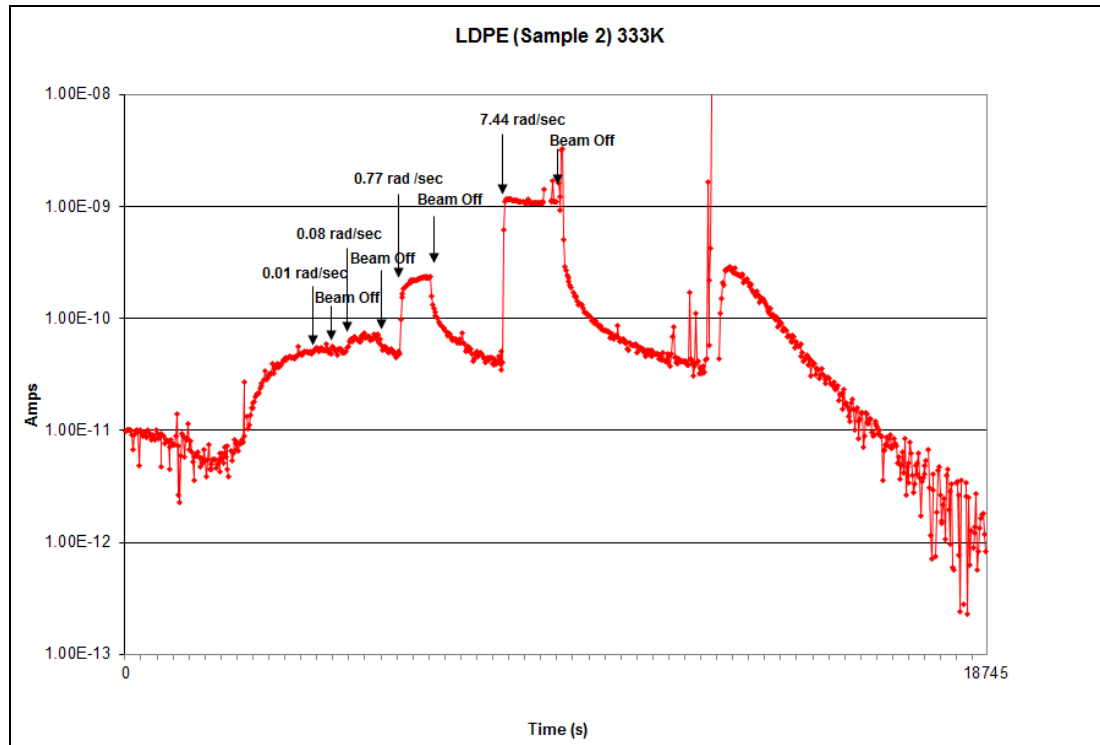FIG. C.8. LDPE data taken at 123 K on June 18, 2007. Raw current data (above). Fit to current data (below).

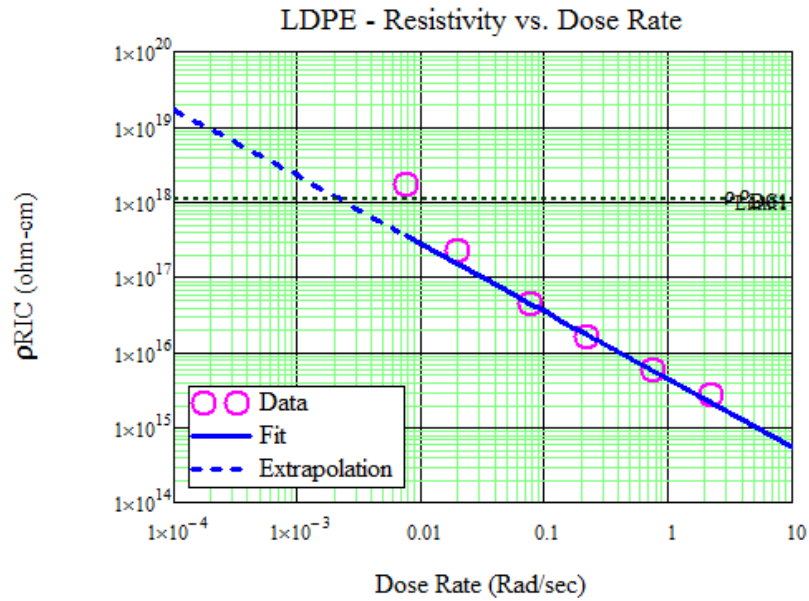FIG. C.9. LDPE data taken at 123 K on June 18, 2007. Raw current data (above). Fit to current data (below).
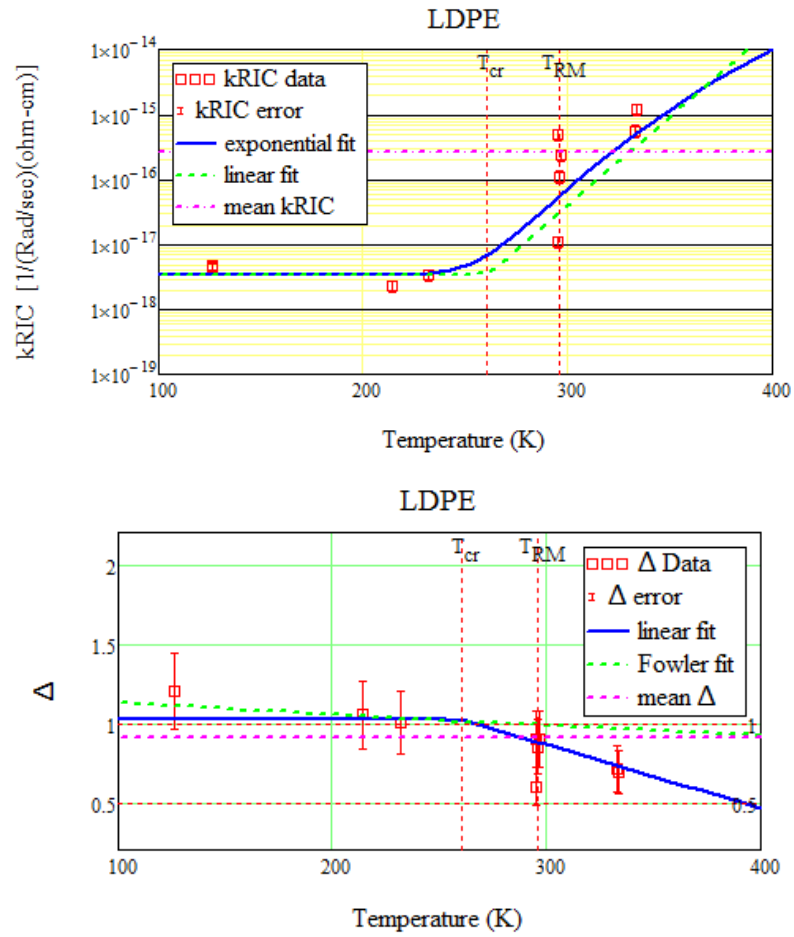
FIG. C.10.   LDPE k and Δ data and temperature-dependent fits. k–value data and temperature-dependent fits (above). Δ–value data and temperature-dependent fits (below).

FIG. C.11. RIC LDPE data and temperature fits. *T*-independent fits to LDPE data (top). *T*-dependent fits to LDPE data (bottom).

APPENDIX D

PTFE TABLE AND GRAPHS

TABLE D.1. Table of results for PTFE.

| Date Acquired Carousel Position	Temp (°C)	Thickness (μm)	Applied (% of Breakdown)		Approximate Resistivity Resolution (Ω-cm)	Dark Current Resistivity (Ω-cm)	RIC Power Law Fit Parameters	
			Voltage (V)	E-Field (MV/m)			k (sec-Rad^{-1}/ Ω-cm)	Δ
2/28/07 Position 5	295 ± 0.5	76.2 ± 6%	(24%)		$6 \cdot 10^{18}$	$1.6 \cdot 10^{19}$ ± 20%	$2.9 \cdot 10^{-17}$ ± 20%	1.23 ± 20%
			2200 ± 1%	29 ± 10%				
3/1/07 Position 5	232 ± 1	76.2 ± 6%	(24%)		$6 \cdot 10^{18}$	$3.9 \cdot 10^{20}$ ± 20%	$6.1 \cdot 10^{-18}$ ± 20%	1.0 ± 20%
			2200 ± 1%	29 ± 10%				
3/2/07 Position 5	214 ± 2	76.2 ± 6%	(24%)		$6 \cdot 10^{18}$	$1.4 \cdot 10^{21}$ ± 20%	$3.9 \cdot 10^{-18}$ ± 20%	1.2 ± 20%
			2200 ± 1%	29 ± 10%				
6/18/07 Position 5	123 ± 3	76.2 ± 6%	(20%)		$5 \cdot 10^{18}$	$2.0 \cdot 10^{23}$ ± 20%	$4.8 \cdot 10^{-18}$ ± 20%	1.2 ± 20%
			1800 ± 1%	24 ± 10%				
6/18/07 Position 6	123 ± 3	76.2 ± 6%	(20%)		$5 \cdot 10^{18}$	$2.0 \cdot 10^{23}$ ± 20%	$4.5 \cdot 10^{-18}$ ± 20%	1.21 ± 20%
			1800 ± 1%	24 ± 10%				
6/19/07 Position 5	103 ± 3	76.2 ± 6%	(18%)		$5 \cdot 10^{18}$	$2.0 \cdot 10^{23}$ ± 20%	$1.0 \cdot 10^{-17}$ ± 20%	0.92 ± 20%
			1675 ± 1%	22 ± 10%				
6/19/07 Position 6	103 ± 3	76.2 ± 6%	(18%)		$5 \cdot 10^{18}$	$2.0 \cdot 10^{23}$ ± 20%	$1.1 \cdot 10^{-17}$ ± 20%	0.91 ± 20%
			1675 ± 1%	22 ± 10%				
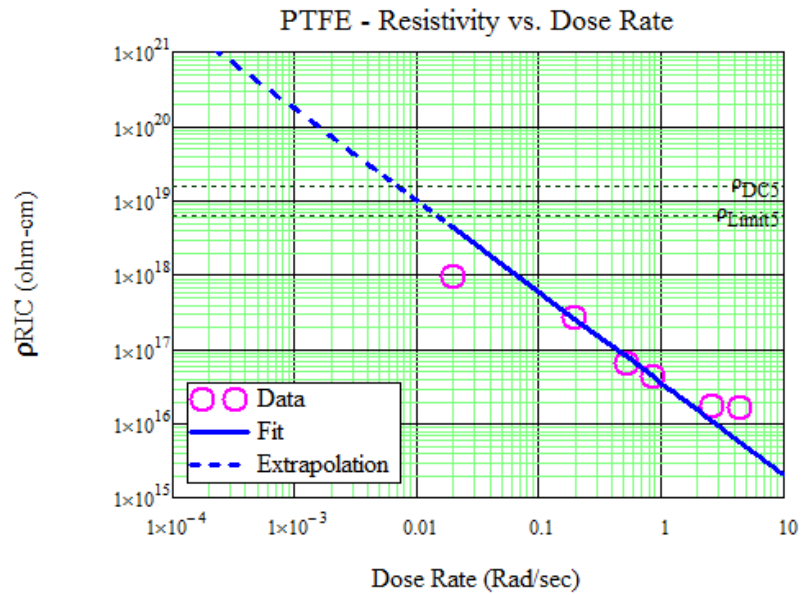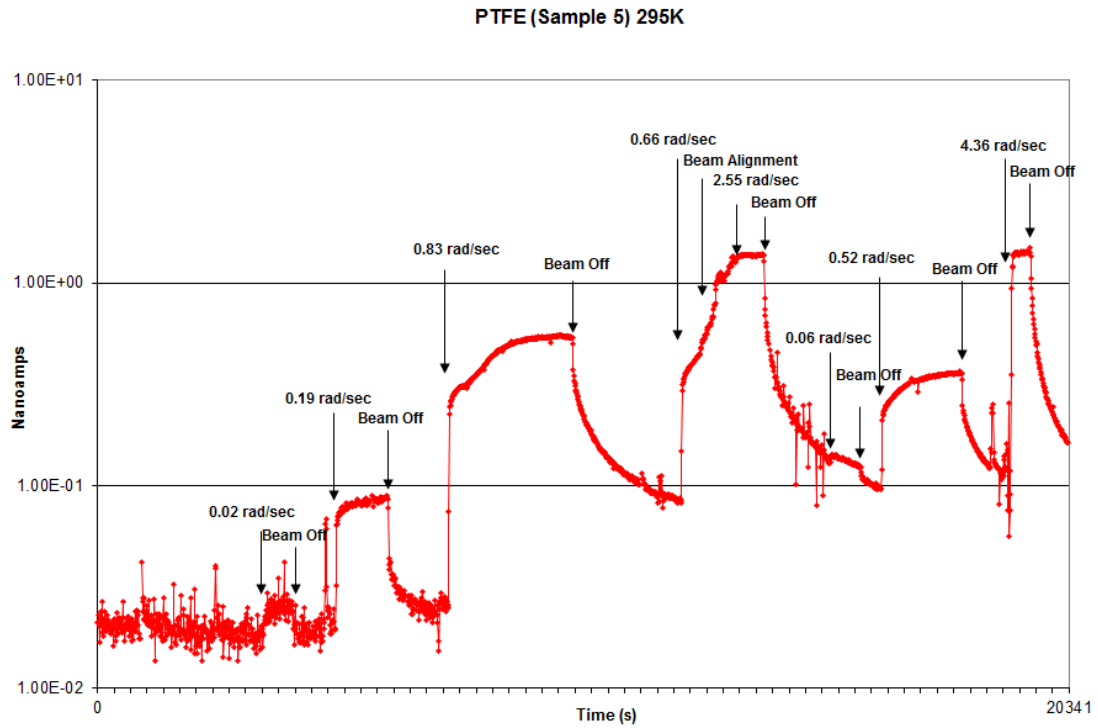
FIG. D.1. PTFE data taken at 295 K on February 28, 2007. Raw current data (above). Fit to current data (below).
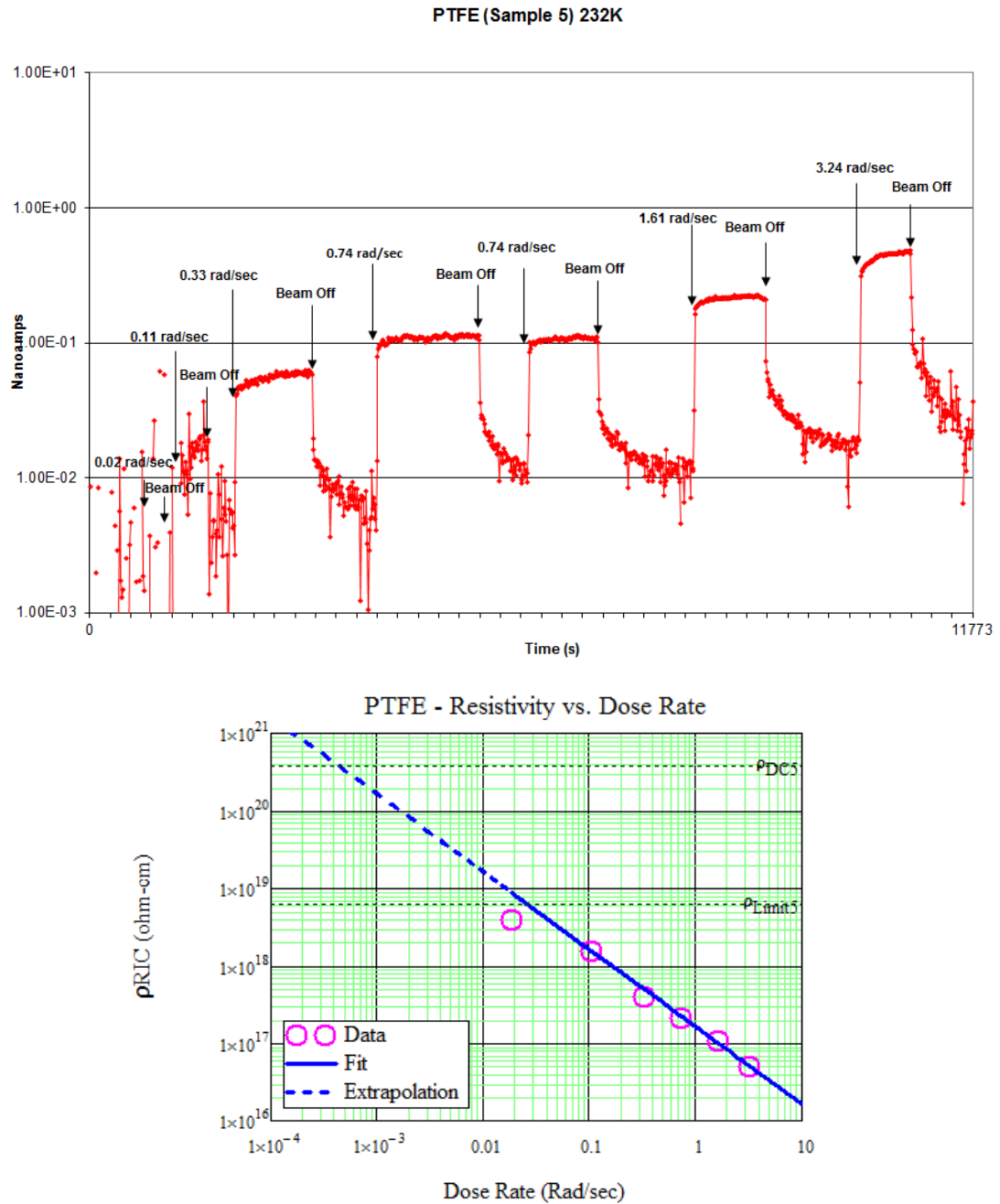
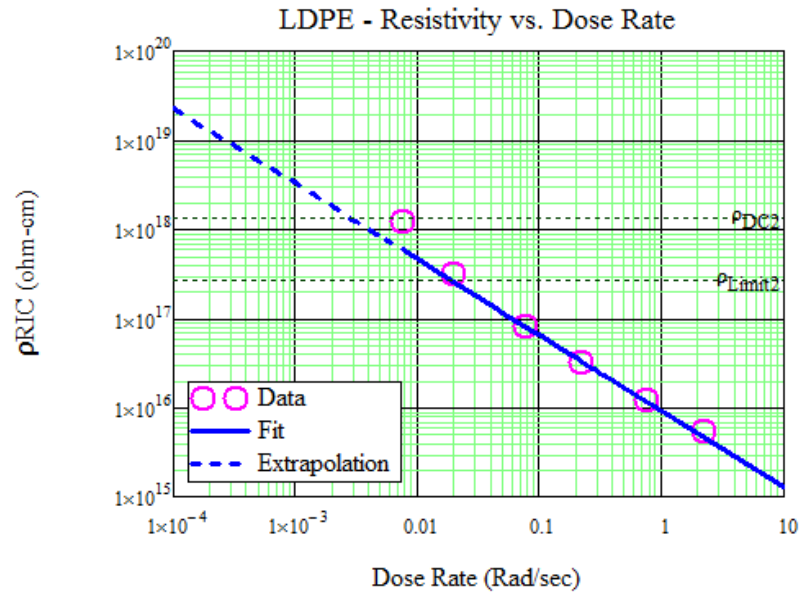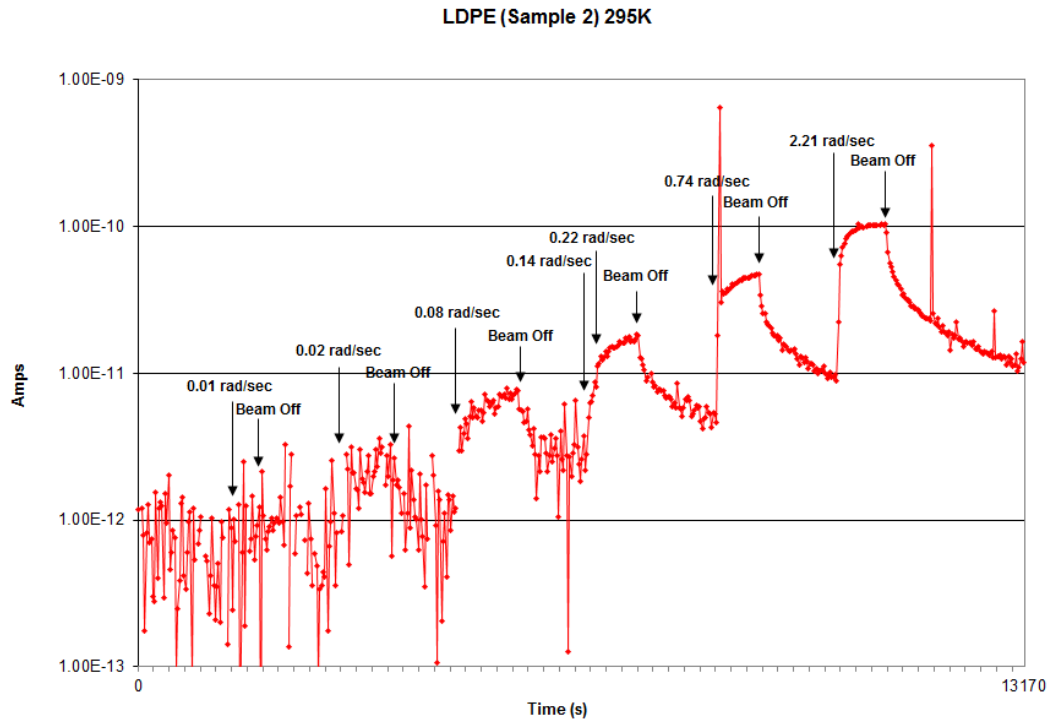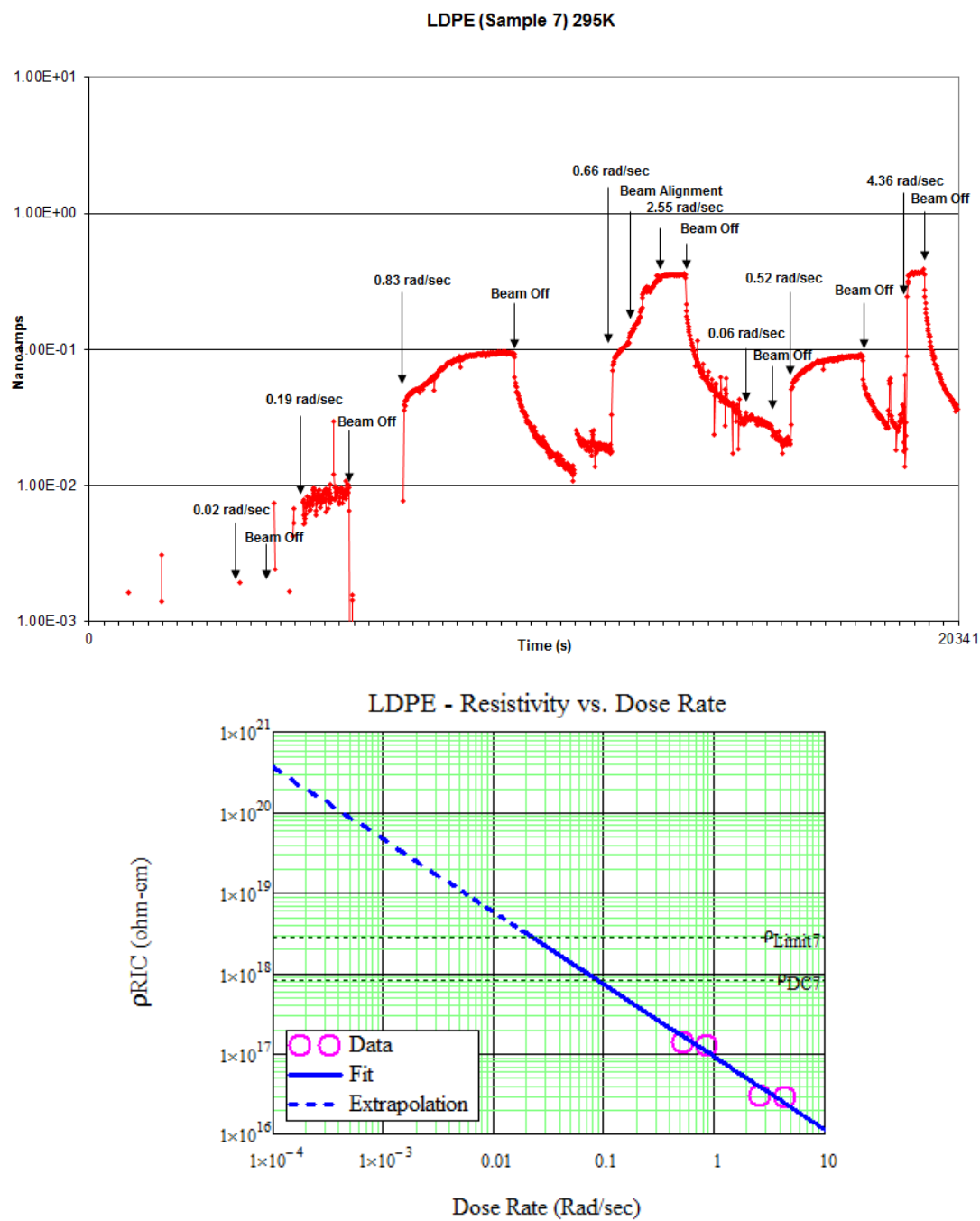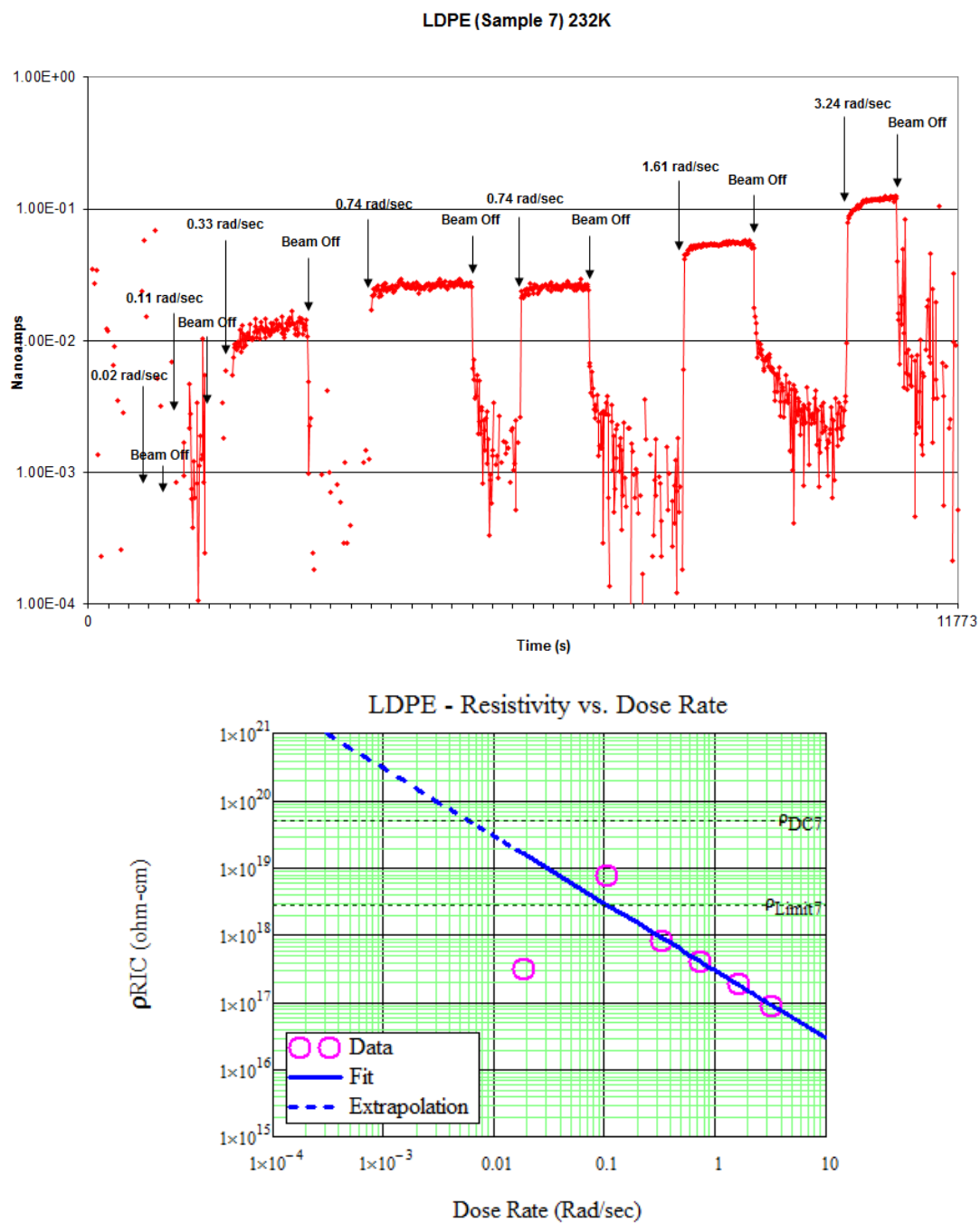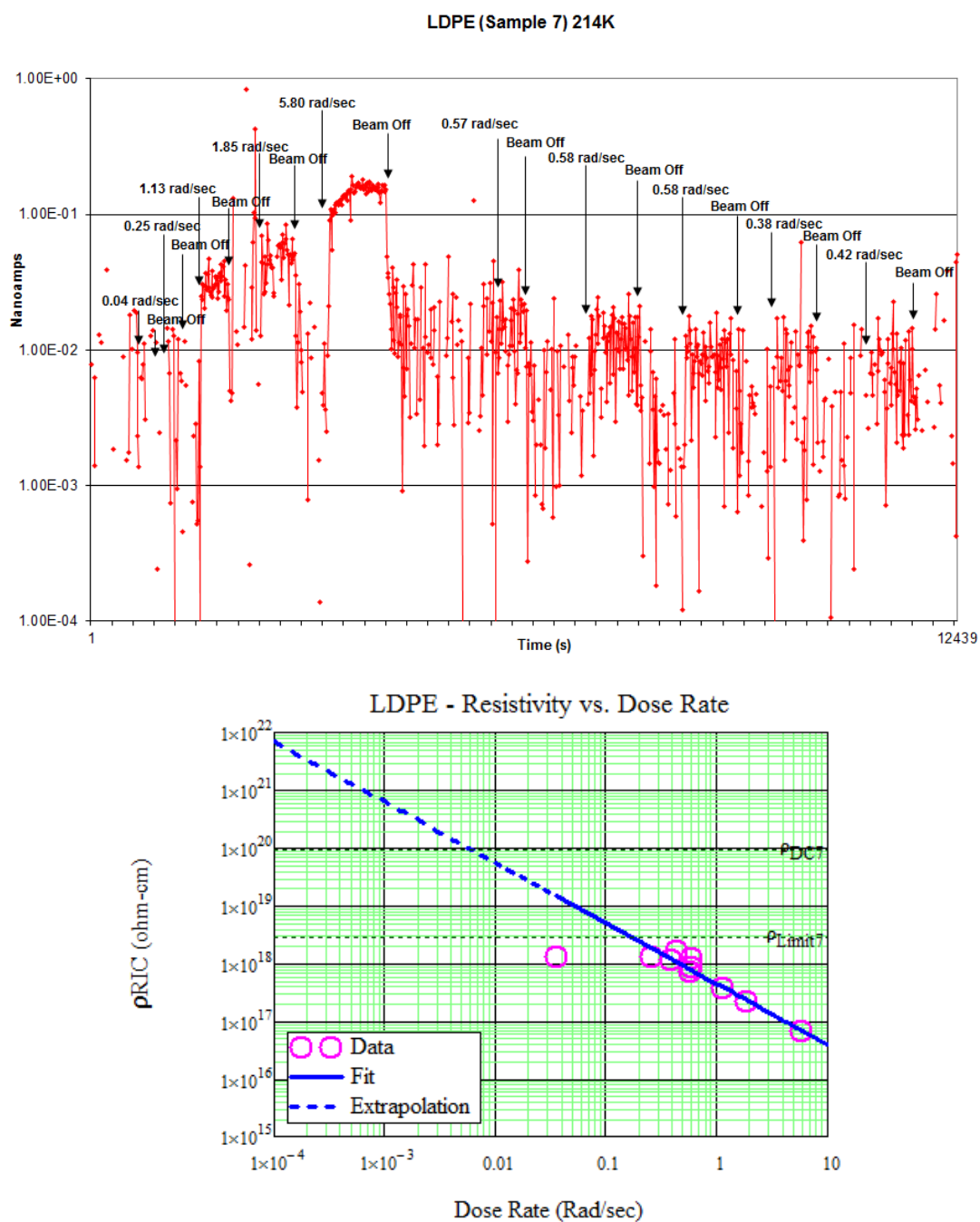FIG. D.2. PTFE data taken at 232 K on March 1, 2007. Raw current data (above). Fit to current data (below).
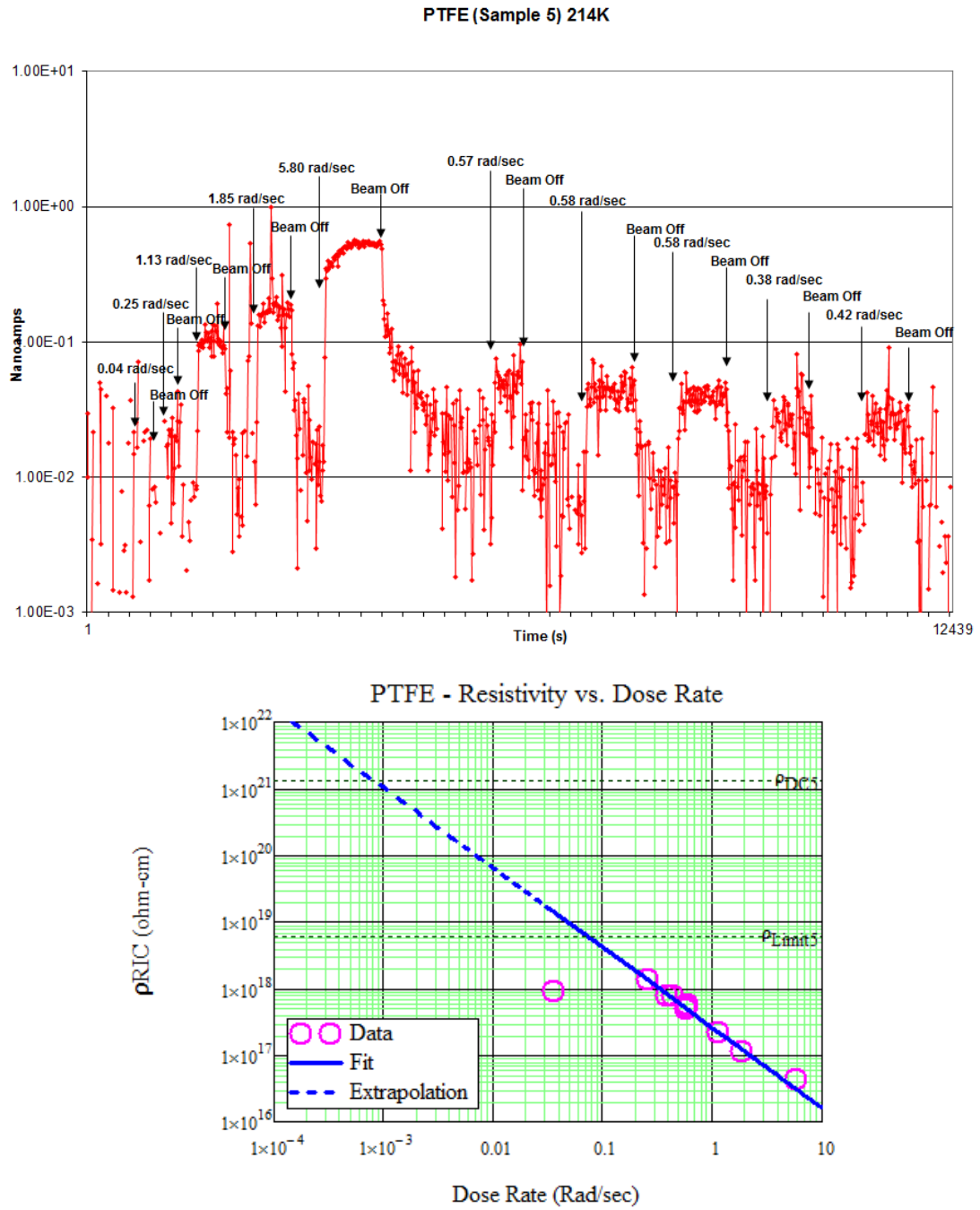
FIG. D.3. PTFE data taken at 214 K on March 2, 2007. Raw current data (above). Fit to current data (below).
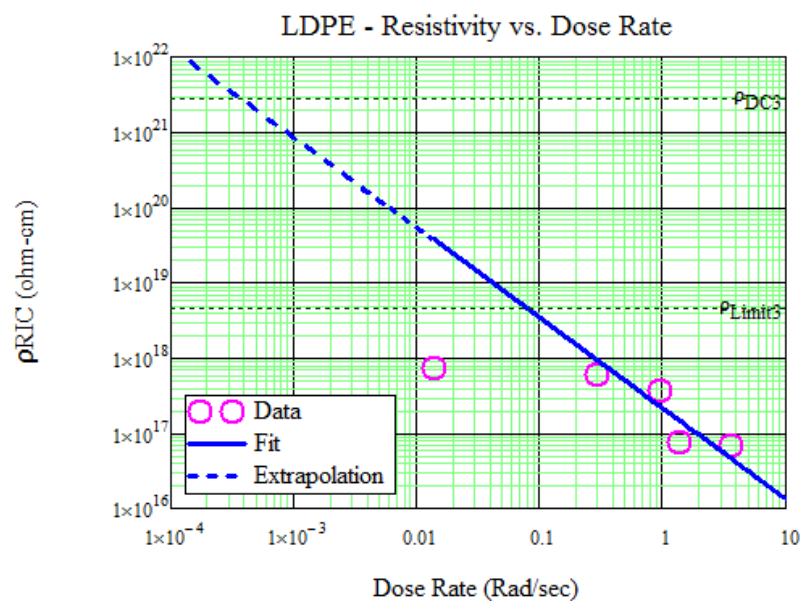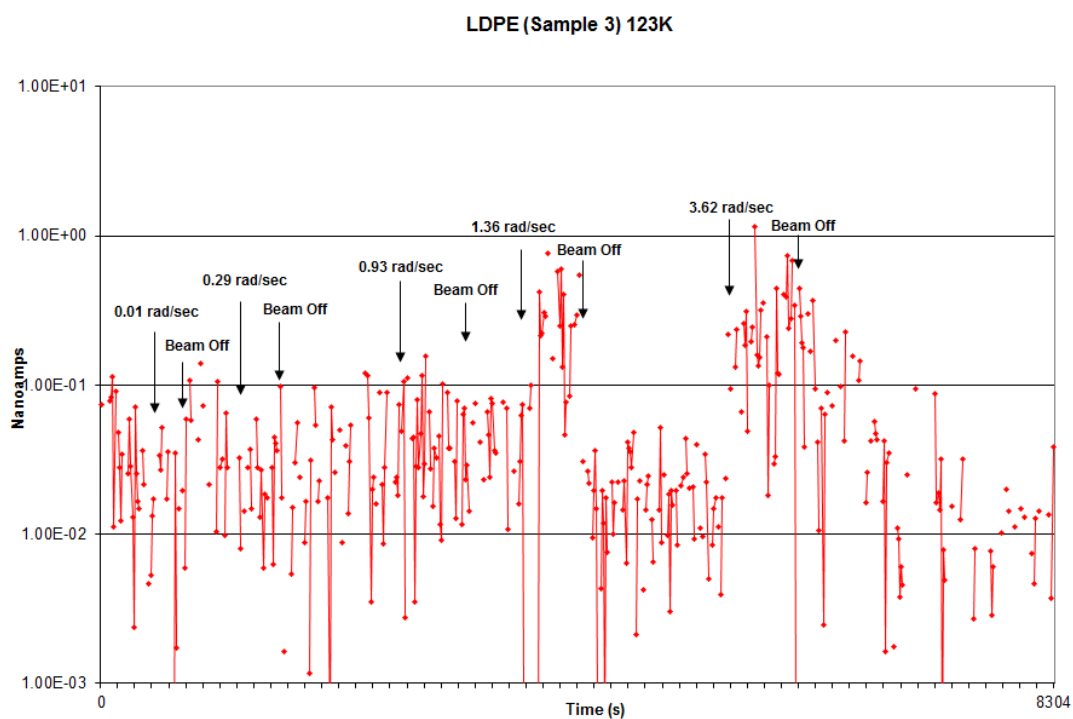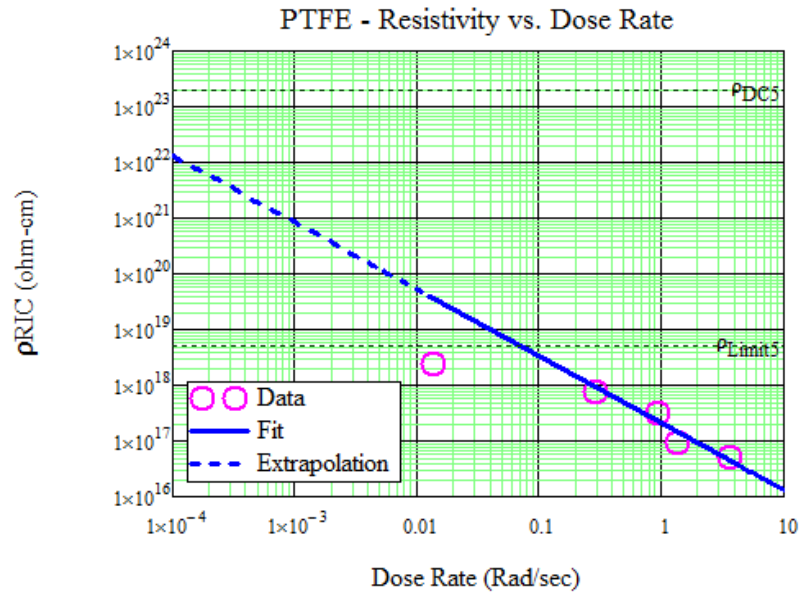
FIG. D.4. PTFE data taken at 123 K on June 18, 2007. Raw current data (above). Fit to current data (below).

FIG. D.5. PTFE data taken at 123 K on June 18, 2007. Raw current data (above). Fit to current data (below).

FIG. D.6. PTFE data taken at 103 K on June 19, 2007. Raw current data (above). Fit to current data (below).
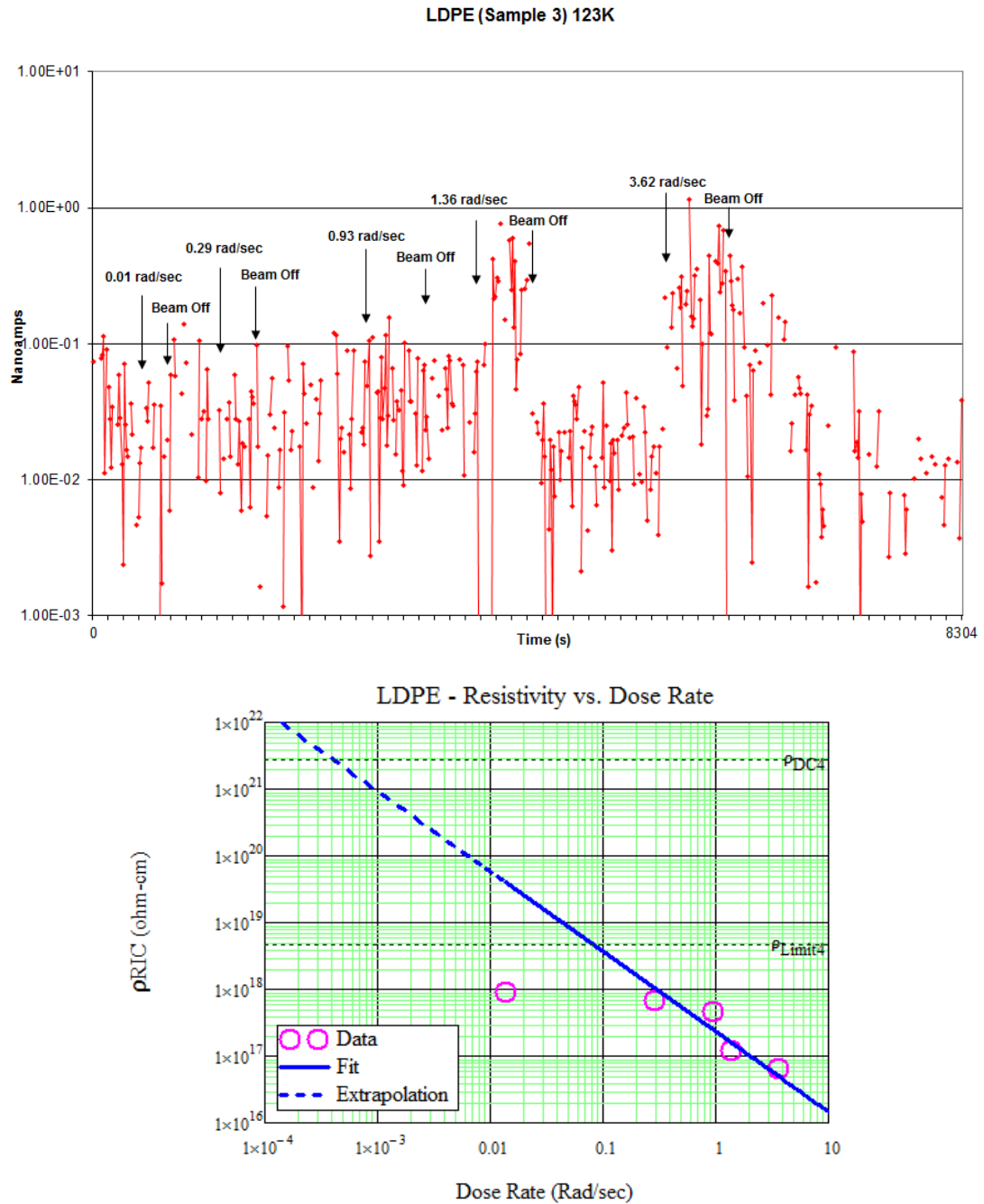
FIG. D.7. PTFE data taken at 103 K on June 19, 2007. Raw current data (above). Fit to current data (below).
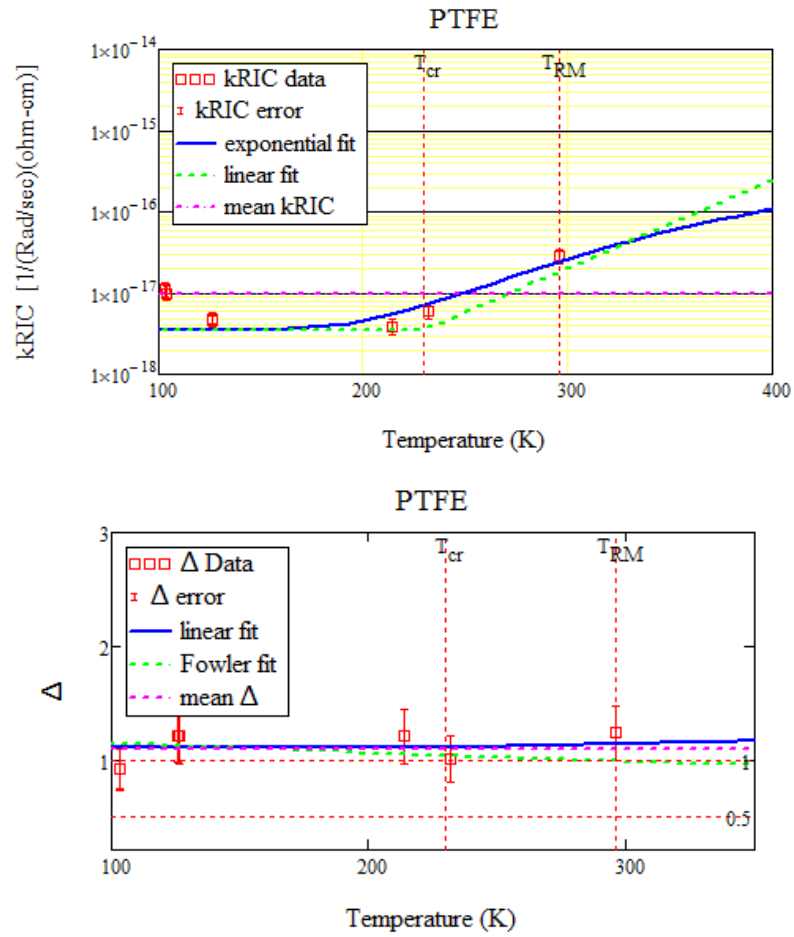
FIG. D.8. PTFE k and Δ data and temperature-dependent fits. k–value data and temperature-dependent fits (above). Δ–value data and temperature-dependent fits (below).
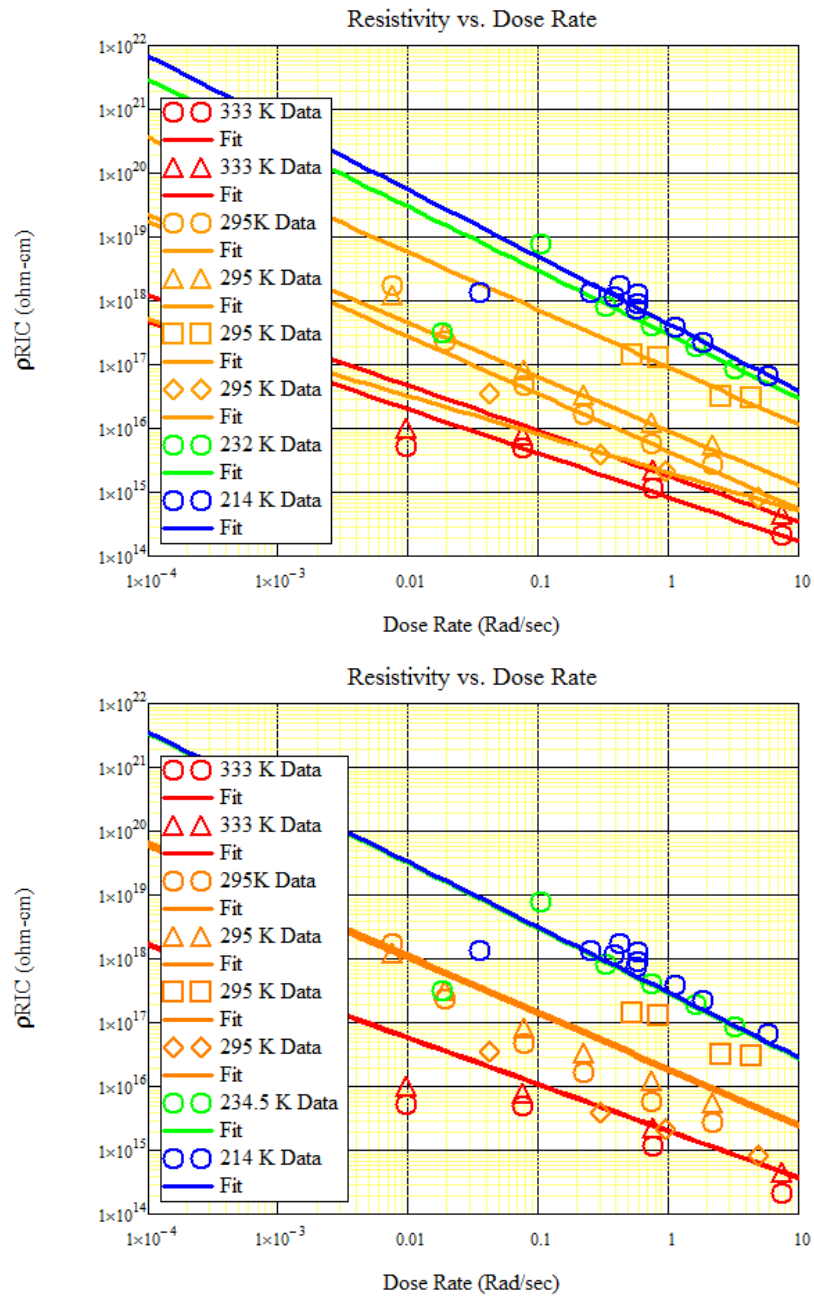
FIG. D.9. RIC PTFE data and temperature fits. *T*-independent fits to PTFE data (top). *T*-dependent fits to PTFE data (bottom).

APPENDIX E

TEFZEL TABLE AND GRAPHS

TABLE E.1. Table of results for Tefzel.

Date Acquired Carousel Position	Temp (°C)	Thickness (µm)	Applied (% of Breakdown)		Approximate Resistivity Resolution (Ω-cm)	Dark Current Resistivity (Ω-cm)	RIC Power Law Fit Parameters	
			Voltage (V)	E-Field (MV/m)			k (sec-Rad^{-1}/ Ω-cm)	Δ
11/21/06 Position 4	333 ± 1	53.1 ± 6%	(4%) 549.5 ± 1%	12 ± 10%	$9 \cdot 10^{16}$	$9.0 \cdot 10^{18} \pm$ 20%	$4.7 \cdot 10^{-17} \pm$ 20%	0.75 ± 20%
11/21/06 Position 6	333 ± 1	53.1 ± 6%	(21%) 2669 ± 1%	50 ± 10%	$4 \cdot 10^{17}$	$3.6 \cdot 10^{18} \pm$ 20%	$8.5 \cdot 10^{-17} \pm$ 20%	0.75 ± 20%
11/20/06 Position 1	295 ± 0.5	53.1 ± 6%	(19%) 2394 ± 1%	45 ± 10%	$2 \cdot 10^{19}$	$1.3 \cdot 10^{19} \pm$ 20%	$2.2 \cdot 10^{-18} \pm$ 20%	0.91 ± 20%
11/21/06 Position 4	295 ± 0.5	53.1 ± 6%	(5%) 612.5 ± 1%	12 ± 10%	$5 \cdot 10^{18}$	$3.3 \cdot 10^{19} \pm$ 20%	$1.1 \cdot 10^{-17} \pm$ 20%	0.95 ± 20%
11/21/06 Position 6	295 ± 0.5	53.1 ± 6%	(23%) 2975 ± 1%	56 ± 10%	$2 \cdot 10^{19}$	$1.1 \cdot 10^{19} \pm$ 20%	$1.7 \cdot 10^{-17} \pm$ 20%	0.90 ± 20%
2/28/07 Position 3	295 ± 0.5	53.1 ± 6%	(24%) 3025 ± 1%	57 ± 10%	$1 \cdot 10^{19}$	$1.1 \cdot 10^{19} \pm$ 20%	$4.4 \cdot 10^{-17} \pm$ 20%	0.95 ± 20%
6/19/07 Position 6	295 ± 0.5	53.1 ± 6%	(15%) 1925 ± 1%	36 ± 10%	$8 \cdot 10^{18}$	$1.6 \cdot 10^{19} \pm$ 20%	$1.5 \cdot 10^{-17} \pm$ 20%	1.10 ± 20%
3/1/07 Position 3	232 ± 1	53.1 ± 6%	(24%) 3025 ± 1%	57 ± 10%	$1 \cdot 10^{19}$	$2.3 \cdot 10^{20} \pm$ 20%	$1.2 \cdot 10^{-17} \pm$ 20%	0.90 ± 20%

Dupont Tefzel (Sample 4) 333K


Tefzel - Resistivity vs. Dose Rate
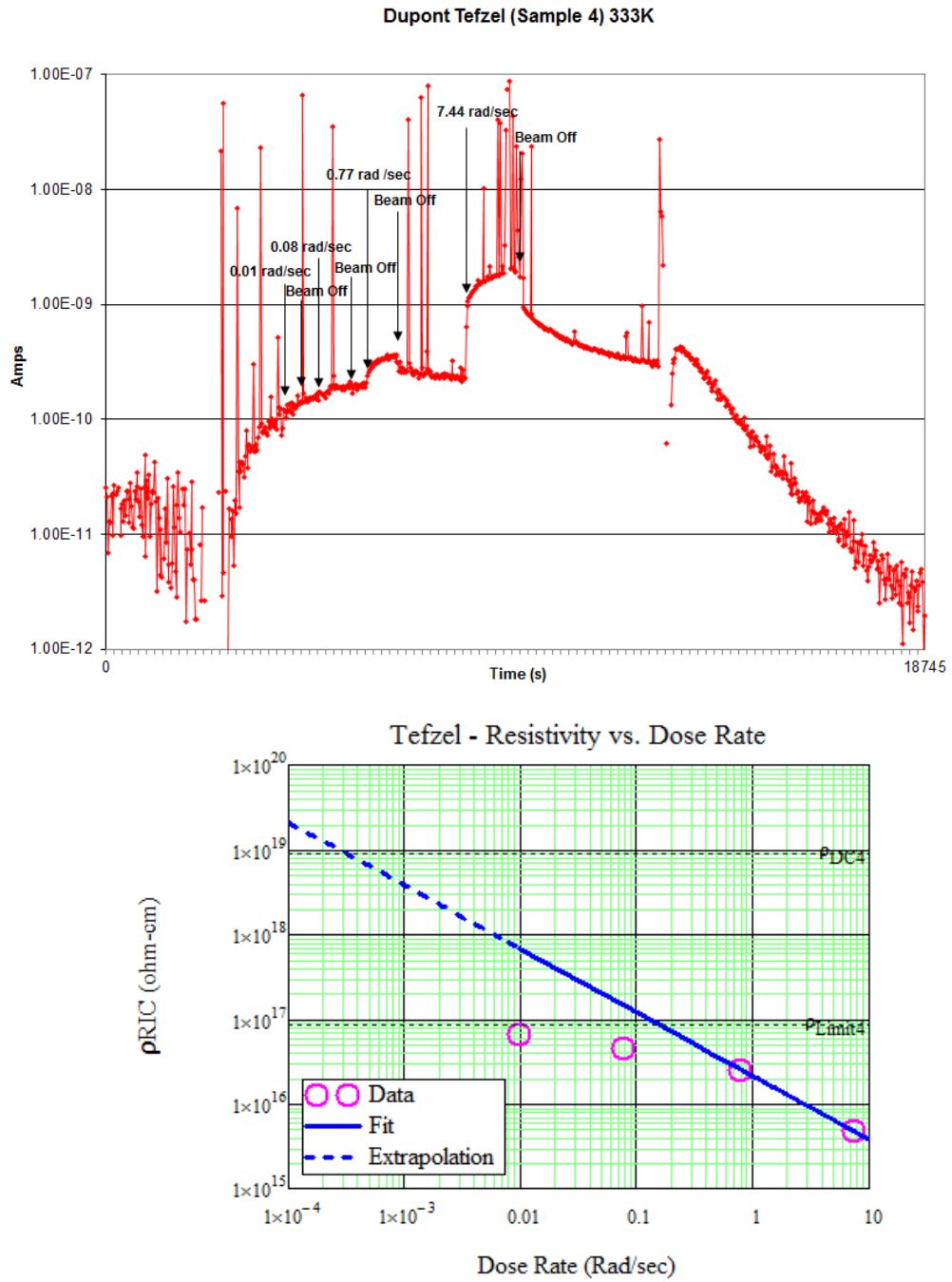
FIG. E.1. Tefzel data taken at 333 K on November 21, 2006. Raw current data (above). Fit to current data (below).
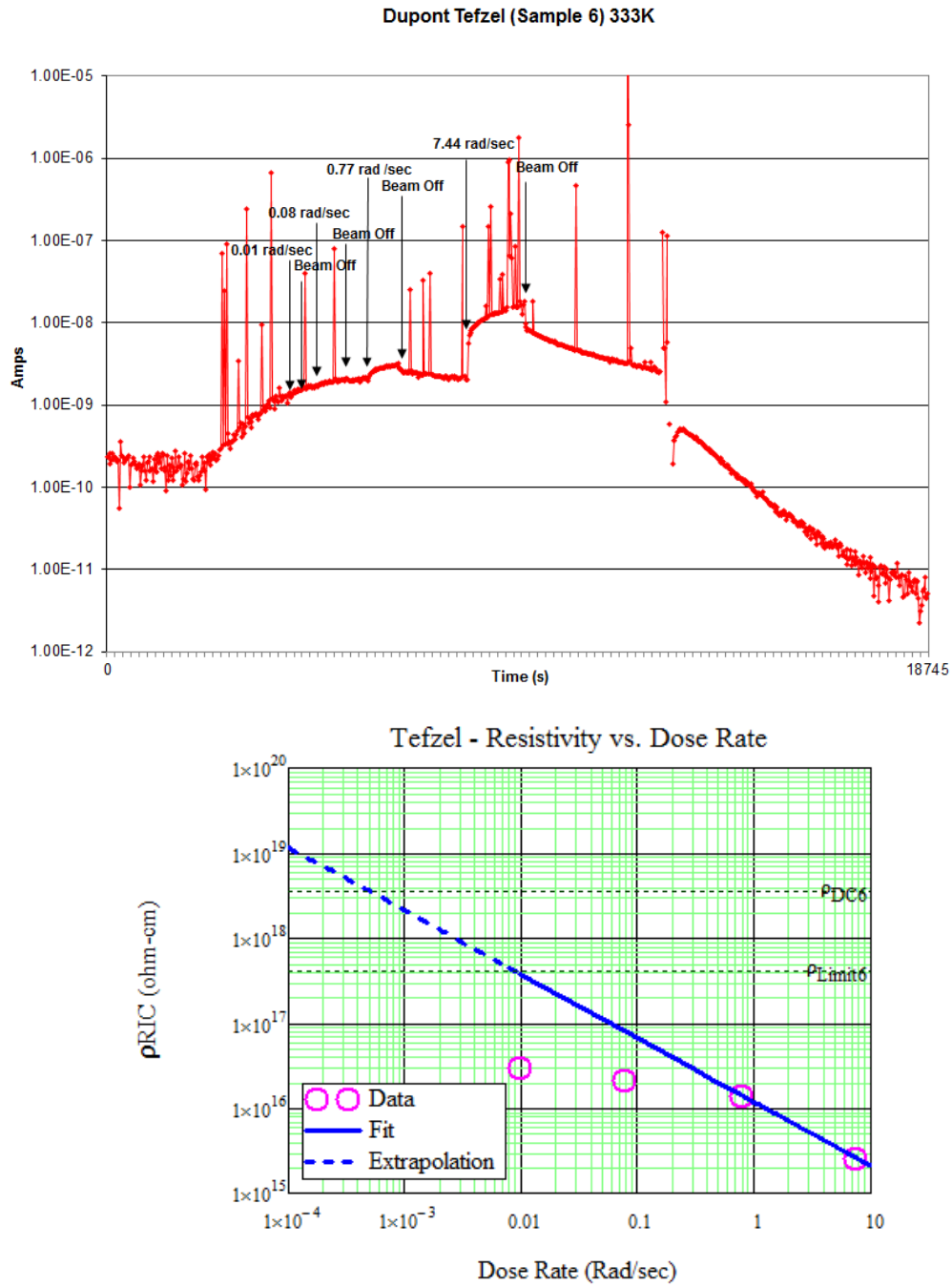
FIG. E.2. Tefzel data taken at 333 K on November 21, 2006. Raw current data (above). Fit to current data (below).
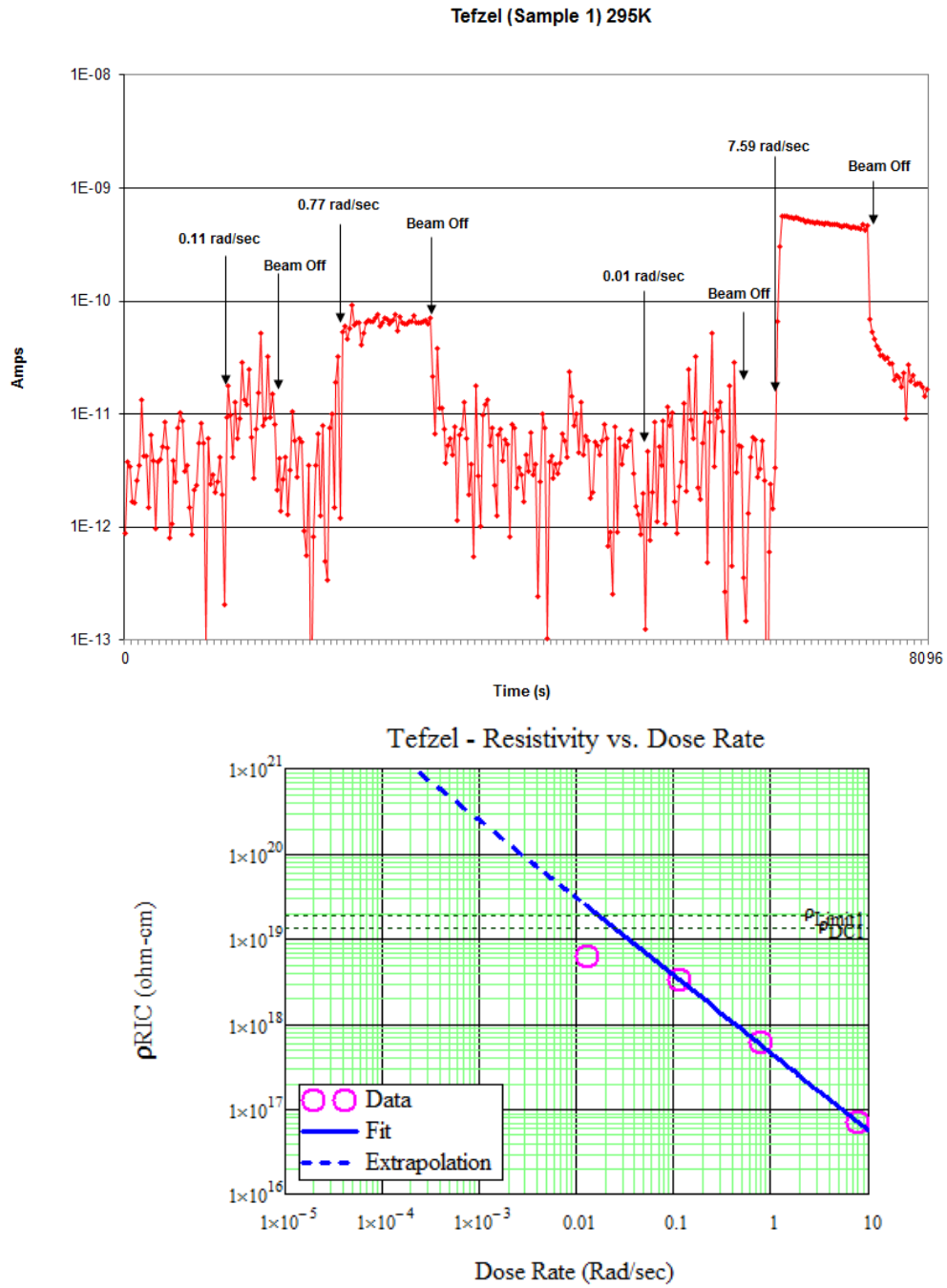
FIG. E.3. Tefzel data taken at 295 K on November 20, 2006. Raw current data (above). Fit to current data (below).
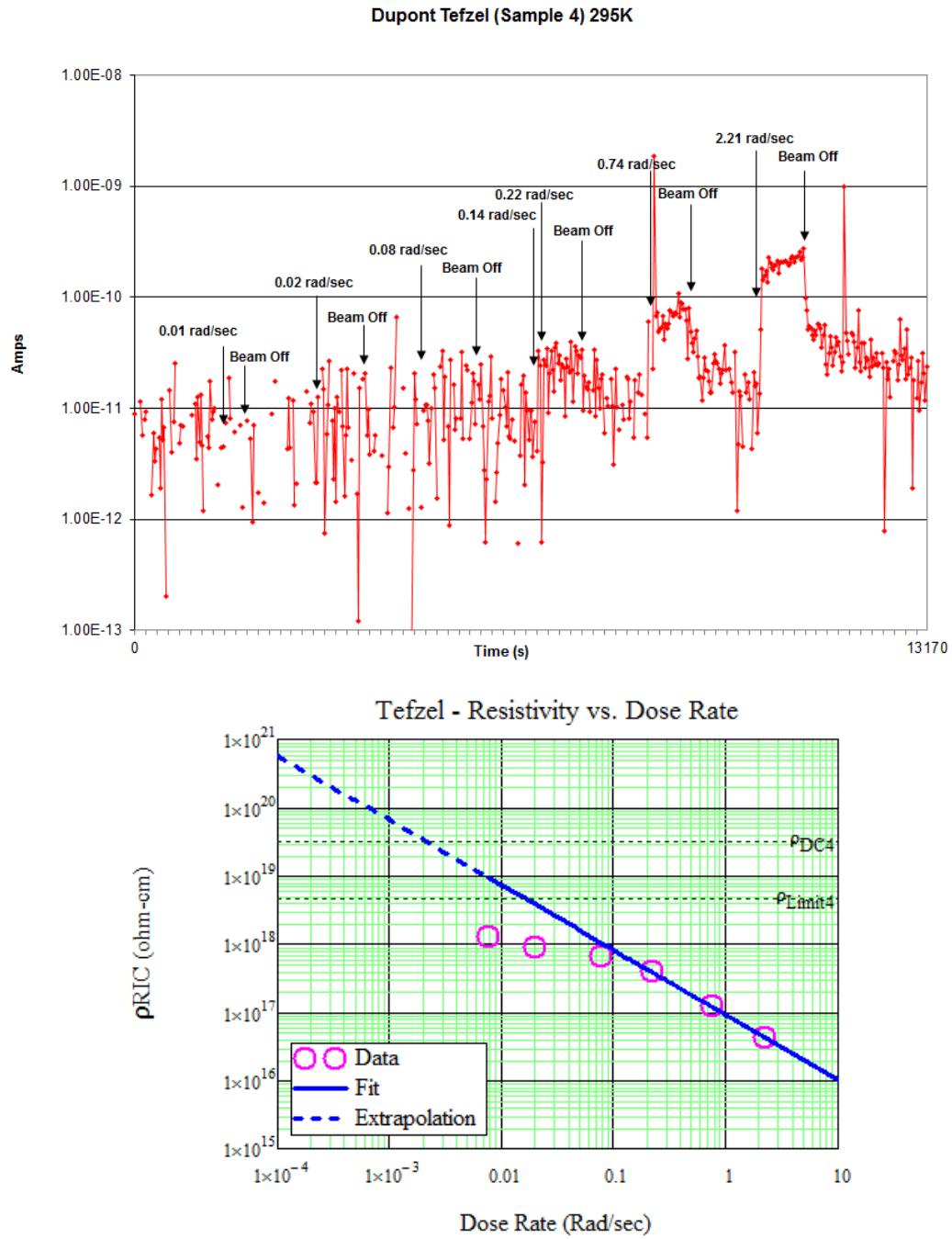
FIG. E.4. Tefzel data taken at 295 K on November 21, 2006. Raw current data (above). Fit to current data (below).

Dupont Tefzel (Sample 6) 295K

Tefzel - Resistivity vs. Dose Rate
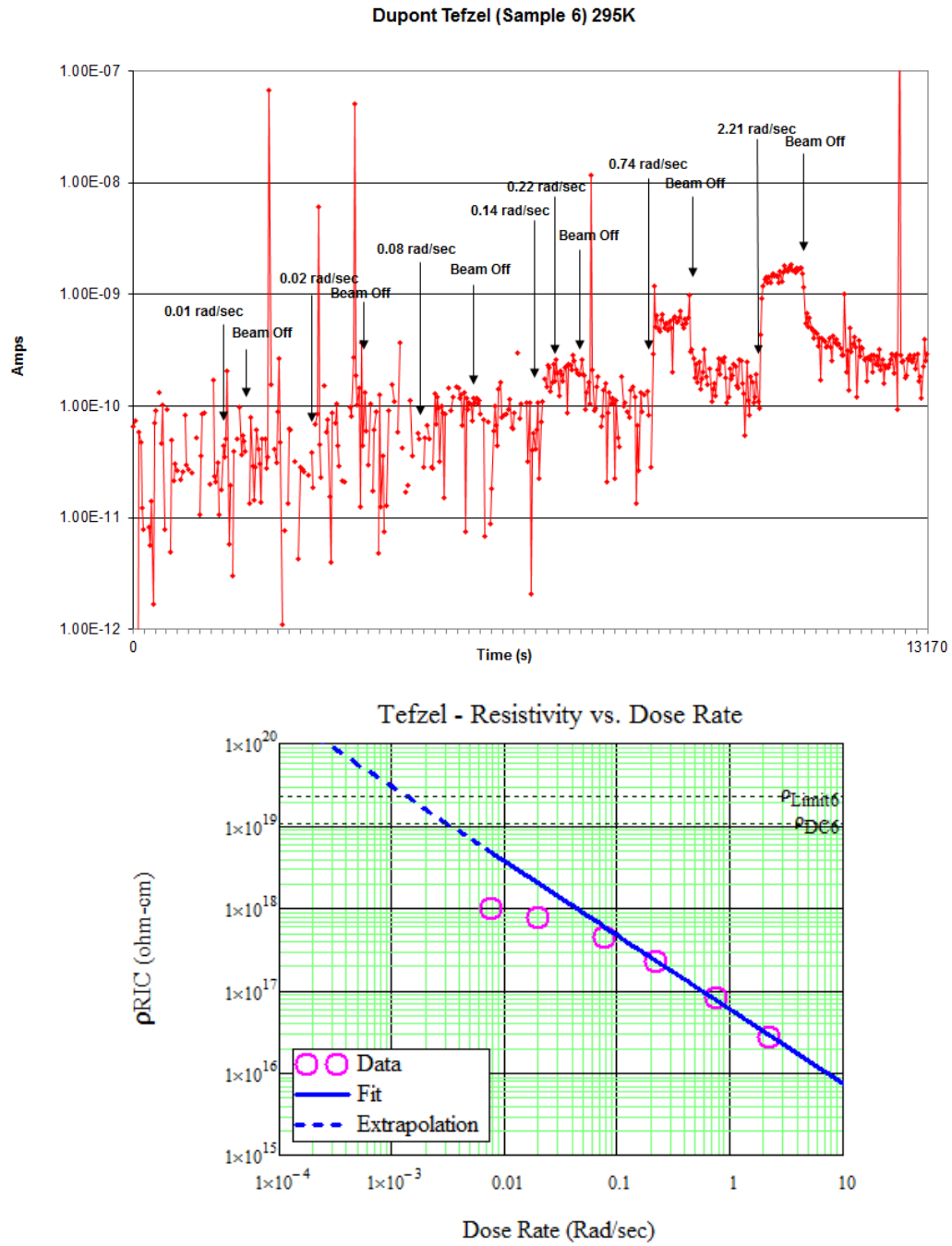
FIG. E.5. Tefzel data taken at 295 K on November 21, 2006. Raw current data (above). Fit to current data (below).

Tefzel (Sample 3) 295K
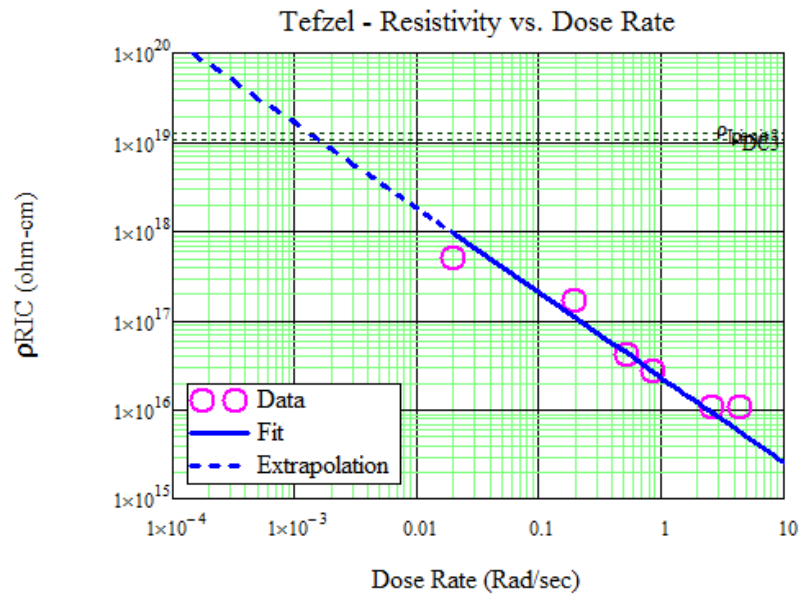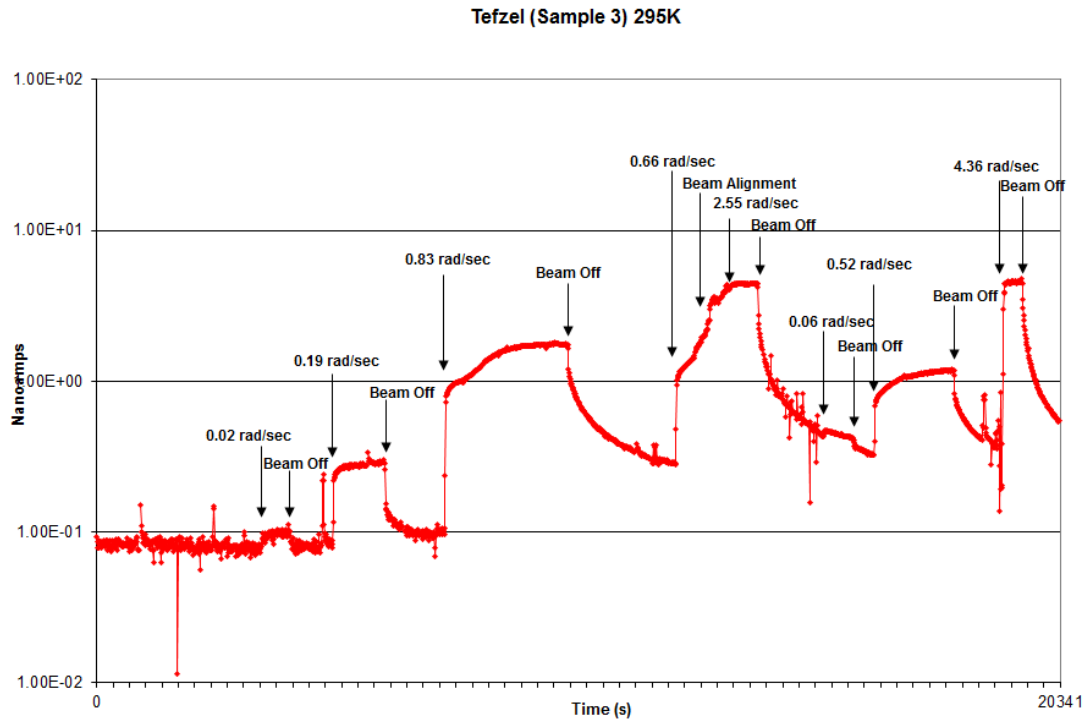
FIG. E.6. Tefzel data taken at 295 K on February 28, 2007. Raw current data (above). Fit to current data (below).
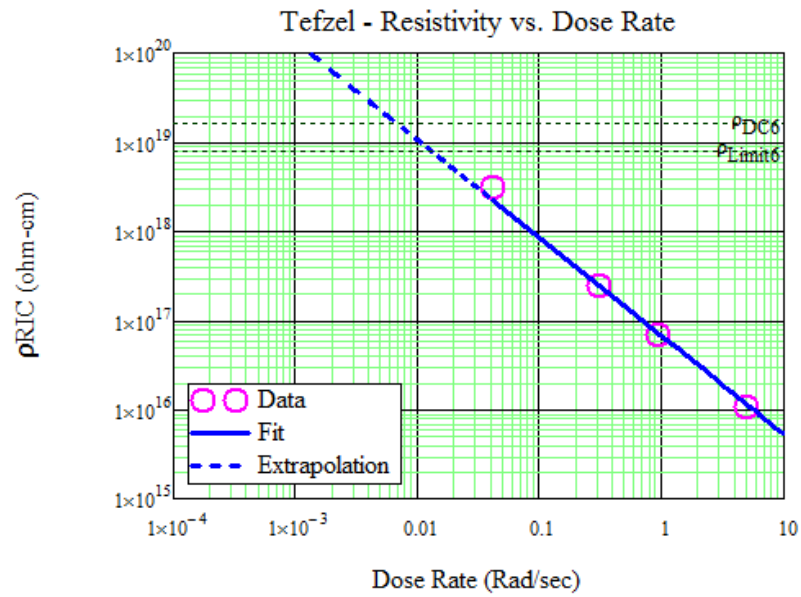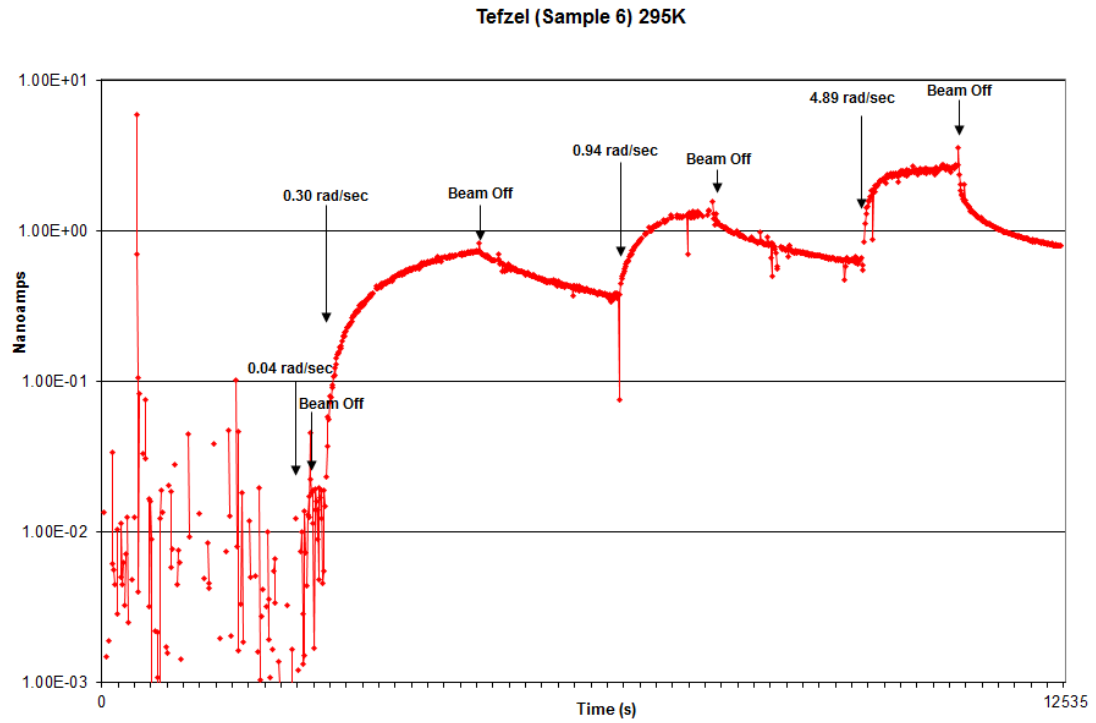
FIG. E.7. Tefzel data taken at 295 K on June 19, 2007. Raw current data (above). Fit to current data (below).
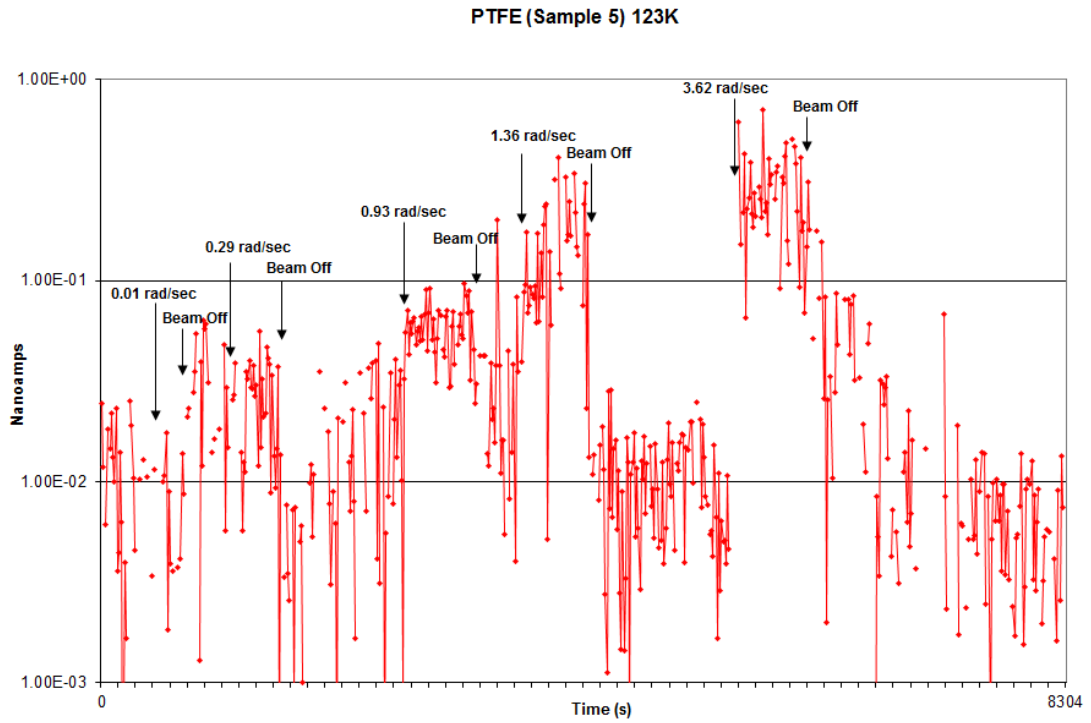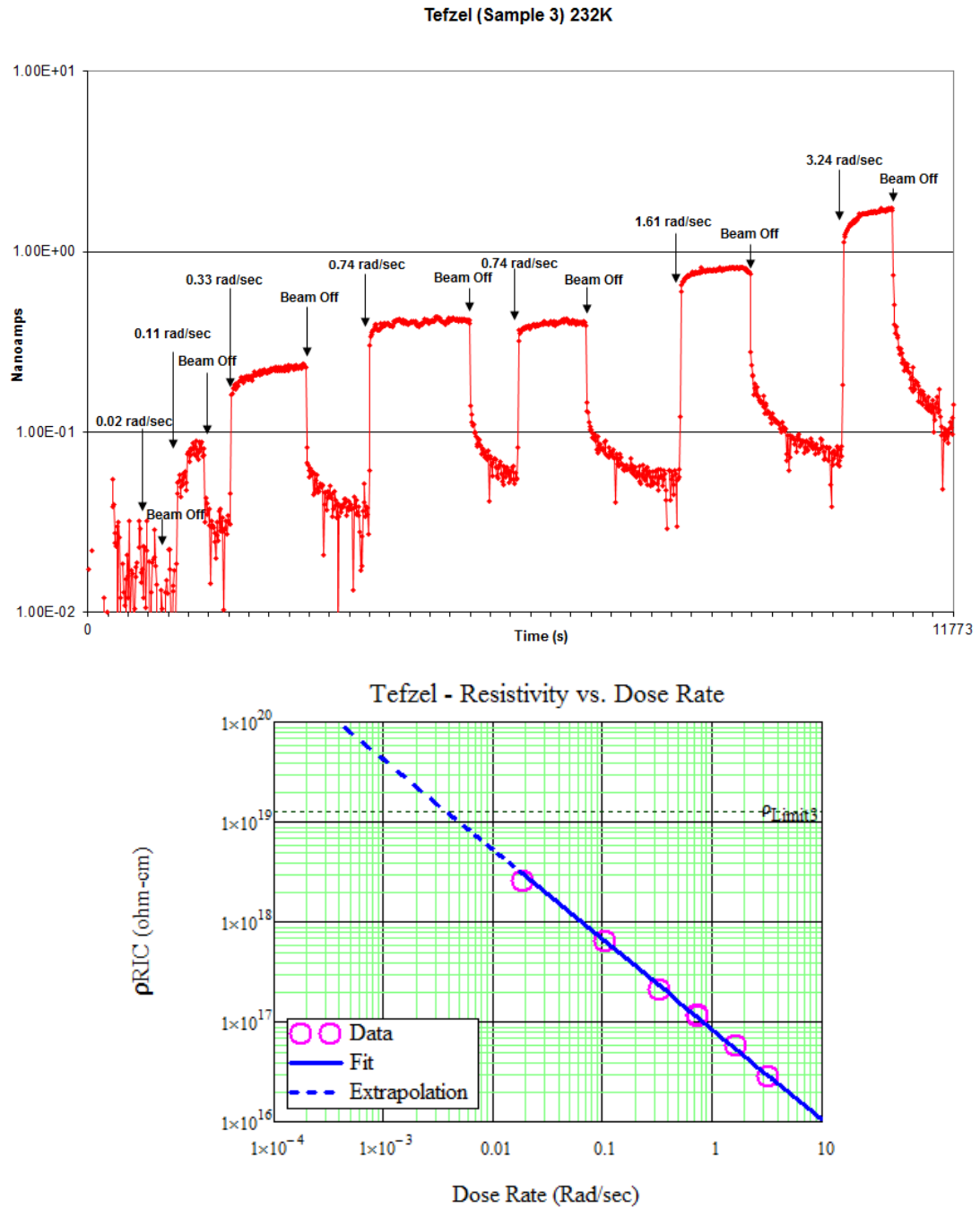
FIG. E.8. Tefzel data taken at 232 K on June 18, 2007. Raw current data (above). Fit to current data (below).
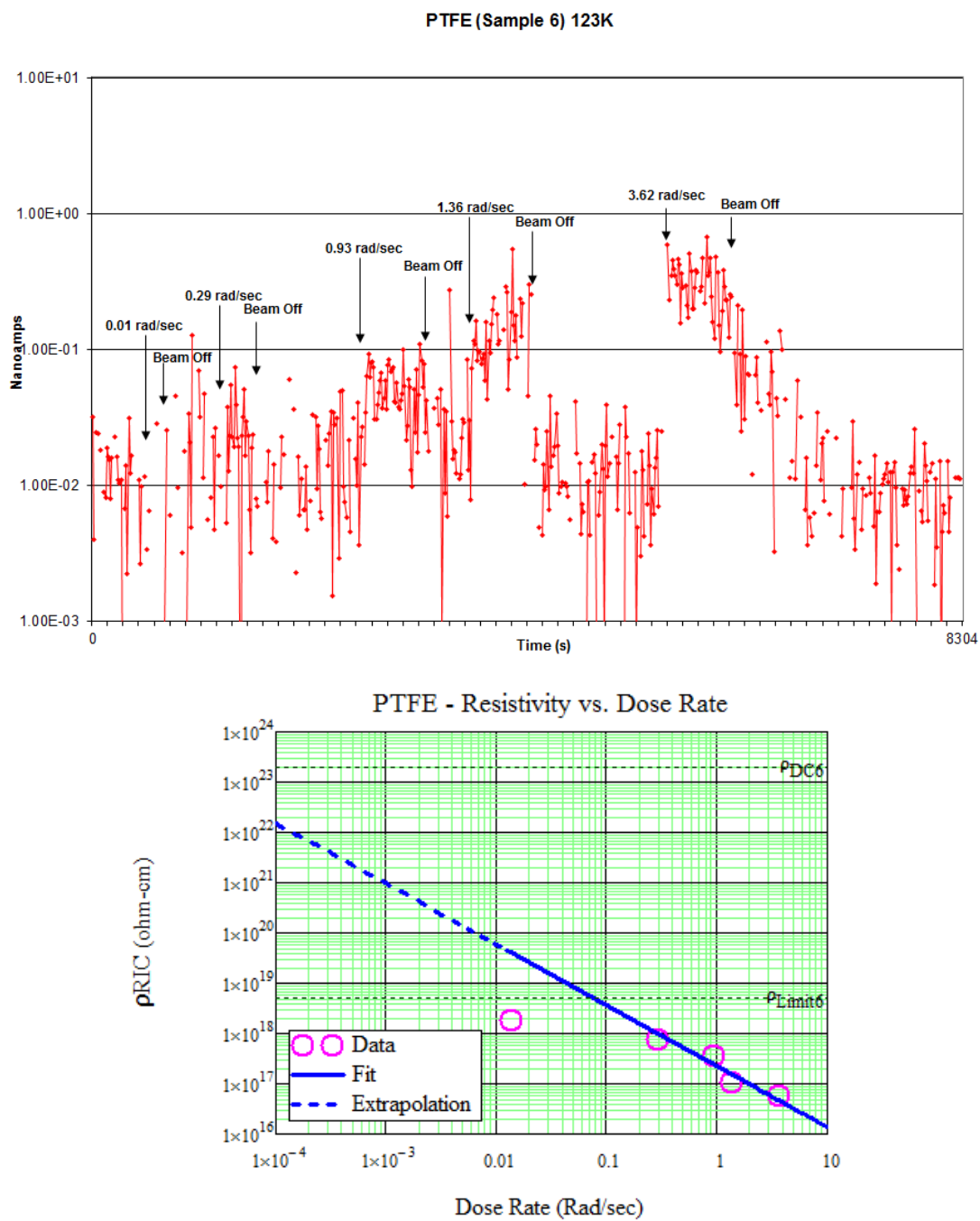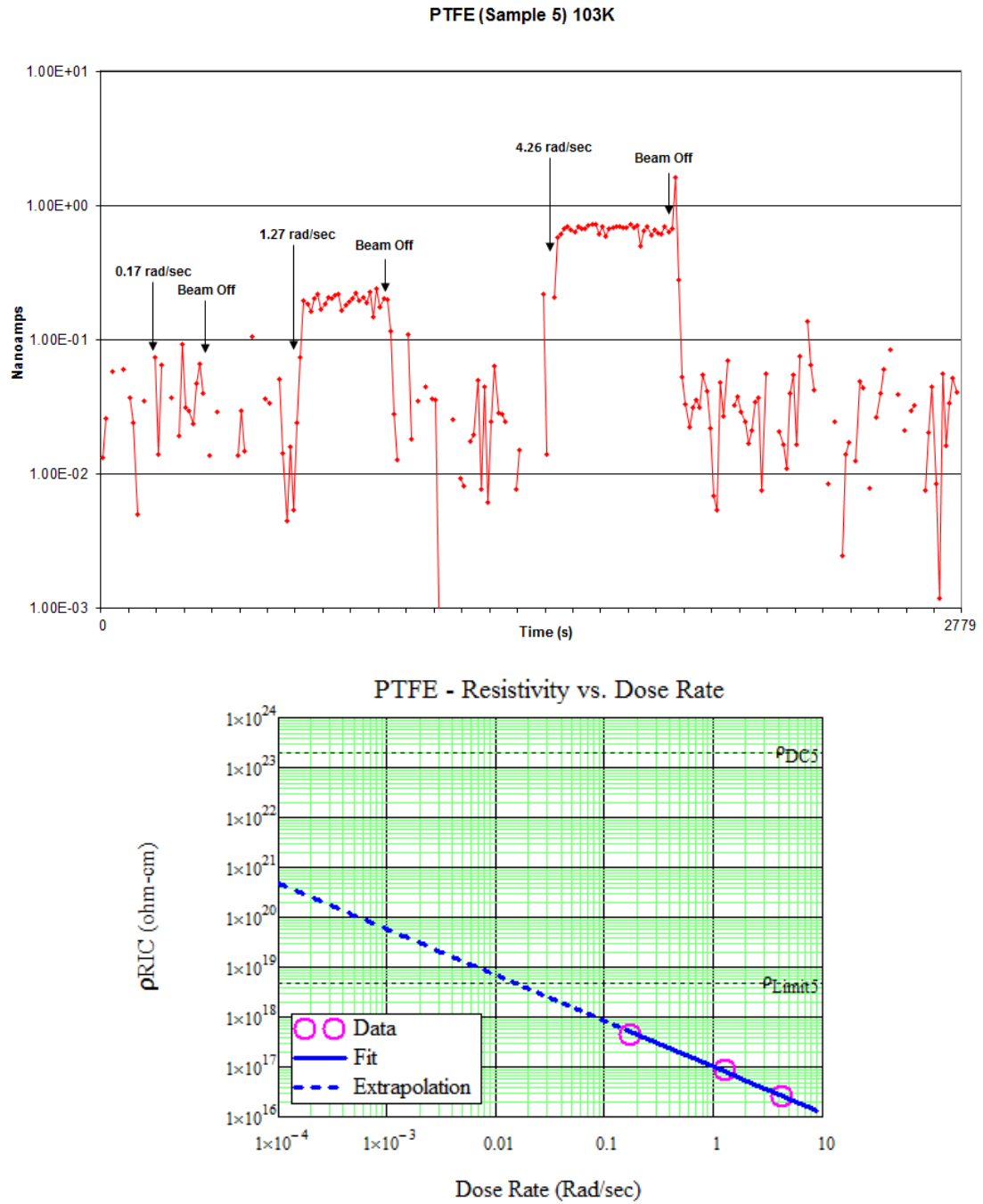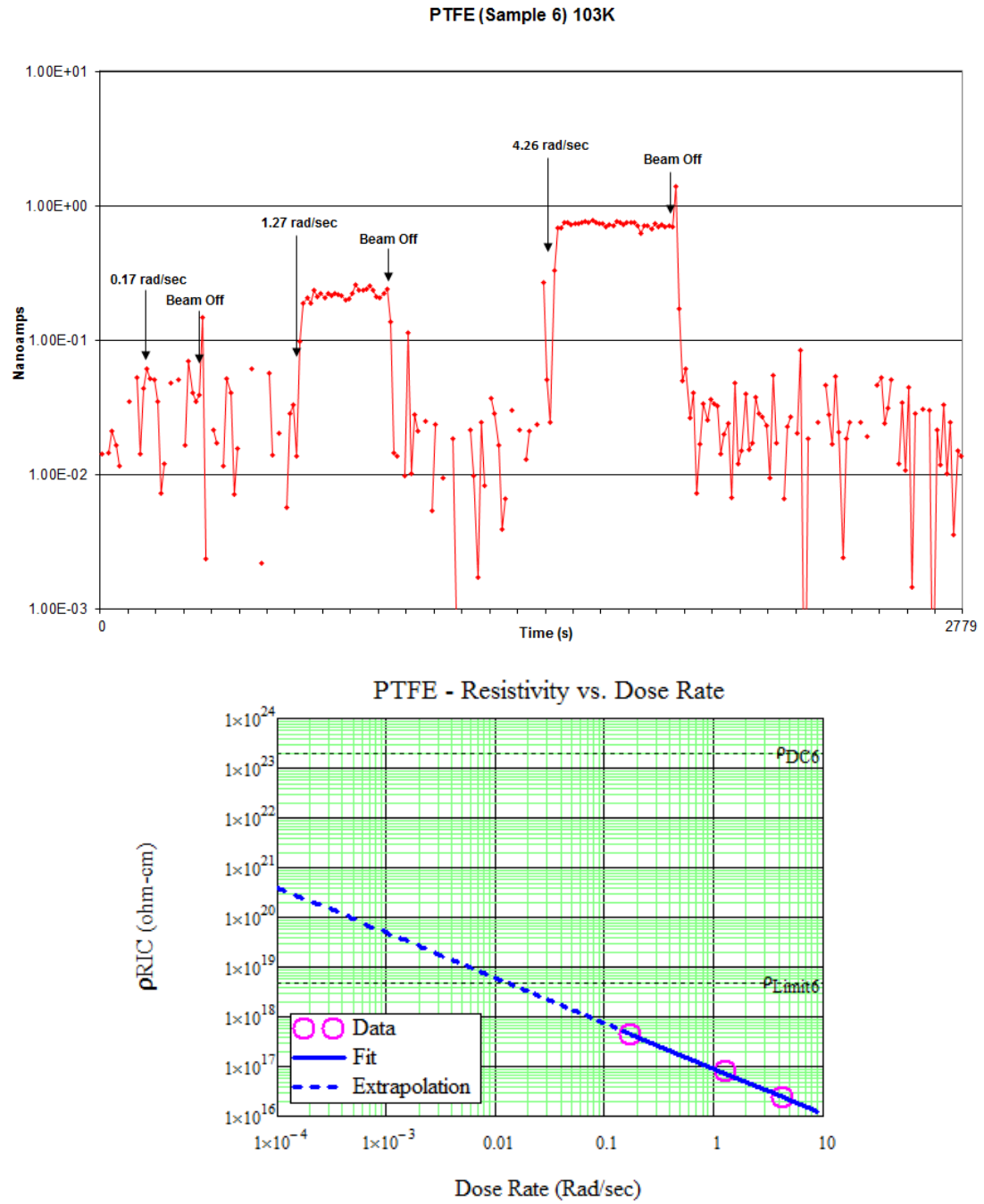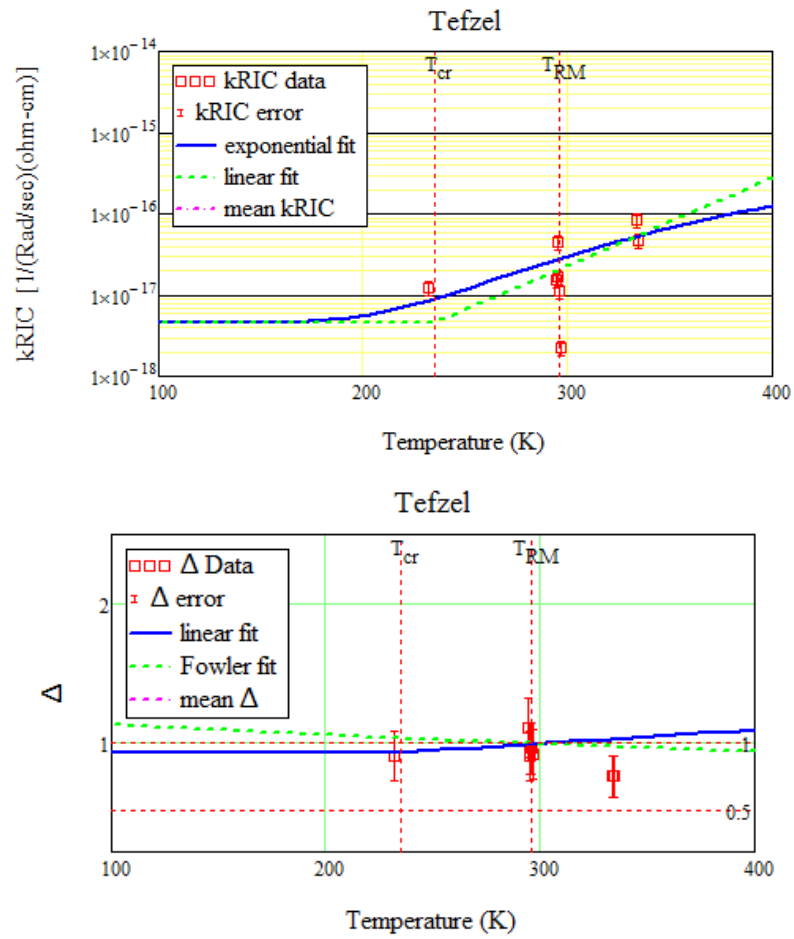
FIG. E.9. Tefzel *k* and *Δ* data and temperature-dependent fits. *k*–value data and temperature-dependent fits (above). *Δ*–value data and temperature-dependent fits (below).
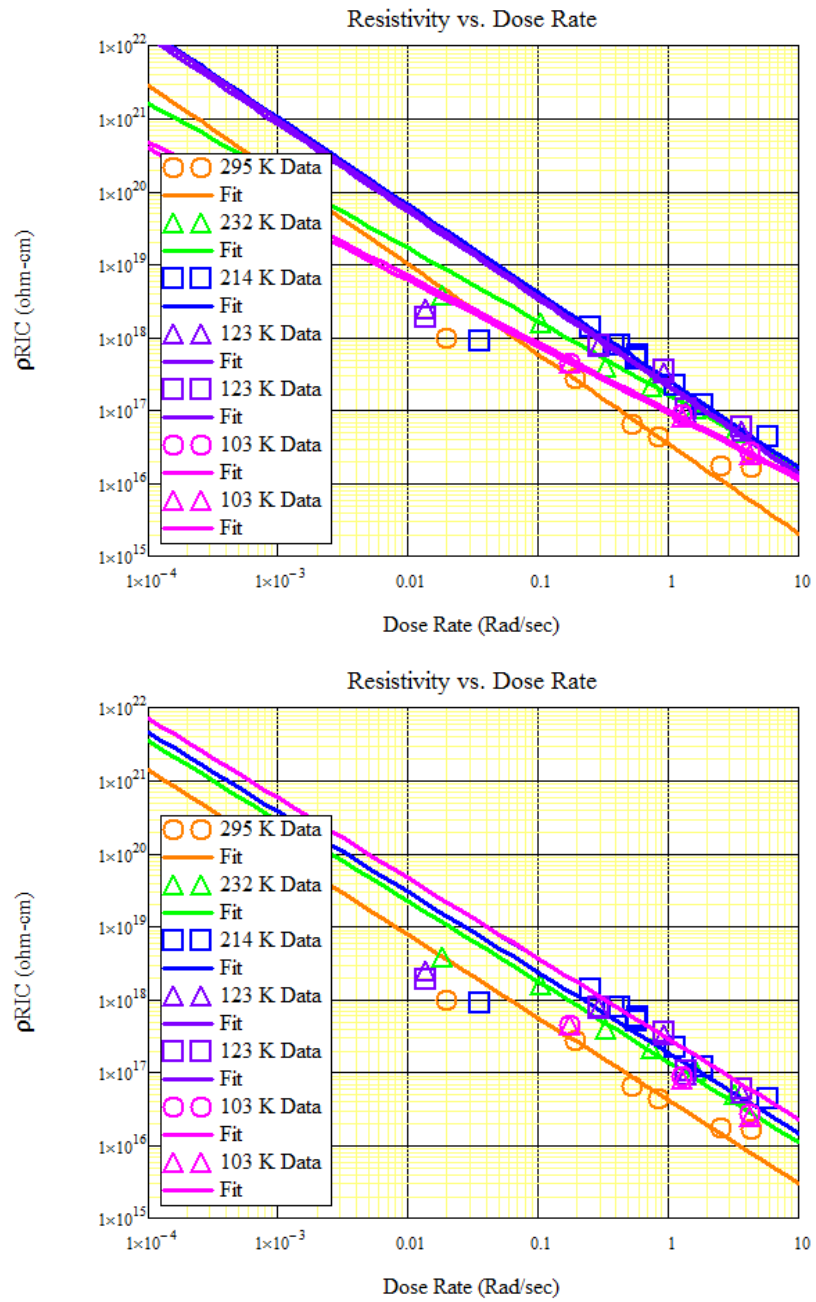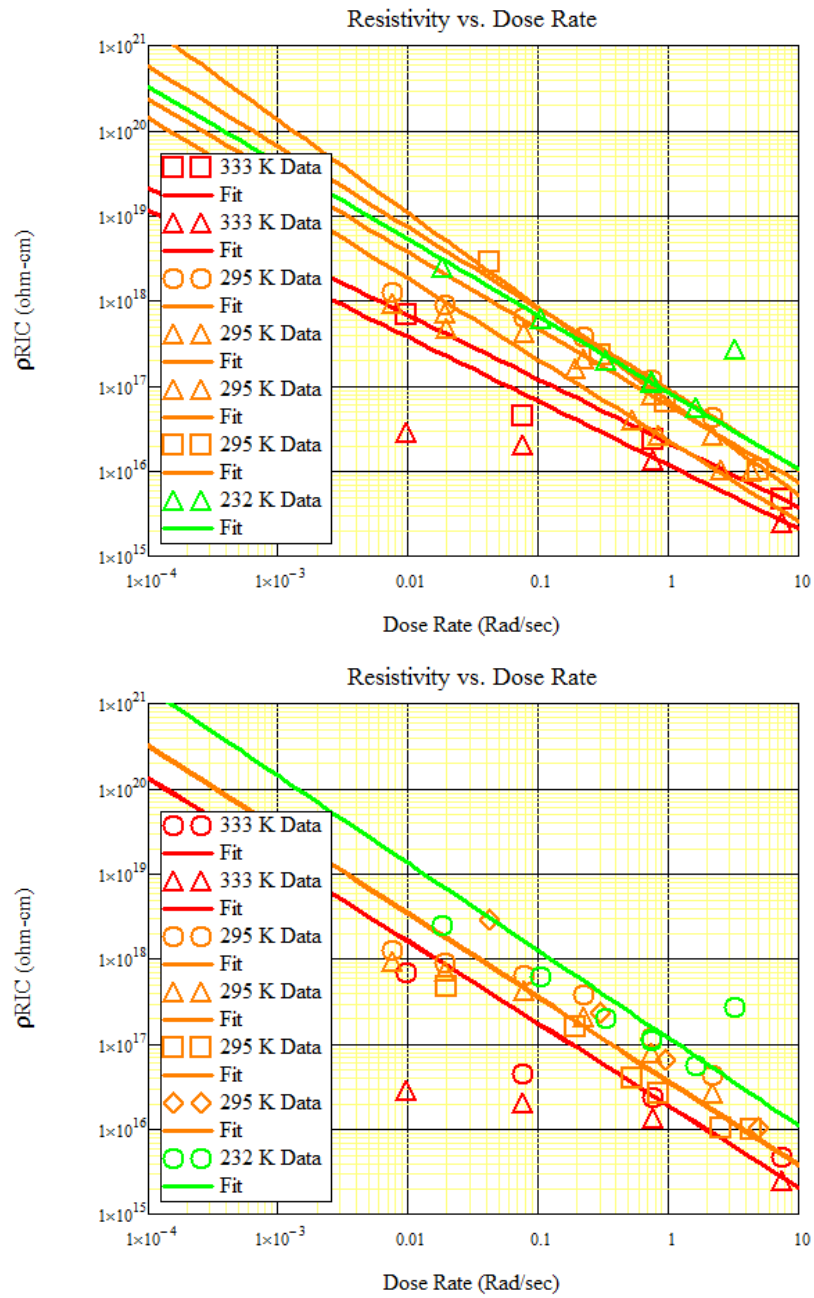
FIG. E.10. RIC Tefzel data and temperature fits. *T*-independent fits to Tefzel data (top). *T*-dependent fits to Tefzel data (bottom).

APPENDIX F

VALIDITY AND REPRODUCIBILITY
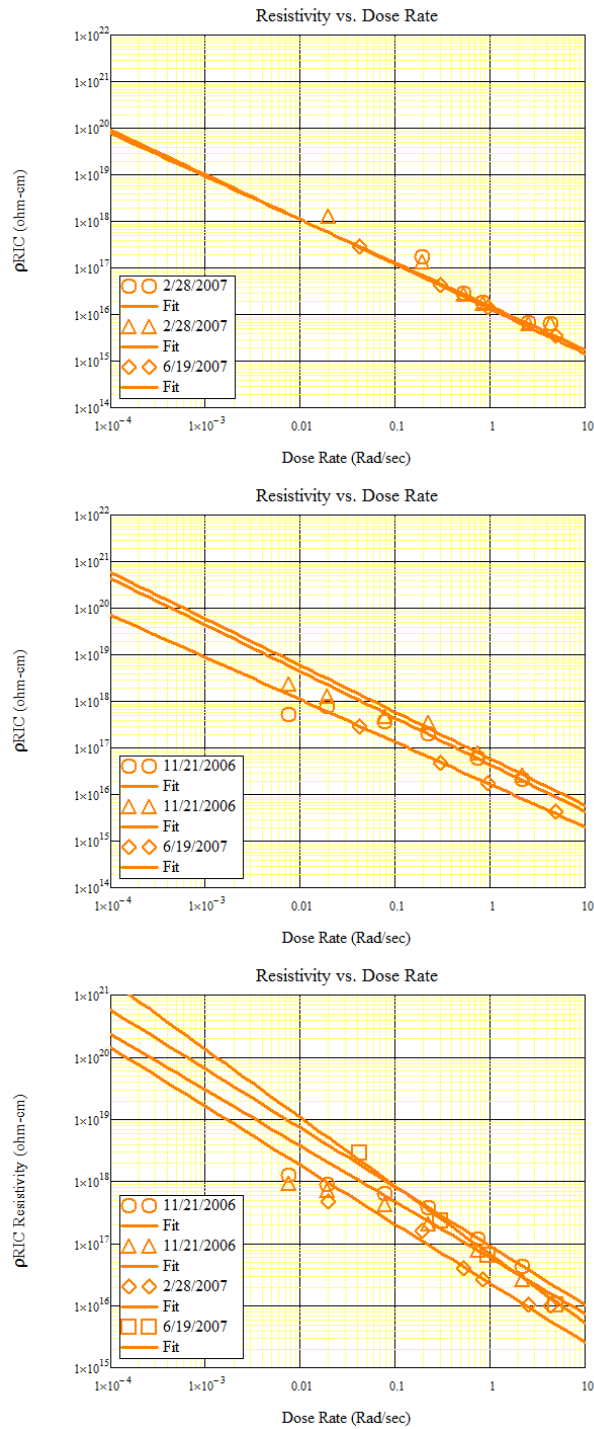
FIG. F.1. Compilation of data taken at 295 K. Kapton E data (top). Kapton HN data (middle). Tefzel data (bottom).
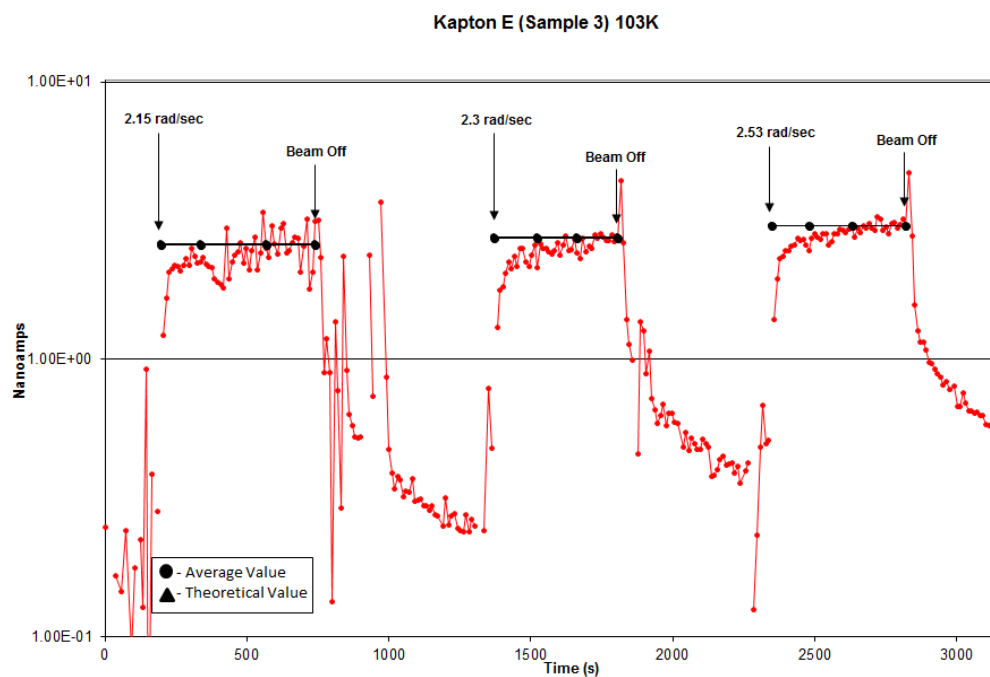
FIG. F.2. Repeat dose rate measurements taken on Kapton E at 103 K. Repeat measurements also varied beam characteristics. The first measurement had a charge per pulse of 86 nC and a repetition rate of 100 Hz. The second measurements had a charge per pulse of 48 nC and a repetition rate of 200 Hz. The last measurement had a charge per pulse of 71 nC and a repetition rate of 150 Hz.
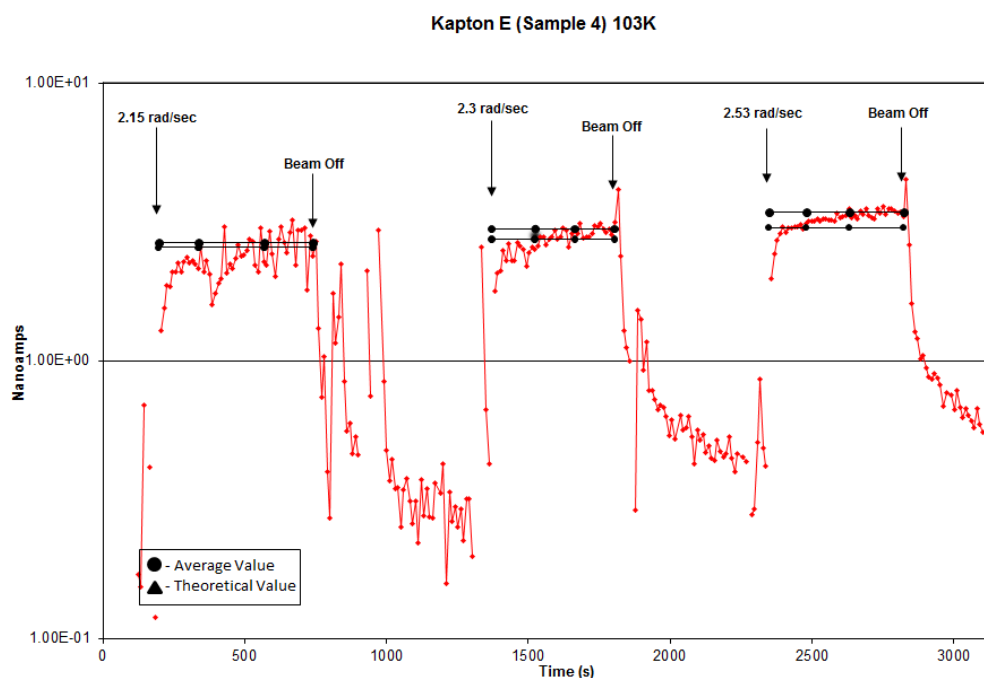
FIG. F.3. Second repeat dose rate measurements taken on Kapton E at 103 K. Repeat measurements also varied beam characteristics. The first measurement had a charge per pulse of 86 nC and a repetition rate of 100 Hz. The second measurements had a charge per pulse of 48 nC and a repetition rate of 200 Hz. The last measurement had a charge per pulse of 71 nC and a repetition rate of 150 Hz.
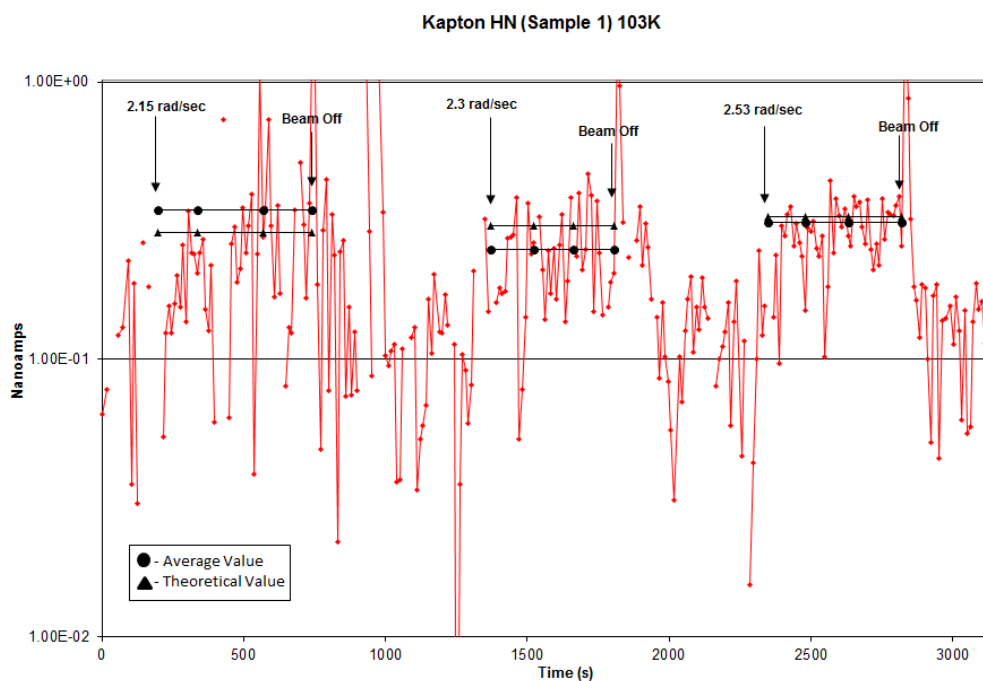
FIG. F.4. Repeat dose rate measurements taken on Kapton HN at 103 K. Repeat measurements also varied beam characteristics. The first measurement had a charge per pulse of 86 nC and a repetition rate of 100 Hz. The second measurements had a charge per pulse of 48 nC and a repetition rate of 200 Hz. The last measurement had a charge per pulse of 71 nC and a repetition rate of 150 Hz.
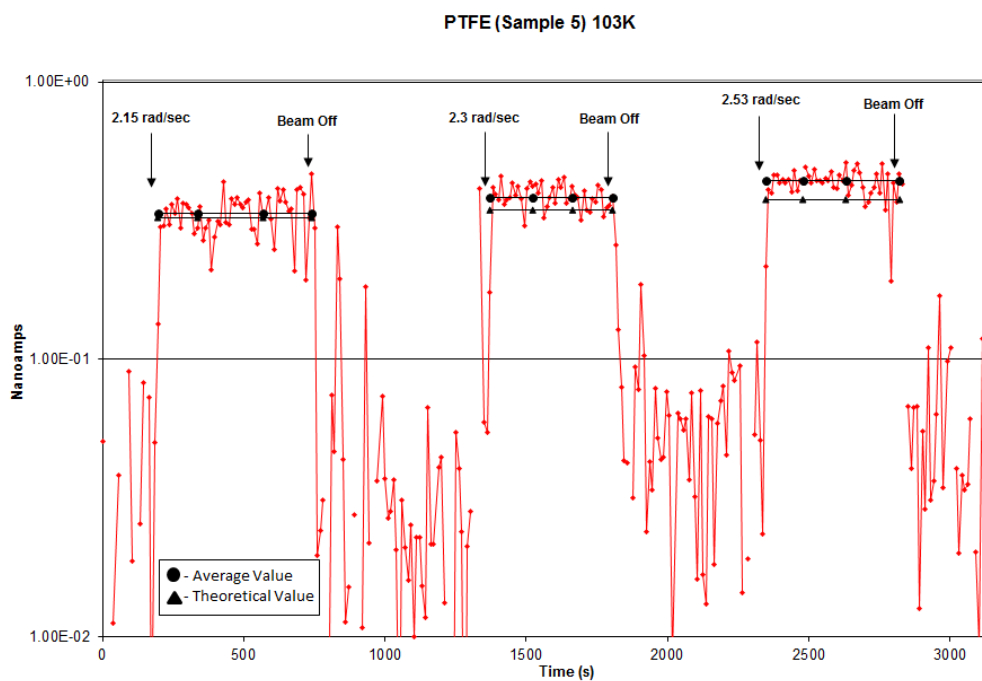
FIG. F.5. Repeat dose rate measurements taken on PTFE at 103 K. Repeat measurements also varied beam characteristics. The first measurement had a charge per pulse of 86 nC and a repetition rate of 100 Hz. The second measurements had a charge per pulse of 48 nC and a repetition rate of 200 Hz. The last measurement had a charge per pulse of 71 nC and a repetition rate of 150 Hz.
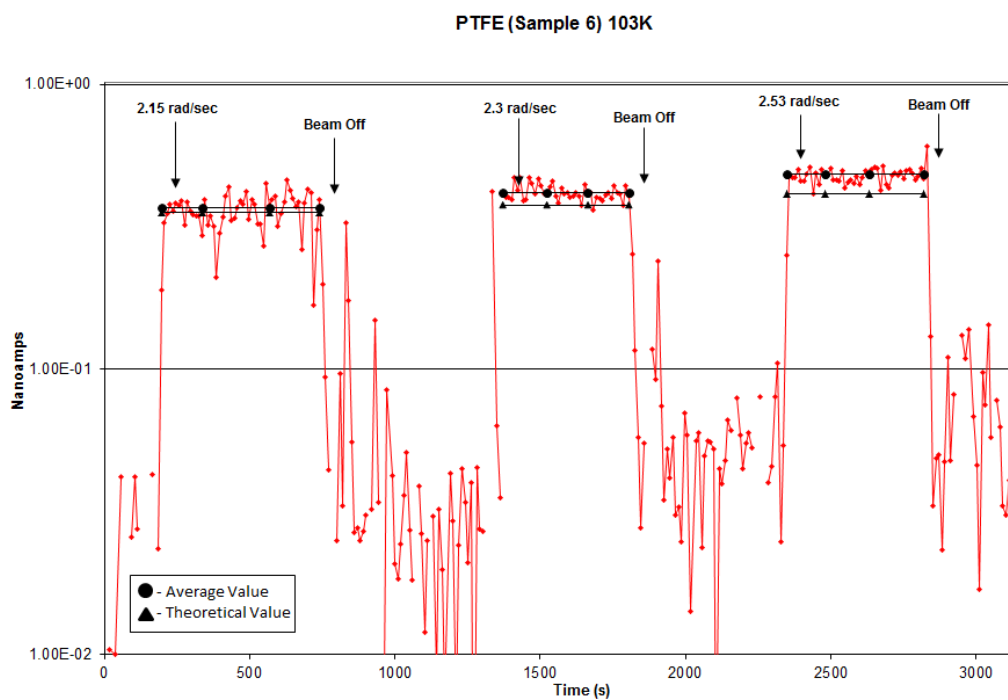
FIG. F.6. Second repeat dose rate measurements taken on PTFE at 103 K. Repeat measurements also varied beam characteristics. The first measurement had a charge per pulse of 86 nC and a repetition rate of 100 Hz. The second measurements had a charge per pulse of 48 nC and a repetition rate of 200 Hz. The last measurement had a charge per pulse of 71 nC and a repetition rate of 150 Hz.

APPENDIX G

RADIATION INDUCED CONDUCTIVITY THEORY

We begin with an analogy to a semiconductor system, with dopant states at a single energy, E_d. As discussed below, we assume a reservoir of trapped electrons pinned to the effective Fermi level, E_F^{eff}; that is, with nearly constant excitation energies such that E_d in the semiconductor system is replaced by E_F^{eff}.

The fundamental equation for conductivity, Eq. (2.0.1), requires expressions for q_i, n_i, and μ_i. As noted above, we restrict our development to electron conduction so $q_i \rightarrow q_e$ and $n_i \rightarrow n_c$. We also need to know the mobility of electron carriers in the conduction band, μ_e, and by extension from Eq. (2.1.1), the mean free lifetime of an electron in the Conduction Band (CB), τ_e. The charge carrier mobility in the free electron model for conductors is given by Eq. (2.1.1). More correctly, we should use the total mobility, where $[\mu_{Tot}]^{-1} = \sum_{all}[\mu_i]^{-1}$, which follows from Matthiessen's rule [see Eqs. (2.1.1) and (2.1.3)]. Here, however, as argued by Rose (1951) for volume-excited photocurrents, we will assume that the mobility is constant and driven only by the free (or nearly free) electron mobility, μ_e.

To some level of approximation, the effective mobility of nearly free electrons in a dielectric medium, μ_e^{NF}, can be found by: (i) replacing the electron mass, m_e, with its effective mass, m_e^*, to model the weak uniform binding potential experienced by electrons traveling in the conduction band, and (ii) including the relative dielectric constant of the material, ε_r, to account for screening or polarization of the trap center charge by the charge background of the medium. That is,

$$\mu_e^{NF} \approx \frac{q_e \tau_e \varepsilon_r^2}{m_e^*} = \left[\frac{q_e \tau_e}{m_e}\right]\left[\frac{m_e}{m_e^*}\varepsilon_r^2\right] = \mu_e\left[\frac{m_e}{m_e^*}\varepsilon_r^2\right] \quad , \tag{G.1}$$

Such an approach is similar to the standard theory for thermally assisted conduction of a bulk homogeneous, semiconducting material with a high density of defect and dopant states that is dominated by extrinsic impurity band conduction for a single donor level energy, E_d (Ashcroft and Mermin, 1976). This theory predicts an Arrhenius behavior using a crude approximation to the donor binding energy, (E_c-E_d),

where the donor state is modeled as a hydrogenic (exciton-like) state in a screened medium of relative dielectric constant, ε_r, with an effective binding energy given as [Ashcroft and Mermin, 1976]

$$\left(E_d - E_c\right) = \frac{m_e^* q_e^4}{8\varepsilon_o^2 \varepsilon_r^2 h^2} = 13.6\,eV \frac{m_e^*}{m_e \varepsilon_r^2} \tag{G.2}$$

Having set q_e and μ_e to fixed values for CB electrons, it is only $n_c(T)$ that controls the conductivity, and the effect of traps is to reduce the fraction of excited carriers that are in the CB. Hence, we develop an expression for the temperature-dependent density of (nearly) free electrons in the CB, $n_c(T)$. Using the usual Boltzmann factor with $C=1$ [see Eq. (2.2.5) and related discussion], $n_c(T)$ is given by

$$n_c(T) = N_c \cdot e^{-E_F^{eff}/k_B T} + n_c^o \quad, \tag{G.3}$$

where N_c is the density of accessible energy states that can be thermally excited into the conduction band (from within a few $k_B T$ of the bottom of the conduction band E_c—in this case, electrons in shallow trap states such that $N_c \approx n_t$); n_c^o is the density of free electrons in the conduction band at $T = 0$—in this case, solely from electrons excited into the conduction band by the incident high energy radiation; T is the absolute temperature; and E_F^{eff} is the excitation energy from the effective Fermi level below the conduction band. For this case, the density of available states has been shown to be (Ashcroft and Mermin, 1976)

$$N_c = 2\left(\frac{m_e k_B T}{2\pi \hbar^2}\right)^{3/2} \left(\frac{m_e^* m_h^*}{m_e m_h}\right)^{3/4} \quad. \tag{G.4}$$

A more advanced treatment replaces the Boltzmann distribution in Eq. (G.3) with the Fermi-Dirac distribution, replacing a Drude-like model with a Sommerfeld-like model.

We employ the same basic assumptions that led to the more general Eq. (2.2.5). We assume that there are no interactions between electrons in trap states, or equivalently that the mean spatial separation of defects is larger than their interaction range. This is the independent electron approximation (Ashcroft and Mermin, 1976). We evoke the free electron (or nearly free electron) approximation (Ashcroft and Mermin,

1976) for electrons moving in the conduction band, whose mobility is solely responsible for RIC. We also assume that in equilibrium, almost all electrons excited from the valence band through electron-hole pair creation by the incident radiation relax into trap states, where they stay for a long time. That is, we assume that the number of trapped electrons must exceed the number of free electrons, such that the density of primary (valence band) positive centers (fixed holes), n_p, is approximately equal to the density of occupied traps, n_t:

$$n_p = n_t + n_c \approx n_t \quad , \tag{G.5}$$

When this assumption is no longer valid, RIC will exhibit saturation effects. If, as assumed, $n_t \gg n_c$, then even at low T, $n_t \gg n_c^o$ and Eq. (G.3) becomes approximately

$$n_c(T) \approx N_c \cdot e^{-E_F^{eff}/k_B T} \quad . \tag{G.6}$$

We can see that the assumption $n_t \gg n_c$ is satisfied for the low temperature limit, where $E_{gap} > E_F^{eff} \gg k_B T > 0$. Eq. (G.6) can be solved for E_F^{eff} to obtain

$$E_F^{eff}(n_c, T) \approx k_B T \cdot ln(N_c/n_c) \quad . \tag{G.7}$$

This restriction for Eq. (G.6) or Eq. (G.7) requires a discussion of the distinction between the Fermi energy, E_F, the Fermi level E_f, and the effective Fermi level, E_F^{eff} [refer to Fig. (G.1) and the discussion and references in Sim (2013) or Rose (1951)]. The Fermi energy denotes the transition energy from filled to empty energy levels at absolute zero. The Fermi level is a weakly temperature-dependent chemical potential at which the occupation of states given by the Fermi-Dirac distribution function, $f_{FD}(E,T)$, equals 50% (Ashcroft and Mermin, 1976). The effective Fermi level includes a spacecharge contribution to the Fermi level or chemical potential. In simple terms, the energy level of the filled trap states at $T = 0$ rises as: (i) additional charge is injected into the material from either an incident beam or an electrode, or (ii) energy from the incident radiation excites electrons from the valence band, into the

conduction band, which quickly relax into the lowest energy shallow trap states available. For small temperature changes,

$$E_F^{eff}(T, n_c) \approx E_{F0}^{eff}(n_c) \cdot (1 - \xi\, k_B T) \quad . \tag{G.8}$$

At finite temperature, as E_F^{eff} moves towards E_C with increased charge stored in trapped states; the excitation energy, E_d, in the general Eq. (2.2.5) is reduced and more electrons can be thermally excited into the conduction band. It is the temperature dependence of the resulting balance of trap charge buildup and thermal depletion of the trapped charge that principally determines the temperature dependence of RIC. [Refer to Sim (2013) for a detailed review of this topic.] For the exponential and uniform density of states (DOS) shown in Fig. G.1, thermal depletion lowers E_F^{eff}; hence, we expect an associated temperature dependence in σ_{RIC}. By contrast, for a delta function DOS, the effective Fermi level is pinned to the single trap energy (i.e., $E_F^{eff} = E_{F0}^{eff} = E_o^t$) irrespective of the number of trapped electron that are thermally excited; hence, we expect no associated temperature dependence in σ_{RIC}.

From the definition of E_F^{eff}, we can calculate the density of filled trap states, n_t, by integrating an expression for the trap state density as a function of energy over all occupied states, that is over all trap states in the distribution $n_t(\varepsilon)$ from E_F^{eff} to the upper bound of the trapped state energies:

$$n_t = \int_0^\infty f_{FD}(E, T)\, n_t(E)\, dE \xrightarrow{\;T \to 0\;} \int_{E_{F0}^{eff}}^\infty n_t(E)\, dE \quad . \tag{G.9}$$

This expression is the only part of the RIC expression that contains information about the material, at least up to a proportionality constant. To proceed further requires a specific expression for $n_t(E)$. We consider here three such distribution functions, as shown in Fig. G.1. Further details of these and other density of state distribution functions are given in the Appendix H. We first consider these DOS at $T = 0$ K, and with respect to the position of E_F^{eff} in comparison to the width of the peaked DOS. We then consider them at finite temperatures.

First, consider an exponential distribution of traps below E_c (see Figs. G.1 and H.1) such that the energy distribution of trap densities below the conduction band, $n_t(E)$, is

$$n_t(E) \rightarrow n_X(E; E_o^X) = N_T \left[\frac{1}{e \cdot E_o^X}\right] \exp\left(\frac{E_o^X - E}{E_o^X}\right) \Theta(E) \quad . \tag{G.10}$$

$\Theta(x)$ is the Heaviside step function. Here $E_o^X \equiv k_B T_o^X$ is equal to the mean energy of all trap states in the band gap or the 1/e width of the distribution. The distribution is normalized such that N_T is the total (occupied and unoccupied) trap state density and $[n_X(E_o^X)/n_X(0)] = 1/e$. With this exponential distribution, the density of filled traps below the steady-state effective Fermi level (at $E_c - E_F^{eff}$) is

$$n_t(T) = \begin{cases} \int_{E_{F0}^{eff}}^{\infty} n_t(E)dE = \int_{E_{F0}^{eff}}^{\infty} N_T \left[\frac{1}{e \cdot E_o^X}\right] \exp\left(\frac{E_o^X - E}{E_o^X}\right) dE = N_T \exp\left(\frac{-E_{F0}^{eff}}{E_o^X}\right) = N_T \exp\left(\frac{-E_{F0}^{eff}}{k_B T_o^X}\right) \\ \qquad ; \quad T \rightarrow 0 \text{ K} \\ \\ \int_{E_F^{eff}}^{\infty} \exp\left(\frac{E_F^{eff} - E}{k_B T}\right) n_t(E)dE \approx \int_{E_F^{eff}}^{\infty} N_T \left[\frac{1}{e \cdot E_o^X}\right] \exp\left(\frac{E - E}{E_o^X}\right) \exp\left(\frac{E_F^{eff} - E}{k_B T}\right) dE \approx N_T \frac{T}{T_o^X} \exp\left(\frac{-E_F^{eff}}{k_B T_o^X}\right) \\ \qquad ; \quad k_B T_o^X \gg E_F^{eff} \gtrsim 2k_B T > 0 \end{cases} .$$

$$\tag{G.11}$$

T_o^X is a physical parameter of the material. It is a temperature higher than room temperature, and physically, could indicate the temperature at which are electrons are "frozen in" traps as the material cools [By `frozen in,` we mean that the material temperature $T \ll T_o^X$ and almost no electrons are not thermally excited into the CB (Rose, 1951).].

We can consider an alternate energy-dependent DOS, as shown in Figs. G.1 and H.1. The more general form of the uniform DOS, referred to as the uniform top hat DOS, has nonzero values for $0 > E_1^U > E > E_2^U$ and width $E_o^U = E_2^U - E_1^U \equiv 2\,k_b T_o^U > 0$, filled at $T = 0$ K from E_F^{eff} to E_o^U:

$$n_t(E) \rightarrow n_{UT}(E; E_1^U, E_2^U) = N_T \left[\frac{1}{E_2^U - E_1^U}\right] \Theta(E_2^U - E)\, \Theta(E - E_1^U) \quad . \tag{G.12}$$

The uniform step DOS has a uniform distribution of traps from E_c down to $E_o^U \equiv 2k_B T_o^U$ (i.e., with $E_1^U \rightarrow 0$):

$$n_t(E) \rightarrow n_{US}\left(E; E_o^U\right) = N_T \left[\frac{1}{E_o^U}\right] \Theta\left(E_o^U - E\right) \Theta(E) \quad . \tag{G.13}$$
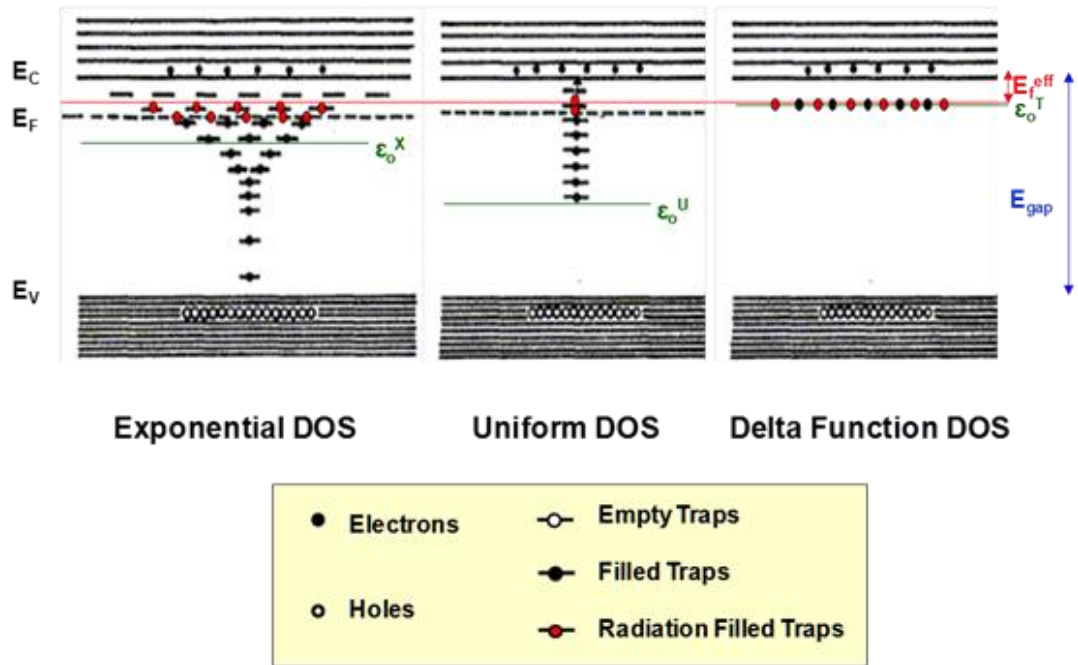
FIG. G.1. Occupation of density of states (DOS) models for HDIM. The graphs show schematically the DOS for extended conduction and valence band states and for localized trap states for exponential, uniform and delta function DOS models. The vertical axis is energy as measured below the conduction band edge. Energies shown include: the conduction band mobility edge, E_C; the valence band mobility edge, E_V; the Fermi energy, E_F; the effective Fermi level, E_F^{eff}; and the band gap energy, $E_{gap}=E_V-E_C$. Also shown are the characteristic widths of the exponential (E_o^X) and uniform (E_o^U) DOS models, as well as the peak of the delta function model at E_o^t. Empty, initially filled and radiation filled traps are denoted as shown in the legend.

Here the mean energy of all trap states in the band gap is $\frac{1}{2} E_o^U = \frac{1}{2} (E_2^U - E_1^U) \equiv k_B T_o^U$. Again, the distribution is normalized such that N_T is the total (occupied and unoccupied) trap state density. With this uniform distribution, the density of filled traps below the steady-state effective Fermi level (at $E_c - E_F^{eff}$) at $T = 0$ K is

$$n_t = \int_{E_F^{eff}}^{\infty} n_t(E)dE =$$

$$\begin{cases} \int_{E}^{E_2^U} N_T \left[\frac{1}{E_o^U}\right] dE = N_T & ; & E_F^{eff} \gg k_B T \geq 0 \text{ and} \\ & & 0 < E_F^{eff} < E_1^U < E_2^U \\ \int_{E_F^{eff}}^{E_2^U} N_T \left[\frac{1}{E_o^U}\right] dE = N_T \left[\frac{\left(E_2^U - E_F^{eff}(T)\right)}{\left(E_2^U - E_1^U\right)}\right] = N_T \left(\frac{\left(E_2^U - E_F^{eff}(T)\right)}{2\,k_B T_o^U}\right) & ; & \left(E_F^{eff} - E_1^U\right) \gg k_B T \geq 0 \text{ and} \\ & & 0 \leq E_1^U < E_F^{eff} < E_2^U \\ \int_{E_F^{eff}}^{\infty} n_t(E)dE = 0 & ; & \left(E_F^{eff} - E_2^U\right) \gg k_B T \geq 0 \text{ and} \\ & & 0 \leq E_1^U < E_2^U < E_F^{eff} \end{cases}$$

.

$$(G.14)$$

For the uniform and delta function (see below) DOS, we have explicitly considered the position of E_F^{eff} relative to the bounds of the distributions. Rose (1951) considered a uniform top hat trap distribution with constant DOS where E_F^{eff} lies in a void above the trap distribution (i.e., $0 < E_F^{eff} < E_1^U$). He found that n_t was a constant, as we find here and for the delta function DOS below. This makes sense, as we would expect that all peaked DOS with a filled trap state below E_F^{eff} would behave similarly, independent of the shape of the DOS, as long as the separation between E_F^{eff} and the edge of the distribution was much large than $k_B T$ so that negligible carriers were excite across the gap. Rose (1951) also considered the constant DOS where E_F^{eff} lies within the uniform DOS (i.e., $0 \leq E_1^U < E_F^{eff} < E_2^U$; he concluded that this led to a temperature-independent expression for n_t, as is found here. If E_F^{eff} lies well below the uniform DOS (i.e., $0 \leq E_1^U < E_2^U < E_F^{eff}$), then the occupancy goes to zero. These three cases are valid when electrons are "frozen in" traps at $T \ll T_o^U$.

We have also considered a fourth case for the uniform DOS at finite $T > 0$, where E_F^{eff} is just a few times $k_B T$ below the lower bound of a distribution, E_2^U. In this case, some electrons are excited from states near E_F^{eff} into the uniform DOS near (within $\sim k_B T$ of E_2^U), with the fraction of occupied states given by a Maxwell-Boltzmann distribution. For small temperature changes $E_F^{eff}(T) \approx E_{F0}^{eff}(1 - \xi k_B T)$, and if $\left(E_{F0}^{eff} - E_2^U\right) \gg E_{F0}^{eff} \xi k_B T$ then the exponential term is $\approx exp\left[-\frac{\left(E_{F0}^{eff} - E_2^U\right)}{k_B T}\right]$.

$$n_t = \int_{E_F^{eff}}^{\infty} n_t(E) dE =$$

$$\int_{E_2^U - k_B T}^{E_2^U} n_t(E) dE = \int_{E_2^U - k_B T}^{E_2^U} exp\left[-\frac{\left(E_{F0}^{eff} - E_2^U\right)}{k_B T}\right] N_T \left[\frac{1}{E_o^U}\right] dE \approx N_T \, exp\left[-\frac{\left(E_{F0}^{eff} - E_2^U\right)}{k_B T}\right] \left[\frac{k_B T}{(E_2^U - E_1^U)}\right] \quad . \quad (G.15)$$

An example of this case is when E_F^{eff} is pinned to a peaked distribution somewhat below the uniform distribution with the peaked DOS width significantly less than the separation between the peaked DOS and the shallow trap distribution. This is a DOS model used to model the temperature-dependent luminescence (Dennison and Sim, 2012) and RIC (Hoffmann *et al.*, 2013) of fused silica. The results are similar to conclusions drawn by Rose (1951).

Finally, consider a delta function distribution of traps centered at a single trap energy, $E_o^t \equiv k_B T_o^t$ $\geq E_F^{eff}$:

$$n_t(E) \rightarrow n_D(E; E_o^t) = N_T \; \delta(E_o^t - E) \quad . \tag{G.16}$$

Again, the distribution is normalized such that N_t is the total (occupied and unoccupied) trap state density. With this delta function distribution, the density of filled traps below the steady-state effective Fermi level at $T = 0$ K is

$$n_t = \int_{E_F^{eff}}^{\infty} n_t(E) dE \rightarrow \int_{E_F^{eff}}^{\infty} N_T \, \delta(E_o^t - E) \, dE = \begin{cases} N_T & ; & \left(E_F^{eff} - E_o^t\right) < 0 \\ 0 & ; & \left(E_F^{eff} - E_o^t\right) \gg k_B T > 0 \end{cases} \tag{G.17}$$

In the steady-state condition, the rate of excitation of valence band (VB) electrons into the CB by radiation equals the rate of recombination of conduction electrons with primary centers (VB holes), that is,

$$v_{eh} = v_{he} = 1/\tau_e = v_T s_c n_c n_p \quad . \tag{G.18}$$

Here v_T is the thermal velocity of electrons, s_c is the capture cross section of primary centers for free electrons, and v_{eh} is the rate of radiation (or optical) excitations of electrons per unit volume per unit time given by Eq. (2.2.3). We can find expressions for v_T, by setting the thermal energy of a free electron equal to its kinetic energy:

$$\frac{3}{2}k_B T = \frac{1}{2}m_e v_T^{\,2} \quad .$$

$$(G.19)$$

Solving for v_T, yields

$$v_T = \sqrt{\frac{3k_B T}{m_e}} \approx 10^7 \sqrt{\frac{T}{300}} \quad .$$

$$(G.20)$$

For the nearly free electron case for shallow trap states, $m_e \to m_e^*$. Solving Eq. (G.15) for n_c, we find

$$n_c = \frac{v_{eh}}{v_T s_C n_p} \approx \frac{v_{eh}}{v_T s_C n_t} = \frac{v_{eh}}{v_T s_C}\left[\int_{E_F^{eff}}^{\infty} n_t(E)dE\right]^{-1} = \frac{\dot{D}\,p}{s_C E_{eh}\sqrt{3k_B T/m_e}}\left[\int_{E_F^{eff}}^{\infty} n_t(E)dE\right]^{-1} \quad ,$$

$$(G.21)$$

where we have made substitutions for v_{eh} and v_T using Eqs. (2.2.3) and (G.19), respectively. From Eq. (G.5), n_p is approximately equal to n_t, which in turn is expressed as an integral using Eq. (G.9). Inserting the expressions for the total number of occupied trap states for the different DOS models [Eqs. (G.11), (G.14), (G.15) and (G.17)], we have

$$n_c = \frac{\dot{D}\,p}{s_C E_{eh}\sqrt{3k_B T/m_e}}\left[\int_{E_F^{eff}}^{\infty} n_t(E)dE\right]^{-1} = \frac{\dot{D}\,p\,N_T}{s_C E_{eh}\sqrt{3k_B T/m_e}}$$

$$\times \begin{cases} \exp\left(-\dfrac{E_F^{eff}}{k_B T_o^X}\right) & ; & \text{exponential DOS with } T \to 0 \text{ K} \\[2ex] \dfrac{T}{T_o^X}\exp\left(\dfrac{-E_F^{eff}}{k_B T_o^X}\right) & ; & \text{exponential DOS with } k_B T_o^X \gg E_F^{eff} \gtrsim 2k_B T > 0 \\[2ex] 1 & ; & \begin{array}{c}\text{uniform DOS with}\\ E_F^{eff} \gg k_B T \text{ and } 0 < E_F^{eff} < E_1^U < E_2^U \end{array} \\[2ex] \left(\dfrac{\left(E_2^U - E_F^{eff}(T)\right)}{2\,k_B T_o^U}\right) & ; & \begin{array}{c}\text{uniform DOS with}\\ \left(E_F^{eff} - E_1^U\right) \gg k_B T \text{ and } 0 \le E_1^U < E_F^{eff} < E_2^U \end{array} \\[2ex] 0 & ; & \begin{array}{c}\text{uniform DOS with}\\ \left(E_F^{eff} - E_2^U\right) \gg k_B T > 0 \text{ and } 0 \le E_1^U < E_2^U < E_F^{eff} \end{array} \\[2ex] \exp\left[-\dfrac{\left(E_{F0}^{eff} - E_2^U\right)}{k_B T}\right]\left[\dfrac{k_B T}{\left(E_2^U - E_1^U\right)}\right] & ; & \begin{array}{c}\text{uniform DOS with}\\ \left(E_F^{eff} - E_2^U\right) \gtrsim 2\,k_B T > 0 \text{ and } 0 \le E_1^U < E_2^U < E_F^{eff} \end{array} \\[2ex] 1 & ; & \text{delta function DOS with } \left(E_F^{eff} - E_o^t\right) < 0 \\[2ex] 0 & ; & \text{delta function DOS with } \left(E_F^{eff} - E_o^t\right) \gg k_B T > 0 \end{cases} \quad .$$

$$(G.22)$$

We can eliminate $E_F^{eff}(T)$ from these expressions in favor of $n_c(T)$ and T using Eq. (G.7) in the forms

$$\frac{E_F^{eff}}{k_B T_o^A} \approx \frac{T}{T_o^A} \cdot ln(N_c/n_c) \tag{G.23}$$

or

$$exp\left[\frac{E_F^{eff}}{k_B T_o^X}\right] \approx exp\left[\left(\frac{T}{T_o^X}\right)ln(N_c/n_c)\right] = exp\left[ln(N_c/n_c)^{\left(T/T_o^X\right)}\right] = \left(\frac{N_c}{n_c}\right)^{\left(T/T_o^X\right)} . \tag{G.24}$$

This yields

$$n_c = \frac{\dot{D}\,p}{s_C E_{eh}\sqrt{3k_B T/m_e}}\left[\int_{E_F^{eff}}^{\infty} n_t(E)dE\right]^{-1} = \frac{\dot{D}\,p\,N_T}{s_C E_{eh}\sqrt{3k_B T/m_e}} \times$$

$$\begin{cases} \left(\frac{N_c}{n_c}\right)^{T/T_o^X} & ; & \text{exponential DOS with } T \to 0 \text{ K} \\[2mm] \left(\frac{T}{T_o^X}\right)\left(\frac{N_c}{n_c}\right)^{T/T_o^X} & ; & \text{exponential DOS with } k_B T_o^X \gg E_F^{eff} \gtrsim 2k_B T > 0 \\[2mm] 1 & ; & \begin{array}{c}\text{uniform DOS with}\\ E_F^{eff} \gg k_B T \text{ and } 0 < E_F^{eff} < E_1^U < E_2^U\end{array} \\[2mm] \left(\frac{E_2^U}{2\,k_B T_o^U}\right)\left\{1 - \left(\frac{2\,k_B T}{E_2^U}\right)ln\left[\left(\frac{N_c}{n_c}\right)^{\frac{1}{2}}\right]\right\} & ; & \begin{array}{c}\text{uniform DOS with}\\ \left(E_F^{eff} - E_1^U\right) \gg k_B T \text{ and } 0 \le E_1^U < E_F^{eff} < E_2^U\end{array} \\[2mm] 0 & ; & \begin{array}{c}\text{uniform DOS with}\\ \left(E_F^{eff} - E_2^U\right) \gg k_B T > 0 \text{ and } 0 \le E_1^U < E_2^U < E_F^{eff}\end{array} \\[2mm] \left[\frac{k_B T}{\left(E_2^U - E_1^U\right)}\right]exp\left[-\frac{E_2^U}{k_B T}\right]\left(\frac{N_c}{n_c}\right) & ; & \begin{array}{c}\text{uniform DOS with}\\ \left(E_F^{eff} - E_2^U\right) \gtrsim 2\,k_B T > 0 \text{ and } 0 \le E_1^U < E_2^U < E_F^{eff}\end{array} \\[2mm] 1 & ; & \text{delta function DOS with } \left(E_F^{eff} - E_o^t\right) < 0 \\[2mm] 0 & ; & \text{delta function DOS with } \left(E_F^{eff} - E_o^t\right) \gg k_B T > 0 \end{cases}$$

$$\tag{G.25}$$

Solving for n_c yields

$$
n_c(T) = \begin{cases}
\left[\dfrac{p\,N_T}{s_C E_{eh}\sqrt{3k_B T/m_e}}\right]^{\left(\frac{T_o^X}{T+T_o^X}\right)} [\mathrm{N_c}]^{\left(\frac{\mathrm{T}}{T+T_o^X}\right)} [\dot{D}]^{\left(\frac{T_o^X}{T+T_o^X}\right)} & ;\ \text{exponential DOS with } T\to 0\ \text{K} \\[3ex]

\left\{\dfrac{T}{T_o^X}\right\}\left[\dfrac{p\,N_T}{s_C E_{eh}\sqrt{3k_B T/m_e}}\right]^{\left(\frac{T_o^X}{T+T_o^X}\right)} [\mathrm{N_c}]^{\left(\frac{\mathrm{T}}{T+T_o^X}\right)} [\dot{D}]^{\left(\frac{T_o^X}{T+T_o^X}\right)} & ;\ \begin{array}{c}\text{exponential DOS with}\\[1ex] k_B T_o^X \gg E_F^{eff} \gtrsim 2k_B T > 0\end{array} \\[3ex]

\left[\dfrac{p\,N_T}{s_C E_{eh}\sqrt{3k_B T/m_e}}\right]\dot{D} & ;\ \begin{array}{c}\text{uniform DOS with}\\[0.5ex] E_F^{eff} \gg k_B T \text{ and}\\[0.5ex] 0 < E_F^{eff} < E_1^U < E_2^U\end{array} \\[3ex]

N_c \exp\left\{W_0^+\left[\dfrac{s_C E_{eh}\sqrt{3k_B T/m_e}}{\dot{D}\,p}\left(\dfrac{N_c}{N_T}\right)\exp\left(\dfrac{E_2^U}{k_B\mathrm{T}}\right)\right]+\dfrac{E_2^U}{k_B\mathrm{T}}\right\} & ;\ \begin{array}{c}\text{uniform DOS with}\\[0.5ex] \left(E_F^{eff}-E_1^U\right)\gg k_B T \text{ and}\\[0.5ex] 0\le E_1^U < E_F^{eff} < E_2^U\end{array} \\[3ex]

0 & ;\ \begin{array}{c}\text{uniform DOS with}\\[0.5ex] \left(E_F^{eff}-E_2^U\right)\gg k_B T > 0 \text{ and}\\[0.5ex] 0\le E_1^U < E_2^U < E_F^{eff}\end{array} \\[3ex]

\begin{aligned}&\left\{\left[\dfrac{k_B T}{(E_2^U-E_1^U)}\right]^{1/2}\exp\left[-\dfrac{E_2^U}{2\,k_B T}\right]\right\}\\[1ex] &\times\left[\dfrac{p\,N_T}{s_C E_{eh}\sqrt{3k_B T/m_e}}\right]^{1/2}[N_c]^{1/2}[\dot{D}]^{1/2}\end{aligned} & ;\ \begin{array}{c}\text{uniform DOS with}\\[0.5ex] \left(E_F^{eff}-E_2^U\right)\gtrsim 2\,k_B T > 0 \text{ and}\\[0.5ex] 0\le E_1^U < E_2^U < E_F^{eff}\end{array} \\[3ex]

\left[\dfrac{p\,N_T}{s_C E_{eh}\sqrt{3k_B T/m_e}}\right]\dot{D} & ;\ \begin{array}{c}\text{delta function DOS with}\\[0.5ex] \left(E_F^{eff}-E_o^t\right) < 0\end{array} \\[3ex]

0 & ;\ \begin{array}{c}\text{delta function DOS with}\\[0.5ex] \left(E_F^{eff}-E_o^t\right)\gg k_B T > 0\end{array}
\end{cases}
$$

$$(G.26)$$

Some additional comments are required for the uniform case with E_F^{eff} within the distribution, with $0 \le E_1^U < E_F^{eff} < E_2^U$. Here $W_0^+(z)$ is the real-valued upper principle branch of the Lambert W function, since the argument in Eq. (G.26) is positive definite. The defining equation for $W(z)$ is $z=W(z)\cdot e^{[W(z)]}$. Evaluation of $n_c(T)$ for this case in general requires numerical calculations. However, the restriction $\left(E_F^{eff}-E_2^U\right)\gg k_B T$ suggests that $\left(E_{F0}^{eff}-E_2^U\right)\gg E_{F0}^{eff}\,\xi\,k_B T$ and, therefore, $E_F^{eff}(T)\approx E_{F0}^{eff}$. This approximation shows $n_c \propto T^{-1/2}$, with temperature dependence only through v_T. Likewise, for this case, Rose (1951) argued that as long as E_F^{eff} remained confined to within the uniform distribution that n_c was nearly temperature-independent. Equation (G.26) becomes

$$n_c(T) =$$

$$
\begin{cases}
\left[\dfrac{p\,N_T}{s_C E_{eh}\sqrt{3k_B T/m_e}}\right]^{\left(\frac{T_o^X}{T+T_o^X}\right)} [N_c]^{\left(\frac{T}{T+T_o^X}\right)} [\dot{D}]^{\left(\frac{T_o^X}{T+T_o^X}\right)} & ; & \text{exponential DOS with } T \to 0\text{ K} \\[2em]

\left\{\dfrac{T}{T_o^X}\right\}\left[\dfrac{p\,N_T}{s_C E_{eh}\sqrt{3k_B T/m_e}}\right]^{\left(\frac{T_o^X}{T+T_o^X}\right)} [N_c]^{\left(\frac{T}{T+T_o^X}\right)} [\dot{D}]^{\left(\frac{T_o^X}{T+T_o^X}\right)} & ; & \begin{array}{c}\text{exponential DOS with}\\[0.5em] k_B T_o^X \gg E_F^{eff} \gtrsim 2k_B T > 0 \end{array} \\[2em]

\left[\dfrac{p\,N_T}{s_C E_{eh}\sqrt{3k_B T/m_e}}\right]\dot{D} & ; & \begin{array}{c}\text{uniform DOS with}\\[0.3em] E_F^{eff} \gg k_B T \text{ and } 0 < E_F^{eff} < E_1^U < E_2^U \end{array} \\[2em]

\left\{\dfrac{\left(E_2^U - E_{F0}^{eff}\right)}{2\,k_B T_o^U}\right\}\left[\dfrac{p\,N_T}{s_C E_{eh}\sqrt{3k_B T/m_e}}\right]\dot{D} & ; & \begin{array}{c}\text{uniform DOS with}\\[0.3em] \left(E_F^{eff} - E_1^U\right) \gg k_B T \text{ and}\\[0.3em] 0 \le E_1^U < E_F^{eff} < E_2^U\end{array} \\[2em]

0 & ; & \begin{array}{c}\text{uniform DOS with}\\[0.3em] \left(E_F^{eff} - E_2^U\right) \gg k_B T > 0 \text{ and}\\[0.3em] 0 \le E_1^U < E_2^U < E_F^{eff}\end{array} \\[2em]

\begin{aligned}&\left\{\left[\dfrac{k_B T}{\left(E_2^U - E_1^U\right)}\right]^{1/2} exp\left[-\dfrac{E_2^U}{2\,k_B T}\right]\right\}\\ &\times \left[\dfrac{p\,N_T}{s_C E_{eh}\sqrt{3k_B T/m_e}}\right]^{1/2}[N_c]^{1/2}[\dot{D}]^{1/2}\end{aligned} & ; & \begin{array}{c}\text{uniform DOS with}\\[0.3em] \left(E_F^{eff} - E_2^U\right) \gtrsim 2\,k_B T > 0 \text{ and}\\[0.3em] 0 \le E_1^U < E_2^U < E_F^{eff}\end{array} \\[2em]

\left[\dfrac{p\,N_T}{s_C E_{eh}\sqrt{3k_B T/m_e}}\right]\dot{D} & ; & \begin{array}{c}\text{delta function DOS with}\\[0.3em] \left(E_F^{eff} - E_o^t\right) < 0\end{array} \\[2em]

0 & ; & \begin{array}{c}\text{delta function DOS with}\\[0.3em] \left(E_F^{eff} - E_o^t\right) \gg k_B T > 0\end{array}
\end{cases}
\quad . \text{ (G.27)}
$$

Finally, σ_{RIC}, is predicted to be

$$\sigma_{RIC} = q_e \mu_e^{NF} n_c$$

$$= q_e \mu_e \left(\frac{m_e}{m_e^*} \varepsilon_r^2 \right) \times$$

$$
\begin{cases}
\left[\frac{p\,N_T}{s_C E_{eh}\sqrt{3k_B T/m_e}} \right]^{\left(\frac{T_o^X}{T+T_o^X}\right)} [N_c]^{\left(\frac{T}{T+T_o^X}\right)} [\dot{D}]^{\left(\frac{T_o^X}{T+T_o^X}\right)} & ; & \text{exponential DOS with } T \to 0\ \text{K} \\[3ex]
\left\{ \frac{T}{T_o^X} \right\} \left[\frac{p\,N_T}{s_C E_{eh}\sqrt{3k_B T/m_e}} \right]^{\left(\frac{T_o^X}{T+T_o^X}\right)} [N_c]^{\left(\frac{T}{T+T_o^X}\right)} [\dot{D}]^{\left(\frac{T_o^X}{T+T_o^X}\right)} & ; & \text{exponential DOS with} \\
& & k_B T_o^X \gg E_F^{eff} \gtrsim 2 k_B T > 0 \\[3ex]
\left[\frac{p\,N_T}{s_C E_{eh}\sqrt{3k_B T/m_e}} \right] \dot{D} & ; & \begin{array}{c} \text{uniform DOS with} \\ E_F^{eff} \gg k_B T \text{ and} \\ 0 < E_F^{eff} < E_1^U < E_2^U \end{array} \\[3ex]
\left\{ \frac{\left(E_2^U - E_{F0}^{eff} \right)}{2\,k_B T_o^U} \right\} \left[\frac{p\,N_T}{s_C E_{eh}\sqrt{3k_B T/m_e}} \right] \dot{D} & ; & \begin{array}{c} \text{uniform DOS with} \\ \left(E_F^{eff} - E_1^U \right) \gg k_B T \text{ and} \\ 0 \le E_1^U < E_F^{eff} < E_2^U \end{array} \\[3ex]
0 & ; & \begin{array}{c} \text{uniform DOS with} \\ \left(E_F^{eff} - E_2^U \right) \gg k_B T > 0 \text{ and} \\ 0 \le E_1^U < E_2^U < E_F^{eff} \end{array} \\[3ex]
\begin{aligned} & \left\{ \left[\frac{k_B T}{(E_2^U - E_1^U)} \right]^{1/2} exp\left[-\frac{E_2^U}{2\,k_B T} \right] \right\} \\ & \times \left[\frac{p\,N_T}{s_C E_{eh}\sqrt{3k_B T/m_e}} \right]^{1/2} [N_c]^{1/2} [\dot{D}]^{1/2} \end{aligned} & ; & \begin{array}{c} \text{uniform DOS with} \\ \left(E_F^{eff} - E_2^U \right) \gtrsim 2\,k_B T > 0 \\ \text{and } 0 \le E_1^U < E_2^U < E_F^{eff} \end{array} \\[3ex]
\left[\frac{p\,N_T}{s_C E_{eh}\sqrt{3k_B T/m_e}} \right] \dot{D} & ; & \begin{array}{c} \text{delta function DOS with} \\ \left(E_F^{eff} - E_o^t \right) < 0 \end{array} \\[3ex]
0 & ; & \begin{array}{c} \text{delta function DOS with} \\ \left(E_F^{eff} - E_o^t \right) \gg k_B T > 0 \end{array}
\end{cases}
$$

$$\text{(G.28)}$$

using Eq. (2.0.1) with Eqs. (G.1) and (G.5).

Standard RIC theory (Fowler, 1956a; Frederickson, 1977; Sim, 2013) predicts that σ_{RIC} is primarily dependent on the radiation dose rate, $\dot{D}$, (a measure of the energy deposited per unit time and unit mass) raised to the power Δ through a power law

$$\sigma_{RIC}(\dot{D}) = k_{RIC}(T)\,\dot{D}^{\Delta(T)} \tag{G.29}$$

with a proportionality constant, k_{RIC}. Both k_{RIC} and Δ are temperature-dependent material parameters. By comparing Eq. (G.29) with Eq. (G.28), Δ and k_{RIC} are seen to be

$$\Delta(T) \begin{cases} \left[\dfrac{T_o^X}{T+T_o^X}\right] & ; & \text{exponential DOS with } T \to 0 \text{ K} \\[2ex] \left[\dfrac{T_o^X}{T+T_o^X}\right] & ; & \text{exponential DOS with } k_B T_o^X \gg E_F^{eff} \gtrsim 2k_B T > 0 \\[2ex] 1 & ; & \text{uniform DOS with } E_F^{eff} \gg k_B T \text{ and } 0 < E_F^{eff} < E_1^U < E_2^U \\[1ex] 1 & ; & \text{uniform DOS with } \left(E_F^{eff} - E_1^U\right) \gg k_B T \text{ and } 0 \le E_1^U < E_F^{eff} < E_2^U \\[1ex] 1 & ; & \text{uniform DOS with } \left(E_F^{eff} - E_2^U\right) \gg k_B T > 0 \text{ and } 0 \le E_1^U < E_2^U < E_F^{eff} \\[1ex] {}^1\!/_2 & ; & \text{uniform DOS with } \left(E_F^{eff} - E_2^U\right) \gtrsim 2 k_B T > 0 \text{ and } 0 \le E_1^U < E_2^U < E_F^{eff} \\[1ex] 1 & ; & \text{delta function DOS with } \left(E_F^{eff} - E_o^t\right) < 0 \\[1ex] 1 & ; & \text{delta function DOS with } \left(E_F^{eff} - E_o^t\right) \gg k_B T > 0 \end{cases} \quad \text{and}$$

(G.30)

$$k_{RIC}(T) =$$

$$\left[q_e \mu_e \left(\frac{m_e}{m_e^*} \varepsilon_r{}^2\right)\right] \times$$

$$\begin{cases} \left[\dfrac{p\,N_T}{s_C E_{eh}\sqrt{3k_B T/m_e}}\right]^{\left(\frac{T_o^X}{T+T_o^X}\right)} [N_c]^{\left(\frac{T}{T+T_o^X}\right)} & ; & \text{exponential DOS with } T \to 0 \text{ K} \\[3ex] \left\{\dfrac{T}{T_o^X}\right\}\left[\dfrac{p\,N_T}{s_C E_{eh}\sqrt{3k_B T/m_e}}\right]^{\left(\frac{T_o^X}{T+T_o^X}\right)} [N_c]^{\left(\frac{T}{T+T_o^X}\right)} & ; & \text{exponential DOS with } k_B T_o^X \gg E_F^{eff} \gtrsim 2k_B T > 0 \\[3ex] \left[\dfrac{p\,N_T}{s_C E_{eh}\sqrt{3k_B T/m_e}}\right] & ; & \begin{array}{c}\text{uniform DOS with}\\ E_F^{eff} \gg k_B T \text{ and } 0 < E_F^{eff} < E_1^U < E_2^U\end{array} \\[3ex] \left\{\left(\dfrac{E_2^U - E_{F0}^{eff}}{2\,k_B T_o^U}\right)\right\}\left[\dfrac{p\,N_T}{s_C E_{eh}\sqrt{3k_B T/m_e}}\right] & ; & \begin{array}{c}\text{uniform DOS with}\\ \left(E_F^{eff} - E_1^U\right) \gg k_B T \text{ and } 0 \le E_1^U < E_F^{eff} < E_2^U\end{array} \\[3ex] 0 & ; & \begin{array}{c}\text{uniform DOS with}\\ \left(E_F^{eff} - E_2^U\right) \gg k_B T > 0 \text{ and } 0 \le E_1^U < E_2^U < E_F^{eff}\end{array} \\[3ex] \left\{\left[\dfrac{k_B T}{(E_2^U - E_1^U)}\right]^{1/2} exp\left[-\dfrac{E_2^U}{2\,k_B T}\right]\right\} \\ \times \left[\dfrac{p\,N_T}{s_C E_{eh}\sqrt{3k_B T/m_e}}\right]^{1/2} [N_c]^{1/2} [\dot{D}]^{1/2} & ; & \begin{array}{c}\text{uniform DOS with}\\ \left(E_F^{eff} - E_2^U\right) \gtrsim 2 k_B T > 0 \text{ and } 0 \le E_1^U < E_2^U < E_F^{eff}\end{array} \\[3ex] \left[\dfrac{p\,N_T}{s_C E_{eh}\sqrt{3k_B T/m_e}}\right] & ; & \text{delta function DOS with } \left(E_F^{eff} - E_o^t\right) < 0 \\[3ex] 0 & ; & \text{delta function DOS with } \left(E_F^{eff} - E_o^t\right) \gg k_B T > 0 \end{cases}$$

(G.31)

Evaluation of k_{RIC} and Δ for the general uniform case requires numerical calculations.

Δ is usually found to be between 0.5 and 1.0, with higher values being more common; this is consistent with Eq. (G.31). In the low temperature limit when $T \ll T_o^X$, $\Delta \rightarrow 1$, and to a good approximation is temperature-independent. When $T \rightarrow T_o^X$, $\Delta \rightarrow 0.5$, and small changes in T have a large effect on Δ. Since $T > 0$, the upper bound on Δ is 1. As $T \rightarrow T_o^X$, essentially all trap states have been emptied by thermal excitations (equivalent to the plateau observed for thermally assisted conduction for a bulk homogeneous, semiconducting material); hence, the model is not applicable for $T > T_o^X$. As can be seen in Eqs. (G.30) and (G.31), the temperature dependence of k_{RIC} and Δ can provide an indication of the extent to which a material has a delta function or uniform trap distribution or an exponential trap distribution. k_{RIC} is comparatively small for most organic dielectrics, as compared with inorganic dielectrics, which can be two or more orders of magnitude higher.

For the sake of clarity in discussing the theoretical behavior of k_{RIC}, consider three quantities $0 \leq K_0 \leq 1$, K_1, and N_C such that

$$K_0(T) =$$

$$\left[q_e \mu_e \left(\frac{m_e}{m_e^*} \varepsilon_r^{\,2} \right) \right] \times$$

$$\begin{cases}
1 & ; & \text{exponential DOS with } T \rightarrow 0 \text{ K} \\
\left\{ \frac{T}{T_o^X} \right\} & ; & \text{exponential DOS with } k_B T_o^X \gg E_F^{eff} \gtrsim 2 k_B T > 0 \\
1 & ; & \begin{array}{c} \text{uniform DOS with} \\ E_F^{eff} \gg k_B T \text{ and } 0 < E_F^{eff} < E_1^U < E_2^U \end{array} \\
\left\{ \frac{\left(E_2^U - E_{F0}^{eff} \right)}{2\, k_B T_o^U} \right\} & ; & \begin{array}{c} \text{uniform DOS with} \\ \left(E_F^{eff} - E_1^U \right) \gg k_B T \text{ and } 0 \leq E_1^U < E_F^{eff} < E_2^U \end{array} \\
0 & ; & \begin{array}{c} \text{uniform DOS with} \\ \left(E_F^{eff} - E_2^U \right) \gg k_B T > 0 \text{ and } 0 \leq E_1^U < E_2^U < E_F^{eff} \end{array} \\
\left\{ [N_c]^{1/2} \left[\frac{k_B T}{\left(E_2^U - E_1^U \right)} \right]^{1/2} exp\left[-\frac{E_2^U}{2\, k_B T} \right] \right\} & ; & \begin{array}{c} \text{uniform DOS with} \\ \left(E_F^{eff} - E_2^U \right) \gtrsim 2\, k_B T > 0 \text{ and } 0 \leq E_1^U < E_2^U < E_F^{eff} \end{array} \\
1 & ; & \text{delta function DOS with } \left(E_F^{eff} - E_o^t \right) < 0 \\
0 & ; & \text{delta function DOS with } \left(E_F^{eff} - E_o^t \right) \gg k_B T > 0
\end{cases} ,$$

$$\text{(G.32)}$$

$$K_1(T) = \left[\frac{p\, N_T}{s_C E_{eh} \sqrt{3 k_B T / m_e}} \right] \quad \text{, and} \tag{G.33}$$

$$N_C(T) = 2 \left(\frac{m_e k_B T}{2\pi\hbar^2} \right)^{3/2} \left(\frac{m_e^* m_h^*}{m_e m_h} \right)^{3/4} . \tag{G.34}$$

In terms of these quantities, k_{RIC} is

$$k_{RIC}(T) = K_0(T) \left[K_1(T)^{\Delta(T)} \right] N_C(T)^{[1 - \Delta(T)]} . \tag{G.35}$$

In the limit of a delta function trap distribution or a low temperature limit when $T \ll T_o^A$, and the exponents for K_1 and N_C reduce to 1 and 0, respectively. The temperature dependence for this case is found in the denominator of the product of K_0 and K_1. It is, however, overwhelmed by $(T_o^A)^2$, so that k_{RIC} is expected to be temperature-independent. In the limiting case of an exponential trap distribution, or when $T \to T_o^X$, the exponents in Eq. (G.33) become highly temperature-dependent.

To summarize overall RIC behavior, materials having a delta function or uniform distribution of traps below the conduction band are expected to have Δ values of approximately 1.0 and to have nearly temperature-independent conductivities. Materials having an exponential distribution, on the other hand, are expected to have Δ values of less than 1 and have more highly temperature-dependent conductivities.

APPENDIX H

DENSITY OF STATES MODELS

We consider a series of models for the energy distribution of the localized defect states (termed the density of states or DOS) found between the mobility edges in highly disordered insulating materials. For a general discussion of DOS, one must consider two types of distributions, one that monotonically decreases below the band edge (or equivalently, that has a peak at energies in the CB) and one that shows a peak in the distribution within the band gap. Stated another way, the two types of distributions have their maximum amplitude at either $E_o^t \leq 0$ or $E_o^t > 0$, respectively. An exponential (or power law) and a Gaussian DOS are appropriate models for these two general types for localized DOS. For the sake of completeness and to make ties to older literature, we consider seven specific DOS modes as shown in Table H.1 and Fig. H.1. These are three monotonically decreasing models (exponential, power law, and linear) and two peaked models (Gaussian and delta function), plus a limiting cases with a uniform DOS for each. Taken together these seven models represent nearly all the expressions used in the literature to describe transport in disordered materials. Sim (2013) provides additional details of these DOS models and a discussion of their use in various electron transport processes and their appearance in the related literature.

Analytic expressions for these distributions are listed in column 2 of Table H.1. Some comments about notation used in Table H.1 are warranted:

1) $\Theta(E)$ is a Heaviside step function, equal to 0 at $E < 0$ and 1 at $E > 0$.

2) $\Phi(E, E_o^T, E_o^G)$ is the cumulative probability distribution function for a Gaussian with mean E_o^T and standard deviation, E_o^G, that is, the probability of the Gaussian distribution function from $-\infty$ to E.

3) $erf(E)$ is the error function evaluated at E.

4) $\delta(E)$ is the Dirac delta function, equal to infinity at E and zero elsewhere.

All the DOS are functions of energy measured from CB edge toward the VB. This is often a source of confusion in the literature, as many authors measure energy from the center of a distribution. All distributions are normalized such that the total defect density, N_t, is obtained by integrating the distribution over the entire bandgap (BG). That is,

$$N_t = \int_0^\infty n_A(E)dE \quad . \tag{H.1}$$

Each distribution has an energy width and corresponding temperature associated with it of the form $E_o^A \equiv k_B T_o^A$ with $A = X$ for exponential, $A = P$ for power law, $A = L$ for linear, $A = U$ for uniform, $A = G$ for Gaussian and $A = D$ for delta function (see Table D.1, column 3).

Each distribution also has an energy centroid (or first moment) associated with it (see Table H.1, column 4). This mean energy of all (occupied and unoccupied) states within the BG is

$$E_{centroid} = \left[\int_0^\infty E\, n_A(E)dE\right]/\left[\int_0^\infty n_A(E)dE\right] = \frac{1}{N_T}\int_0^\infty E\, n_A(E)dE \quad . \tag{H.2}$$

For the decreasing distributions (exponential, power law, linear and uniform step) the centroid can be expressed in terms of the width, while for the peaked distributions (Gaussian, delta function and uniform top hat) there is an independent centroid, E_o^t, at the maximum of the trap distribution.

The mean energy of all occupied states within the BG is

$$\langle E_A \rangle = \left[\int_0^\infty E\, f_{FD}(E)\, n_A(E)dE\right]/\left[\int_0^\infty n_A(E)dE\right] = \frac{1}{N_T}\int_0^\infty E\, f_{FD}(E)\, n_A(E)dE \quad . \tag{H.3}$$

The temperature dependence of E_A is contained in the Fermi-Dirac distribution function, $f_{FD}(E)$, that describes occupation of the trap states:

$$f_{FD}(E) = \begin{cases} \left\{1 + exp\left[(E - E_F^{eff})/k_B T\right]\right\}^{-1} & ; & \text{all } T \\ \Theta\left(E - E_F^{eff}\right) & ; & T = 0\ K \\ \frac{1}{2}\left\{1 - \left[\frac{1}{2}(E - E_F^{eff})/k_B T\right]\right\} & ; & \text{low } T \\ exp\left[-\left(E - E_F^{eff}\right)/k_B T\right] & ; & \text{high T (Maxwell} - \text{Boltzmann distribution)} \end{cases} \tag{H.4}$$

Expressions at higher temperatures are not calculated explicitly here. For $T \rightarrow 0$ K,

$$\langle E_A \rangle_0 = \int_{E_F^{eff}}^\infty E\, n_A(E)d\varepsilon \quad . \tag{H.5}$$

The fraction of occupied state is

$$f_{A0} = \left[\int_0^\infty f_{FD}(E)\, n_A(E)dE\right] \Big/ \left[\int_0^\infty n_A(E)dE\right] = \frac{1}{N_T}\int_0^\infty f_{FD}(E)\, n_A(E)dE \quad . \tag{H.6}$$

For $T \to 0$ K,

$$f_{A0} = \frac{1}{N_T}\int_{E_F^{eff}}^\infty n_A(E)dE \quad . \tag{H.7}$$

The fraction of occupied states at $T = 0$ K for each distribution is listed in column 5 of Table H.1. For the decreasing distributions (exponential, power law, linear and uniform step) f_{A0} can be expressed in terms of the width, E_o^A and E_F^{eff}. For the peaked distributions (Gaussian, delta function and uniform top hat), expressions for f_{A0} include E_o^A and E_F^{eff} and an additional independent centroid, E_o^t, at the maximum of the trap distribution. Specific comments about each of the DOS models follow.

Monotonically Decreasing DOS

  Exponential DOS: The exponential DOS is one of two prevalent models for HDIM and the primary DOS model used in this thesis. Note the width of the exponential DOS, E_o^X, is the width at $1/e$ amplitude. The exponential distribution is limited to zero for $E < 0$ using a Heaviside step function, $\Theta(E)$, which is equal to 0 at E < 0 and 1 at E > 0; the distribution extends nominally to $+\infty$. The exponential DOS can be expanded as a power series in small energies, $|E_o^t - E| \ll E_o^X \equiv k_b T_o^X$ —where T_o^X is called a characteristic temperature that determines the strength and shape of the DOS—leading to constant, linear or parabolic terms in the DOS:

$$N_X(E; E_o^X) = N_T \left[\frac{1}{e \cdot E_o^X}\right] \exp\left(\frac{E_o^T - E}{E_o^X}\right) = N_t \left[\frac{1}{e \cdot E_o^X}\right]\left\{1 - \left(\frac{E_o^T - E}{E_o^X}\right) + \frac{1}{2}\left(\frac{E_o^T - E}{E_o^X}\right)^2 + \cdots\right\} \quad . \tag{H.8}$$

This expansion emphasizes the relation of the exponential DOS to the power law, linear and uniform step DOS.

  Power law DOS: This model follows reasonably from the power law-like behavior of conduction band states in crystalline materials, such as Eq. (2.2.6) for which the power $p \to 1/2$. It was used in the early descriptions of energetically dependent DOS models for HDIM. The width of the power law DOS is set to E_o^P using the Heaviside step function, such that the distribution is zero at $E > E_o^P \equiv k_b T_o^P$.

Linear DOS: The linear DOS was used in the early analytical and computational descriptions of energetically dependent DOS models for HDIM. The width of the linear DOS is set to ε_o^L using the Heaviside step function, such that the distribution is zero at $E > E_o^L \equiv k_b T_o^L$. The linear DOS is a special case of the Power law DOS, with $p = 1$.

Uniform step DOS: The uniform or constant DOS is perhaps the most well known model, as it was first used (in a slightly different form) to describe VRH [see Sim (2013) and references therein]. The low energy bound of this DOS is set to $E = 0$. The width of the uniform DOS is set to E_o^U using the Heaviside step function, such that the distribution is zero at $0 > E > E_o^U \equiv k_b T_o^U$. The uniform step DOS is a special case of the Power law DOS with $p = 0$, although it differs in that it is not strictly a monotonically decreasing function. A closely related distribution with a constant density of states at all energies (i.e., $E_o^U \to +\infty$) has the interesting property that is a limiting case for both the exponential ($E_o^X \equiv k_b T_o^X \to \infty$) and Gaussian $E_o^G \equiv k_b T_o^G \to \infty$) DOS's in the limit of infinite width. Alternately, the uniform step DOS is the limiting case for the uniform top hat DOS model with $E_1^U \to 0$. Refer to Sim (2013) and references therein for further details and applications of these limiting cases.

Peaked DOS

Gaussian DOS: This DOS distribution is the second prevalent model used to describe HDIM, for DOS that are peaked in the BG. The width of the energetic distribution is given by $2E_o^G$ and the center of the distribution is E_o^t. Note the width of the Gaussian DOS is twice the standard deviation of the normal distribution, E_o^G. The distribution extends nominally to $+\infty$, but is truncated for $E < 0$ using a Heaviside step function, $\Theta(E)$. Note the additional factor of $[1 - \Phi(0, E_o^t, E_o^G)]^{-1} = \left[\frac{1}{2} - erf\left(\frac{-E_o^t}{\sqrt{2} \cdot E_o^G}\right)\right]^{-1}$, which accounts for normalization due to this truncation. $\Phi(E, E_o^t, E_o^G)$ is the cumulative probability distribution function for a Gaussian with mean E_o^t and standard deviation E_o^G, which is the probability of the Gaussian distribution function from $-\infty$ to E_o^t. $erf(E)$ is the error function evaluated at E. The Gaussian DOS can be expanded as a power series in small energies, with $|E_o^t - E| \ll E_o^G \equiv k_b T_o^G$ leading to constant or parabolic terms in the DOS:

$$N_G(E; E_o^t, E_o^G) = N_T \left[\frac{1}{\sqrt{2\pi}\, E_o^G}\right] \exp\left[-\frac{1}{2}\left(\frac{E_o^t - E}{E_o^G}\right)^2\right] = N_t \left[\frac{1}{\sqrt{2\pi}\, E_o^G}\right]\left\{1 - 2\left(\frac{E_o^t - E}{2E_o^G}\right)^2 + \frac{1}{2}\left(\frac{E_o^t - E}{2E_o^G}\right)^4 + \cdots\right\} \quad \text{.(H.9)}$$

This expansion emphasizes the relation of the Gaussian DOS to the power law and uniform top hat DOS. It can be seen if E_o^G is large or the energy (as measured from the center, E_o^t) is very small, this system should act like a constant (energy-independent DOS). Conversely, if the width of the distribution $E_o^G \rightarrow 0$, then the Gaussian DOS will act like a delta function (Jackson, 1975).

Delta function DOS: Perhaps the oldest DOS model is the delta function, with a single well defined trap energy, E_o^t. It is useful in many applications: examples are singly doped crystalline semiconductors, narrow distributions of trap states, and distributions where the Fermi level or the effective Fermi level is pinned at a constant value. In addition, in complex dynamic trapping models where analytical solutions are difficult, the use of this DOS allows for a first order expression of the model. The delta function model is a limiting case of a Gaussian DOS, with a negligible width $E_o^G \equiv k_b T_o^G \rightarrow 0$. $\delta(E)$ is the Dirac delta function, equal to infinity at E and zero elsewhere.

Uniform top hat DOS: This uniform or constant DOS differs from the monotonically decreasing uniform step DOS in that the low energy bound of this DOS is set to $E_1^U > 0$. This DOS model has been used by Friedel (1969) to describe the DOS of d electrons in transition metals (Harrison, 1989). The width of the uniform DOS is set to $E_o^U = E_2^U - E_1^U \equiv k_b T_o^U$ using two Heaviside step functions, such that the distribution is nonzero at $0 > E_1^U > E > E_2^U$. This distribution is similar to a truncated Gaussian DOS in the limit of infinite width, $E_o^G \equiv k_b T_o^G \rightarrow \infty$ or a delta function DOS with finite width.
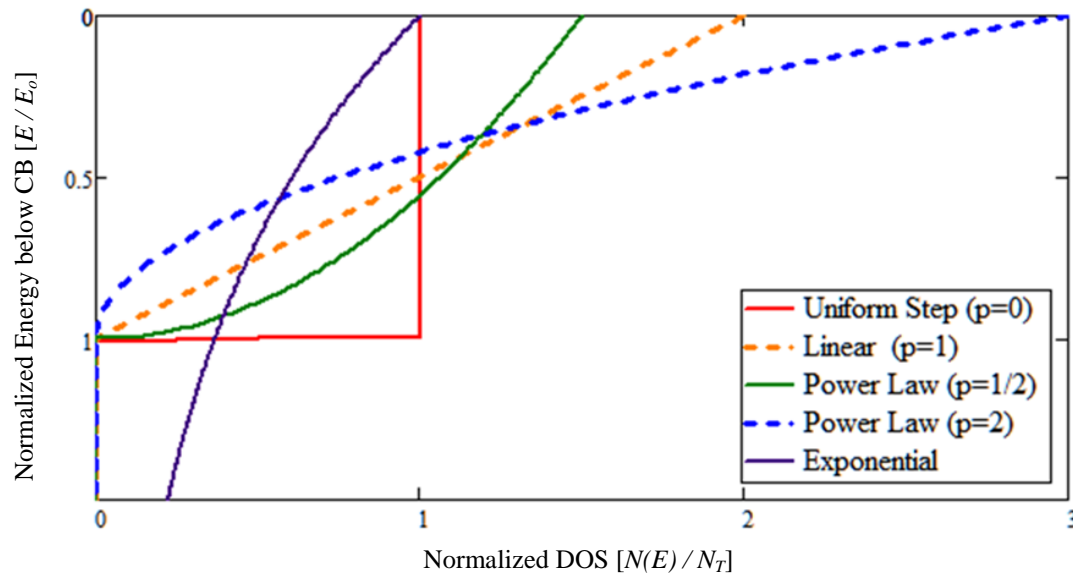
(a)
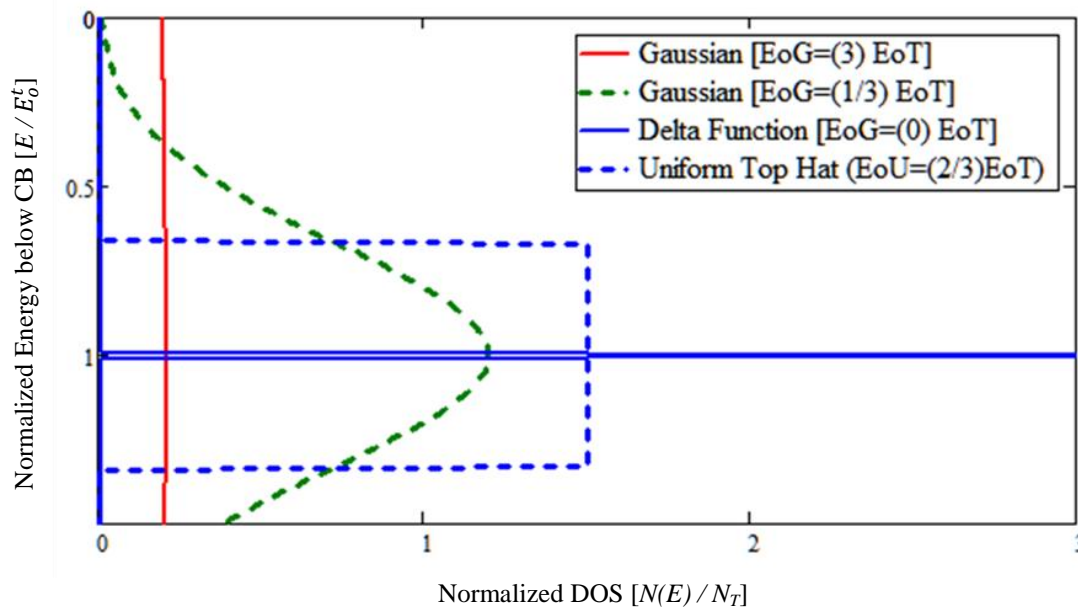
(b)

FIG. H.1. DOS models for HDIM. The graphs plot the normalized energy below the conduction band edge as a function of the normalized DOS, $n_A(E) / N_T$. (a) Monotonically decreasing DOS models, including the linear, power law and exponential models, as well as the limiting case uniform model. Power law distributions are shown for two cases, $p = \frac{1}{2} < 1$ and $p = 2 > 1$. The energies are normalized by dividing by the width of the distributions, E_o^A. (b) Peaked DOS models, including the Gaussian and delta function models. Gaussian distributions are shown for two cases, $(E_o^G / E_o^t) = \frac{1}{3} < 1$ and $(E_o^G / E_o^t) = 3 > 1$; the later approaches the limiting case uniform top hat model. The energies are normalized by dividing by the peak of the distributions, E_o^t.

TABLE H.1 Density of states models.

DOS Type	Normalized DOS Function	Width	Centroid*	Fraction of Filled Traps
Decreasing DOS ($E_o^t \leq 0$)				
Exponential	$n_X(E; E_o^X) = N_T \left[\dfrac{1}{e \cdot E_o^X} \right] \exp\left(\dfrac{E_o^X - E}{E_o^X} \right) \Theta(E)$	$E_o^X \left(\tfrac{1}{e} \text{ width} \right)$	$E_o^X = k_B T_o^X$	$\exp\left(\dfrac{-E_F^{eff}}{E_o^X} \right)$
Power Law	$n_P(E; E_o^p) = N_T \left[\dfrac{(p+1)}{E_o^p} \left(\dfrac{E_o^p - E}{E_o^p} \right)^P \right] \Theta(E_o^p - E)\, \Theta(E)$	E_o^p	$\left(\dfrac{1}{p+2} \right) E_o^p$	$\left(\dfrac{E_o^p - E_F^{eff}}{E_o^p} \right)^{(p+1)}$
Linear (Power Law, $p=1$)	$n_L(E; E_o^L) = N_T \left[\dfrac{2}{E_o^L} \left(\dfrac{E_o^L - E}{E_o^L} \right) \right] \Theta(E_o^L - E)\, \Theta(E)$	E_o^L	$\left(\dfrac{1}{3} \right) E_o^L$	$\left(\dfrac{E_o^L - E_F^{eff}}{E_o^L} \right)^2$
Uniform Step (Top Hat, $E_1^U \to 0$) (Power Law, $p=0$)	$n_{US}(E; E_o^U) = N_T \left[\dfrac{1}{E_o^U} \right] \Theta(E_o^U - E)\, \Theta(E)$	E_o^U	$\dfrac{1}{2} E_o^U$	$\left(\dfrac{E_o^U - E_F^{eff}}{E_o^U} \right)$
Peaked DOS ($E_o^t > 0$)				
Gaussian	$n_G(E; E_o^G, E_o^t) = N_T [1 - \Phi(0, E_o^t, E_o^G)]^{-1} \left[\dfrac{1}{\sqrt{2\pi} \cdot E_o^G} \exp\left[-\dfrac{1}{2}\left[\dfrac{(E_o^t - E)}{E_o^G} \right]^2 \right] \right] \Theta(E)$ $= N_T \left[1 + erf\left(\dfrac{E_o^t}{\sqrt{2} \cdot E_o^G} \right) \right]^{-1} \left[\dfrac{2}{\sqrt{2\pi} \cdot E_o^G} \exp\left[-\dfrac{1}{2}\left[\dfrac{(E_o^t - E)}{E_o^G} \right]^2 \right] \right] \Theta(E)$	$2\, E_o^G$ (2X Standard Deviation)	Centroid: $E_o^t + \dfrac{2}{\sqrt{2\pi}} \cdot E_o^G \left[1 + erf\left(\dfrac{E_o^t}{\sqrt{2} \cdot E_o^G} \right) \right]^{-1} e^{-\frac{1}{2}\left(E_o^t / E_o^G \right)^2}$	Mean Energy: $\left[1 + erf\left(\dfrac{E_o^t - E_F^{eff}}{\sqrt{2} \cdot E_o^G} \right) \right] \Big/ \left[1 + erf\left(\dfrac{E_o^t}{\sqrt{2} \cdot E_o^G} \right) \right]$
Delta Function (Gaussian, $E_n^G \to \infty$)	$n_D(E; E_o^t) = N_T\, \delta(E_o^t - E)$	$E_o^G \to 0$	E_o^t	1
Uniform Top Hat (Constant) (Gaussian, $E_o^G \to \infty$)	$n_{UT}(E; E_1^U, E_2^U) = N_T \left[\dfrac{1}{E_2^U - E_1^U} \right] \Theta(E_2^U - E)\, \Theta(E - E_1^U)$	$E_o^G \to \infty$ $E_o^U = E_2^U - E_1^U$	$E_o^t = \dfrac{1}{2}(E_2^U + E_1^U)$	$\left(\dfrac{E_o^U - E_F^{eff}}{E_o^U} \right)$

* Mean energy of trap state within band gap